Development of Advanced Plasma Surface Technologies for High Performance Carbon Paper Gas Diffusion Layer and 316 Stainless Steel Bipolar Plates

by

KAIJIE LIN

A thesis submitted to
the University of Birmingham
for the degree of
DOCTOR OF PHILOSOPHY

School of Metallurgy and Materials

College of Engineering and Physical Sciences

The University of Birmingham

August 2015

Synopsis

Proton exchange membrane fuel cells (PEMFC) have been regarded as one of the most promising alternative energy sources due to their high energy conversion efficiency and nearly zero greenhouse gas emissions. However, the wider commercialisation of this advanced energy conversion technique has been retarded by its high cost, mainly due to the expensive platinum catalyst layer and the high manufacturing cost of the graphite bipolar plates.

Therefore, this project was directed at generating novel multi-functional surfaces for high-performance, cost-effective and long-life PEMFC components (gas diffusion electrodes and bipolar plates) through developing innovative surface engineering technologies based on advanced active-screen plasma surface engineering.

In this work, a portfolio of novel active screen plasma (ASP) surface engineering technologies has been developed, including: active screen plasma surface modification of carbon paper for gas diffusion layer (GDL); and active screen plasma surface co-alloying of 316 austenitic stainless steel with both interstitial alloying element of nitrogen and substitutional alloying with elements such as silver (Ag), niobium (Nb) and platinum (Pt).

The active screen plasma surface modification of GDL carbon paper was treated at a low temperature (100 - 210 °C) for a short period of time (10 - 50 min) in a gas mixture of 25 % N_2 + 75 % H_2 and the results have shown that low temperature and short duration active screen plasma treatment can effective activate the carbon paper surface mainly due to the removal of the hydrophobic PTFE coating and introduction of many functional groups, thus contributing to the improved growth of Pt nano-wires. Accordingly, the electrochemical and catalysis performance can effectively be

improved by the ASP treated and Pt nano-wire coated carbon paper GDL in terms of increased electrochemical surface areas (ECSA) by 67 % and the increased output power density by up to 3 times.

The novel ASP surface alloying technique developed from this research has been applied to modify the 316 stainless steel surface using: nitrogen for active screen plasma nitriding (ASPN); nitrogen and silver (N&Ag); nitrogen and niobium (N&Nb); and nitrogen and platinum (N&Pt). The influence of ASP treatment parameters on the microstructure, interfacial contact resistance and corrosion resistance were fully studied.

The experimental results have demonstrated that the layer structure of the ASP treated 316 SS surfaces can be tailored by using different alloying elements and/or adjusting treatment parameters. The surface electrical conductivity of 316 SS can be reduced from 157.8 $m\Omega\ cm^2$ for the untreated materials to around 30, 18.9 ~ 24.4, 8.9 ~ 9.1, 6.4 ~ 6.9 $m\Omega\ cm^2$ by ASPN, ASPA(N&Ag), ASPA(N&Nb) and ASPA(N&Pt), respectively. The ASPN, ASPA(N&Ag) and ASPA(N&Nb) increase the corrosion potential, lower the corrosion current density and raise the passive current density of 316 SS.

Among all the surface alloying treatments, the active screen plasma co-alloying with nitrogen and platinum (ASPA(N&Pt)) treatment has delivered the best performance and fulfilled the technique target set by the Department of Energy (DoE), USA.

Acknowledgements

First and foremost, I would like to express my deep and sincere gratitude to my supervisor Prof. Hanshan Dong and co-supervisor Dr. Xiaoying Li for their advice, patient guidance and assistance throughout this study. I would also like to thank the School of Metallurgy and Materials, University of Birmingham and the China Scholarship Council for providing scholarships.

I am grateful for Dr. Shangfeng Du (School of Chemical Engineering, University of Birmingham) for conducting the electrochemical tests and his advice and cutting insight. I would also like to thank Dr. Yong Sun (De Montfort University) for allowing me to conduct corrosion resistance tests in his lab.

I would like to thank all the members of the surface engineering group for help and advice, including Dr. Linhai Tian, Dr Zhenxue Zhang, Dr. Yangchun Dong, Dr. Santiago Corujeira Gallo, Dr. Xia Luo, Dr. Ran Ji, Dr. Dennis Formosa, Miss Qiongxi Liu, Miss Shiling Zhang, Mr. Jun Zhou, Mr Ran Liu, Mr Shaojun Qi, Mr Xiaochao Ji and Miss Yana Liang. I would also like to thank the visiting scholars to our group, Dr. Xiaohua Zhang and Dr. Chunbei Wei.

Last but not least, I would like to express gratitude towards my family and my wife Ping Guo for their constant love and support through my study.

Publications

K. Lin, X. Li, X. Lou, Y. Sun, H. Dong, Active screen plasma nitriding of 316 stainless steel for the application of bipolar plates in proton exchange membrane fuel cells, International Journal of Hydrogen Energy (2014 39: 21470)

K. Lin, X. Li, L. Tian and H. Dong, Active screen plasma surface alloying of 316 stainless steel with nitrogen and niobium for the application of bipolar plates in PEMFCs, International Journal of Hydrogen Energy (2015 40 :10281)

S. Du, ***K. Lin,*** S. K. Malladi, Y. Lu, Q. Xu, R. Steinberger-Wilckens and H. Dong, Plasma nitriding induced growth of Pt-nanowire arrays as high performance electrocatalyst for fuel cells, Scientific Reports (4 : 6439) (IF : 5.078)

K. Lin, X. Li, L. Tian and H. Dong, Active screen plasma surface co-alloying treatments of 316 stainless steel with nitrogen and silver for fuel cell bipolar plates, Surface and coatings technology (under review)

Kaijie Lin**,** Linhai Tian, Xiaoying Li and Hanshan Dong, Development of novel plasma surface engineering technologies for multi-functional surfaces, IFHTSE 22nd Congress / European Conference on Heat Treatment (Paper No. : TT167)

S. Yang, K. Cooke, H. Sun, X. Li, ***K. Lin***, and H. Dong, Development of advanced duplex surface systems by combining CrAlN multilayer coatings with plasma nitrided steel substrates, Surface and Coatings Technology, (2013 236: 2–7)

Xiaoying Li, Linhai Tian, Wenbo Dou, ***Kaijie Lin***, and Hanshan Dong, Microstructure and corrosion wear resistance of plasma nitride LDX2101lead duplex stainless steel, China Surface Engineering, (2015, 28 (3))

Content

List of figures

List of tables

Chapter 1. Introduction

1.1 Background

Fossil fuels, such as petroleum, natural gas and coal, are the most important energy sources, which meet about 80% of the world energy demand nowadays [1]. However there are two issues relating to continued use of these resources. One is that after about half century [1] they will be depleted and the other is worldwide serious environment problems.

Many types of alternative energies have been researched during the last 25 years and a fuel cell is an excellent energy converter, which is more efficient and cleaner than current power generator [1]. The proton exchange membrane fuel cell (PEMFC) is one type of fuel cell, which uses hydrogen and oxygen as fuels, and the byproducts are pure water and heat. The catalyst layer and bipolar plate are important components in the PEMFC stacks. However, the high cost of the catalyst (usually platinum) and the high cost of fabricating bipolar plates (currently graphite), have retarded the wider application of PEMFCs [1].

To reduce the high cost of the platinum catalyst, many efforts have been made to develop non-precious metal catalysts [16] [18]. However, the reduction of cost is achieved at the expense of performance and/or durability [36]. One promising approach is to produce platinum nano-wires as a catalyst layer, which provides much larger electrochemical surface area (ECSA) than that of the bulk materials, thus lowering the Pt loading [2]. But this wet chemical process is adversely affected by the hydrophobicity property of the catalyst supporting layer (gas diffusion layer, GDL), leading to the undesirable growth of Pt catalyst. To the author's knowledge, little

work has been conducted to modify the GDL surface in order to enhance the growth of the platinum catalyst layer.

316L stainless steel is considered to be a good candidate to replace the current graphite bipolar plates, due to its relatively low cost and good mechanical properties. However, the corrosion behaviour and the interfacial contact resistance (ICR) of 316 stainless steel in the acidic PEMFC operating environment are still major concerns. Much effort has been devoted to modifying the surface of 316 stainless steel bipolar plates, such as physical vapour deposition, or ion implantation [3] [4]. However, the performance of those modified 316 stainless steel hasn't satisfied the requirement set by Department of Energy, USA.

1.2 Aims and objectives

The overall aim of this project was to generate novel multi-functional surfaces for high-performance, cost-effective and long-life PEMFC components (gas diffusion layers and bipolar plates) through developing innovative surface engineering technologies based on advanced active-screen plasma surface engineering. The specific scientific and technological objectives are:

- To develop a novel active-screen plasma surface modification technique to modify GDL surfaces, in order to improve its wettability, promote the growth of Pt catalyst layer on its surface and enhance the catalysis performance of the catalyst layer.
- To develop novel active-screen plasma surface co-alloying technology for 316 stainless steel bipolar plates to improve their surface electrical conductivity and corrosion resistance.

- To characterise the surface morphology, phase constituents, chemical composition, microstructure of the active-screen plasma modified gas diffusion layer and active-screen plasma co-alloyed 316 stainless steel.
- To evaluate the electrochemical and catalysis performance of Pt catalyst layer grown on active screen plasma modified GDL surface; to assess the ICR and corrosion resistance of the active screen plasma surface alloyed 316 stainless steel surfaces.
- To investigate the mechanisms involved in the active-screen plasma modification of GDL and bipolar plates and the resulting properties enhancement to advance scientific understanding.

Chapter 2. Literature review

2.1 Introduction to fuel cells

In 1839, William Grove discovered the basic principle of fuel cells by reversing water electrolysis to generate electricity from hydrogen and oxygen [1].

A fuel cell is an electrochemical power source designed to directly convert chemical energy, stored in fuels (such as hydrogen and methanol), to electrical energy. Because the process is based on an one-step reaction, without other energy conversions [5], the fuel cell is much more efficient than conventional thermal engines and the efficiency of its electrical energy conversion process can reach values as high as 60% (proton exchange membrane fuel cell) [1]. Compared with other electrochemical power sources, such as batteries, the fuel cell exhibits extended working duration, without periodic replacement, as long as it is continuously supplied with reactants and the reaction products are eliminated [5]. When hydrogen and oxygen are used as fuels, the only byproduct of the conversion process is pure water. Therefore, a fuel cell is a so-called 'zero-emission engine'. The working principle of fuel cells is schematically shown in Figure 2.1.1.

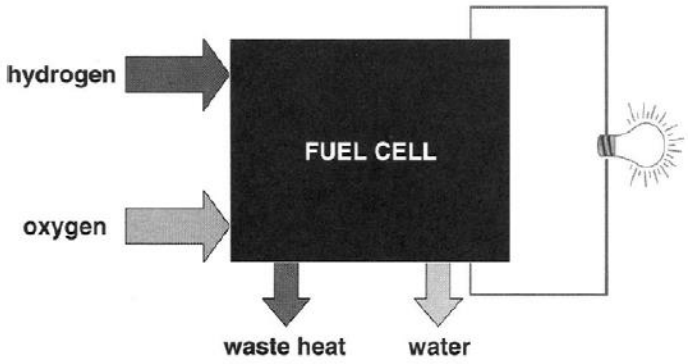

Figure 2.1.1 The working principle of Fuel Cells [1]

Fuel cells can be classified by the electrolyte they use and six categories of fuel cells have received major attention (Figure 2.1.2), namely: (1) direct methanol fuel cells (DMFCs), (2) solid oxide fuel cells (SOFCs), (3) alkaline fuel cells (AFCs), (4) phosphoric acid fuel cells (PAFCs), (5) molten carbonate fuel cells (MCFCs) and (6) polymer electrolyte membrane fuel cells or proton exchange membrane fuel cells (PEMFCs). Among them, PEMFCs have received great attention in many applications, especially transportation, due to their low noise, low working temperature and quick-start. Therefore, PEMFC is the type of fuel cell of interest to this project [1].

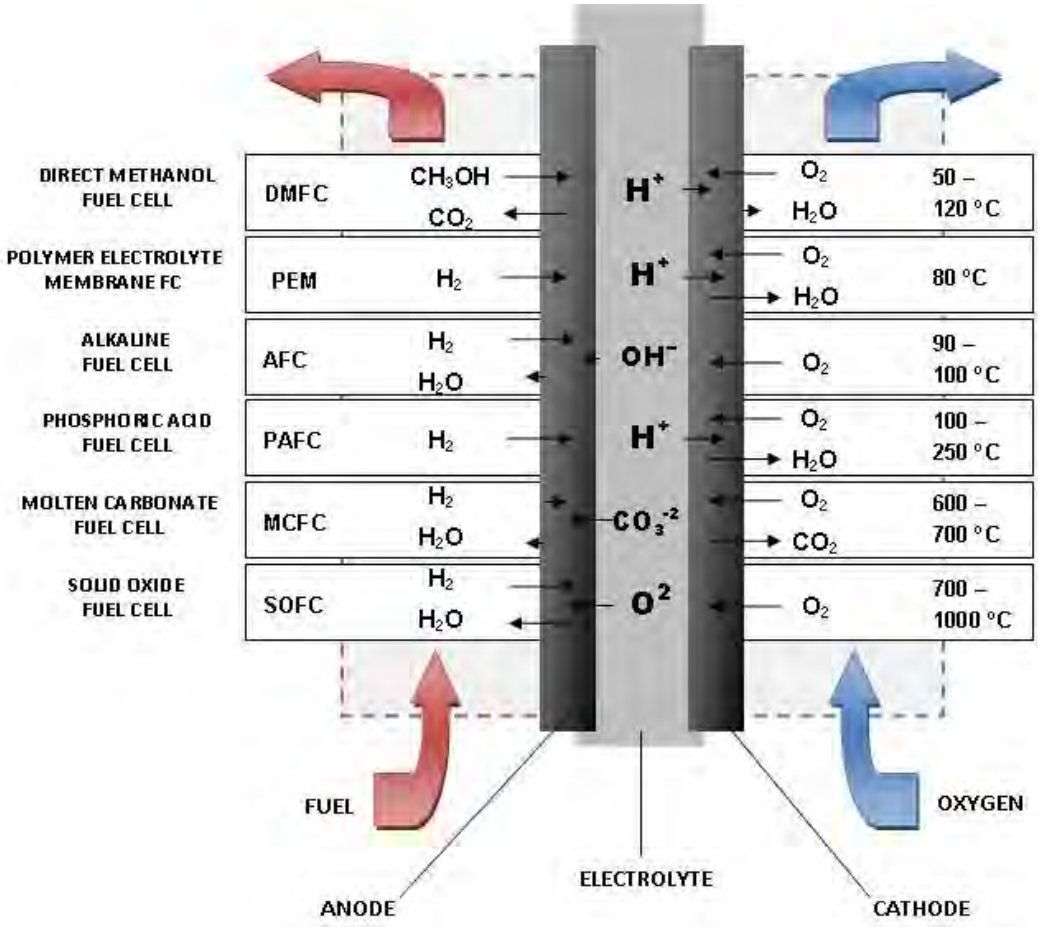

Figure 2.1.2 Types of fuel cell [6]

2.1.1 Proton Exchange Membrane Fuel Cells (PEMFCs)

2.1.1.1 The working principle of PEMFCs

PEMFCs are constructed using a polymer membrane as proton conducting electrolyte and carbon-supported platinum (Pt) as a catalyst. The membrane is sandwiched between two layers of catalyst, and this multilayer structure is called the membrane electrode assembly (MEA). The MEA is then placed between two collector plates, called bipolar plates. Usually, gas flow channels are fabricated on the surface of bipolar plates, to provide the pathways for gas feeding and for elimination of byproducts (Figure 2.1.3).

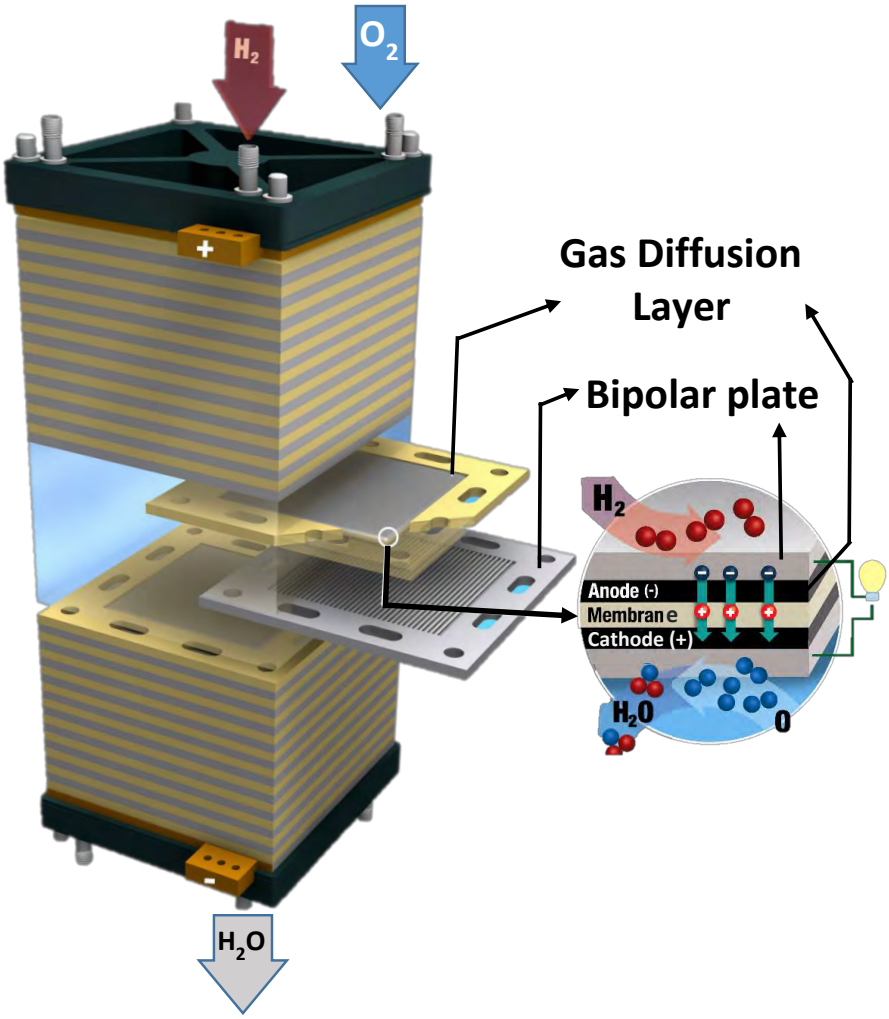

Figure 2.1.3 The basic operating principles of PEMFCs [1]

The hydrogen gas delivered to the anode is split into protons and electrons in the presence of the catalyst. The protons permeate through the membrane to the cathode side, while the electrons travel along the external circuit to the cathode and generate power. On the cathode side, the oxygen molecules react with the protons, which passed through the membrane, and with the electrons, which travelled through the external circuit, to form water molecules. The reactions at the anode and cathode are as follows (Equation 2.1.1, Equation 2.1.2 and Equation 2.1.3) [1]:

Anode: $H_2 \rightarrow 2H^+ + 2e^-$ Equation 2.1.1

Cathode: $\frac{1}{2}O_2 + 2H^+ + 2e^- \rightarrow H_2O$ Equation 2.1.2

Overall reaction: $H_2 + \frac{1}{2}O_2 \rightarrow H_2O$ Equation 2.1.3

2.1.1.2 The history of PEMFCs and the current state of PEMFCs application

History

In the 1830s, the British chemist Sir William Robert Grove studied the opposite reaction to water electrolysis. He observed that the produced hydrogen and oxygen were polarised at corresponding electrodes, and current was found to flow in an external circuit. Consequently, Grove called this invention “gas voltaic battery”, and his experiment is regarded as the first prototype of fuel cell [1].

In 1889, two German chemists, Ludwig Mond and Carl Langer, successfully fabricated a hydrogen-oxygen cell to generate electric current. However the poor and un-stable performance and the unacceptable high cost greatly limited its application [1].

Not many efforts were spent in this area until the worldwide oil crisis. In addition, the space race and the cold war between the USA and the USSR greatly stimulated the interest in fuel cells. In the 1960s, fuel cell technology found its first application in the Gemini spacecraft, as an auxiliary means of electric power generation. This fuel cell was developed by Thomas Grubb and Leonard Niedrach at General Electric, using a solid proton exchange membrane as the electrolyte, which was the predecessor of PEMFCs [7]. However, due to its relatively low efficiency, PEM fuel cells were replaced by alkaline fuel cells in the following program, and almost no work was carried out on PEMFCs until the late 1980s.

A breakthrough in the field of PEMFCs was achieved after 1990, when the performance of PEMFCs was enhanced significantly and the cost was reduced remarkably. The reason for this striking improvement was a combination of three aspects [1]:

- The replacement of polystyrene sulfonic acid membrane with perfluorosulfonic acid membrane (Nafion proton-exchange membrane).
- The significant improvement in the catalytic performance of the platinum catalyst layer.
- The optimisation of composition and structure of the membrane-electrode-assemblies (MEA)

In recent years, the proton exchange membrane has become the leading technology in fuel cells, and it currently dominates the market. In 2012, 88% of the total shipments of fuel cell systems were PEMFCs and this trend is expected to continue in the future [8].

Application

Transport The application of PEMFCs in transportation has attracted great interest due to their low noise; high-efficiency; and most importantly, low or zero greenhouse gas emissions. Most of the mainstream automotive manufacturers dedicate significant efforts to the development of fuel cell electric vehicles (FCEV). Three alliances were formed in 2013, to accelerate the commercial development of FCEV, namely: BMW with Toyota; Renault-Nissan with Daimler and Ford; and General Motors with Honda. They all announced plans to release commercial FCEVs in the coming decade. The leading manufacturer in this industry is Hyundai, who already delivered its first fifteen FCEVs to the European market in June 2013, and released 1,000 vehicles in June 2015 [9].

Stationary power supply Stationary PEMFCs are prefect candidates for off-grid power supply and backup power units, especially for telecommunications. Ballard, one of the leading manufacturers of stationary PEMFCs, launched its first commercial unit in 2001, which had an output power of 1.2 kW. The company continued to sell units in recent years, and the latest model it commissioned was a 1 MW system for Toyota USA [8].

Portable devices PEMFCs are also being evaluated for small scale devices, such as personal electronic gadgets (cell phones, tablets and laptops). Portable PEMFCs can be produced with output power ranging from 5 W up to 500 W. Compared with batteries, PEMFCs exhibit longer run-times, rapid recharging and lower system weight.

2.1.2 Direct methanol fuel cells

The direct methanol fuel cell (DMFC) is a relatively new member to the family of fuel cell technologies. It was invented and developed in the 1990s by researchers from several institutions in the United States, including NASA's Jet Propulsion Laboratory [10]. The working principle is similar to the PEM fuel cell, although pure methanol, rather than hydrogen, is used as the fuel, hence the name.

At the anode, the methanol and water mixture is electro-oxidised to CO_2, protons and electrons through the reaction: $CH_3OH + H_2O \rightarrow CO_2 + 6H^+ + 6e^-$. The protons are transported through the proton exchange membrane to the cathode, and the electrons travel through the external circuit and produce work. At the cathode, the protons and electrons recombine to reduce oxygen to water through the reaction: $3/2O_2 + 6H^+ + 6e^- \rightarrow 3H_2O$. The anode and cathode reactions are catalysed by Pt/Ru and Pt catalysts, respectively. The working temperature of DMFC is 60 ℃ -120 ℃ [10].

Methanol offers several advantages over hydrogen as a fuel. In addition to having a high energy density and being relatively cheap, it is easy to store and distribute. However, liquid methanol is easily transported through the membrane and cause the direct oxidation of cross-over methanol on the cathode, which leads to the significant decrease in power density. Moreover, the CO_2 formed on the anode can block the feed pathway of methanol [10].

2.1.3 Phosphoric acid fuel cells

The phosphoric acid fuel cells (PAFCs) were developed to use natural gas as fuel, but this fuel must be reformed to hydrogen first, producing carbon monoxide as a byproduct. In order to eliminate carbon monoxide, the working temperature has to be increased to around 180 ℃. Consequently, phosphoric acid was used as the

electrolyte, due to its chemical stability in the presence of platinum at high temperatures. The chemical reactions at the anode and cathode are similar to a PEMFC.

This type of fuel cell is frequently used in stationary power generators, with an output power in the range of 100 kW to 400 kW. However, the high cost, relatively low efficiency and poor long-term operation performance hinder their wider commercial application [11].

2.1.4 Alkaline fuel cells

Alkaline fuel cells (AFC) use a solution of potassium hydroxide (KOH) as the electrolyte, which is the most conductive alkaline hydroxide. Pure hydrogen is fed to the anode side and it reacts with hydroxyl anions to generate electrons and water. The electrons are transferred through the external circuit to do work and are collected on the cathode, where they react with oxygen and water to generate hydroxyl ions. The anode and cathode reactions are as follows:

$$\text{Anode } 2H_2 + 4OH^- \rightarrow 4H_2O + 4e^- \qquad \text{Equation 2.1.4}$$

$$\text{Cathode } 4e^- + O_2 + 2H_2O \rightarrow 4OH^- \qquad \text{Equation 2.1.5}$$

The operating temperature of AFCs is in the range 20 °C- 90 °C [12].

Compared with acidic environment fuel cells, the reaction kinetics of AFCs are higher at the electrodes, resulting in higher cell voltages. In addition, AFCs exhibit higher electrical efficiency, allowing the use of lower quantity of platinum. However, AFCs exhibit a crucial problem regarding the sensitivity of KOH to the presence of CO_2. If a stream of air is used as oxidant, instead of pure oxygen, the KOH may react with the CO_2 contained in the air and form carbonate precipitates (K_2CO_3). The precipitates

may block the electrolyte pathways, leading to a significant power decrease. This behaviour seriously limits the application of AFCs in transportation [13].

2.1.5 Solid-oxide fuel cells

A solid oxide fuel cell consists of an anode, a cathode, and a solid ceramic electrolyte, such as zirconium oxide stabilised with yttrium oxide, instead of a liquid or membrane. Hydrogen is fed to the anode, and oxygen from the air is fed to the cathode. The reactions that take place on the anode and the cathode are as follows:

$$\text{Anode: } H_2+O^{2-} \rightarrow H_2O+2e^- \qquad \text{Equation 2.1.6}$$

$$CO+O^{2-} \rightarrow CO_2+2e^- \qquad \text{Equation 2.1.7}$$

$$CH_4+4O^{2-} \rightarrow 2H_2O+CO_2+8e^- \qquad \text{Equation 2.1.8}$$

$$\text{Cathode: } O_2+4e^- \rightarrow 2O^{2-} \qquad \text{Equation 2.1.9}$$

Solid oxide fuel cells operate at extremely high temperatures, usually from 800 ℃ to 1000 ℃ . This extremely high operating temperature allows the fuels to be reformed within the cell itself, leading to the flexible choice of fuel, such as coal gas. In addition, the high operating temperature eliminates the need for noble metal catalysts and increases the overall efficiency of the fuel cell to over 80 %. On the other hand, there are some disadvantages related with the high operating temperature such as the long start-up time, the need for external shielding devices to prevent heat losses, and the decrease in the lifetime of the fuel cell [14].

Stationary SOFCs, ranging from several kilowatts to hundred thousand kilowatts, are frequently utilised for domestic supply of heat and power.

2.1.6 Molten carbonate fuel cells

Molten carbonate fuel cells utilise a molten carbonate salt as the electrolyte. The electrolyte is suspended in a porous ceramic, sandwiched between the anode and the cathode. The reactions occurring on the anode and the cathode are as follows:

$$\text{Anode: } 2H_2 + 2CO_3^{2-} \rightarrow 2H_2O + CO_2 + 4e^- \qquad \text{Equation 2.1.10}$$

$$\text{Cathode: } O_2 + 2CO_2 + 4e^- \rightarrow 2CO_3^{2-} \qquad \text{Equation 2.1.11}$$

The operating temperature of MCFCs is around 650 °C. Much alike the SOFCs, this high temperature offers some advantages, such as high reaction kinetics, elimination of expensive noble metal catalysts and high efficiency. The internal reforming of the fuel is also possible below this temperature. Therefore, a variety of fuels can be used, like natural gas and methane. On the other hand, the high temperature raises some problems, such as long start-up time, the oxidation of the electrolyte and the need for external devices to maintain the operating temperature.

MCFCs are suitable for stationary power plants, with heat recovery to increase their efficiency.

2.2 Catalyst layer of PEMFCs

2.2.1 Introduction of electrocatalytic reactions

The catalyst layer, which is sandwiched between the membrane and the gas diffusion layers (GDL), is a key component in PEM fuel cell stacks. This is because the surface of the catalyst is where the electrochemical reactions occur.

At the anode, H_2 is firstly adsorbed onto the catalyst surface. The H-H bonds break to produce two hydrogen atoms which subsequently lose an electron before leaving the

surface of the catalyst as protons (Equation 2.2.1, Equation 2.2.2). The reaction that takes place on the surface of the anode is frequently called the hydrogen oxidation reaction (HOR)

$$H_2 \xrightarrow{catalyst} 2H \qquad \text{Equation 2.2.1}$$

$$H \xrightarrow{catalyst} H^+ + e^- \qquad \text{Equation 2.2.2}$$

The electrons flow to the cathode along an external circuit, thus creating an electrical current. Meanwhile, the protons pass through the membrane to the cathode side.

At the cathode, O_2 is adsorbed onto the catalyst surface and the O-O bonds break to form adsorbed O atoms. The O atoms react with incoming H^+ and are subsequently reduced by the electrons to form hydroxyl groups (OH). The OH reacts again with H^+ and another electron before leaving the surface of the catalyst as water (Equation 2.2.3, Equation 2.2.4 and Equation 2.2.5). The reaction that takes place on the cathode is called the oxygen reduction reaction (ORR).

$$O_2 \xrightarrow{catalyst} 2O \qquad \text{Equation 2.2.3}$$

$$O + H^+ + e^- \xrightarrow{catalyst} OH \qquad \text{Equation 2.2.4}$$

$$OH + H^+ + e^- \xrightarrow{catalyst} H_2O \qquad \text{Equation 2.2.5}$$

In PEMFCs, the kinetics of the HOR is very fast, so a low load of catalyst is required for this reaction to occur. However, the mechanism of ORR is complicated and its kinetics is several orders of magnitude slower than that of the HOR. The sluggish kinetics of ORR leads to a large over-potential. In order to facilitate the ORR, the load

of catalyst required on the cathode is much higher compared to the anode. As a consequence, most research efforts have aimed to enhance the catalytic efficiency of the cathode, which is also the interest of this study.

2.2.2 The development of PEMFC catalyst layer

From the brief description of electrocatalytic reactions presented above, it is clear that the catalyst layers play an essential role in those reactions. To date, platinum is the most commonly used catalyst for both reactions occurring at the anode and the cathode. In the early stage of PEMFC development, a mixture of platinum black, which is an especially finely divided form of platinum (particle size: 1 nm to 1 μm) [15], and Teflon® was hot pressed directly onto the membrane. As a result of this manufacturing process, large portions of the platinum catalyst were not in intimate contact with the ionomer, and a large amount of Pt had to be used in order to achieve the required performance. In the Gemini program (1963), the required load of Pt catalyst was approximately 4 mg/cm^2 [16]. Considering that the price of platinum is naturally high and steadily increasing, the incredibly high cost of PEMFCs limited their use to aerospace and military applications. If the PEMFC technology is to compete with the traditional internal combustion engine and gain commercial success, the cost of the catalyst must be reduced. With this regard, two main approaches have been developed to reduce the cost of catalyst layer. One approach is to lower the loading of platinum, and the second approach is to replace platinum with platinum base alloys or non-precious metal catalysts.

2.2.2.1 Platinum base alloys

The improvements in catalytic performance with platinum alloys were first found in phosphoric acid fuel cells (PAFC) by Keck [17]. The selection of alloying elements,

such as transition elements, was based on the Appleby's volcano plot model [18], aiming to balance the O binding strength to achieve the optimum catalytic performance. The development of highly active Pt alloys for PEMFC also drew extensive interest. Mukerjee and Srinivasan [19] investigated the performance of some binary alloys of Pt, such as Pt+Ni, Pt+Cr and Pt+Co, under the PEMFC operating conditions. Those Pt-based catalysts exhibited a twofold to threefold enhancement in cell performance compared with the conventional Pt/C catalyst with the same Pt loading. Wakabayashi and et al. [20] investigated the oxygen reduction activity of various Pt alloys ($Pt_{54}Fe_{46}$, $Pt_{68}Co_{32}$, and $Pt_{63}Ni_{37}$) under different temperature ranges. These Pt alloys resulted in higher ORR activity than pure Pt in the temperature range of 20-50 ℃ . However, when the temperature increased to above 60 ℃ , the activity of the Pt alloys decreased to the level of pure Pt. Other Pt alloys, such as Pt-V and Pt-Fe [21], also exhibited higher electro-catalytic activity than pure Pt catalyst.

The widely accepted mechanism [20] to explain the improvement of catalytic activity of Pt alloys claims that the addition of alloying elements modifies the electronic state of the Pt surface. This modification might increase the coverage of oxygen and decrease the adsorption of H_2O, thus contributing to the improvement in catalytic activity.

However, the major problem of those Pt-based alloys is their insufficient stability. The alloying elements are prone to corrode under the acidic operating conditions of PEMFC, leading to leaching of the alloying metal and, ultimately, to the degradation of the cell performance [22]. In addition, the rather complicated fabrication process [21][23] would increase the fabrication cost, thus hindering the commercialisation of Pt alloys.

2.2.2.2 Non-precious metal catalysts

Many efforts have been devoted to developing non-precious catalysts to replace the expensive Pt and Pt alloys. The electro-catalytic properties of tungsten carbide in the conversion process of H_2 was first reported by Böhm [24], and this finding was confirmed by Binder [25]. The sulphides of tungsten (WS_2) and molybdenum (MoS_2) also exhibit the ability to catalyse the oxidation reaction of hydrogen in acid solutions [26].

The research by Mazza and Trassatti [27] indicated that WC showed catalytic ability for oxygen reduction reaction in an acid electrolyte, which suggested that the WC could be used as the cathode catalyst in PEMFC. However, the stability of pure WC in this acid solution was poor, resulting in performance degradation after long-term operation. The addition of Ta into the WC [28] not only enhanced the corrosion resistance, but also the electro-catalytic activity. Many different kinds of compounds, like ternary non-noble metal chalcogenide (W–Co–Se) [29], transition metal nitrides, sulphides and oxides (Mo_2N [30] Fe-N and Co-N [31]; FeS_2 [32]; TiO_2 [33] and Ta_2O_5 [34]), were all reported to exhibit some level of catalytic activity for the oxygen reduction reaction.

Even though the use of non-precious catalysts could reduce the cost, the performance of those catalysts in PEMFCs is far lower than that of the Pt and Pt-based alloys. In the review of catalysts for low temperature fuel cells [35], Ralph claimed that the development of cathode catalysts should be concentrated on improving performance, instead of reducing cost. To date, considering the activity, selectivity, stability and poisoning resistance, pure Pt is still the only material which meets the overall requirements for cathode catalyst in a PEMFC environment [36].

2.2.2.3 Low platinum loading catalyst

Since the pure Pt is the only material that currently satisfies the PEMFC requirements, lowering the platinum loading is the only approach to reduce the catalyst cost.

The surface area of catalyst is crucial for the catalytic activity. Enlarging the surface area of catalyst can enhance the catalytic performance and thus reduce the use of catalyst. Petrow and Allen [37] invented a wet chemical process to produce very fine platinum particles (1.5-2.5 nm) on the surface of a carbon black substrate, which can be used as fuel cell catalytic electrode. These carbon-supported platinum nano-particles exhibited a remarkable cathode performance with a Pt loading of only 0.25 mg/cm^2. By using the conventional catalyst layer, the same cathode performance would only be achieved with a platinum loading 10 times higher. At the anode, even lower Pt loading between, 0.05 to 0.25 mg/cm^2, were needed to achieve great performances. Additionally, this carbon-supported catalyst layer could significantly improve the tolerance to carbon monoxide and the long-duration performance compared to the conventional one.

A new preparation process of platinum catalysts was reported by Wilson [38][39]. A thin layer of ultra-low platinum loading (lower than 0.35 mg/cm^2) catalyst was cast from a mixture of suspended Pt/C catalyst and solubilised Nafion® ionomer. This thin film was then directly applied onto the membranes at high temperature. This novel process improved the uniformity of ionomer in the catalyst layer applied on the membrane, which reduced the contact resistance and thus enhanced the catalytic performance. This method not only enhanced the utilisation of platinum catalyst, but also simplified the production process.

All the studies mentioned above were done at scale of laboratory. Ralph and Hards [40] devoted their efforts to the high volume production of low cost platinum cathodes and manufacture into electrodes by printing technology. By means of the aqueous deposition and chemical reduction technology, carbon black supported cathode catalysts could be fabricated in large-scale. The cell tests revealed that these low-cost platinum cathodes (with Pt loading $\leq$ 0.6 mg/cm^2) produced an equivalent performance to the platinum black cathodes (with 8.0 mg/cm^2 Pt loading). The durability and reproducibility of all these cathode catalysts proved to be superior to the Pt black cathodes.

Many approaches have been explored to further reduce the Pt loading. O'Hayre et al. [41] fabricated the catalyst layer by directly depositing Pt on the membrane surface. This work investigated the effect of the thickness of the catalyst layer on the fuel cell performance. Results indicated that the 5-10 nm thick catalyst layer exhibited the best performance, the maximum power output was three-fifths of the commercial MEA, but the loading of Pt was only one-tenth of the commercial MEA.

2.2.3 Nano-structured platinum catalyst layer

Compared with bulk materials, nano-sized materials exhibit different properties in many aspects [42]. Regarding the catalyst applications, nano-sized materials provide higher specific surface area and thus better catalytic activity than bulk materials. Therefore, many efforts have been made to develop nanostructured catalysts for PEMFCs, including nanoparticles (0-dimensional) and nanowires (1-dimensional).

The traditional methods to prepare Pt nanoparticles consist in reducing a Pt salt in an aqueous solution by bubbling hydrogen [43], ethylene glycol [44], or sodium borohydride [45]. The shape of Pt nanoparticles is essential for the catalytic activity.

Ahmadi et al. [46] reported that, by changing the ratio of ingredients in the solution, the shape of the Pt nanoparticles could be controlled, varying among cubic, tetrahedral and irregular-prismatic. Antoine and Durand [47] developed a method combining impregnation and in-situ electrochemical reduction to produce Pt nanoparticles directly onto the surface of carbon and inside the Nafion® membrane.

Tian et al. [48] developed an electrochemical method for the synthesis of shape-controlled high-index Pt nano-crystals (NCs). This method started from Pt nano-spheres electrodeposited on a glassy carbon electrode, subsequently subjected to a square-wave potential treatment in an ascorbic acid solution. In this way, Pt NCs with an unusual tetrahexahedral (THH) shape, proved by SEM and HRTEM, were fabricated at high yield. The THH Pt NCs exhibited improved catalytic activity compared with Pt nano-spheres or commercial Pt/C catalysts. This improvement may be related with the high density of edge atoms on the high-index surfaces.

Although the nano-sized Pt particles exhibit improved catalytic activity, the high surface energies could lead to severe Oswald ripening, resulting in the decline of performance [49]. In contrast to 0-dimensional nanoparticles, 1-dimensional structures, like nanotubes and nanowires, exhibit even higher catalytic activity, because of their anisotropy and unique structure.

Xia and co-workers [50] [51] developed an approach to synthesise Pt nanotubes based on template-engaged replacement reactions. Through this method, the voids and thickness of wall could be controlled. Chen et al. [52] used this method to synthesise a self-supported Pt nanotube catalyst for fuel cell applications, which exhibited improved catalytic activity and durability.

A template-less method which directly synthesises Pt nanowires on the surface of a metallic gauze was reported by Lee et al. [53]. With this method, a high density of single crystal Pt <111> nanowires directly grew on the surface of Pt and W gauze. The electro-catalytic performance of the Pt nanowires was evaluated by cyclic voltammetry (CV) and electrochemical impedance spectroscopy [54]. The results indicated that the Pt nanowires supported on a Pt-gauze exhibited the best catalytic activity. The electrochemically active surface area (ECSA) of the Pt nanowires covering the Pt gauze was 4 times larger than that of the pristine Pt gauze. However, an increase in the density of Pt nanowires blocked the removal of poly(vinylpyrrolidone) (PVP) from the surface, leading to the degradation of performance.

Sun and co-workers reported the formation of flower-like clusters [55], 3D superstructures [56] and multi-armed star-like platinum nanowires [49] via simple chemical reduction of a Pt precursor (hexachloroplatinic acid) with formic acid at room temperature without surfactant or template and investigated the catalytic activity and durability. From the comparison against a state-of-the-art commercial Pt catalyst, improved catalytic activity and better durability were observed for the platinum nanowire catalysts.

Du [57] reported a simple and effective method, without any template or catalyst, to grow Pt nanowires on the surface of gas diffusion layer via reduction reaction of chloroplatinic acid with formic acid in the presence of PVP at room temperature. The adhesion of Pt nanowires on the surface of carbon fibres, tested by long-time sonication treatment, was good. The Pt nanowires deposited on GDL exhibited better catalytic activity and about 25 % higher power density compared with the commercial

Pt/GDL. The enhanced performance of membranes with Pt nanowires grown in-situ, using similar method, was also published [58].

2.2.4 Surface modification of catalyst supports

The preparation of Pt nanowires requires an aqueous environment and, as a consequence, the growth of Pt nanowires is largely influenced by the wettability of the supporting materials (gas diffusion layer or membrane). Unfortunately, the surface of GDL or membrane is frequently coated with a polymer (usually PTFE), in order to prevent water flooding and to facilitate the gas permeation [59]. The resulting hydrophobicity greatly affects the growth of Pt nanowires on the surface of the supporting material, leading to aggregation and non-uniform growth, consequently lowering the catalyst utilisation. Hence, a surface modification step is needed to enhance the wettability of the polymer coated GDL.

Several surface techniques have been developed to modify the surface properties of polymers, including mechanical treatments, wet-chemical treatments, flame treatments and low-temperature plasma treatments. Compared with the other methods, low temperature plasma treatments are more environmentally friendly, safe, reproducible and exhibit good treatment uniformity. Consequently, plasma treatments have drawn considerable interest in recent [60].

The interactions between the plasma and the surface of a polymer could be classified into four categories: (1) removal of contamination [61]; (2) etching of the surface [62]; (3) cross-linking between near-surface molecules [63] [64] and (4) modification of the chemical structure of the surface [65]. Many efforts have been devoted to the understanding of these four interactions.

One of the most apparent results of the modification of the surface chemical structure of polymers after the plasma treatment is the change in wettability. Many researchers showed that plasma treatments have the ability to modify the hydrophobicity of polymers. Kong et al. [66] reported that inductive coupled plasma (ICP) treatments could significantly increase the wettability of polystyrene (PS), reducing the water contact angle from 75° to 14°. The reduction of contact angle was also observed after low temperature plasma treatments with Ar [67] and O_2 [68].

Plasma treatments were also employed to modify the surface properties of membranes, for their application in PEM fuel cells. The polymer coating makes the surface of the membrane hydrophobic, leading to a poor adhesion of the catalyst layer on the surface of the membrane. Kim and co-workers [69] found that plasma treatments could turn the surface of Nafion membranes from hydrophobic to hydrophilic. The electrochemical performance was also enhanced, and the electrochemical surface area of the plasma-treated membrane was almost ten times larger than that of the untreated one.

Recently, our group developed a novel plasma treatment technique, called Active screen plasma, to modify different kinds of polymers for biomedical applications, including polyurethane [70] and polycaprolactone [71]. Compared with other plasma treatment techniques, Active Screen is a simpler process, with low equipment requirements (lower power and vacuum), which introduces less surface damage on the treated surfaces. The surface analysis revealed that the Active Screen plasma treatment could change the chemical composition and structure of polymer surfaces, e.g. introducing hydrophilic functional groups, thus improving their wettability.

2.3 Bipolar plates of PEMFCs

2.3.1 Introduction to the bipolar plates

Bipolar plates are among the most important components of PEMFCs, and account for about 80 % of the total weight and 45 % of the stack cost [72]. A more recent report shows that the cost share of bipolar plates was reduced to about 25 % of the total cell cost [73], which remains a large share. Bipolar plates are designed to be multi-functional, and their main functions are: (i) be the backbone of the fuel cell stacks; (ii) separate individual cells in the stack and carry current between cells; (iii) uniformly distribute the fuel and oxidant within the cell; (iv) facilitate the management of water and heat; and (v) prevent the leakage of reactant gases and coolant. According to these functions, bipolar plates must exhibit high mechanical strength, high gas tightness, good electrical conductivity and thermal conductivity. The operating conditions of bipolar plates are harsh, and involve acidic environments (pH 3-5), containing SO_4^{2-}, NO_3^-, Cl^- and F^-, so excellent chemical stability and corrosion resistance are essential requirements for bipolar plates. In addition, in order to be mass-produced, bipolar plates should be easy to manufacture. Finally, for their application in transportation, low weight and low volume are also required.

The requirements for bipolar plate materials were established by the United States Department of Energy (DOE) and shown in Table 2.1. All the criteria shown in this table must be fulfilled for candidate materials to become qualified bipolar plate materials.

Depending on the materials, bipolar plates can be classified into three categories, namely graphitic bipolar plates, composite bipolar plates and metallic bipolar plates.

Table 2.1 Requirements of bipolar plate materials established by DOE [74]

Characteristic	Units	2011 Status [a]	2017 Targets	2020 Targets
Cost[b]	$ / kW	5-10	3	3
Plate H_2 permeation coefficient[c]	Std $cm^3/(sec\ cm^2 Pa)$ @ 80°C, 3 atm 100% RH	N/A	$<1.3 \times 10^{-14}$ [d]	$<1.3 \times 10^{-14}$ [d]
Corrosion, anode[e]	$\mu A / cm^2$	<1	<1	<1
Corrosion, cathode[f]	$\mu A / cm^2$	<1	<1	<1
Electrical conductivity	S / cm	>100	>100	>100
Areal specific resistance[g]	$Ohm\text{-}cm^2$	0.03	0.02	0.01
Flexural strength[h]	MPa	>34 (carbon plate)	>25	>25
Forming elongation[i]	%	20–40	40	40

[a] Status is based on information found in 2010 & 2011 Annual Progress Reports – project description write ups of TreadStone Technologies, Inc. and Oak Ridge National Laboratory.

[b] Costs projected to high volume production (500,000 stacks per year), assuming MEA meets performance target of 1000 mW/cm^2.

[c] Per the standard gas transport test (ASTM D1434).

[d] Blunk, *et al*, J. Power Sources 159 (2006) 533-542.

[e] pH 3 0.1ppm HF, 80°C, peak active current $<1x10^{-6}$ A/cm^2 (potentiodynamic test at 0.1 mV/s, -0.4V to +0.6V (Ag/AgCl)), de-aerated with Ar purge.

[f] pH 3 0.1ppm HF, 80°C, passive current $<5x10^{-8}$ A/cm^2 (potentiostatic test at +0.6V (Ag/AgCl) for >24h, aerated solution.

[g] Includes interfacial contact resistance (on as received and after potentiostatic test) measured both sides per Wang, *et al.* J. Power Sources 115 (2003) 243-251 at 200 psi (138 N/cm^2).

[h] ASTM-D 790-10 Standard Test method for flexural properties of unreinforced and reinforced plastics and electrical insulating materials.

[i] Per ASTM E8M-01 Standard Test Methods for Tension Testing of Metallic Materials.

2.3.2 Graphite

Currently, graphite is the most commonly used bipolar plate material, due to its great chemical stability and corrosion resistance in acidic PEMFC operating environment. The interfacial ohmic losses of graphite are negligible compared with metallic bipolar plates. However, the disadvantages of graphite are obvious. Graphite is inherently porous and, in order to meet the requirement of low gas permeability, graphite bipolar plates must be impregnated with a binder or a resin. In addition, graphite is naturally brittle and, in order to bear the vibration in automotive application, graphite bipolar plates must be bulky and heavy. The brittle nature also increases the difficulty to fabricate incorporating gas diffusion channels on their surface, makes the fabrication

process costly. Moreover, the conductivity of graphite is about three orders of magnitude lower than that of the metallic materials [75]. For these shortcomings, graphite bipolar plates are unsuitable for the transportation applications.

Great effort has been made to try to develop alternative bipolar plate materials to replace the high-cost graphite bipolar plates. All these materials can be classified into composites and metals.

2.3.3 Composites bipolar plates

Composite materials have been proposed for their application in bipolar plates and they have attracted considerable interest in recent years because of their low cost, low weight and ease of manufacture. In general terms, these kinds of composites are composed of two main constituents, namely the binder and the filler. Polymers, such as thermoplastic and thermoset resins [76], are chosen as binders to act as matrix and hold the fillers in place. The binder materials are usually electrically insulating, hence materials with good electrical conductivity must be chosen as fillers, to fulfil the electrical conductive requirement of bipolar plates. Metals and carbon derivatives have been considered as filler materials. Compared with carbon derivatives, very few research efforts have been focused on the metal-composite bipolar plates, because of the associated manufacturing challenges (difficult to combine metal and polymer) and relatively poor performance (low corrosion resistance and electrical conductivity) [76]. In terms of carbon derivative materials, graphite [77], carbon black [78], carbon fibres [79] and carbon nanotubes [80] are the most commonly used filler materials. Many manufacturing methods have been employed to make the composite bipolar plates, including slurry molding [79], bulk-moulding compound processes [77], hot pressing

[81] and injection molding [78]. All these methods are relatively low-cost and suitable for mass production.

The performance of composite bipolar plates was evaluated by many researchers, and some promising results have been reported. Cho et al. [81] found that the hot-pressed carbon composite bipolar plates exhibited comparable electrical contact resistance and single-cell performance as graphite bipolar plates. Moreover, the physical properties, especially the electrical properties, could be easily modified by changing the proportion of the constituents and the molding methods [77].

However, the inherent problems of composite bipolar plates are obvious. The high bulk electrical resistance usually results in the loss of output power density [79]. Although the electrical conductivity could be improved by increasing the content of graphite, the brittleness is also increased. The poor mechanical strength [81] is the main barrier for the use of this kind of material as bipolar plates in vehicle applications.

2.3.4 Metallic bipolar plates

Metallic bipolar plates exhibit good mechanical strength, no gas permeability, and better tolerance to shocks and vibration. In addition, metals can be easily fabricated into thin sheets and stamped with different patterns onto the surface, leading to low cost, low volume and ease of manufacturing, and making them promising candidates for transportation applications. Many kinds of metals have been studied as alternatives to the conventional graphite bipolar plates.

2.3.4.1 Aluminium alloys

Aluminium alloys exhibit good bulk electrical conductivity, light weight, low material cost, high specific strength and rigidity and good manufacturing performance. It is

relatively easy to fabricate the gas-diffusion channels on the surface of aluminium alloys by many different methods, such as stamping [82], rubber-pad-forming [83], thixoforming [84] and vacuum die casting [85].

However, the corrosion resistance of Al alloys in the PEMFC working environment, which involves high temperature, highly acidic and humid conditions, cannot meet the DoE requirements [86]. In addition, the protective oxide layer which forms on the surface would significantly reduce the surface conductivity.

In order to address the relatively poor corrosion resistance and the decreasing surface conductivity, surface coating techniques have been employed. The coatings include Ni-Fe-Mo-Cr [87], Ni-P [86] [88], conductive polymers [89] [90] and TiN/TiC [91]. After applying the protecting coating on the surface, the corrosion and conductivity performances of Al alloys exhibited different levels of enhancement [92]. However, the coating processes increase the cost and the complexity of fabrication.

2.3.4.2 Titanium and titanium alloys

Titanium and its alloys are well known for their light weight, good mechanical strength, high electrical conductivity and great corrosion resistance. They have also been considered as candidate materials for bipolar plates. Ti alloys owe their good chemical stability to the formation of a dense oxide film on their surface. However, this passive oxide film causes poor electrical conductivity and is harmful to the fuel cell efficiency and performance.

Many methods have been tried to address the problems of Ti bipolar plates. Different coatings have been used, including gold [93] [94], platinum [95] and TiN [96] [97]. Surface alloying techniques have also been employed, such as plasma nitriding [98] and nitrogen ion implantation [99]. Neil and co-workers reported that the electrical

conductivity of the oxide film can be enhanced by introducing some alloying elements (Nb and Ta) into the titanium matrix, to alter the composition and structure of the oxide film.

Among all these treatments, the noble-metal (Au) coated titanium bipolar plates exhibited promising results, which were comparable to their graphite counterparts [93]. However, the high price and poor long-term performance remain to be addressed.

2.3.4.3 Amorphous alloys

The amorphous alloys possess many unique characteristics, such as homogeneous chemical composition and lack of defects (including grain boundaries and dislocations) [100]. Because of these characteristics, amorphous alloys show high corrosion resistance, high hardness and strength. Fleury and co-workers [101] [102] firstly proposed the application of amorphous alloys as bipolar plate materials. Their studies revealed that the corrosion resistance of Fe-base amorphous alloys was higher than that of the 316 stainless steel, but the bulk and contact electrical conductivity were lower than that of the 316 stainless steel. After these findings, many different kinds of amorphous alloys have been investigated as candidate materials for bipolar plates and most of those alloys are Ni-based [103] [104] [105] [106] [107]. All these amorphous alloys exhibited promising resistance compared with conventional (crystalline) metals.

The amorphous alloys possess another interesting characteristic, namely the super plasticity behaviour in the super cooled liquid region. In this window of temperature, the flow channels could be easily fabricated on the amorphous alloys. Hot-pressing has proved to be an appropriate technology to produce bipolar plates with amorphous alloys [97] [98].

In addition to their bulk form, amorphous alloys have also been used as coating materials. Spray coating [99] and electroplating [108] technologies were the common methods of producing coatings from amorphous alloys.

In spite of the benefits of these alloys, the mobility of conduction electrons is slow in the amorphous-metal state, which results in the relatively low electrical conductivity compared with crystalline metals [100]. In addition, the corrosion resistance of amorphous alloys is better than that of the stainless steel, but still cannot meet the DoE requirement [101]. Furthermore, the high addition of alloying elements (Ni, Cr, Nb, Zr and etc.) significantly increases the cost of the material, which is unfavourable for commercial reasons [109].

2.3.4.4 Stainless steel bipolar plates and their challenges

The stainless steels offer many advantages over the conventional graphite bipolar plates, such as low-cost, high mechanical strength, gas tightness and ductility. The high density of stainless steel can be mitigated by shaping it into thin sheets, thus significantly improving the power-to-volume ratio. Their chemical stability is superior to most metals and the wide range of choice is also an advantage of stainless steels [109].

Several research projects have focused on the development of stainless steel bipolar plates. Different kinds of stainless steels have been investigated as alternative materials for bipolar plates , including austenitic [110] [111] [112], ferritic [110] [113] and duplex stainless steels [110] [114]. Taking into account the overall performance and the cost, 316 and 316L stainless steels are the best candidates for the bipolar plate materials [110].

However, the operating environment of bipolar plates is highly acidic, and contains many kinds of corrosive ions, such as F^-, SO_4^{2-}, SO_3^{2-}, HSO_4^-, HSO_3^-, CO_3^{2-}, HCO_3^-, etc. [115]. The challenges for stainless steels, in such a harsh working condition, fall into three areas, namely the formation of a passive film, the corrosion resistance and the poisoning of the membrane.

Formation of passive films

The high corrosion resistance of stainless steel is primarily due to the formation of a dense passive film on their surface. These dense and passive oxide films work as barrier, isolating the substrate from the corrosive medium. However, the passive films are electrically insulating, which may induce unacceptable ohmic losses and decrease the efficiency of PEM fuel cells significantly [116].

A research team at Loughborough University evaluated the potential of a number of commercial stainless steel as candidates for bipolar plates [117]. Their research revealed that different stainless steels displayed various interfacial contact resistances. The Auger electron spectroscopy (AES) results showed that high alloy stainless steels possessed a thinner passive film, resulting in lower electrical resistance. Wang [118] reported a similar finding, i.e. that the interfacial contact resistance of different commercial stainless steels decreased with increasing Cr content.

Yang [119] employed X-ray photoelectron spectroscopy (XPS) to identify the chemical state and compositions of passive films formed under anodic and cathodic environments. The thickness of the passive film formed under the anodic environment was thinner than its counterpart formed under the cathodic environment, and the latter passive film was thicker than the one formed in air. The composition and structure of the passive films formed in different environments were also different: the passive

films formed in the anodic environment were dominated by Cr oxide and had a single-layer structure; whereas in the cathodic environment, the iron oxide dominated the passive film and a bi-layer structure was observed.

Insufficient corrosion resistance

As mentioned above, the high corrosion resistance of stainless steels arises from the formation of a protective passive film. Some researchers claimed that stainless steels were suitable for bipolar plate. Davies [116] found that after an endurance test of 3000 hour, there was no evidence of corrosion taking place on the surface of stainless steels, and the performance of the cell with stainless steel bipolar plates was similar to that of the graphite bipolar plates. An unknown type of stainless steel was assessed as PEMFC bipolar plate materials in [120]. The results revealed that this special stainless steel had sufficient electrochemical stability in both anodic and cathodic working environments of a simulated PEMFC.

However, most studies indicated that the corrosion resistance of bare stainless steels cannot satisfy the corrosion requirement. According to Li's studies [121], the passive films of the stainless steel cannot form spontaneously in the simulated working environment, which means that the stainless steel is completely exposed to the harsh solution for a certain period of time. In addition, the adsorbed hydrogen atoms might deteriorate the passive film. The unsatisfactory corrosion resistance of stainless steels might lead to the degradation of the fuel cell performance [122] [123] [112] [124] [125].

Feng [126] pointed out that the reason for the inconsistent conclusions about the corrosion resistance of stainless steel was that different solutions were used to simulate the PEMFC working environment. Those solutions could be grouped into

two categories, namely simulated and accelerated conditions. According to his work, the corrosion behaviour of 316 stainless steel was governed by the composition and structure of the passive film, which was completely different in simulated and accelerated conditions. So he concluded that the corrosion environments should be carefully considered when investigating the corrosion behaviour of stainless steels.

Many efforts have been directed at investigating the influence of alloying element in the corrosion behaviour of 316 stainless steel. From the comparison of corrosion performance between 316 and 310 stainless steels [117], Davies found that the high alloyed 310 stainless steel exhibited better corrosion resistance. According to Wang's work [118], the Cr content played an important role in the anodic corrosion behaviour, as higher Cr content contributed to a lower passive current density. André [123] also confirmed that the bulk composition of the alloy would influence the corrosion resistance.

Poisoning of membrane

The corrosion of stainless steel would result in the release of metallic cations, which would poison the membrane and the catalyst layers. Makkus [127] found that the constituents of stainless steel, such as Fe, Cr and Ni, would dissolve into the membrane, and the direct contact with the membrane significantly increased the contamination level. The high level of cations released from 316 stainless steels was also detected by Wind [128].

The investigation by Pozio [129] showed that the iron contamination from the 316 stainless steel bipolar plate poisoned the membrane electrode assemblies, and led to polymer degradation. This finding was supported by the massive fluoride loss from the membrane. Inaba [130] reported that the presence of impurities (Fe^{2+} and Cu^{2+})

triggered the formation of reactive oxygen radicals, which were harmful to the membrane and accelerated its degradation. In a separate article [131] it pointed out that the contamination with metallic cations decreased the ionic conductivity of the membrane and caused a fast degradation of its performance.

2.4 Surface engineering of stainless steel

From the literature review presented in the previous section, it is clear that stainless steels cannot be directly used as bipolar plates. In his review, Antunes [132] claimed that "*non-coated stainless steels almost always lack corrosion resistance leading to an increasingly poor performance in the fuel cell environment when used as bipolar plates*." Therefore, surface engineering treatments, which provide a convenient path to improve the surface properties of stainless steels, are required to make them suitable for bipolar plates. As stated by Bell [133] "*surface engineering is an enabling technology, applicable to all classes of materials and capable of greatly enhancing a range of properties*."

Based on the literature, the methods used to modify the surface of stainless steel bipolar plates can be classified into surface coating and surface co-alloying.

The coatings used to enhance the corrosion resistance and electrical conductivity of stainless steel bipolar plates, should be conductive, have good adhesion with the substrate, and have a compatible thermal expansion coefficient with that of the substrate [134]. The coating materials can be divided into two groups: carbon-based materials [135] [136] and metallic materials [137] [138] [139]. Carbon-based materials include graphite [140], conductive polymers [141], and amorphous carbon [142]; whereas metallic materials include noble metals [143], metal nitrides [144], and metal carbides [134].

Surface co-alloying is an effective method to alter the surface composition and, as a result, change the surface physical and chemical properties. The chemical stability and the surface electrical conductivity are among those surface properties, which are closely related with the surface composition.

The literature survey presented in the following section reviews the elements used to modify the surface of stainless steels, classified into three groups, namely niobium and its compounds, noble metals and nitrogen.

2.4.1 Surface modification with niobium and its compounds

Transition metals and their nitrides have many attractive characteristics such as high electrical conductivity, good mechanical properties and corrosion resistance. Among them, Nb and its compounds have attracted considerable attention due to the high chemical stability, good mechanical properties, and superconducting characteristics, and have been widely utilised in many applications.

Niobium is well known for its excellent corrosion resistance in acidic environments and has attracted considerable attention in the corrosion protection industry. Many studies have been conducted to evaluate the corrosion behaviour of Nb in different acidic environments [145], [146]. More recently, Asselin [147] et al. investigated the corrosion behaviour of Nb in different concentrations of H_2SO_4 and HCl solutions at different temperatures. Their results indicated that a passive film formed on the surface and protected the Nb substrate from the attack of concentrated acid at a temperature below 95 ℃ . This testing environment is very close to the PEMFC operating environment, which means that niobium is a good candidate material for bipolar plates.

The excellent corrosion resistance of Nb is not limited to its bulk form, and numerous researchers have reported that the addition of Nb could positively affect the corrosion resistance of many kinds of materials, including ferritic stainless steels [148] [149], zirconium alloys [150], titanium alloys [151] and FeCuNbSiB alloys [152].

The other important advantage of niobium and its compounds is their high electrical conductivity. In 1941, the superconductive property of niobium-nitride was found at a temperature of 16 K (-257 °C), and in 1962, the first commercial superconducting wire ever developed was made of an alloy of niobium and titanium. More recently, other alloys of niobium, with tin and aluminium, were found to be superconductive as well, and pure niobium is a superconductor itself when cooled below 9.25 K (-263.75 °C). [153]

Due to the superconductive behaviour of niobium and its alloys, many scientists have proposed a method to improve the electrical conductivity of different kinds of materials by alloying them with Nb. Furubayashi and co-workers [154] first reported that Nb-alloying could significantly improve the electrical conductivity of TiO_2, a transparent conducting oxide (TCO), which was further verified by other research groups [155] [156] [157]. The improvement in conductivity is due to the donation of electrons into the conduction band of the oxide lattice, thus increasing the concentration of charge carriers [155]. Another reported reason [157] is that Nb-alloying increased the concentration of electrons in the oxide film and changed the mechanism of electron passage from the thermionic emission to the electron tunnelling, which reduced the effective barrier and increased the electron collection efficiency. Nb-alloying was also employed to modify the electrical behaviour of tin oxide (SnO_2), another widely studied TCO material, and positive results were reported by many researchers [158] [159].

Niobium finds its application in the field of bipolar plates due to its ability to impart good electrical conductivity and corrosion resistance. However, bulk Nb is unacceptable for massive production of bipolar plate because of its relatively high cost. Therefore, the concept of coating and surface alloying low-cost stainless steel bipolar plates with Nb seems to be a promising method which could combine the merits of Nb and stainless steels.

2.4.1.1 Niobium coating

A research group in the University of Ulsan, South Korea, has conducted much work on combining the good corrosion resistance and surface conductivity of Nb with the low-cost stainless steel, for their use as bipolar plates in PEMFC. Firstly, they employed hot-rolling to fabricate a relatively thick (50 μm) pure Nb cladding on the surface of stainless steel [160] [161]. The results of corrosion tests and surface conductivity tests of Nb/SS were promising. However, the bond strength between the Nb cladding and the substrate and the mechanical properties were insufficient for subsequent stamping processes. Therefore, an annealing process was conducted after rolling, to obtain sufficient ductility [162]. However, the annealing process also led to the undesired formation of a brittle interfacial intermetallic layer, which resulted in poor performance in mechanical and bending tests.

In view of the problems of the rolling technique, the Nb sputter coating approach was proposed [163]. The performance of the Nb sputter coating was superior to that of the Nb roll-cladding one, in terms of both corrosion resistance and surface conductivity. Most importantly, the thickness of the Nb sputter coating was only 10 % of the Nb roll-cladding, which would significantly reduce the material cost. Kim et al. [164] also investigated the feasibility of Nb sputter-coated stainless steel for bipolar plate

applications. They observed improved corrosion resistance and surface conductivity, but failures of the Nb coating were found after the corrosion test. The failure of the coating led to serious galvanic corrosion, caused by the great difference in corrosion resistance between the Nb coating and the stainless steel substrate, and thus undesirable power degradation.

A plasma surface alloying method was used to niobize the 304 stainless steel [165]. A niobium-rich layer, 3 μm in thickness, was fabricated on the surface. The evaluation tests in a simulated PEMFC environment indicated that the niobized 304 SS exhibited better hydrophobicity compared with the untreated 304 stainless steel, as well as an interfacial contact resistance (ICR) value one order of magnitude lower and better corrosion resistance. No corrosion occurred on the surface of the niobized sample after potentiostatic tests. The same method was employed to fabricate a niobium nitride coating on the surface of 304 SS [166], and showed improved corrosion resistance and surface conductivity.

The nitrides and carbides of niobium also possess good chemical stability and electrical conductivity, and have been selected as candidates for an effective protective layer on stainless steel bipolar plates. Cha et al. [167] used N_2 as a reactive gas to sputter Nb and successfully fabricated niobium nitride films onto the surface of 304 stainless steel. The results revealed that the niobium nitride film improved the corrosion resistance and, even though the ICR value was lower after the introduction of NbN film, it was still higher than the requirement. Wang et al. prepared niobium nitride [165] and carbide [168] coatings by a plasma surface alloying technique. Because of the excellent chemical stability of niobium nitride and carbide, the coated stainless steels exhibited a dramatic improvement in corrosion behaviour. An enhancement in the surface electrical conductivity was also observed for the coated

sample, whereas the ICR value of NbN-coated and NbC-coated samples were in the same level as graphite.

2.4.1.2 Niobium alloying

Lee et al. [169] added 3.0 wt.% Nb to 316 SS by means of vacuum arc melting, followed by a high temperature solution and ageing treatment. The formation of highly electrically conductive Nb carbides contributed to the enhanced electrical conductivity. The surface treatment (shot blasting and pickling in acid solution) dispersed and exposed the precipitates of NbC, which functioned as electrical paths, leading to further improvement in electrical conductivity. However, this paper did not report any corrosion results.

The ion implantation method was applied to introduce niobium into a matrix of 316 stainless steel [170]. A niobium-rich layer with a thickness of 60 nm was formed on the surface after ion implantation. The authors reported improved corrosion resistance after Nb ion implantation. However, the results indicated that the corrosion behaviour of implanted stainless steel was mainly governed by the duration of the ion implantation. Longer implantation times would introduce more defects and damage by the high ion flux, leading to the degradation of the corrosion resistance. Although the ICR value of implanted stainless steel under certain treatment condition was reduced, the value was still too high to be accepted.

2.4.2 Surface modification with noble metals

Noble metals are well known for their excellent corrosion resistance in highly acidic environments and their superior electrical conductivity. However, their high cost limits the wider use of noble metals in bulk. Surface engineering techniques, such as coatings and surface-alloying, have been investigated to combine small amounts of

noble metals with stainless steel, which could offer a compromise solution between performance and cost.

2.4.2.1 Noble metal coatings

The bipolar plates made of stainless steel and coated with noble metals have received increasing attention because they combine the excellent properties of noble metals with the low cost of stainless steel.

Electrochemical plating was firstly used to fabricate noble metal coatings, including gold [93] [171], sliver [172] and palladium [173]. The noble metal coatings offer low contact resistance and high chemical stability. However the wide-spread use of the electrochemical plating methods is restricted by their inherent drawbacks, such as their environmental impact, complex processing conditions, hazardous working environment, and the poor quality and adhesion strength of the plated-coatings.

Compared with electrochemical plating, the physical vapour deposition (PVD) [94] method has lower environmental impact, it is easier to operate and to control with a high level of precision. Hence, the PVD method has been widely used to produce noble metal coatings. Many researchers revealed that micro- [174] [171] or nano- [143] [175] scale Au coatings, produced by PVD, can significantly improve the corrosion resistance, electrical conductivity and cell performance, exhibiting better performance than the commercial Poco^{TM} graphite [174].

Platinum, as a member of the platinum group of elements, is well known for its excellent corrosion resistance, especially in harsh acidic environments, and considered as a noble metal. Hence, platinum is widely used in surface modification application, due to its great corrosion resistance. The potential of platinum for application in bipolar plates has also been studied. Much like other noble metal

coatings, electrochemical plating was also used to fabricate Pt coatings on the surface of stainless steel substrates [176]. The in-situ contact resistance measurements revealed that the platinum coating could significantly reduce the contact resistance of stainless steel. Results also showed that after Pt plating, the contact resistance was much more stable. The same method was also used to deposit a platinum coating on the surface of titanium bipolar plates [177] [95]. The Pt coating acted as a protective layer, to prevent the oxidation of titanium, resulting in the improvement of cell performance. However the drawbacks of electrochemical deposition, such as bad adhesion strength of the coating and pinholes, could affect the long-term performance.

2.4.2.2 Noble metals alloying

Kai Feng et al. [178] conducted silver ion implantation to modify the surface of austenitic 316 stainless steel. The XPS analysis indicated that silver ion implantation decreased the thickness of the passive layer on the surface of 316 stainless steel. The results showed that the corrosion resistance of the implanted samples was enhanced remarkably compared to the uncoated samples. Although the ICR value of implanted stainless steel was only 25 % of the untreated material, this was still much higher than that of the graphite bipolar plates. In addition, the high-cost and line-of-sight nature are barriers to the application of ion implantation.

The alloying of stainless steel with platinum has been studied from 1940s. The research work conducted by Tomashov and Mdme. Chernova indicated that small additions of Pt (0.1 %) into commercial stainless steel (18 % Cr, 9 % Ni) can significantly reduce the corrosion rate in sulphuric acid environments [179]. This early study claimed that the mechanism behind this improvement might be related with the composition of the passive layer formed on the surface, in the presence of Pt,

which improved its protective nature and, ultimately, the corrosion resistance [180]. However, to the author's knowledge, no work has been conducted on the surface alloying of stainless steel with Pt for its application of bipolar plates.

2.4.3 Surface nitriding

Surface nitriding is a conventional technique to harden surface, including thermal nitriding and plasma nitriding. Due to the extremely high nitriding temperature (above 1000 ℃) [181] [182], thermal nitriding is not economic compared to plasma nitriding. Moreover, when austenitic stainless steels are nitrided above 450 ℃ , a discontinuous layer of nitride precipitates forms on the surface, which depletes the material from Cr , thus leading to a remarkable deterioration of the corrosion resistance [183] [184] [185].

Low temperature plasma nitriding offers an economic and more convenient surface modification process for austenitic stainless steels than gas nitriding. This is because low temperature plasma nitriding can retain or even improve the corrosion resistance of austenitic stainless steels [186]. Therefore, many studies have evaluated the potential application of plasma nitriding to modify stainless steels for bipolar plates.

Tian et al. used low temperature plasma nitriding to modify the surface of 304L stainless steel [187] and 316 stainless steels [188]. The results of the electrochemical measurements implemented in simulated PEMFC environments showed that low temperature plasma nitriding slightly improved the corrosion resistance of 304L stainless steel. The results of ICR tests showed that the ICR value decreased significantly after plasma nitriding, becoming almost equal to the ICR value of graphite. However, after potentiostatic polarisation, the ICR value of nitrided 304L stainless steel increased, due to the depletion of iron from the surface.

Wang et al. [189] [185] compared the surface properties of 349 stainless steel nitrided in nitrogen plasma and ammonia plasma. The results revealed that the samples nitrided in nitrogen plasma had a much higher ICR value compared with the untreated sample. In contrast, the ICR value of stainless steel nitrided in an NH_3 plasma was significantly lower than the untreated material. The corrosion resistance of all nitrided samples, whether treated in nitrogen plasma or ammonia plasma, were similar to that of the untreated one.

W. Hong et al. [190] used inductively coupled plasma to nitride austenitic 316 stainless steel. The XRD patterns and cross-sectional SEM showed that a nitrogen-expanded austenite phase, the so-called S-phase, was formed on the surface of the nitrided 316 stainless steel. The results of ICR measurement and the corrosion tests showed that the ICR value of nitrided samples decreased significantly to about 10 mΩ cm^2. The formation of chromium nitride at high nitriding temperature leads to the slight deterioration of the corrosion resistance.

2.4.4 The limitation of present surface modification methods

From the literature review presented above, it becomes apparent that the coating methods could improve the electrical conductivity of stainless steel bipolar plates, which could significantly reduce the ICR value. However, the inherent shortcomings of coating technology, such as pinholes and micro-cracks, are fatal when coated bipolar plates are operating in the aggressive PEMFC environment. The acidic solution could easily penetrate through the defects and result in severe galvanic corrosion at the coating-substrate interface, leading to the catastrophic failure of the coating.

One approach to improve the quality of the coating is to increase the thickness [191], which would clearly increase the cost, especially when noble metals are used. Another approach is to increase the corrosion resistance of the substrate, which would diminish the intensity of the galvanic corrosion, even if the solution penetrates through the coating.

It has been demonstrated that nitriding can enhance the corrosion resistance of stainless steels in the PEMFC working environment. Therefore, a combination of a surface coating with nitriding, the so-called duplex surface treatments, may be a promising method. Some efforts [185] [193] [187] have been dedicated to the production of hard and wear-resistant surfaces by duplex surface treatments. However, the discontinuous nature of this treatment reduces its efficiency and increases its cost. Therefore, it is technically important to develop a surface modification process which could simultaneously nitride the stainless steel substrate and produce a coating on its surface.

2.5 Active screen plasma technology

2.5.1 Introduction

The idea of active screen (AS) plasma technology was first proposed by Georges [195]. A schematic comparison between the conventional direct current (DC) plasma technology and the active screen plasma technology is presented in Figure 2.5.1. The main difference between these two plasma technologies is the part acting as cathode. In DC plasma technology, the cathode is connected to the work table and to the samples, where the plasma directly forms once the high voltage is applied. On the other hand, the cathode in the AS plasma technology, is connected to a metal screen which surrounds the work table in floating potential. Under this electrical

configuration, the plasma is formed on the surface of the metal screen instead of the work table and the samples. This special set-up can address the inherent problems of DC plasma technology, such as edge effect, arcing and non-uniform nitriding caused by non-uniform temperature [196].

In the past decade, active screen plasma technology has been successfully employed to treat many different materials, including low alloy steel [197] [198] [199], and ferritic [200], duplex [201] and austenitic stainless steels [202] [203] [204]. Thanks to this innovative set-up, non-conductive materials can also be treated by active screen plasma technology [205] [206] [207].

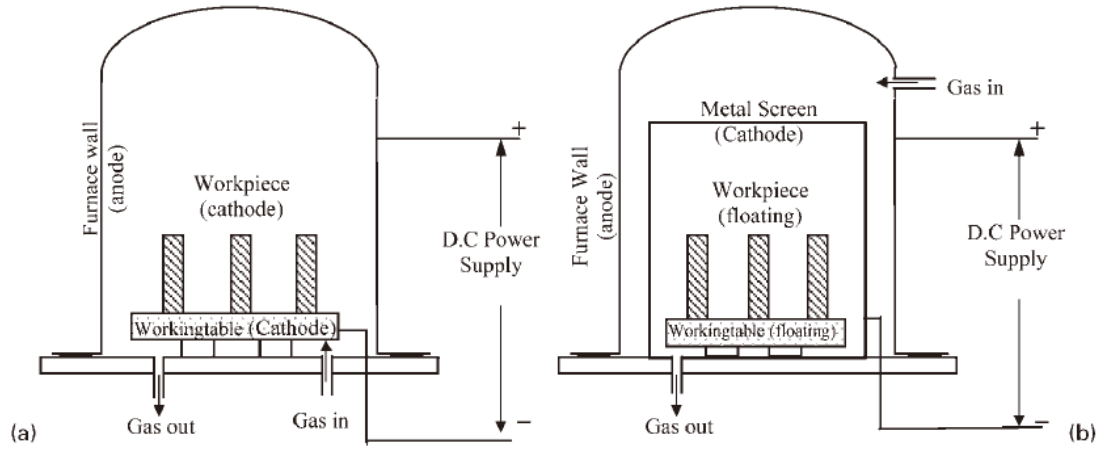

Figure 2.5.1 The schematic comparison between DC plasma and AS plasma technology [196]

Most of the studies on active screen plasma nitriding (ASPN) focus on the improvement of mechanical properties, such as hardness and wear resistance. The results proved that the ASPN treatment can achieve a similar improvement in hardness [201], [202] and wear resistance [200], [202] compared with the conventional direct current plasma nitriding (DCPN).

The other improvement brought by the ASPN treatment is the improvement in corrosion resistance. Li [208] assessed the corrosion resistance of ASPN treated 316 stainless steel by means of immersion tests in 10 % HCl and anodic polarisation tests. The results indicated that the low temperature (420 ℃) treated samples exhibited a considerable improvement in corrosion resistance. However, high temperature (500 ℃) treated samples showed degraded corrosion resistance due to the formation of chromium nitride precipitates. Similar improvements in the corrosion resistance of ASPN treated 316 stainless steel [203], ferritic stainless steel [200] and low alloy steel [199] were also reported.

All the studies mentioned above were conducted using a laboratory-scale active screen set-up. In the work by Corujeira Gallo [209], an industrial active screen plasma unit, Plasma Metal 75 kW unit, was used. He compared the corrosion resistance of untreated 316 stainless with direct current (DCPC) and active screen plasma carburised (ASPC) 316 stainless steel in a boiling sulphuric acid solution. The results revealed that the ASPC samples had better corrosion resistance, as a result of the elimination of the edge effect.

Another important difference between ASPN and DCPN is the formation of a deposition layer on the ASPN treated surfaces. This deposition layer is closely related with the unique mechanism of ASPN, which has attracted the attention of several researchers.

2.5.2 Mechanism of active screen plasma technology

Inspired by the mechanism of DCPN, Li [197] proposed a “sputtering and recondensation model” to explain the ASPN process, after systematically investigating the influence of different factors, such as gas mixture and active screen

setup, on the ASPN treated surface. According to this model, the mass transfer of nitrogen takes place by the sputtering of iron from the cathodic screen, its reaction with nitrogen in the gas/plasma phase, and its deposition onto the sample surface as iron nitride.

Zhao [198] [203] further investigated this mechanism and proposed a modified "sputtering and deposition" model, which is shown in Figure 2.5.2. In his research work, Zhao pointed out that the particles sputtered from the active screen and subsequently deposited on the surface acted as nitrogen carrier. When passing through the plasma, these particles physically adsorbed active nitrogen atoms, after depositing on the sample surface, the active nitrogen atoms desorbed and diffused inward, into the substrate, to form an S-phase layer.

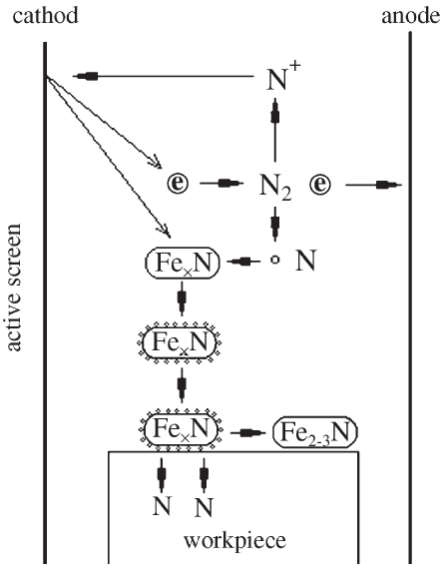

Figure 2.5.2 The model of ASPN proposed by Zhao [198]

In other study, Corujeira-Gallo and Dong [210] investigated the deposition layer. The XRD patterns of the ASPN treated glass revealed that the deposition layer was a mixture of iron nitrides, and the FeN accounted for the largest share. This iron nitride

would easily decompose on ferrous alloys but seemed stable on the inert glass. In addition, he also found that the deposition layer played an important role in the hardening effect.

In other paper by Corujeira-Gallo [211], he found a special patterned deposition of fine particles on the surface of ASPN treated 316 stainless steel, using an industrial active screen plasma furnace (Figure 2.5.3(a)). High magnification SEM images revealed that some grains were covered by fine particles while no particles could be found on the surface of other grains. With the help of electron backscattered diffraction (EBSD) technique (Figure 2.5.3(b)), this special pattern of fine particles was correlated with the different nitrogen diffusion rates among different crystal orientations, which influenced the decomposition rate of the deposited particles. This finding further proves the sputtering and deposition model proposed for active screen plasma nitriding.

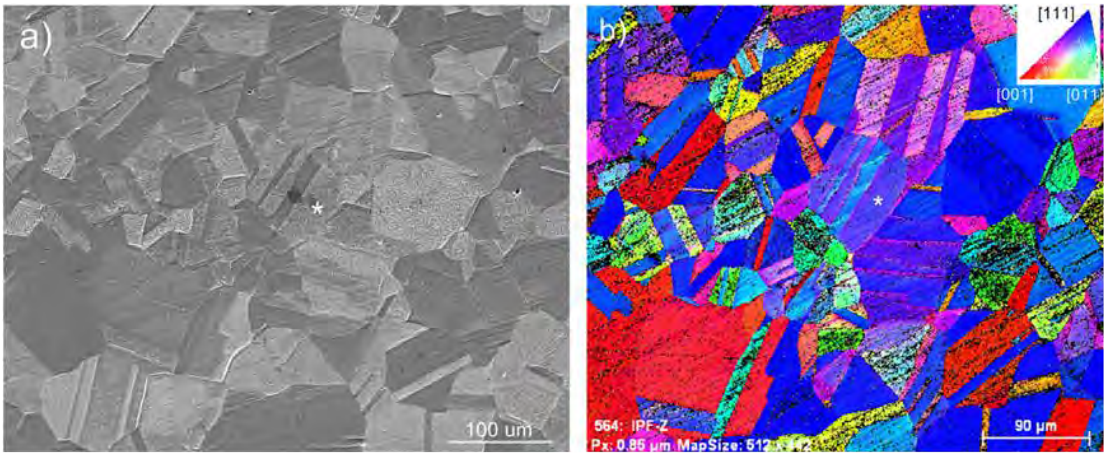

Figure 2.5.3 (a) SEM and (b)EBSD images of ASPN treated 316 stainless steel

By investigating the influence of the open area ratio of the screen on the nitriding results, Nishimoto [204] found that the screen with the lowest open area ratio produced the largest hardness and thickness. He offered a schematic illustration based

on the results, which is shown in Figure 2.5.4. This finding also supports the sputtering and deposition model.

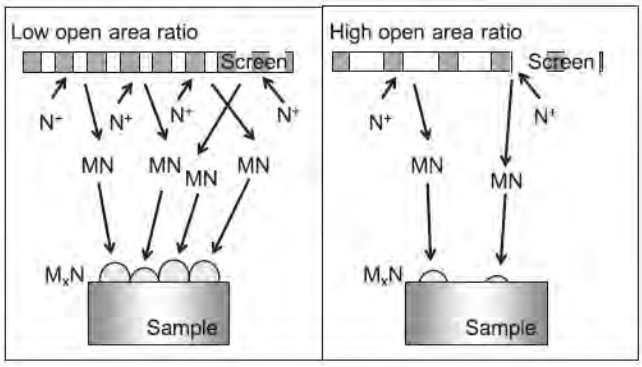

Figure 2.5.4 The model of ASPN proposed by Nishimoto [204]

However, Hubbard and co-workers claimed in their research work [207] [208] that there was no direct evidence for nitrogen mass transfer between the deposition layer and the substrate. The model they proposed is shown in Figure 2.5.5. They believed that a flux of energetic nitrogen species generated by the active screen bombarded the samples and conveyed the nitrogen to the surface of samples.

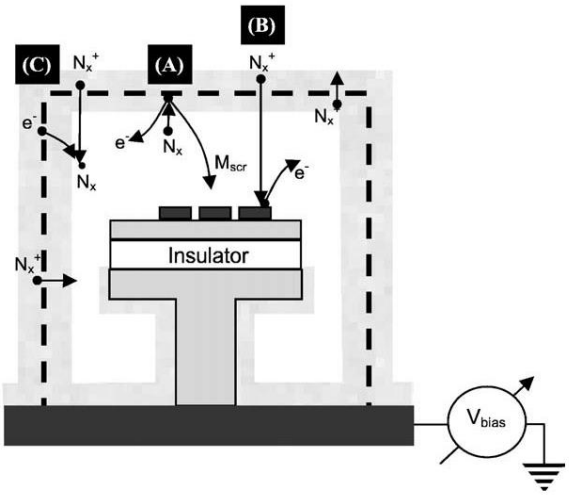

Figure 2.5.5 The model of ASPN proposed by Hubbard [212]

2.5.3 Potential application in one-step duplex surface modification

Although the formation mechanism of the deposition layer in ASPN is not clear yet, the potential application of this duplex surface layer, consisting of a deposition layer and an S-phase underneath, has attracted some attention.

Li [197] tried to use lids of different materials (Ti and Cu) to conduct ASPN treatments, in order to investigate the mechanism of ASPN. Although, the hardening effect of samples nitrided with Ti and Cu lids was insignificant, the deposition layers of the lid material were observed. This finding suggests that it is possible to produce deposition layers, i.e. coatings, by means of ASPN technology with different materials.

Inspired by the pioneer work of Li, Dong [214] employed active screen plasma technology to fabricate a Cu-containing nitride layer on the surface of 316 L stainless steel. The comprehensive characterisation of microstructures and compositions revealed that a homogeneous Cu-containing nitride layer was formed on the surface of the substrate. This layer exhibited a multi-layer structure, containing a deposition layer of nano-crystalline nitrides, a Cu-containing co-deposition layer and a Cu-containing S-phase. By tailoring the composition of the screen lid, Dong developed another duplex layer structure, by active screen plasma nitriding, consisting of an Ag-rich coating and an S-phase layer underneath [215].

Dong's research work indicated that the active screen plasma technology has the ability to produce surfaces with a duplex layer structure in one-step, and the composition of the coating layer can be tailored by changing the composition of the active screen lid.

Chapter 3. Experimental Procedures

3.1 Active screen plasma treatment of carbon paper

3.1.1 Preparation of carbon paper

SIGRACET® GDL 35BC carbon paper was selected as the substrate for growing Pt-nanowires. The carbon paper was cut from the as-received carbon paper sheet into 5 cm^2 pieces, which is the size required for subsequent fuel cell tests. Before the treatments, the carbon paper was blown using an Air Duster to remove any dust and contaminations.

3.1.2 Active screen plasma treatment

The active screen plasma treatments of carbon paper were conducted in a DC Klöckner Ionon 60 kVA furnace (chamber size: 720 mm height; 660 mm in diameter), with an active screen experimental set-up. The schematic diagram of this experimental setting can be found in Figure 3.1.1. The carbon paper was placed on the small worktable, which was electrically insulated from the worktable of the furnace, inside the active screen. The distance from the sample surface to the top lid of the screen was set to 15 mm, and the gas mixture during the treatment was 25 % N_2 and 75 % H_2. These parameters were selected basing on previous research in our group [70] [71]. The principal variables of the active screen plasma treatment of carbon paper were the treatment temperature and the duration.

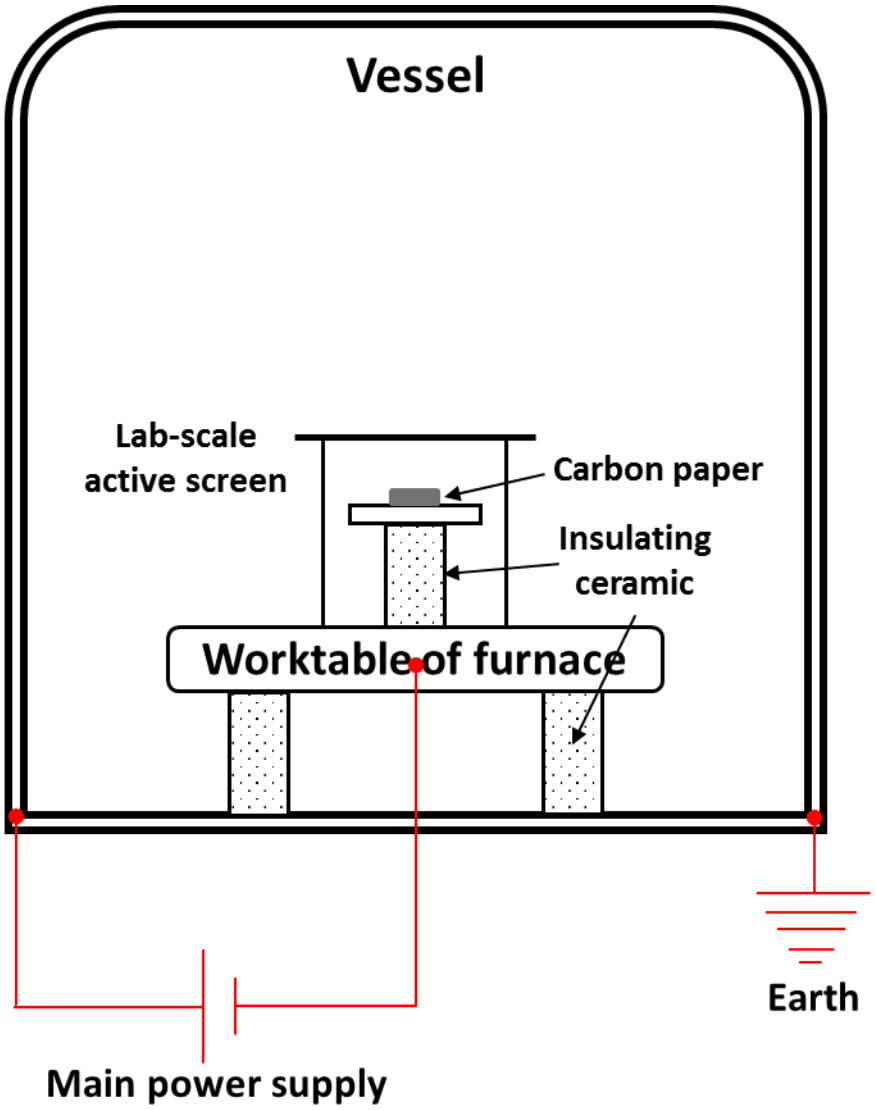

Figure 3.1.1 Schematic diagram of active screen set-up

3.1.3 Growth of Platinum nanowire catalyst layer

In this project, all chemicals were used in the as-received condition, without any further purification. Sulphuric acid (H_2SO_4), hydrogen peroxide (H_2O_2), tetrahydrofuran (THF), ethanol (C_2H_6O), hydrogen hexachloroplatinic acid ($H_2PtCl_6 \cdot 6H_2O$, 99.95 %) and formic acid (HCOOH, 98 %) were acquired from Sigma-Aldrich.

ASP treated and untreated carbon paper samples were first ultrasonically cleaned for 3 minutes in a 5 vol% solution of ethanol in water, and subsequently immersed in an aqueous solution of H_2PtCl_6 and formic acid at room temperature. Normally, for the growth of 2 mg cm^{-2} Pt nanowires on carbon paper, 26.5 mg $H_2PtCl_6 \cdot 6H_2O$ (10 mg Pt, 2 mg cm^{-2} on 5 cm^2 carbon paper) and 0.80 ml formic acid were added to 32 ml of water. The samples were immersed in the solution for 72 hours at room temperature. After the completion of the Pt reduction reaction and the growth of nanowires onto the substrates, the samples were rinsed with water 3 times, ethanol 3 times and water 3 times, followed by drying at 40 ℃ for 24 hours. The carbon paper samples with in-situ grown Pt nanowires were used directly as integrated cathodes in the following electrochemical characterisation tests.

3.1.4 Membrane electrode assembly (MEA) and single cell fabrication

The Nafion® 117 membrane was pre-treated by boiling for 1 hour in 3 % H_2O_2, water, 0.5 M H_2SO_4 and water, respectively. The carbon paper covered with Pt nanowires was assembled with pre-treated Nafion 117 membranes and commercial JM Anode (PtRu 4 mg cm^{-2}) to form the MEA. The commercial Johnson-Matthey (JM) Anode (PtRu 4 mg cm^{-2}) was painted using a THF solution of Nafion DE 1021 (volume ratio of DE 1021 to THF = 1:2), followed by drying at room temperature for 1 hour, to form a thin Nafion ionomer layer. The electrodes were then hot-pressed against the Nafion 117 membrane at 135 °C for 2 min under a constant pressure of 50 kg cm^{-2}. For comparison purposes, MEAs were simultaneously fabricated with Nafion 117 membrane and commercial JM cathode (Pt 4 mg cm^{-2}) and JM Anode (Pt Ru 4 mg

cm^{-2}). The MEA was sandwiched between two graphite bipolar plates to form a single cell with an active electrode area of 5 cm^2.

3.1.5 Electrochemical characterization of carbon paper with Pt nanowire catalyst layer

Cathode cyclic voltammetry: The growth of Pt nanowires was evaluated by cyclic voltammetry analysis of the electrochemical surface area (ECSA). This consists in measuring the amount of gas (H_2 in the case of PEMFC) adsorbed or desorbed, which corresponds to the number of metal atoms that can be accessed because one metal atom adsorbs one gas atom. By calculating the charge under the voltammetric peaks, the amount of absorbed or desorbed gas atoms, and consequently metal atoms, can be determined. In the case of PEMFC, the reaction of gas adsorption is described as follows (Equation 3.1.1):

$$Pt - H_{ads} \leftrightarrow Pt + H^+ + e^- \qquad \text{Equation 3.1.1}$$

In this work, the electrochemical surface areas (ECSA) were calculated by measuring the charge associated with the H desorption (Q_H) between 0 and 0.4 V and assuming Q_{ref} = 0.21 mC cm^{-2}, corresponding to a surface density of 1.3 $\times 10^{15}$ Pt atoms per cm^2, which is generally accepted for polycrystalline Pt electrodes. The ECSA of Pt was calculated based on the relation (Equation 3.1.2):

$$ECSA = Q_H / (Q_{ref} \times m) \qquad \text{Equation 3.1.2}$$

where Q_H is the charge for H desorption (mC), m is the amount of Pt (mg) on the electrode, and Q_{ref} is the charge required for the monolayer adsorption of hydrogen on a Pt surface (0.21 mC cm^{-2}). In this project, the Pt loading was 2 mg cm^{-2}, the electrode area was 5 cm^2, so the total Pt loading (m) was 10 mg.

The experiments were carried out at 75 °C, with the cathode being fed with ultra-pure water, at a constant flow of 1 mL min^{-1}, and the anode being fed with non-humidified hydrogen at a flow rate of 100 sccm. The anode, also designated as a dynamic hydrogen electrode (DHE), served as both reference and counter electrode. The cathode potential was cycled between 0 and 1.2 V versus the DHE at 20 mV s^{-1} for 5 cycles, and the fifth cycle was recorded.

Anode polarisation voltammetry: The anode potential was scanned at 5 mV s^{-1} starting at 0 V, versus DHE, and ending when the current reached 1 A. The experiment was conducted at 75 ℃ , with the anode side being fed with a solution of 1 mol L^{-1} methanol at a rate of 1 mL min^{-1}, and the cathode being fed with non-humidified hydrogen at a flow rate of 100 sccm without back pressure. In this case, the cathode served as both reference and counter electrode, designated as DHE.

Single cell performance test: The experiments were performed at 75 ℃ using an EZstat-Pro system. The anode was fed with a solution of 1 mol L^{-1} methanol at a flow rate of 1 mL min^{-1}, without back pressure. The cathode was fed with non-humidified air at a flow rate of 100 sccm, without back pressure. The cell voltage was looped between 0.2 and 0.7 V at 5 mV s^{-1} for 5 cycles, and the fifth cycle was recorded.

3.1.6 Microstructure characterisation of catalyst layer

The surface morphologies of catalyst layer grown on the carbon paper surface were observed using a scanning electron microscope (SEM, Jeol 7000). A Siemens 5005 X-ray diffractometer (using Cu $K\alpha$, λ = 1.5418 Å) was used to obtain the X-ray diffraction (XRD) patterns. High-resolution transmission electron microscopy (HR-TEM) images were recorded on a FEI Tecnai F20ST microscope operating at 200 kV. Samples for TEM were prepared by scraping the top layer off the GDE pieces,

dispersing in ethanol, and placing a drop of the dispersion on a Cu grid covered with carbon film [2].

3.1.7 X-ray photoelectron spectroscopy analysis of carbon paper

The X-ray photoelectron spectroscopy (XPS) analysis of ASP treated and untreated carbon paper was conducted in a VG Escalab 250 spectrometer, using a high intensity monochromatic Al Kα source.

3.2 Active screen plasma treatments of 316 stainless steel

3.2.1 Sample Preparation

3.2.1.1 Preparation of 316 stainless steel samples

The commercial austenitic stainless steel AISI316 was selected as the substrate; the chemical composition is given in Table 3.1. Coupon samples were cut from a hot rolled bar using a Struers Accutom-5 cutting machine, with a SiC cutting wheel. The final size of the coupon samples was 25.4 mm (1 inch) in diameter and 6 mm in thickness.

Table 3.1 The chemical composition of 316 stainless steel

Element	C	Cr	Mn	Mo	Ni	S	P	Si	Fe
Content (wt %)	0.06	17.20	1.30	2.20	11.70	0.014	0.026	0.60	balanced

The grinding and polishing steps of the sample preparation were conducted using a Struers LaboPol-5 machine. The back side of the samples was wet-ground using SiC grinding paper from grit #120 up to grit #1200. The front side of the samples was prepared to a different surface finishing, between grit #800 and 1 μm, depending on the applied surface treatment. Diamond pastes (from 9 μm to 1 μm) were used in the polishing process. Before treatments, the samples were washed using cotton dipped

with detergent, ultrasonically cleaned in acetone for 5 min and finally dried in flowing hot air.

3.2.1.2 Preparation of cross sectional samples

Cross sections were cut from the treated coupon samples using Struers Accutom-5 cutting machine with SiC cutting wheel, and mounted in conductive bakelite using an Opal 400 automatic mounting press. The mounted samples were firstly wet ground up to grit #1200 and then polished using diamond pastes from 9 μm to 1 μm.

In order to reveal the micro-structure of the cross sections, an etching process was necessary. The composition of the etching solution was 25 ml H_2O, 25 ml HNO_3 and 50 ml HCl. Usually, samples were immersed in the etching solution for about 20 seconds and stirred during immersion. After etching, samples were rinsed immediately with water, cleaned with acetone, and dried in hot flowing air.

3.2.1.3 Preparation of transmission electron microscope (TEM) samples

Firstly, two small samples, approximately 1 mm in thickness, 1.5 mm in width and 3.0 mm in length, were cut from the surface of a treated coupon. The two samples were glued together, with their treated surfaces face-to-face, using GATAN two-component epoxy adhesive, with a ratio of hardener to resin of 1:10. This glued stack was thinned by gentle grinding with grit #800 grinding paper, to a thickness of approximately 50 μm. Subsequently, the two samples were separated by removing the glue in an ultrasonic bath with acetone. The separated samples were moved into a FEI Quanta 3D FEG to conduct the final milling process with a focused ion beam (FIB). Before milling, the FIB unit was used to deposit a protective layer of Pt on the area of interest. The final thickness of the TEM samples after milling was in the order of a

few hundred nanometers. The milled area, still attached to the substrate, was moved into a TEM for further analysis.

3.2.2 Surface treatments

3.2.2.1 Active screen plasma nitriding of 316 stainless steel.

Two plasma furnaces were used to treat 316 stainless steels: (i) AS Plasma Metal 75 kVA + 15 kVA industrial scale unit (Figure 3.2.1 (a)); (ii) DC Klöckner Ionon 60 kVA unit with experimental active screen arrangements (Figure 3.2.1 (b)). The instrumentation in these two plasma furnaces was different, but in general, they all comprise of a sealed chamber, a vacuum pump, a power supply, a gas feeding system, water cooling, a temperature measurement and a computer control system.

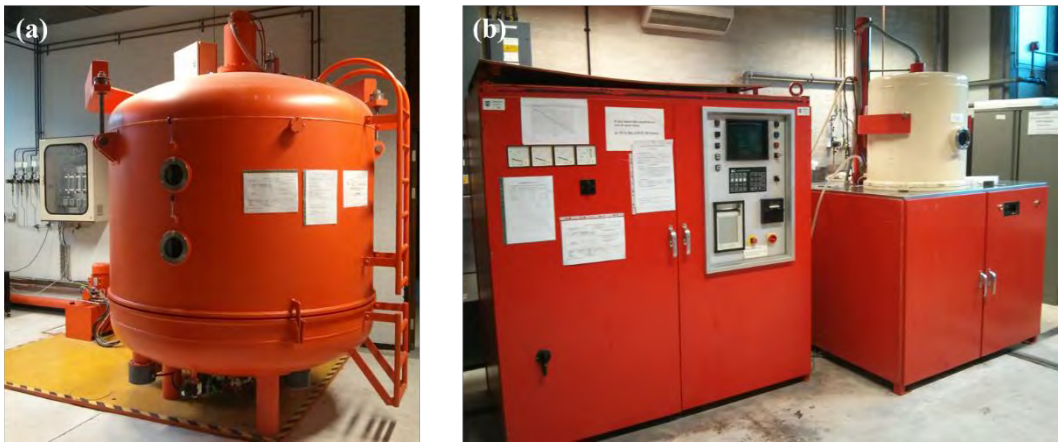

Figure 3.2.1 Plasma furnaces (a) AS Plasma Metal 75 kVA + 15 kVA industrial scale unit (b) DC Klöckner Ionon 60 kVA

The schematic diagrams of the experimental setup used in these two furnaces are shown in Figure 3.2.2. As discussed in section 2.5.2, a high voltage was applied between the anode and the cathode, connected to the vacuum vessel and the active screen, respectively. Under this electrical configuration, the plasma formed on the surface of the active screen instead of the sample surface. In the case of the industrial

plasma furnace (Figure 3.2.2 (a)), an additional power supply was connected to the worktable, to apply an electrical bias. The bias is necessary to attract the active species to the samples because of the large size of the industrial furnace. The bias was selected in terms of power. The material of the active screen inside the industrial plasma furnace was carbon steel.

The size of the lab-scale active screen setup, shown in Figure 3.2.2 (b), was 120 mm in diameter and 130 mm in height, made of perforated 0.7 mm thick 316 stainless steel sheet, with round holes 8 mm in diameter.

The procedure of active screen plasma nitriding can be briefly described as follows: (1) the cleaned samples were placed on the worktable inside the screen; (2) the chamber was hoovered to remove dust and other contaminants; (3) the vessel was sealed, the ventilation valve was closed and the vacuum pumps were turned on; (4) when the base pressure reached 1 Pa, the hydrogen gas was fed into the chamber and the main power supply was turned on, to generate plasma; (5) when the temperature reached 300 ℃ , the gas mixture of 25 % N_2 and 75 % H_2 was fed into the furnace until the end of the treatment; (6) the treatment time was controlled by a timer, which started counting when the temperature reached the set point value; (7) once the treatment finished, the gas flow was stopped and the samples were left to cool down inside the furnace; (8) when the temperature decreased to below 80 ℃ , the chamber was opened to collect the samples.

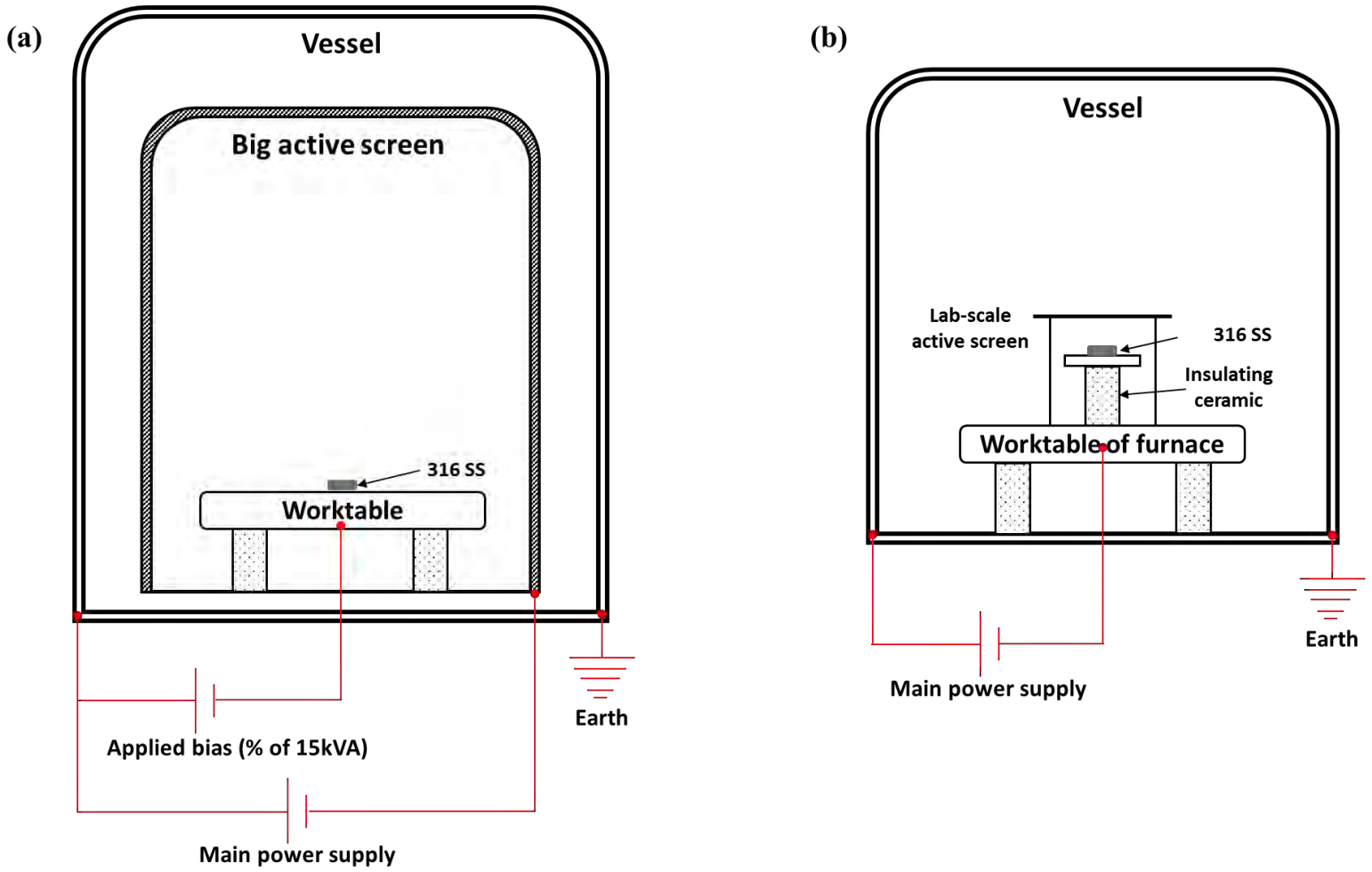

Figure 3.2.2 Schematic diagrams of ASPN setting (a) AS Plasma Metal 75 kVA + 15 kVA industrial scale unit (b) DC Klöckner Ionon 60 kVA

An orthogonal test was designed to investigate the influence of temperature, treatment duration and applied bias on the surface properties of ASPN treated 316 stainless steel using plasma Metal 75 kVA + 15 kVA industrial scale plasma furnace. Because this method could significantly reduce the number of test cases and improve experimental efficiency [216]. The orthogonal setting of nitriding parameters is shown in Table 3.2. From the previous studies [217][208], if the treatment temperature increased to above 450 ℃, the formation of chromium nitride precipitation causes the depletion of chromium and leads to the significant degradation of corrosion resistance of ASPN treated 316 stainless steel. Therefore, the maximum treatment temperature was set as 450 ℃. The working pressure was set as 0.75 mbar and the gas mixture was 25%N_2 + 75%H_2 for all the plasma treatments.

Table 3.2 The orthogonal layout of nitriding parameters setting

Sample	Temperature (℃)	Time (h)	Bias (%)
O-370/3/2	370	3	2
O-370/5/5	370	5	5
O-370/7/8	370	7	8
O-410/3/5	410	3	5
O-410/5/8	410	5	8
O-410/7/2	410	7	2
O-450/3/8	450	3	8
O-450/5/2	450	5	2
O-450/7/5	450	7	5

3.2.2.2 Active screen plasma alloying of 316 stainless steel with N and Ag

Active screen plasma co-alloying treatments with Ag were carried out in a 60 kW Klöckner unit, a conventional DC plasma nitriding furnace, with a laboratory ASPN set-up, shown in Figure 3.2.3. The removable lid was fabricated by a hot isostatic pressing (HIP) method, using a powder mixture composed of 95 wt % 316 stainless steel and 5 wt % silver. The procedure is similar with the ASPN treatments.

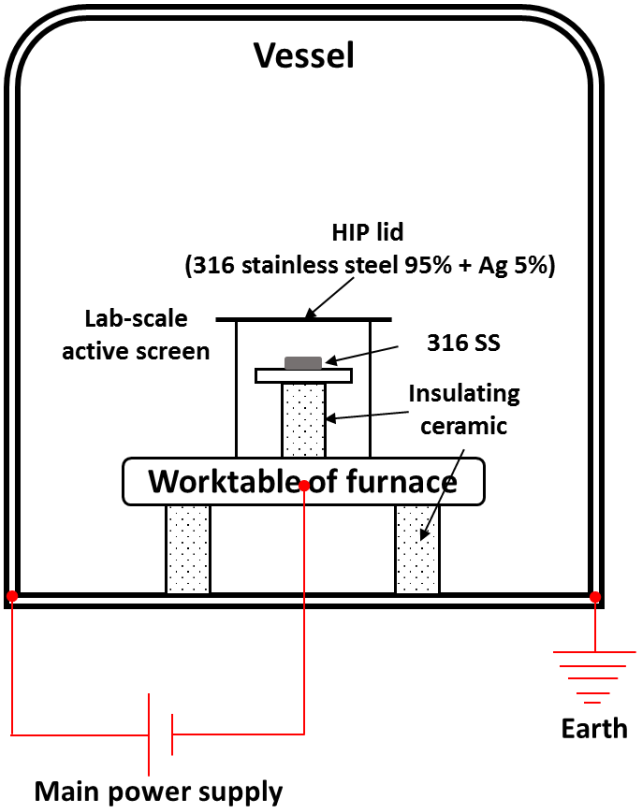

Figure 3.2.3 The schematic diagram of ASPN (Ag) treatment of 316 stainless steel

3.2.2.3 Active screen plasma co-alloying of 316 stainless steel with Nb and Pt

The active screen plasma co-alloying treatments with Nb and Pt were conducted in the AS Plasma Metal 75 kVA + 15 kVA industrial scale unit. The schematic diagram is presented in Figure 3.2.4. A small active screen with a lid containing alloying elements, in this case Nb and Pt, was placed on the worktable of the furnace. The 316 SS samples were placed inside the small active screen setup, on a surface which was electrically insulated from the worktable. The procedure was similar to the normal active screen plasma nitriding.

Besides the variables of normal active screen plasma nitriding, the length of alloying wires was another principal variable for active screen plasma co-alloying treatment with Nb and Pt.

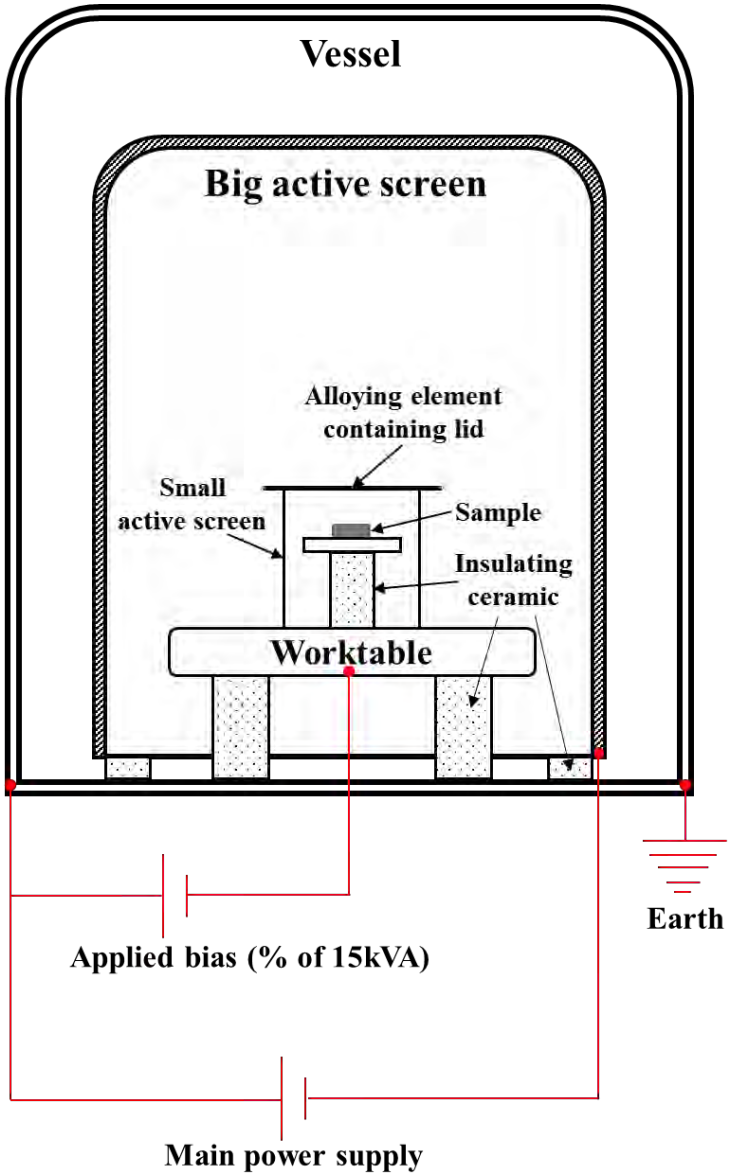

Figure 3.2.4 The schematic diagram of active screen plasma alloying treatments

3.2.3 Characterisation techniques

3.2.3.1 Roughness

The roughness measurements were conducted in an AMBIOS XP-200 stylus profiler (shown in Figure 3.2.5). The measured sites were selected randomly and the reported values are the average of, at least, three measurements.

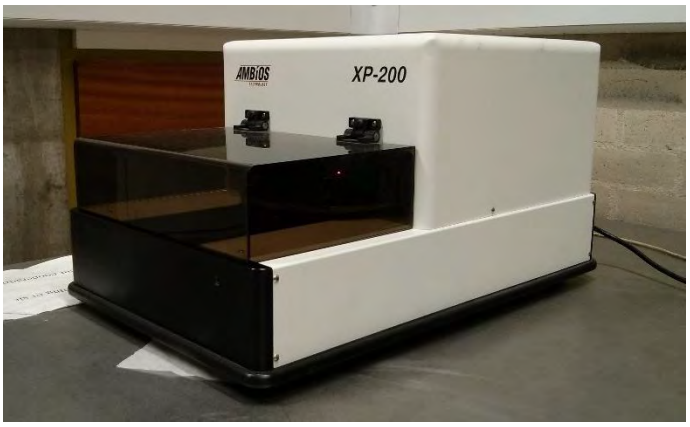

Figure 3.2.5 AMBIOS XP-200 stylus profiler

3.2.3.2 Nano-indentation

The nano-hardness was measured by a computer controlled Nano Test 600 machine, fitted with a Berkovich indenter. Different loads were selected for different experiments. The dwell time of each loading was 20s.

3.2.3.3 Glow discharge optical emission spectroscopy (GDOES)

A Leco GDS-750 GDOES unit (shown in Figure 3.2.6) was employed to obtain the chemical composition profiles, as a function of depth. In this equipment, a glow discharge forms inside the chamber, under the high applied voltage, and Ar ions uniformly sputter material from the sample. The sputtered material spreads into the plasma and some of the atoms become excited. The excited atoms emit light when they decay back to their base energy levels. By measuring the wavelengths and the intensity of the emitted light, it is possible to identify and qualify the materials present in the sample. The size of the measured area was 4 mm in diameter.

Figure 3.2.6 Leco GDS-750 GDOES unit

3.2.3.4 X-ray diffraction (XRD)

The phase structure was analysed by an X-ray diffractometer (Bruker D8 Advance) with Cu Kα radiation (λ=0.154 nm). The spectra were analysed using the commercial software X'Pert HighScore Plus.

3.2.3.5 Scanning electron microscope (SEM) and energy dispersive X-Ray spectroscopy (EDS)

A Jeol 7000 field emission SEM unit was used to observe the surface and cross-section morphology of the samples (show in Figure 3.2.7). The accelerating voltage was set to 20 kV. This SEM unit equipped with an Oxford Instrument Inca energy dispersive X-Ray spectroscopy (EDS) detectors, which is controlled by means of a commercial Inca software. The electron microscope was optimised before each observation.

Figure 3.2.7 Jeol 7000 field emission SEM unit

3.2.3.6 X-ray photoelectron spectroscopy

The surface composition and the element chemical states of untreated and active screen plasma alloyed 316 SS surfaces were investigated using a Thermo Scientific K-Alpha unit or a Theta Probe unit, located at NEXUS NanoLAB, in Newcastle University. The results from different machines could be compared. The depth profiling of elements was obtained by sputtering with Ar ions. The obtained spectra were analysed by CasaXPS through the Newcastle University's Remote Application Service (RAS).

3.2.3.7 Transmission electron microscope (TEM)

A JEOL 2100 LaB_6 TEM, with Oxford Inca EDS, was employed to conduct the TEM analysis with an operating voltage of 200 kV. The samples were investigated by means of bright field (BF) TEM, dark field (DF) TEM and selected area diffraction (SAD).

3.2.4 Evaluation of performance

3.2.4.1 Corrosion tests

In this project, two different set-ups were used for the corrosion tests. The first set-up was used to evaluate the corrosion behaviour of the active screen plasma nitrided samples, and the second set-up was used to evaluate the corrosion behaviour of the active screen plasma co-alloyed samples.

In the first set-up for corrosion tests, untreated and nitrided samples were tested in a 0.05 M H_2SO_4 solution, which was prepared from analytical grade chemicals and distilled water. All the corrosion tests were conducted at room temperature (20 °C) and in open air. A conventional three-electrode system was employed for this setup, in which a platinum plate served as the counter electrode, Ag/AgCl was used for the reference electrode, and the nitrided sample was the working electrode. Figure 3.2.8 shows the schematic arrangement of the electrochemical cell. Before starting a corrosion test, the sample was cathodically polarised to -1.2 V for 3 min, while immersed in the solution, to remove the air-formed film and it was subsequently left to stabilise in the electrolyte at open circuit potential for 15 min. After such reduction and stabilisation treatments, all samples are expected to have a similar initial surface condition.

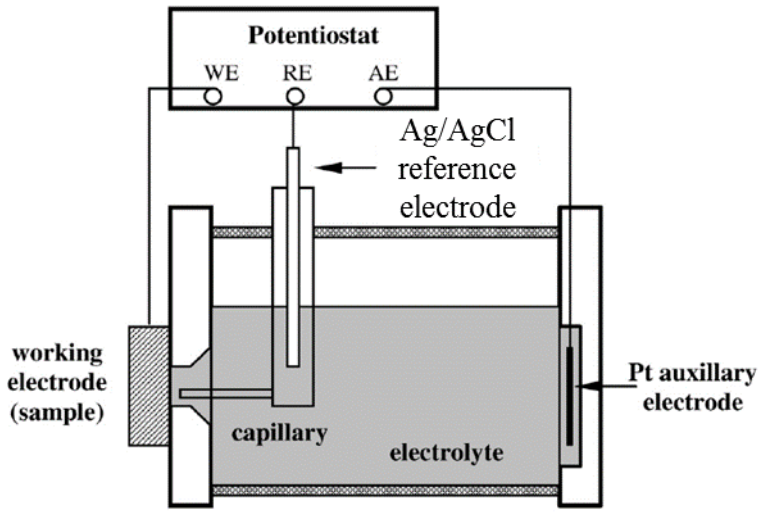

Figure 3.2.8 Schematic diagram showing the arrangement of the electrochemical cell [218]

In the second set-up for corrosion tests, a different assembly was used, and its schematic diagram is shown in Figure 3.2.9. A standard three electrode system was also employed, although a saturated calomel electrode (SCE) was used as the reference electrode, instead of Ag/AgCl. The Gamry electrochemical workstation was used to measure and record the corrosion data. All the corrosion tests were conducted at room temperature (20 °C) and in open air.

To simulate the working environment of PEMFC, a sulphuric acid aqueous solution (0.5M H_2SO_4 + 2 ppm HF) was selected as the corrosion solution. Prior to the potentiodynamic polarisation, an open circle potential test was conducted for 1 h, to stabilise the sample in the corrosive solution. The potentiodynamic polarisation curve started from -0.6 V (vs SCE) to 1.2 V (vs SCE) at a sweep rate of 1 mV/s. For the potentiostatic polarisation, a constant potential of 0.6 V (vs SCE) and -0.1 V (vs SCE) were applied to the sample for the duration of 4 hours, to simulate the cathode and anode environments, respectively.

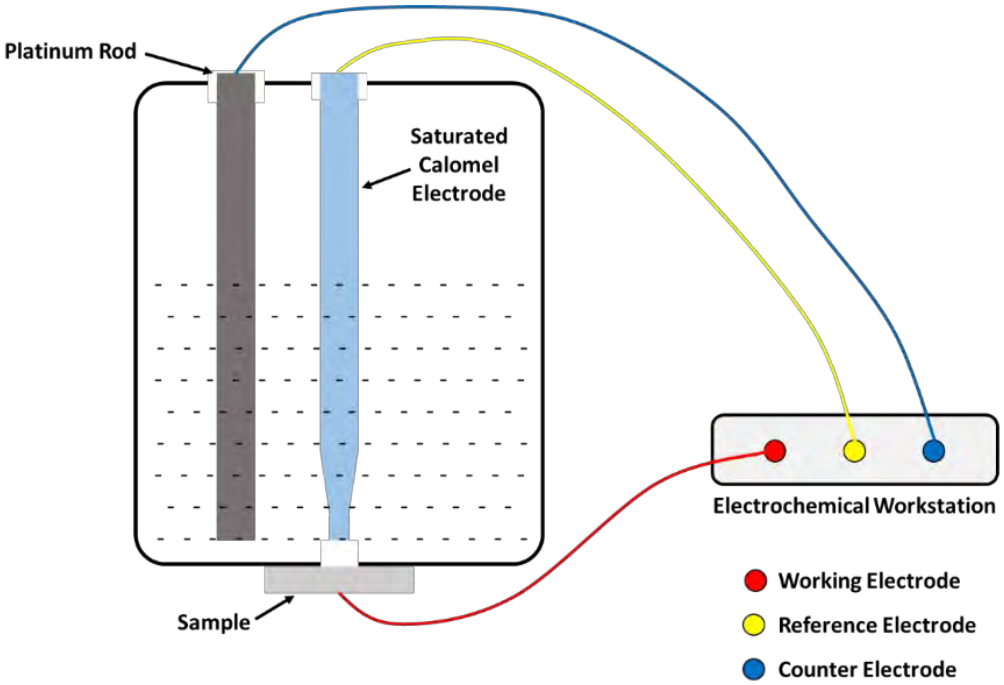

Figure 3.2.9 Schematic diagram of the electrochemical cell

3.2.4.2 Surface electrical conductivity

The interfacial contact resistance (ICR) was measured by Wang's method [118]. In simple terms, the sample was sandwiched between two pieces of carbon paper (Tonry), and further sandwiched between two copper plates under the compaction force of 140 N/cm^2. A constant current was applied to such cell through the copper plates. By measuring the voltage drop across this cell, the total resistance can be calculated. A micro-ohm meter was used to apply the current and measure the resistance directly. To obtain the final ICR value, two measurements should be conducted. The schematic of the first measurement is shown in Figure 3.2.10.

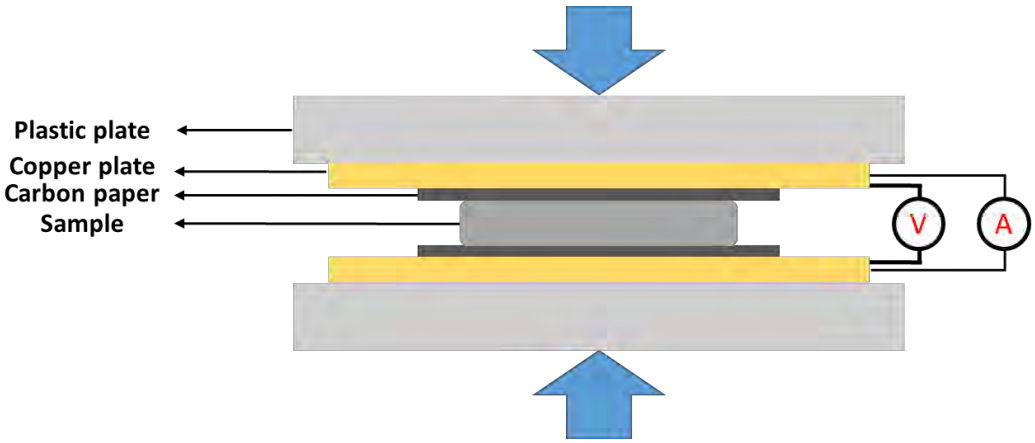

Figure 3.2.10 Schematic diagram of the first measurement of ICR tests

The total resistance of this setup, R_1, consists of the bulk resistance (the two copper plates, the two pieces of carbon paper and the sample) and the contact resistance (the two copper plate-carbon paper interfaces and the two sample-carbon paper interfaces). In general, only one side of the sample was surface treated. To eliminate the influence of the back side of the specimens, a gold-coating was deposited on it, so that the resistance could be neglected. The equation used to calculate R_1 is shown below (Equation 3.2.1):

$$R_1 = 2R^{bulk}_{copper\ plate} + 2R^{bulk}_{carbon\ paper} + R^{Bulk}_{sample} + 2R^{contact}_{copper\ plate-carbon\ paper} + R^{contact}_{carbon\ paper-treated\ surface}$$

Equation 3.2.1

The other measurement, with only one piece of carbon paper, was conducted and in this case the surface area of the carbon paper is the same as with the couple sample. The schematic of the measurement is shown in Figure 3.2.11.

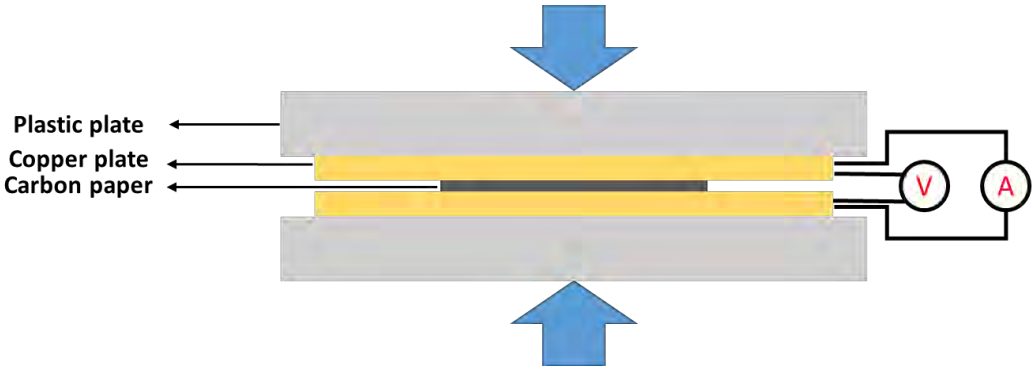

Figure 3.2.11 Schematic diagram of the second measurement of ICR tests

The equation used to calculate R_2 is shown below (Equation 3.2.2):

$$R_2 = 2R^{bulk}_{copper\ plate} + R^{bulk}_{carbon\ paper} + 2R^{contact}_{copper\ plate-carbon\ paper} \quad \text{Equation 3.2.2}$$

Subtracting R_2 from R_1, we can obtain a new equation (Equation 3.2.3),

$$R_3 = R^{bulk}_{carbon\ paper} + R^{Bulk}_{sample} + R^{contact}_{carbon\ paper-treated\ surface} \quad \text{Equation 3.2.3}$$

The bulk resistance is several orders of magnitude lower than that of the interfacial resistance, thus it could be neglected [219] [220] [221]. Hence, the equation above could be simplified into equation (Equation 3.2.4):

$$R_3 = R^{contact}_{carbon\ paper-treated\ surface} \quad \text{Equation 3.2.4}$$

Finally, the value of ICR could be calculated by the following equation (Equation 3.2.5):

$$ICR = S \times R^{contact}_{carbon\ paper-treated\ surface} = S \times R_3 \quad \text{Equation 3.2.5}$$

where S is the surface area of the couple sample.

Chapter 4. Results and Interpretation

4.1 Active-screen plasma treatment of carbon paper

In order to study the influence of active screen plasma treatment on the surface properties of carbon paper and the subsequent growth of Pt nanowires on its surface, two important parameters, namely treatment duration and treatment temperature, were investigated systematically. Although the experimental details have been given in Section 3.1, it is worthwhile to summarise the optimisation process before presenting the results. The best treatment duration was first identified for a given temperature and then further temperatures were investigated in order to optimise the treatment temperature.

When optimising the treatment duration, the growth of Pt nanowires on the surface of carbon paper was preliminarily evaluated by means of electrochemical surface area measurement (ECSA), which is calculated from cyclic voltammogram (CV) curves. The larger the ECSA value, which means that a larger surface area of Pt nanowire catalyst is involved in the electrochemical reaction, the better the growth of Pt nanowires. When optimising the treatment temperature, both the electrochemical surface area measurement and the single cell tests were conducted. The surface morphology and microstructure of the platinum nanowire layer was investigated by means of SEM, XRD and TEM. The chemical state of the ASP treated carbon paper, which conferred the best electrochemical performance, was analysed by XPS to explain the mechanism of enhanced growth of Pt nanowire by ASP treatment.

4.1.1 Influence of ASP treatment duration

To investigate the influence of the duration of ASP treatment of carbon paper on the growth of Pt nanowires, the temperature and pressure of the ASP treatments were set as 120 ℃ and 4 mbar, respectively. Two different treatment durations were selected, namely 10 min (C/Pt-120/10) and 50 min (C/Pt-120/50). After the ASP treatments, platinum nanowires were grown on the surfaces of the treated carbon paper under the same conditions used by the collaborators within the University of Birmingham [2].

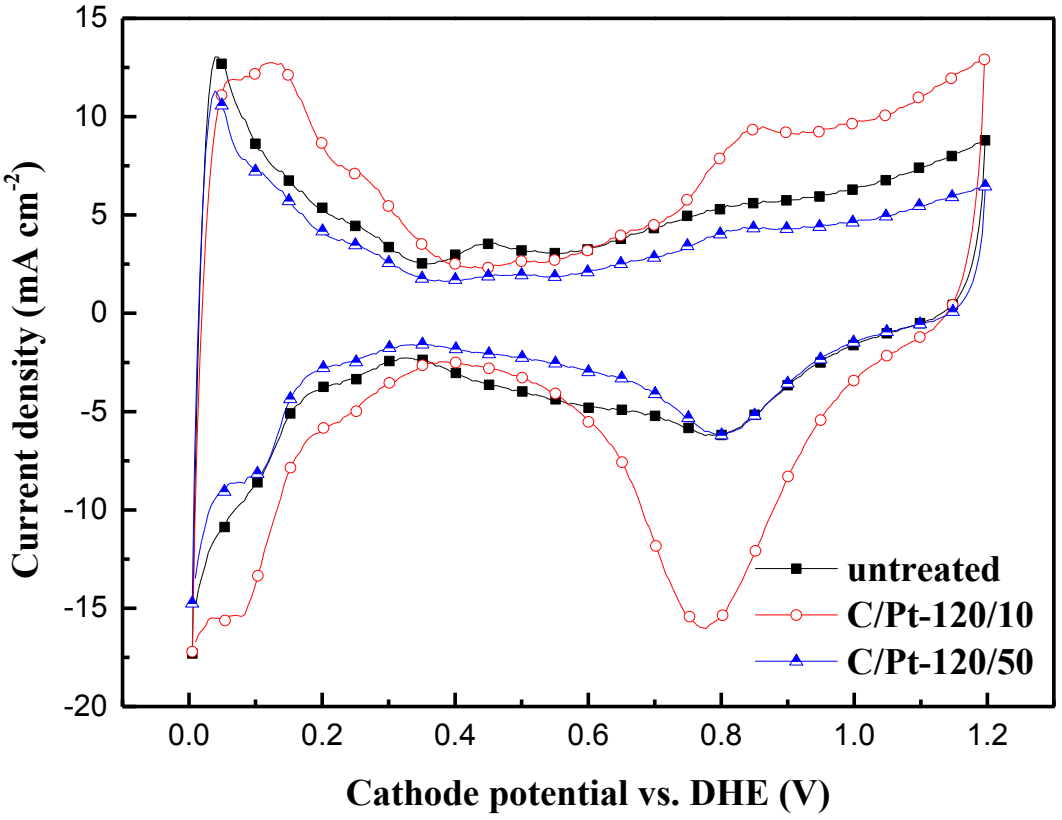

Figure 4.1.1 Cyclic voltammetry of Pt nanowires covered carbon paper treated under 4 mbar at 120 °C

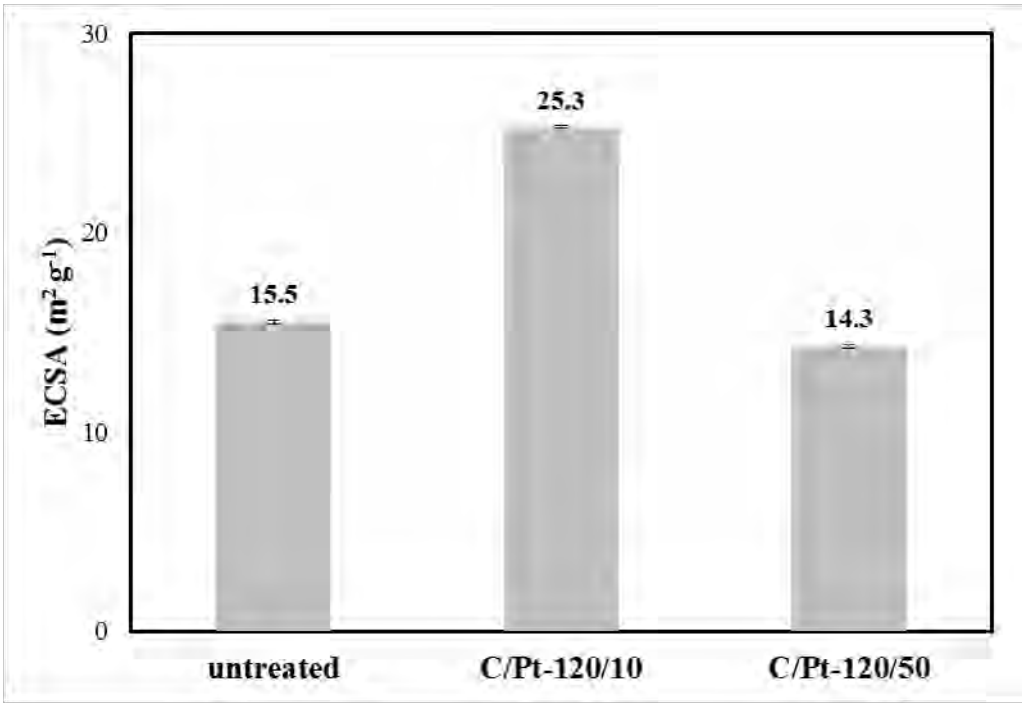

Figure 4.1.2 ECSA of Pt nanowires covered carbon paper treated under 4 mbar at 120 °C

The CV curves of Pt-grown carbon paper are plotted in Figure 4.1.1, and the calculated ECSA values of the corresponding carbon paper are showed in Figure 4.1.2. It can be seen clearly from the figures that C/Pt-120/10 sample shows the highest ECSA value among all the samples, which means that the growth of Pt nanowires is the best on the surface of the 10 min treated carbon paper.

In order to test if 10 min is the optimal treatment duration, another group of samples were treated at 150 °C for 10 min (C/Pt-150/10) and 50 min (C/Pt-150/50) before the growth of Pt nanowires. The CV curves and the ECSA values of these two samples are plotted in Figure 4.1.3 and Figure 4.1.4, respectively. It can be seen again that the short-time ASP treated sample (C/Pt-150/10) exhibits a higher ECSA value than that of the untreated one. When increasing the treatment duration to 50 min, the ECSA

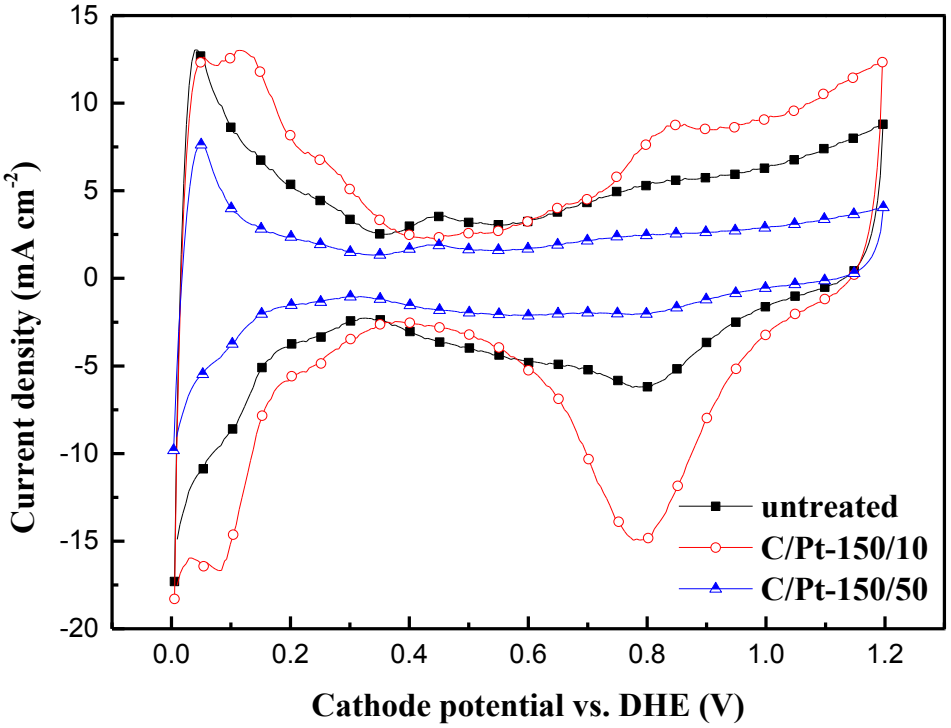

Figure 4.1.3 Cyclic voltammetry of Pt nanowires covered carbon paper treated under 150 °C

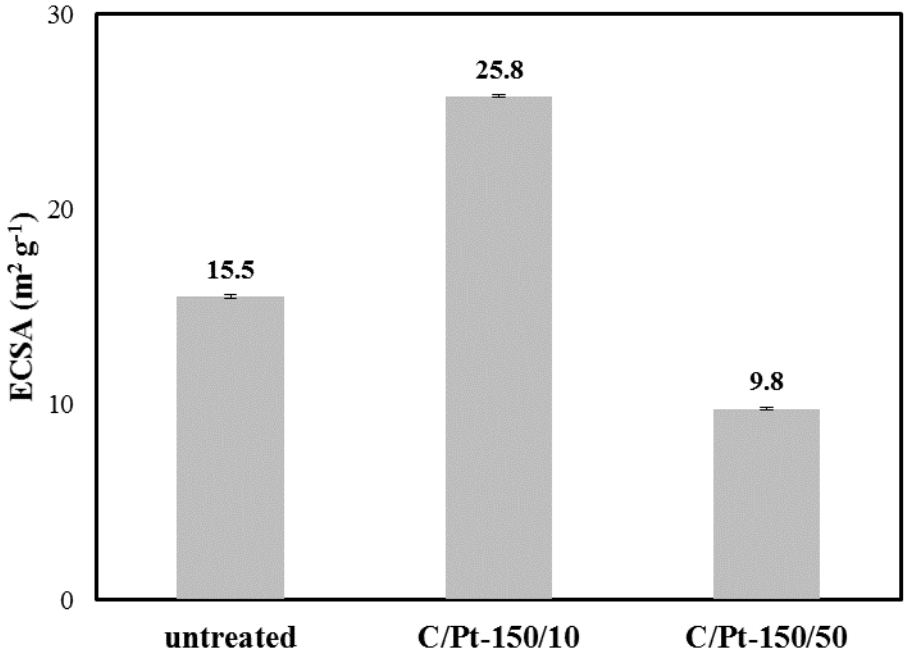

Figure 4.1.4 ECSA of Pt nanowires covered carbon paper treated under 150 °C

value of the C/Pt-150/50 sample reduces significantly to less than half that of the untreated one. This trend is in agreement with the 120 °C treated samples.

From the results of these two groups of samples, it can be confirmed that active screen plasma treatment for 10 min can promote the growth of Pt nanowires on the surface of the ASP treated carbon paper, and longer treatment durations reduced the growth of Pt nanowires.

4.1.2 Influence of ASP treatment temperature

Five different temperatures were chosen for the optimisation of ASP treatment temperature with a fixed treatment duration of 10 min, namely 100 °C (C/Pt-100/10), 120 °C (C/Pt-120/10), 150 °C (C/Pt-150/10), 180 °C (C/Pt-180/10) and 210 °C (C/Pt-210/10). The pressure of the ASP treatments was set as 4 mbar.

4.1.2.1 ECSA measurements

The CV curves of all these five samples are plotted in Figure 4.1.5 and the calculated ECSA values are summarised in Figure 4.1.6. From those two figures, it can be seen that the ECSA values of all the ASP treated carbon paper are higher than that of the untreated one. The samples treated at 120 °C and 150 °C exhibit higher ECSA values than the others. The ECSA values of these two samples show about 65 % increase than that of the untreated one.

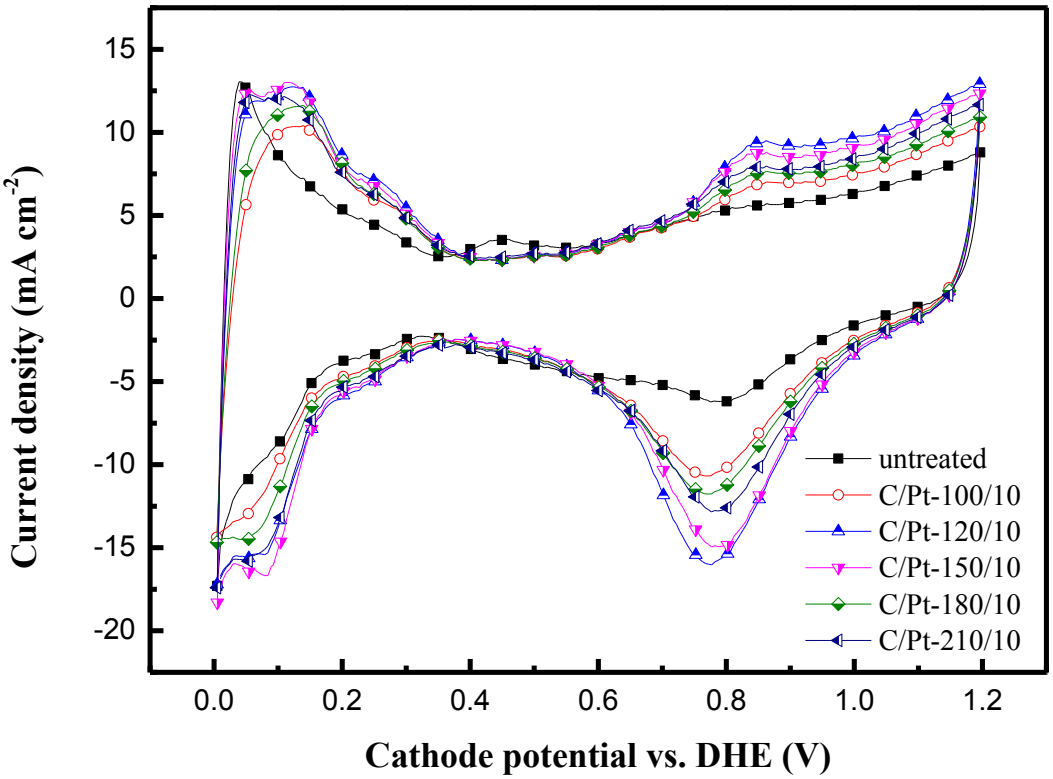

Figure 4.1.5 Cyclic voltammetry of Pt nanowires covered carbon paper ASP pre-treated for 10 min as a function of the treatment temperature

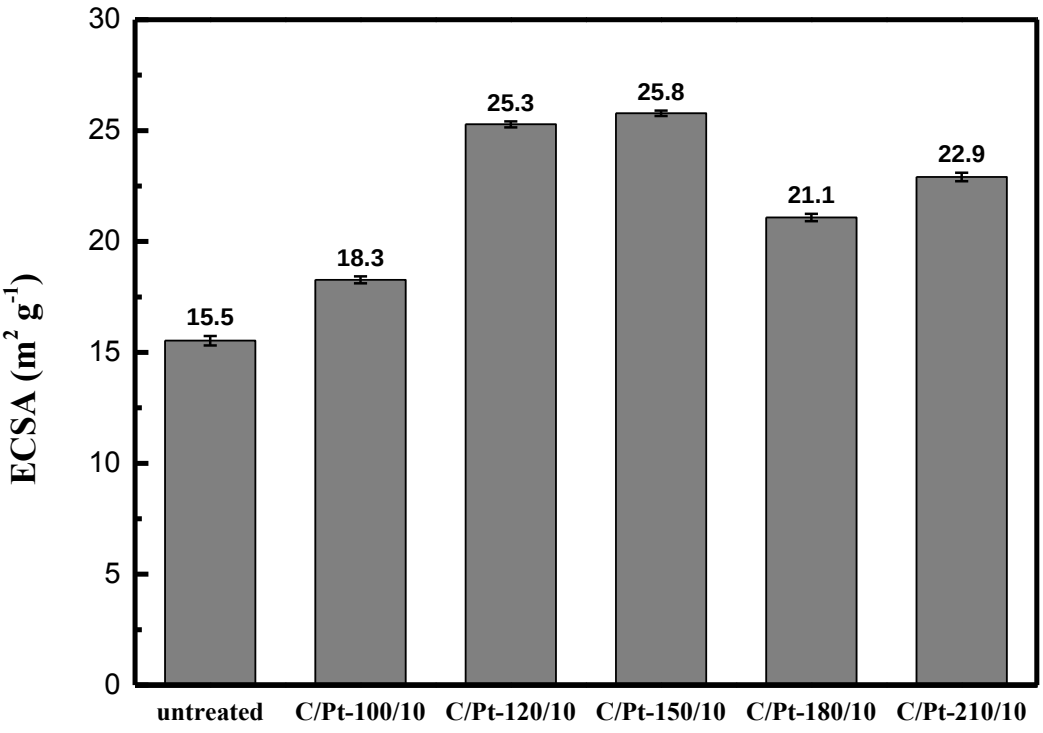

Figure 4.1.6 ECSA values of Pt nanowires covered carbon paper ASP pre-treated for 10 min as a function of the treatment temperature

4.1.2.2 Single cell performance

The polarisation curves and power density of the Pt nanowires grown carbon paper treated at different temperatures are plotted in Figure 4.1.7. All ASP treated carbon paper exhibits a better performance than that of the untreated carbon paper. Among the treated carbon paper, the C/Pt-120/10 and C/Pt-150/10 treated samples show an outstanding performance. The output power densities at 0.4 V of these samples are presented in Figure 4.1.8. The carbon paper treated under low temperatures (<120 °C) and high temperatures (>150 °C) exhibits similar output power density to that of the untreated one. However, C/Pt-120/10 and C/Pt-150/10 samples show a great improvement in output power density, about 3 times higher than that of the untreated one. This is in line with the ECSA values shown in Figure 4.17.

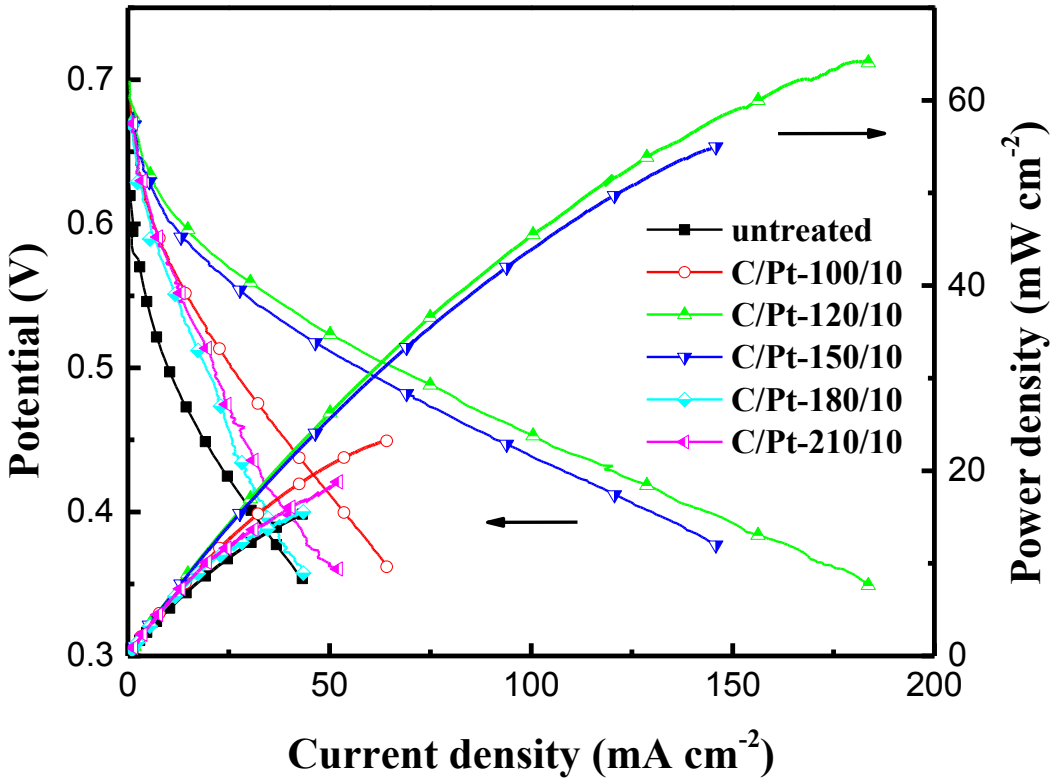

Figure 4.1.7 The polarisation curves and power density of Pt nanowires covered carbon paper ASP pre-treated for 10 min as a function of the treatment temperature

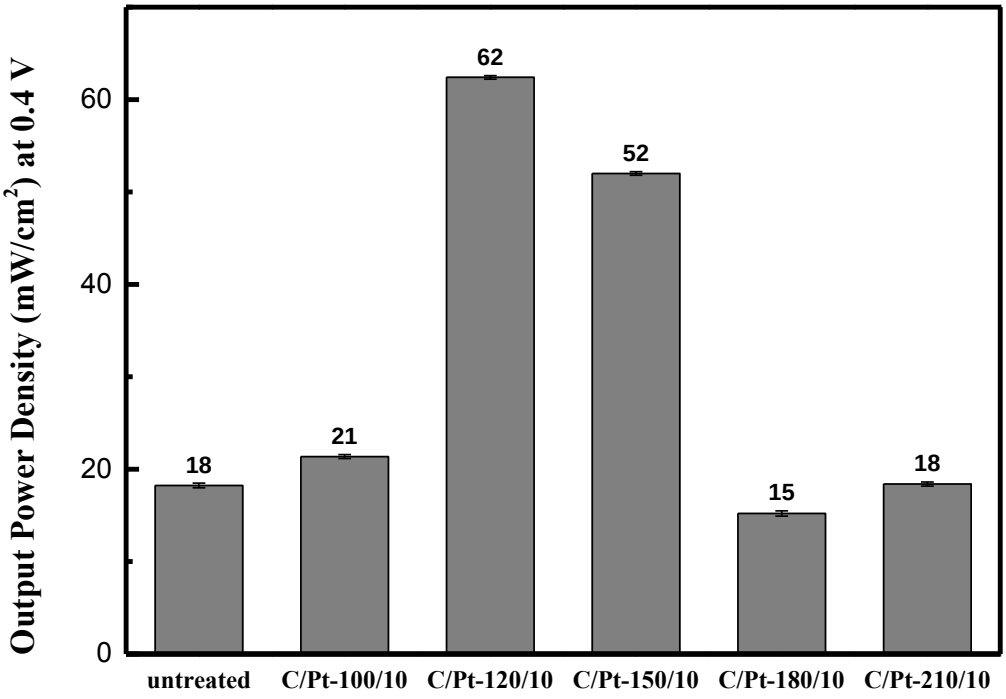

Figure 4.1.8 The output power density at 0.4 V of Pt nanowires covered carbon paper ASP pre-treated at different temperatures for 10 min

Combining the results of ECSA and single cell tests, it can be concluded that the C/Pt-120/10 sample shows the best electrochemical performance among all the ASP treated carbon paper samples. Hence the significantly improved output power density could be attributed to the enhanced growth of Pt nanowires on the ASP treated carbon paper.

4.1.3 Effect of ASP treatment on the surface morphology and microstructure of Pt nanowire layer on carbon paper

4.1.3.1 Surface morphology

Due to the outstanding ECSA and single cell performances, the morphology of the Pt nanowire layer on the surface of C/Pt-120/10 carbon paper was compared with that of the untreated carbon paper to better understand the mechanism of enhanced catalytic performance induced by ASP treatments.

The SEM surface morphology of the Pt-nanowire layer on the untreated carbon paper and C/Pt-120/10 carbon paper is compared in Figure 4.1.9. It can be clearly seen that many unevenly distributed large white lumps formed on the surface of carbon paper without pre-ASP treatment (Figure 4.1.9(a)). In contrast, much fewer large white lumps can be found on the surface of the C/Pt-120/10 carbon paper (Figure 4.1.9(b)) than on the untreated carbon paper.

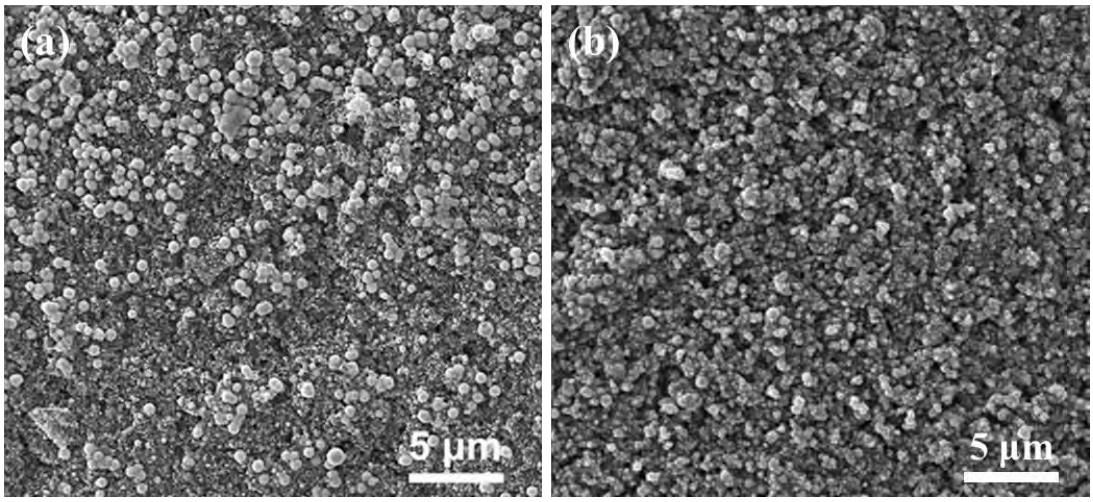

Figure 4.1.9 Low magnification SEM image of Pt nanowires grown on the carbon paper: (a) Untreated sample (b) C/Pt-120/10 carbon paper [2]

The high magnification SEM images taken of both at the corner and in the centre of the untreated and C/Pt-120/10 carbon paper are shown in Figure 4.1.10. Under high magnification, the large white lumps on the surface of untreated carbon paper (Figure 4.1.10 (a) (c)) were determined to be the aggregates of many nanowires and the diameter of those aggregates is around 500 nm. Compared the corner area with the centre area of the untreated carbon paper (Figure 4.1.10 (a) vs (c)), it can be found that more nano-wire aggregates are observed at the corner area than that of in the centre area. In the rest area (Figure 4.1.10 (b) (d)), the carbon paper was covered by a

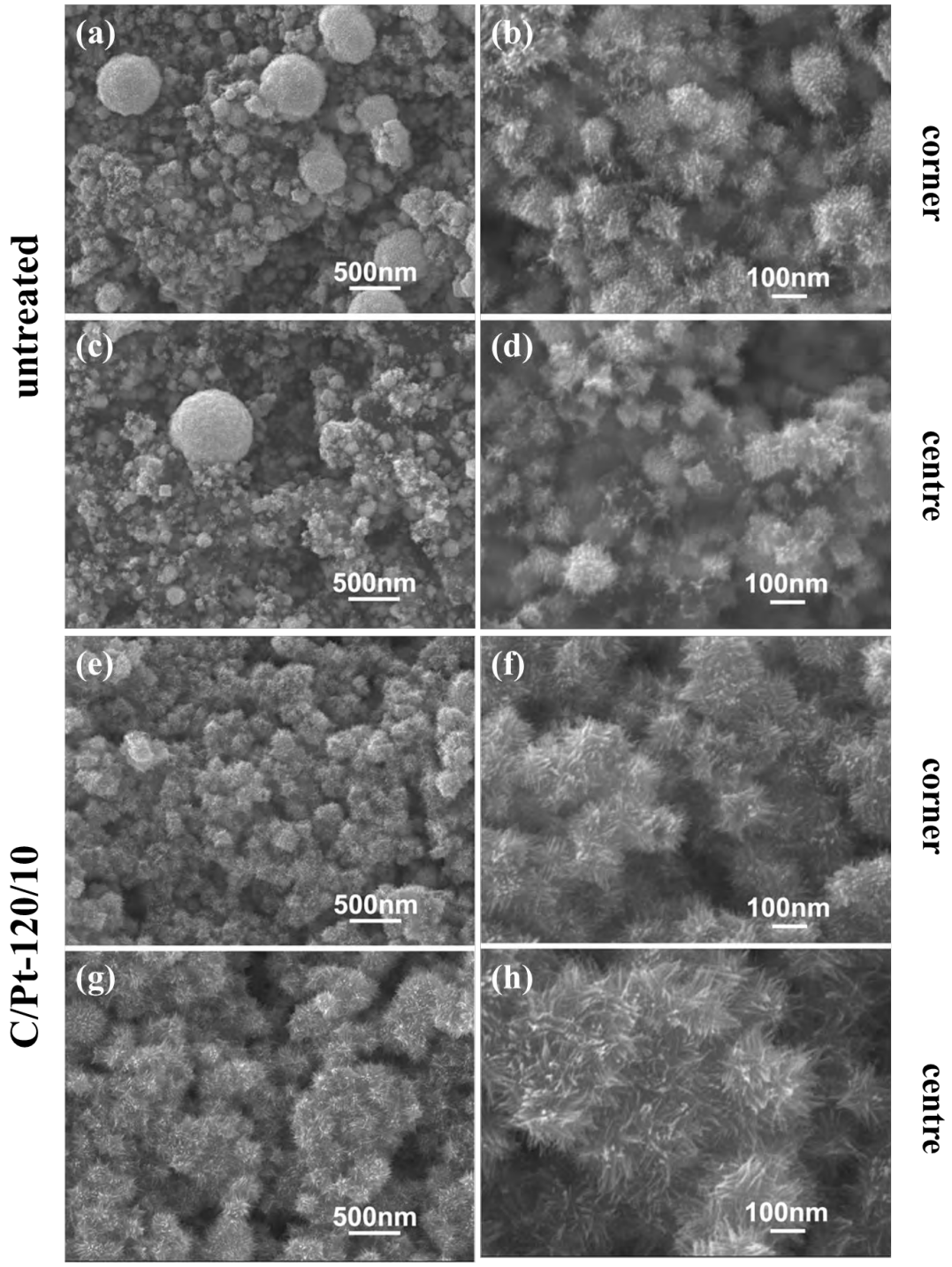

Figure 4.1.10 High magnification SEM images of Pt nanowires grown (a)&(b) at the corner area (c)&(d) in the centre area of untreated carbon paper (e)&(f) at the corner area (g)&(h) in the centre area of ASP treated carbon paper [2]

layer of short and fine flower-like nanowires. It can be seen from the SEM images of the corner area and the centre area that the growth of nanowires on the surface of untreated carbon paper is not uniform. The coverage rate of the nanowires layer is higher at the corner area than in the centre area.

The high magnification SEM images of nanowires on C/Pt-120/10 carbon paper at the corner and in the centre area are shown in Figure 4.1.10 (e) (f) (g) (h). It can be clearly seen that no aggregates of nanowires can be found from the surface of C/Pt-120/10 carbon paper. Almost all carbon nano-spheres are covered by a fur-like nanowires layer. The length of the nanowires is much longer than that formed on the untreated sample surface. The corner and the centre areas exhibit similar surface morphology except for the fact that the Pt nanowires is slightly longer and denser in the centre area than at the corner area.

From the comparison of the surface morphology of Pt nanowire layer formed on the untreated carbon paper and on the C/Pt-120/10 carbon paper, it is clear that the growth of Pt nanowire layer has been effectively enhanced on the ASP treated C/Pt-120/10 carbon paper. The aggregates of the Pt nanowires formed on the surface of untreated carbon paper significantly reduced the specific surface area, which is harmful to their catalytic performance. The coverage rate of the Pt nanowires is also lower than that of the ASP treated one. In addition, the Pt nanowires on the surface of ASP treated carbon paper are much longer than that formed on the untreated one, which increases the surface area exposed in solution. All these aspects should have contributed to the significantly increased electrochemical surface area (ECSA) of the ASP treated carbon paper and thus the effectively enhanced single cell performance.

4.1.3.2 Microstructures

XRD

The XRD pattern of the nano-wire arrays grown on the C/Pt-120/10 carbon paper is presented in Figure 4.1.11. The pattern of pure Pt can be easily detected with the preferred orientation of <111>.

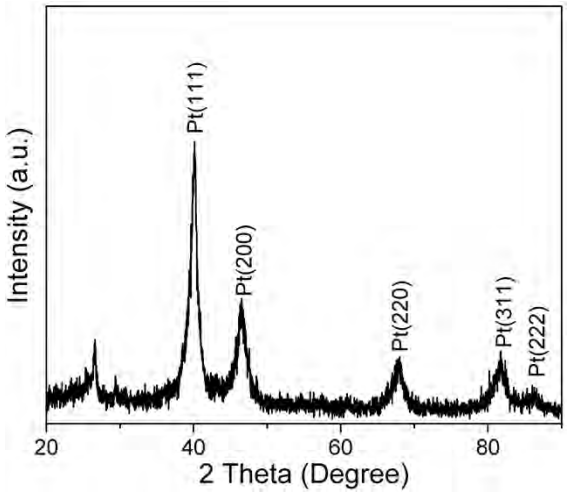

Figure 4.1.11 XRD pattern of the nano-wire arrays grown on ASP treated carbon paper [2]

TEM

The TEM images of the Pt nanowires formed on the surface of the untreated and the C/Pt-120/10 carbon paper are given in Figure 4.1.12. It can be seen that the average length of the nanowires formed on the surface of the C/Pt-120/10 carbon paper (50-100 nm) is longer than that of the untreated carbon paper (10-40 nm). The HR-TEM images of nanowires on the surface of ASP treated carbon paper shown in Figure 4.1.12 (c) reveals that the individual nanowires have a single crystal feature and the lattice spacing of the nanowires is about 0.23 nm, which matches with that of the {111} planes of bulk Pt crystal.

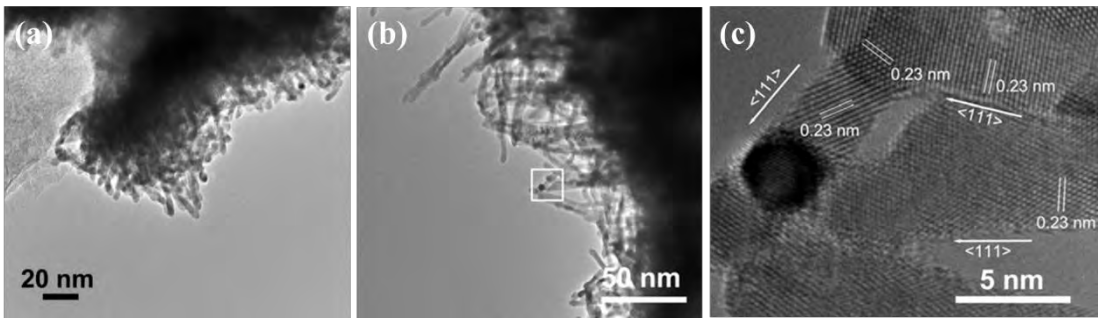

Figure 4.1.12 TEM image of the Pt nanowires grown on (a) the untreated and (b) (c) the C/Pt-120/10 carbon paper [2]

From the XRD pattern and the HR-TEM images, it can be concluded that the Pt nanowires formed on the ASP treated carbon paper are pure platinum with the preferred orientation of <111>.

4.1.4 XPS analysis of the ASP treated carbon paper surface

From the results presented above, it can be seen that active screen plasma treatments can significantly improve the growth of Pt nanowires on the surface of carbon paper, in terms of uniformity of distribution and length of individual nanowires. In order to advance scientific understanding of the mechanism involved in the improvement, further surface characterisation was conducted by XPS (see Section 3.1.7). Among the active screen plasma treated samples, the C/Pt-120/10 sample exhibited the best electrochemical and single cell performance. Therefore, the surface of the ASP treated carbon paper at 120 ℃ for 10 min (C-120/10) was investigated by XPS analysis and compared with the untreated carbon paper to find out the changes of the surface induced by the active screen plasma treatments.

4.1.4.1 Survey spectra

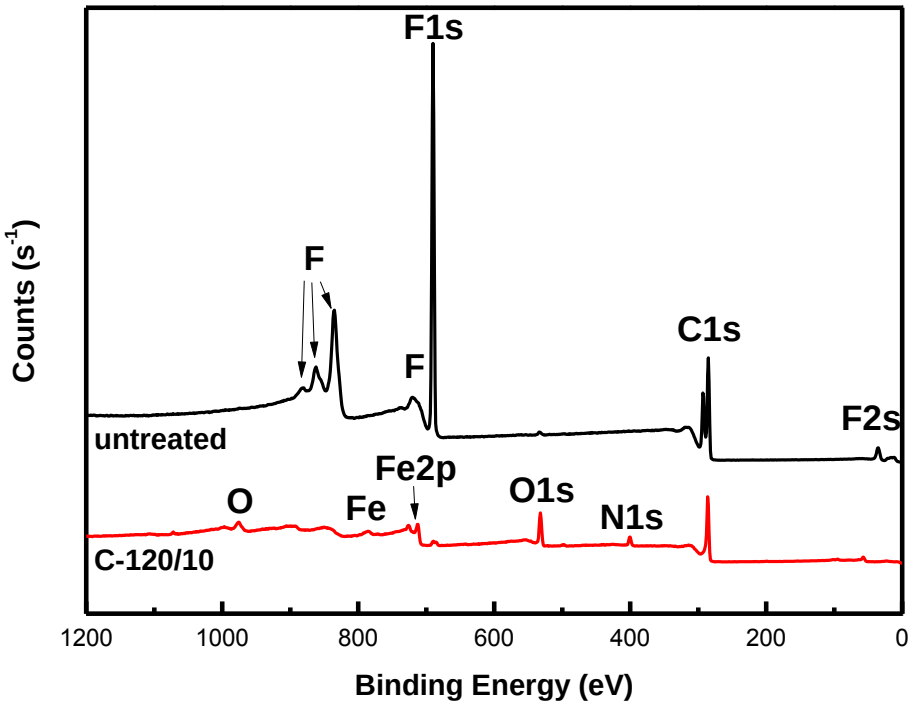

Figure 4.1.13 XPS survey spectra of untreated and ASP treated carbon paper

The XPS survey spectra of untreated and C-120/10 carbon paper are shown in Figure 4.1.13. The differences between these two spectra could be summarised as follows: the peaks of F almost vanish after active screen plasma treatment; only the lower binding energy peak of C1s peak remains; and peaks of O 1s, N 1s and Fe 2p appear after the active screen plasma treatment.

4.1.4.2 Individual elements

In order to deeply investigate the change of individual element before and after active screen plasma treatment, the detailed XPS analysis of those elements were conducted and results are reported in this section.

Fluorine

The XPS fluorine spectra are shown in Figure 4.1.14 (a) (b). It can be seen clearly that after treatment, the intensity of the peak at around 690 eV reduced to only 1/1200 of that of the untreated one. Judging by the position of the peak, the 690 eV peak is related to the CF_2-groups in the polymer chains [222]. In addition, a new peak at the binding energy of around 685 eV appears after active screen plasma treatment, which was identified as F 1s.

Carbon

The XPS spectra of carbon are shown in Figure 4.1.14 (c) (d). The peak at 292.6 eV almost vanishes after active screen plasma treatment. According to literature [222], this peak is related to the CF_2-groups. This finding is in agreement with XPS spectrum of fluorine. The peak intensity of C-C at 285 eV also reduces significantly. Besides that, a relatively weak peak of O=C at around 288 eV appears after active screen plasma treatment.

Nitrogen

The XPS spectra of nitrogen are given in Figure 4.1.14 (e) (f). The untreated carbon paper does not show any nitrogen related peaks. However, after active screen plasma treatment, a peak at around 400.2 eV appears. This N peak might be related to N-containing functional groups.

Oxygen

As shown in Figure 4.1.14 (g) (h), on the untreated carbon paper, a very weak peak at around 533.2 eV could be found. After ASP treatment, two oxygen related peaks can be found, one of the peaks is at the same position as the untreated one and the other peak is at around 530.8 eV. The latter peak might be related with O-H functional groups.

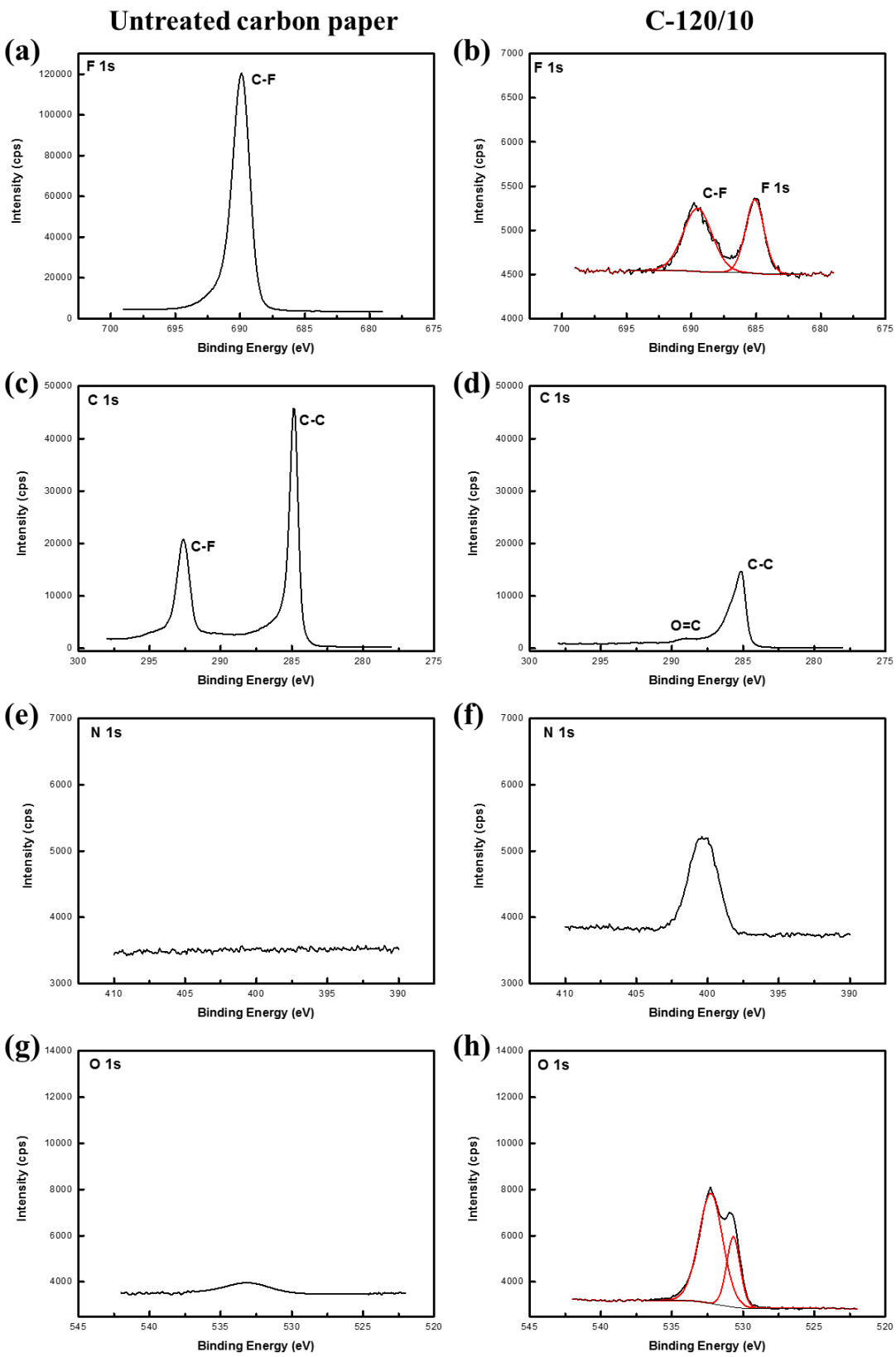

Figure 4.1.14 XPS spectra of individual elements

(a) F1s (c) C1s (e) N1s and (g) O1s of untreated carbon paper

(b) F1s (d) C1s (f) N1s and (h) O1s of C-120/10 carbon paper

From the XPS results presented above, the change of the surface chemical states induced by active screen plasma treatments can be summarised as follows:

1. The significant intensity reduction of the CF_2 chains, shown in F1s spectra (Figure 4.1.14 (a) (b)) and C1s (Figure 4.1.14 (c) (d)), indicates the etching of the polytetrafluoroethylene (PTFE) coating on the surface of original carbon paper by the active screen plasma treatment.
2. The active screen plasma treatments have introduced many functional groups to the surface of carbon paper.

Although, the carbon paper was in floating potential during ASP treatments, the sample surface was very close to the screen, where plasma generated. Therefore some bombardment would occur on the sample surface to remove the PTFE coating on the surface of as-received carbon paper. As discussed in the literature (Section 2.2.4), the role of the PTFE coating is to increase the hydrophobicity of the carbon paper. However, the high hydrophobicity significantly affects the electrochemical reaction on the surface of carbon paper, leading to the un-uniform and low coverage of the Pt nanowires (Figure 4.1.10 (a) (b)). The removal of PTFE could significantly improve the hydrophilicity of carbon paper, thus resulting in the enhanced growth of Pt nanowires. The etching effect of the active screen plasma treatment could also introduce many defects on the carbon paper surface and increase the number of nucleation sites for the growth of Pt nanowires. In addition, the introduction of functional groups by active screen plasma treatment not only activates the surface of carbon paper, but also increases the number of nucleation sites on the surface.

These two effects of active screen plasma treatment significantly improve the uniformity of Pt nanowires growth and increase the number of nucleation sites for the

growth of Pt nanowires. The enhanced growth of Pt nanowires on the ASP treated carbon paper surface contributes to the effectively increased electrochemical performance of the C/Pt-120/10 carbon paper and hence the single cell performance.

4.1.5 Summary

The growth of Pt nanowire layer on the surface of ASP treated carbon paper was evaluated by means of ECSA measurements and single cell performance tests. Results have indicated that the short duration (10 min) and low temperature (120 °C) ASP treated carbon paper exhibited the best catalytic performance. The surface morphology observation of the Pt nanowire layer implies that the improved electrochemical performance could be attributed to the enhanced Pt growth on the ASP treated carbon paper. The XPS analysis of the ASP treated carbon paper indicates that the ASP treatments can effectively activate the carbon paper surface by removing the PTFE coating and increasing the nucleation site for the growth of Pt nanowires.

4.2 The orthogonal test of low-temperature ASPN of 316 stainless steel

As described in Section 3.2.2.1, an orthogonal test was designed to evaluate the influence of three important parameters, namely temperature, processing time and bias, of active-screen plasma nitriding (ASPN) treatment on the microstructure and surface properties of 316 stainless steel.

4.2.1 Microstructure

The low and high magnification SEM images of as-received 316 stainless steel after wet grinding up to 800 grit and ASPN treatment at different temperatures are shown in Figure 4.2.1, Figure 4.2.2 and Figure 4.2.3.

The grinding tracks can be easily seen from the untreated surface (Figure 4.2.1 (a) (b)). Under low magnification (Figure 4.2.1 (c) (e) (g)), no significant differences in surface morphology can be found among three 370 ℃ treated samples, which are similar to that of the untreated one. However, under high magnification, some small particles, which are absent on the surface of untreated samples, were found to be uniformly distributed on the treated surfaces. On the surface of O-370/3/2, individual particles (around 50 nm in diameter) can be easily identified and the surface is not covered completely by those particles (Fig. 4.2.1(d)). With the increase of treatment duration, the amount of particles increases remarkably, and they are all connected or piled up together. The particles on the surface of O-370/7/8 sample may be difficult to identify, because all the particles are connected together and covered the entire surfaces (Fig. 4.2.1(h)). The particles observed from the treated surface are also found

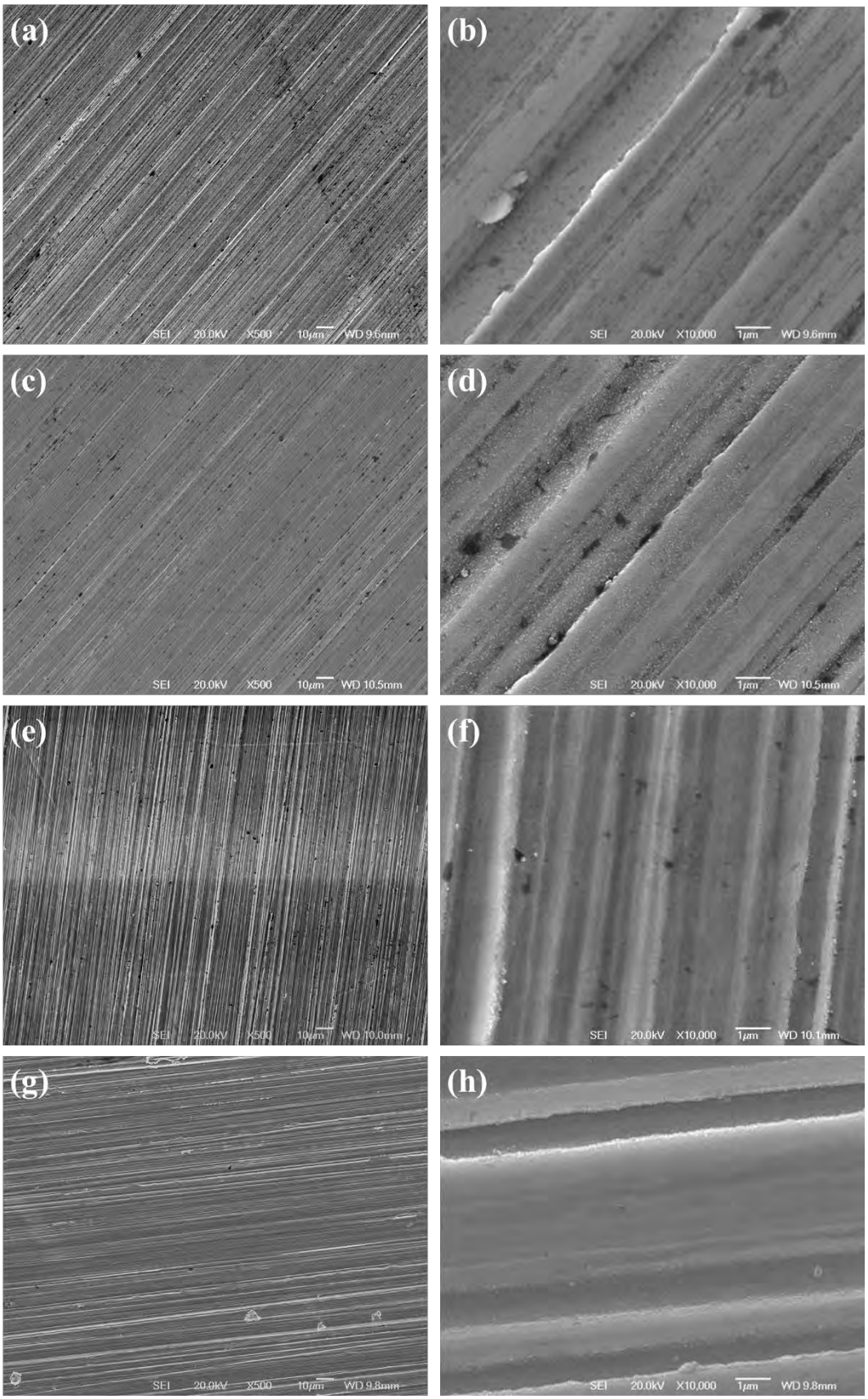

Figure 4.2.1 Low and high magnification SEM surface images of
(a) (b) untreated (c) (d) O-370/3/2 (e) (f) O-370/5/5 (g) (h) O-370/7/8

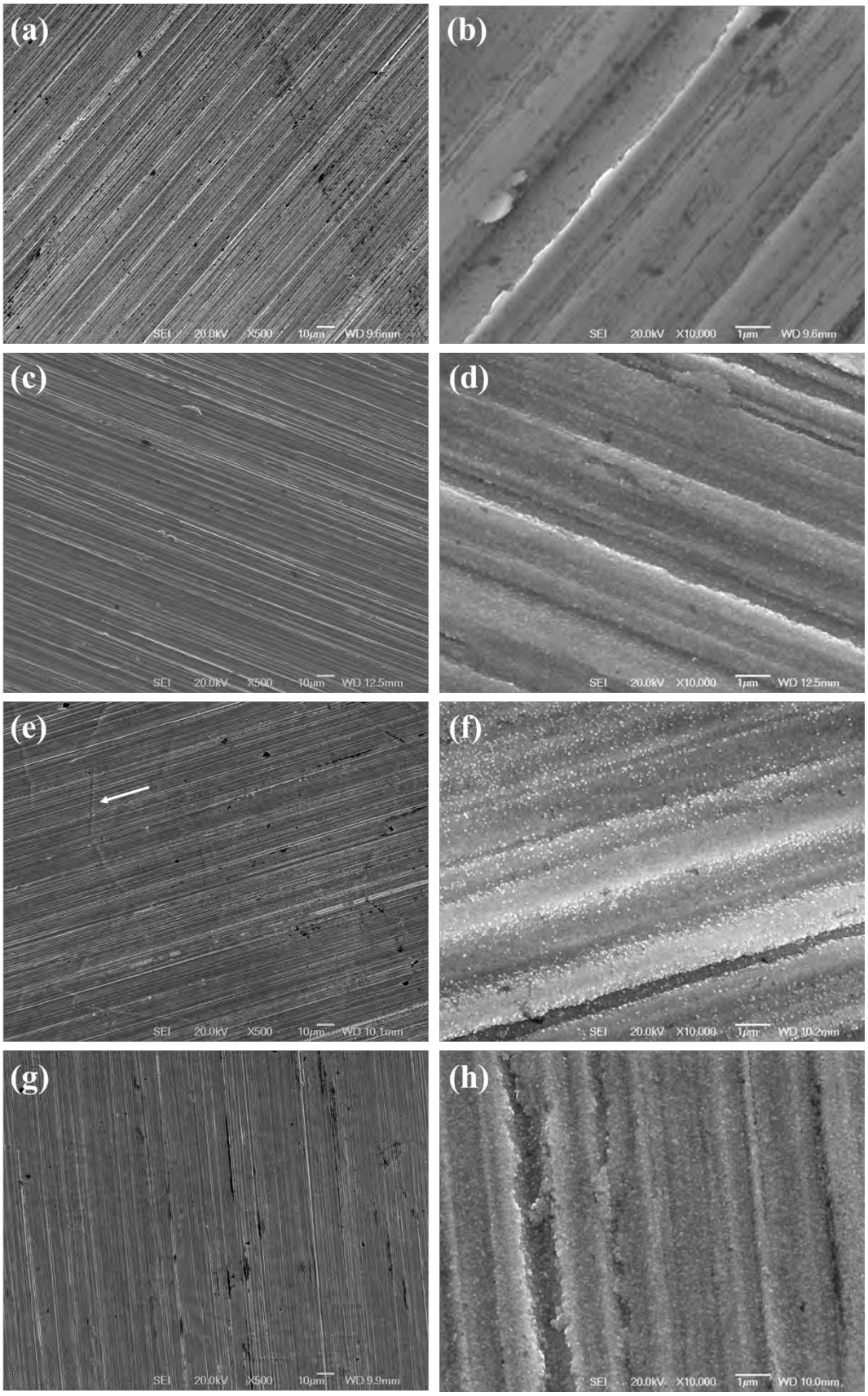

Figure 4.2.2 Low and high magnification SEM surface images of
(a) (b) untreated (c) (d) O-410/3/5 (e) (f) O-410/5/8 (g) (h) O-410/7/2

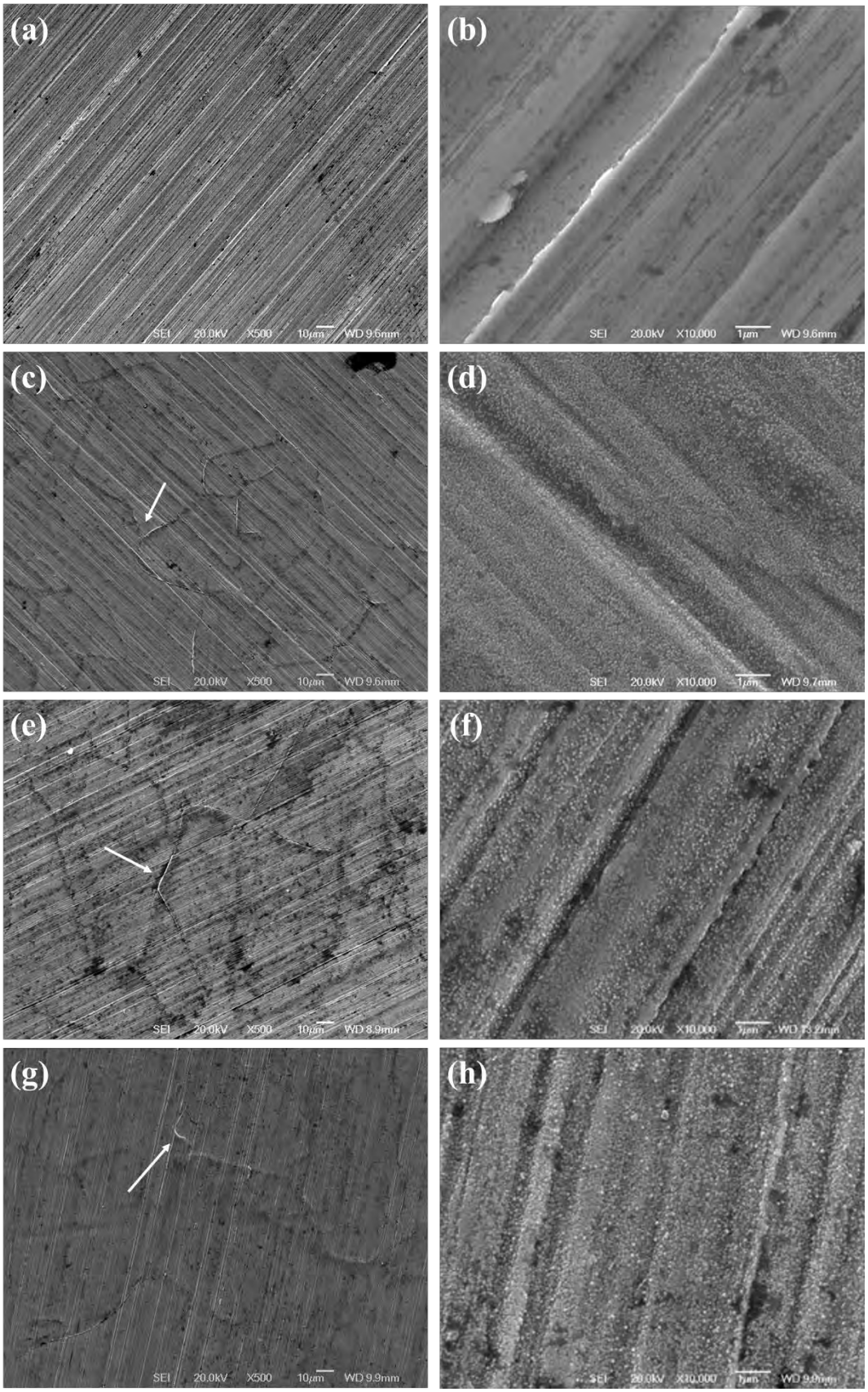

Figure 4.2.3 Low and high magnification SEM surface images of
(a) (b) untreated (c) (d) O-450/3/8 (e) (f) O-450/5/2 (g) (h) O-450/7/5

by other researchers [197]. As reported by Gallo and Dong [210], these particles are sputtered from the metal mesh and deposited onto the surface during nitriding.

For those samples treated at 410 °C (Figure 4.2.2), in low magnification images, the O-410/3/5 sample (Figure 4.2.2 (c)) is similar to the untreated and 370 °C treated samples. While on the surface of O-410/5/8 (Figure 4.2.2 (e)), some embossment (marked by arrow) could be observed following the grain boundaries. The reason for the formation of the embossment will be explained in Section 4.2.3. For O-410/7/2 sample (Figure 4.2.2 (g)), no embossment could be found. Under high magnification, the nano-sized particles can be easily found, which cover the whole surfaces (Figure 4.2.2 (d) (f) (h)), and the size of individual particle is larger than that on the 370 °C treated samples.

When increasing the treatment temperature to 450 °C (Figure 4.2.3), the embossment can be found from all three surfaces in low magnification SEM images and the extent is higher than that of the 410 °C treated samples. Under high magnification, the particles observed in other temperature groups can still be found from the surfaces with the particle size increasing with the treatment duration.

The SEM images in Figure 4.2.4 illustrate the typical cross-sectional morphologies of samples under low and high magnification from each treatment temperature group. It can be seen that on the top of each ASPN treated sample, there is a distinct layer, which is featureless, dense and uniform. Compared with the severely corroded substrate, this layer shows superior corrosion resistance to aggressive etchant, which can be deduced form the featureless appearance. Underneath the featureless layer, a dark line can be seen for all the samples, which did not appear before etching. In high magnification SEM images, it can be found that this dark line is a trough (by titling

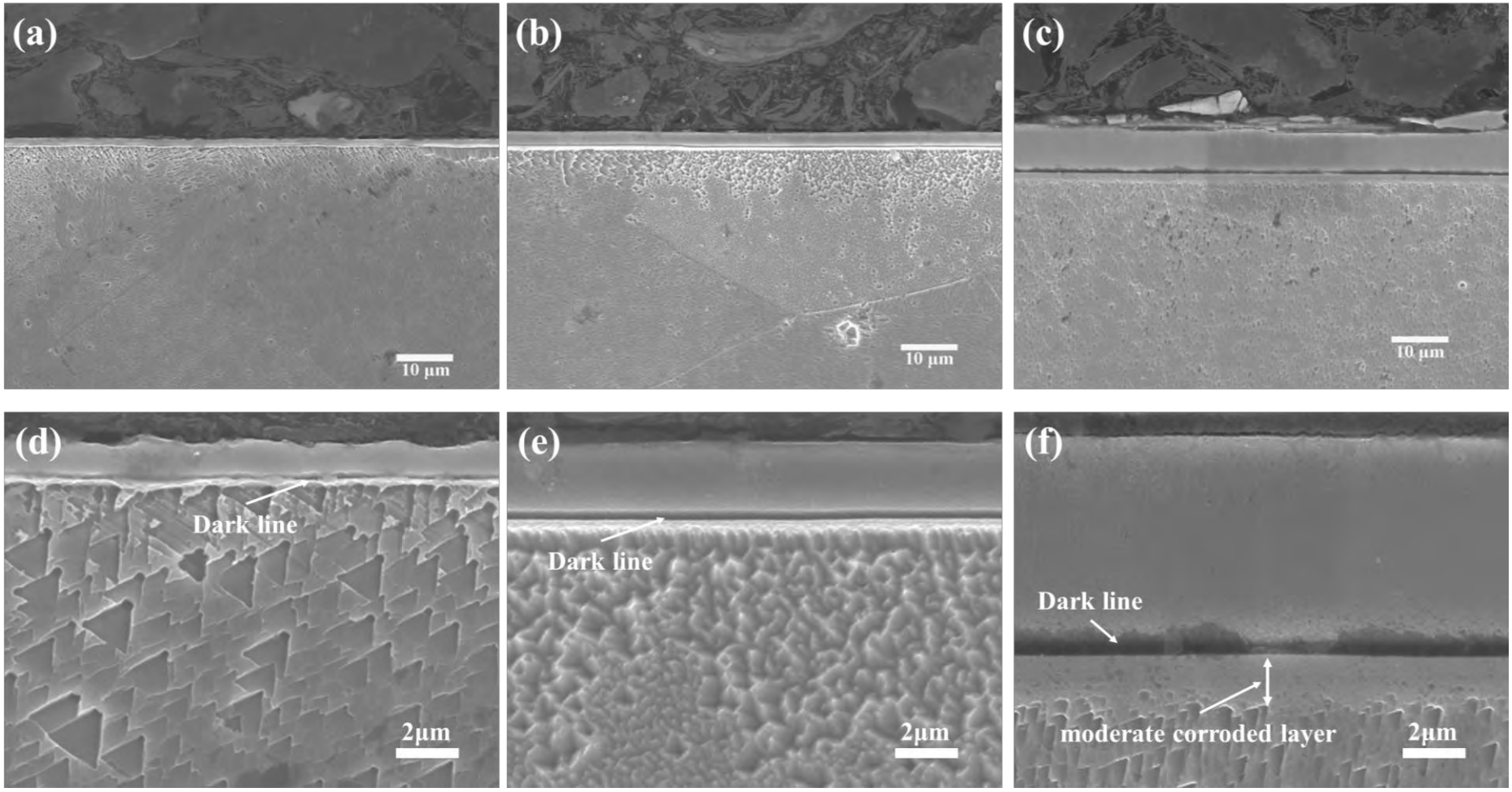

Figure 4.2.4 Cross-sectional SEM micrographs of ASPN treated samples (a) (d) O-370/3/2 (b) (e) O-410/3/5 (c) (f) O-450/7/5

the sample when doing SEM observation, images no shown). The formation of the trough should be related to the huge difference in corrosion resistance between the featureless layer and the substrate, causing severe galvanic corrosion and more mass-lose in this area. Between the dark line and the corroded substrate, a moderate corroded layer about 2 μm in thickness can be seen (Figure 4.2.4 (f)). The formation of this layer will be discussed in the next section.

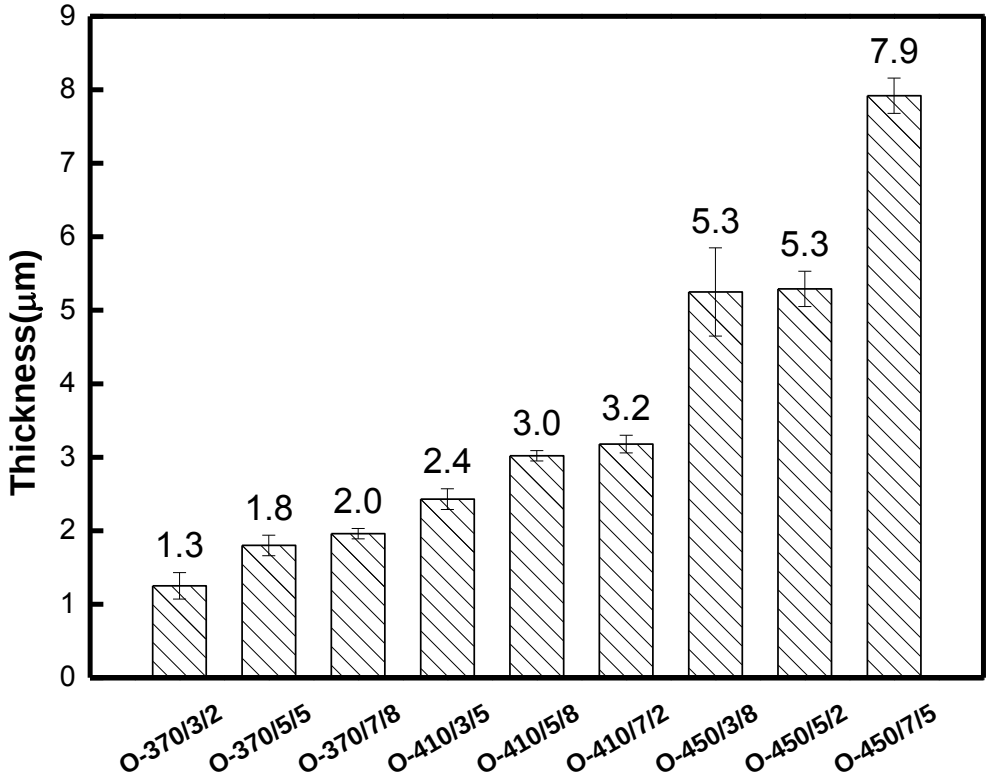

Figure 4.2.5 The thickness of the nitrided layer formed under different conditions

The layer thickness of these samples is summarised in Figure 4.2.5. It can be seen form Figure 4.2.5 that, the thickness of the featureless layer increases with the increase of the nitriding temperature and time.

4.2.2 Chemical composition

The depth profiles of elements were measured by means of GDS and the results are shown in Figure 4.2.6. The depth profiles of all the elements in the plasma treated layers formed on O-370/7/8 and O-450/7/5 are shown in Figure 4.2.6 (a) and (b), respectively. It can be seen from those two figures that except for nitrogen, the content of other elements increase towards the substrate. The typical nitrogen depth profiles selected from three treatment temperatures are plotted in Figure 4.2.6 (c). It can be seen that the content and depth of nitrogen for those three samples increase with the increase of the treatment temperature, and the depth of the high-nitrogen region is in agreement with the thickness of the featureless layer shown in Figure 4.2.5.

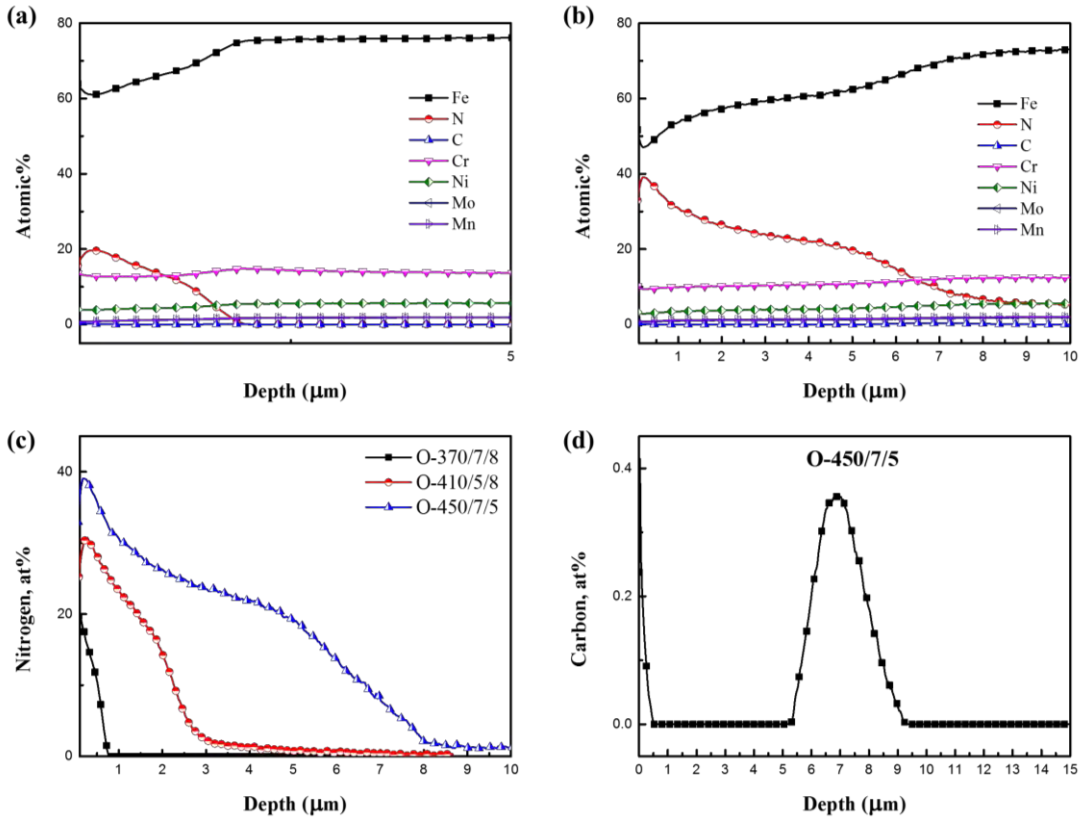

Figure 4.2.6 Element depth profiles of samples (a) O-370/7/8 (b) O-450/7/5 (c) nitrogen depth profiles (d) carbon depth profiles

The trend is similar for these three nitrogen profiles (Figure 4.2.6 (c)), showing a relatively high nitrogen region near the surface, following by a rapid decrease region and finished with a gradual decline. The shape of the nitrogen depth profiles differ from the typical profile for a pure diffusion-controlled process. The widely accepted model for this characteristic shape is that chromium would trap nitrogen and slow down the diffusion of nitrogen towards the substrate; but in the nitrogen rich region the trap sites of chromium are all occupied, and so the diffusion of nitrogen in this region is fast which leads to the unique profile [223]. It is worthwhile to point out that the maximum nitrogen solid solubility in fcc iron is 8.7 at% [224], and it is clear from Figure 4.2.6 (c) that the nitrogen weight percentage in the majority part of the high-nitrogen region in all the three samples is higher than the maximum nitrogen solid solubility, indicating that the featureless layers of nitrided samples are supersaturated with nitrogen.

A small carbon peak was observed at the nitrogen diffusion front for all samples and a typical depth profile of carbon is shown in Figure 4.2.6 (d) for O-450/7/5. The high C content in the near-surface-region is due to the contamination of the surface; the high carbon peak appeared at a depth of around 7.5 μm, which is close to the thickness of the plasma treated layer (see Figure 4.2.5). According to trapping theory, because nitrogen has a stronger affinity to chromium than carbon, carbon atoms are pushed inward when nitrogen diffused into the surface. The carbon peak depth of O-450/7/5 matches the position of the moderately corroded layer shown in Figure 4.2.4 (f), which indicates that the moderately corroded layer between the dark line and the substrate is rich in carbon.

4.2.3 Phase identification

Figure 4.2.7 shows the XRD patterns for untreated and typical nitrided samples selected from different temperature groups. The untreated 316 stainless steel shows a typical fcc structure, and the peaks from the left to right are γ (111), γ (200), γ (220) and γ (311). For the samples treated at 370 ℃ , another set of peaks can be found from the XRD pattern, which shifts to low angles compared to the corresponding austenite peaks. These new peaks are from a new phase, called S-phase, which is an expended austenite formed by supersaturated nitrogen in the matrix lattice [225]. Taking the results of cross-sectional morphology (Section 4.2.1) and GDS (Section 4.2.2) into account, the featureless and nitrogen-rich layers are S-phase layers. Apart from the S-phase peaks, the peaks of austenite with similar intensity can still be seen from the XRD pattern of 370 ℃ group of samples, but the intensity is much lower than that of the untreated sample. For the 420 ℃ group of samples, the short duration treated sample exhibits similar XRD pattern as that of the 370 ℃ group of samples, containing both peaks of austenite and S-phase, but the peak intensity of austenite is lower than that of the S-phase. With the increase of treatment duration, the peak intensity of austenite keeps reducing and finally vanishes after 5 hours treatment. When the treatment temperature increased to 450 ℃ , only S-phase peaks can be observed from the XRD patterns.

The change of austenite peak intensity is related to the thickness of S-phase. When the S-phase is thin (treated under low temperature and short duration), the X-ray could penetrate through it and reach the austenite substrate, and so the peaks of austenite can be seen. With the increase of S-phase thickness, the amount of substrate which can be detected by X-ray is less, and so the peak intensity of austenite decreases and finally disappears.

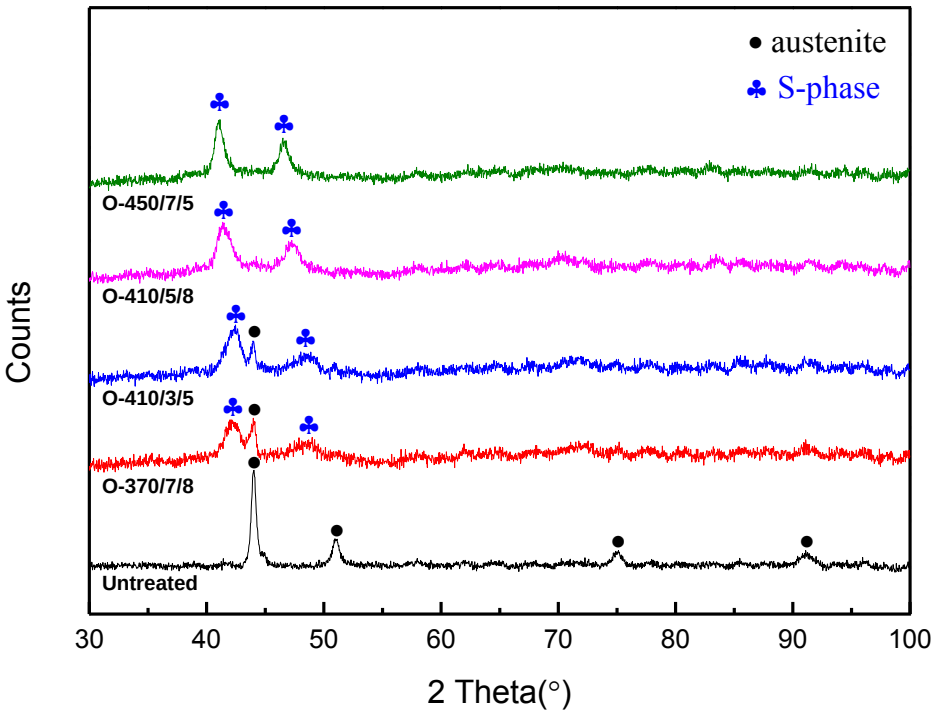

Figure 4.2.7 XRD patterns of untreated and nitrided samples

Another finding from the XRD pattern is that the position of S-phase peaks shift to a lower angle with the increase of treatment temperature. The larger shift of peak means increased d-spacing caused by the supersaturated nitrogen in the fcc crystal lattice. This finding is in agreement with the GDS results (Figure 4.2.6 (c)), that the nitrogen content in the S-phase increases with the treatment temperature.

Other consequence induced by the superstaturation of nitrogen is the volume expansion of grains. For the grains away from the surface, the expansion would be constrained by the surrounding gains, resulting in a high level of residual compressive stresses [226]. For the grains in the very surface, the volume expansion releases towards the surface direction and causes the embossment, i.e. surface relief, on the surface (Figure 4.2.3).

4.2.4 Surface roughness

Figure 4.2.8 illustrates the surface roughness of untreated and nitrided samples. The roughness of all ASPN treated samples is higher than that of the untreated sample. In general, the roughness increases with the increase of treatment temperature. The samples treated at 370 ℃, especially O-370/3/2 and O-370/5/5 samples, show little increase in roughness compared with the untreated sample and the roughness also increases with the treatment duration. For 410 ℃ treated samples, the roughness gradually raises with the increase of treatment duration. For 450 ℃ treated samples, the roughness gradually increases from 3 h treated to 5 h treated sample, and then a dramatic jump is witnessed when the treatment duration increased from 5 h to 7 h.

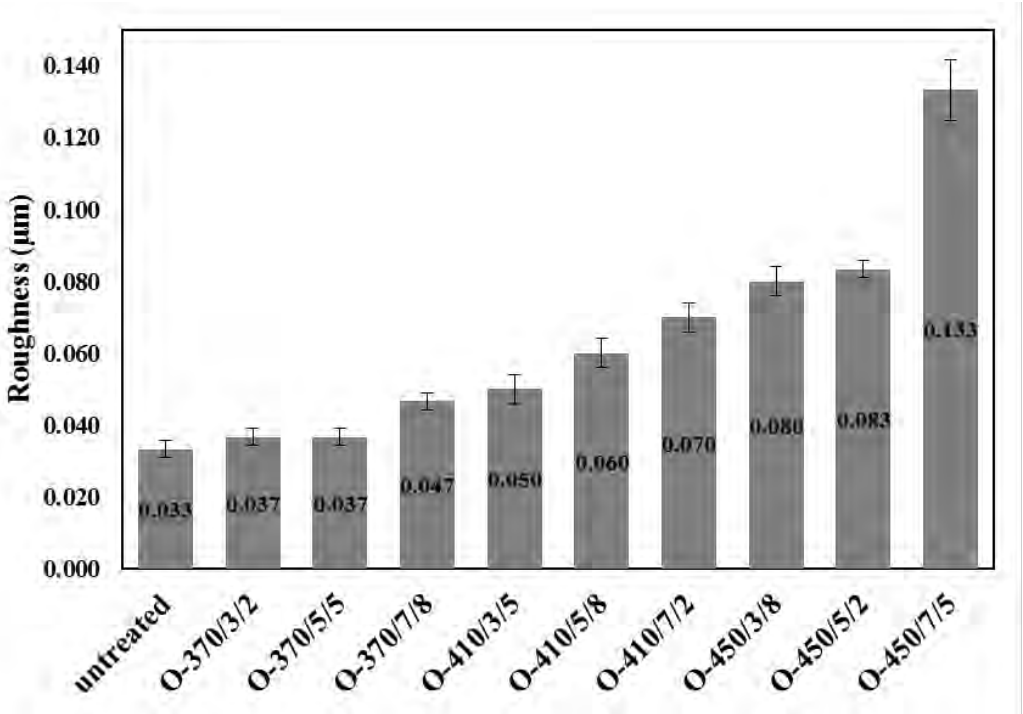

Figure 4.2.8 Surface roughness of untreated and nitrided samples

4.2.5 Hardness

The surface hardness of untreated and ASPN treated samples was measured using micro-hardness machine with a Vickers indenter under 50g loading, and the results are shown in Figure 4.2.9. All treated samples show a higher surface hardness than that of the untreated sample, and the highest hardness value of the treated sample (O-450/7/5) is about 4.6 times higher than that of the untreated one. In general, the surface hardness value increases with both treatment temperature and treatment duration.

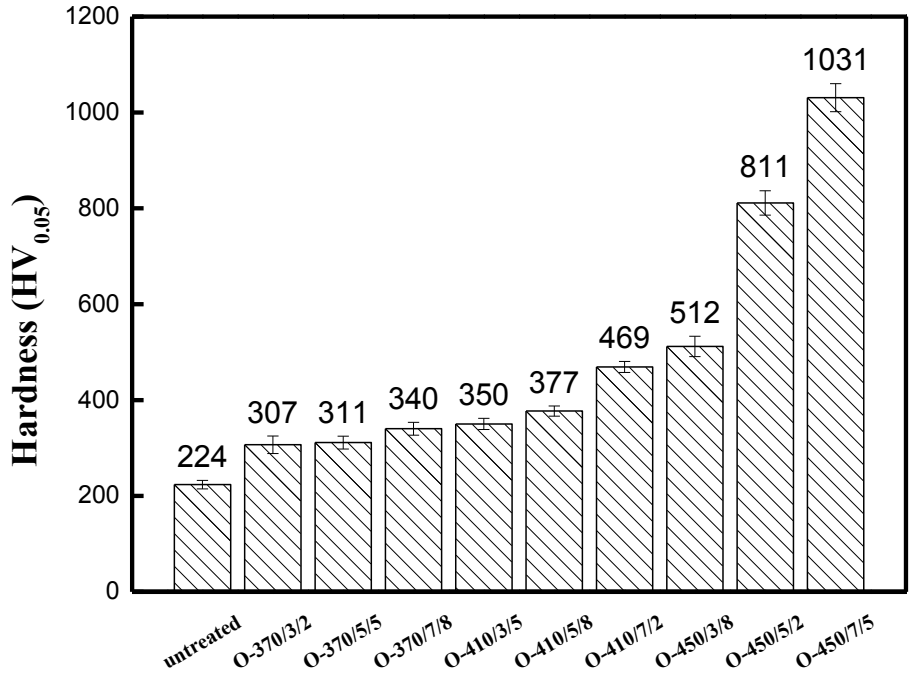

Figure 4.2.9 The surface hardness of samples

The depth profiling of hardness values was conducted by means of nano-hardness, and the result for O-450/7/5 is shown in Figure 4.2.10. A nano-hardness plateau at a high value about 17 GPa is observed from the surface to a depth of around 7-8 μm. Then, a dramatic drop of nano-hardness value occurs followed by a second plateau with the hardness of 4 GPa within the depth from 11 μm to 17 μm before it gradually

reduces to the substrate. The depth of high hardness region matches with the thickness of nitrogen supersaturated S-phase layer, which is in agreement with previous research [227]. The relatively low hardness plateau following the rapid decline is related to the high carbon content in this region, shown in Figure 4.2.6 (d).

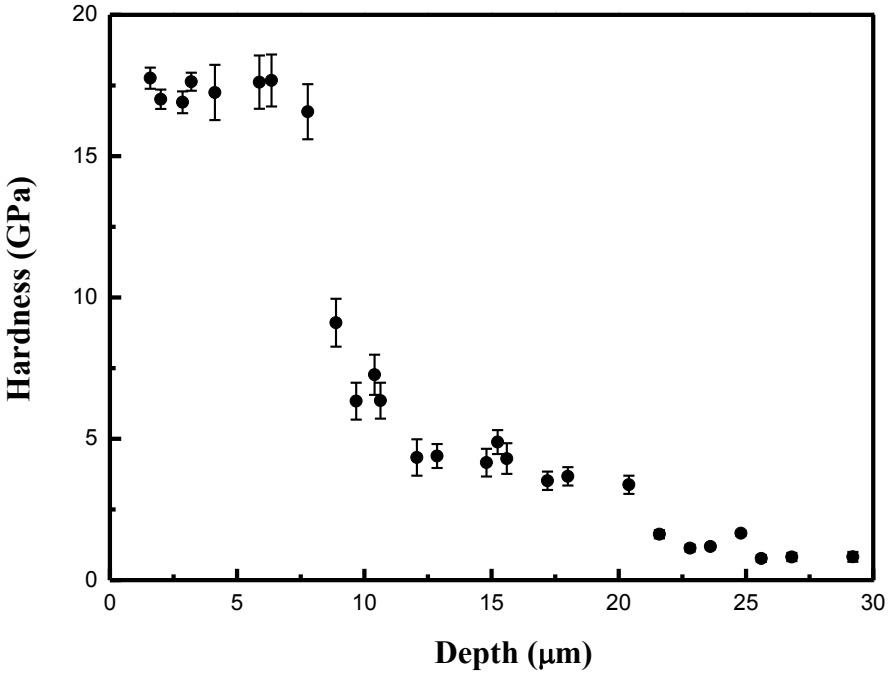

Figure 4.2.10 Nano-hardness depth profile of O-450/7/5

4.2.6 Interfacial contact resistance (ICR)

A compaction force of 140 N/cm^2 was selected to measure the ICR values of untreated and all treated samples, which is commonly applied in fuel cell stacks and widely used in many literatures. The ICR values of untreated and nitrided samples are presented in Figure 4.2.11. It can be seen that ASPN treatments can dramatically reduce the ICR values of 316 SS. The highest ICR value for treated samples (O-370/5/5) is less than one-third that of the untreated 316 stainless steel and the lowest value (O-450/3/8) is less than one-tenth that of the untreated sample. In general, the ICR value decreases with the increase of the nitriding temperature.

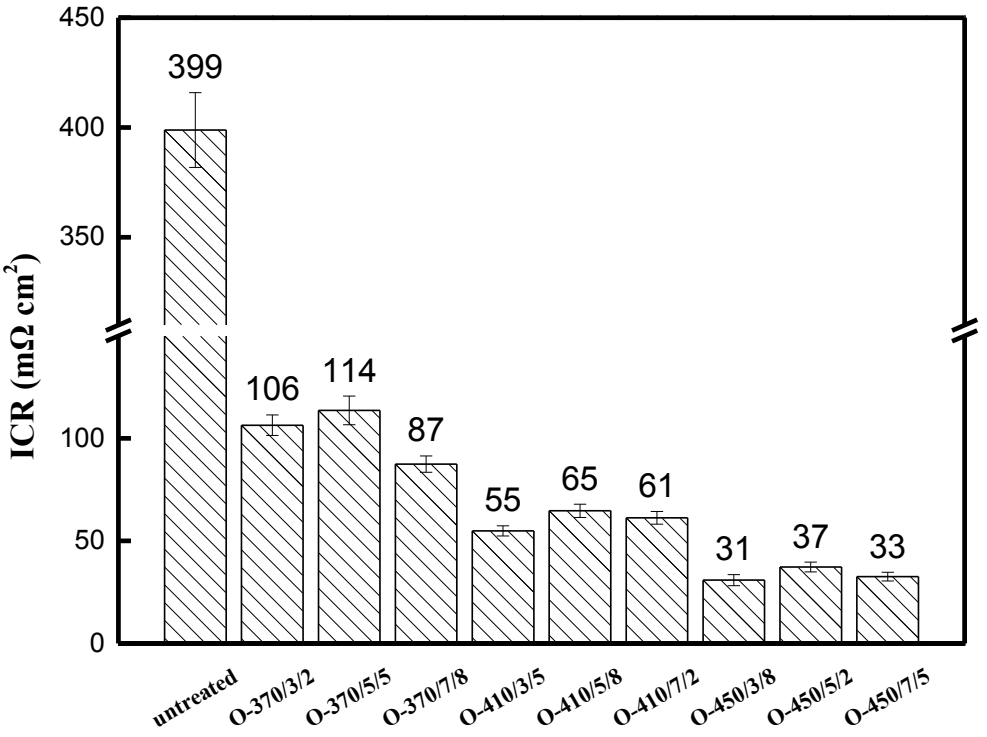

Figure 4.2.11 ICR value of untreated and nitrided sample at the compaction force of 140 N/cm^2

Table 4.1 shows the analysis result of the orthogonal test based on the ICR values. Factor A represents the nitriding temperature, and "1" "2" and "3" equal to 370 ℃, 410 ℃, and 450 ℃, respectively. Factor B represents nitriding time, and "1" "2" and "3" equal to 3 h, 5 h, and 7 h, respectively. Factor C represents applied bias, and "1" "2" and "3" equal to 2 %, 5 %, and 8 %, respectively.

In Table 4.1, K^X_i in the column of Factor X (X = A, B, C), is calculated based on Equation 4.2.2:

$$K_i^X = \text{average}\left(\sum_{Factor\ X=i} ICR\right) \quad \text{Equation 4.2.1}$$

which is the average ICR value of samples with Factor X is "i" (i =1, 2, 3), and the rest can be done in the same manner. R^X in the column of Factor X is calculated using Equation 4.2.3:

$$R^X = \max(\mathrm{K}_i^X) - \min(\mathrm{K}_i^X) \qquad \text{Equation 4.2.2}$$

which is the difference of the largest and smallest $K^X{}_i$ in the same column of Factor X. The larger the R^X value, the greater influence of the corresponding Factor X on ICR value [228].

Table 4.1 Analysis of ICR orthogonal array test values

Sample	Factor A (Temperature)	Factor B (Time)	Factor C (Bias)	ICR value (mΩ cm^2)
O-370/3/2	1	1	1	106
O-370/5/5	1	2	2	114
O-370/7/8	1	3	3	87
O-410/3/5	2	1	2	55
O-410/5/8	2	2	3	65
O-410/7/2	2	3	1	61
O-450/3/8	3	1	3	31
O-450/5/2	3	2	1	37
O-450/7/5	3	3	2	33
Data analysis	Factor A	Factor B	Factor C	
$K^X{}_1$	$K^A{}_1 = 102.3$	$K^B{}_1 = 64.0$	$K^C{}_1 = 68.0$	
$K^X{}_2$	$K^A{}_2 = 60.3$	$K^B{}_2 = 72.0$	$K^C{}_2 = 67.3$	
$K^X{}_3$	$K^A{}_3 = 33.7$	$K^B{}_3 = 60.3$	$K^C{}_3 = 61.0$	
R^X	68.6	11.7	7.0	

From the analysis results listed in Table 4.1, it can be seen that the value of R^A is the largest, which indicates that the influence of Factor A (Temperature) on the ICR value is the greatest, followed by Factor B (Time) and Factor C (Bias).

The other important function of the orthogonal test is to predict the optimised parameters. For the factor of temperature and applied bias, the $K^X{}_i$ value decreases respectively with the increase of temperature and applied bias, which means that the

ICR would decrease if the temperature and the bias were increased further. However, as mentioned in Section 2.4.3, if the treatment temperature is above 450 ℃ , the corrosion resistance of the treated samples will be greatly impaired due to the formation of chromium nitride, and so 450 ℃ should be the optimal temperature. For the applied bias, further increase would lead to the problems of DCPN, such as arcing and edge effect, and therefore the bias cannot be set too high. For the factor of time, the K^B_i first increases and then decreases with the increase of treatment duration. From this trend, further increasing the treatment duration might reduce the ICR value.

4.2.7 Electrochemical corrosion tests

Potentiodynamic corrosion tests were carried out to evaluate the corrosion resistance of untreated sample and ASPN treated samples. The polarisation curves for all the samples are plotted in Figure 4.2.12. The parameters of polarisation curves, namely corrosion potential (E_{corr}) and the corrosion current density (I_{corr}), are summarised in Table 4.2.

From Figure 4.2.12, it can be seen that all nitrided samples exhibit similar polarisation curves to that of the untreated 316 SS, consisting of an activated stage, a passive stage and a transpassive stage. The open corrosion potential (OCP) of some nitrided samples (O-370/5/5, O-370/7/8, O-410/5/8, O-450/3/8) is slightly shifted to more positive direction than the untreated sample, while the OCP of other samples is close to that of the untreated sample.

It can be seen from Table 4.2 that the corrosion current density (I_{corr}) of all ASPN treated samples are lower, in different degrees, than that of the untreated 316 stainless steel. The I_{corr} of most surface treated samples is one order of magnitude lower than that of the untreated one. The comparison of E_{corr} and I_{corr} reveals that the active

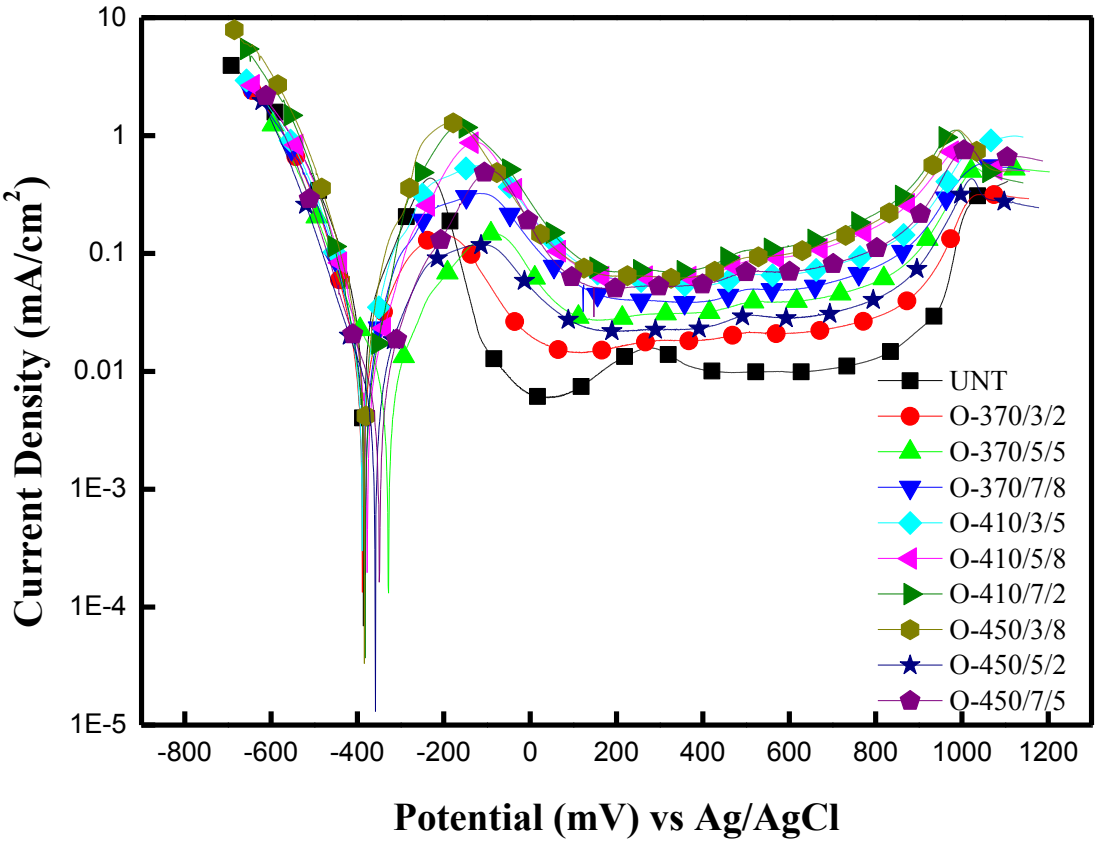

Figure 4.2.12 Polarisation curves of untreated sample and as-nitrided samples

Table 4.2 Corrosion current density and corrosion potential of all tested samples

Sample	I_{corr}(mA/cm^2)	E_{corr} (mV) vs Ag/AgCl
Untreated	0.0290	-386
O-370/3/2	0.0100	-388
O-370/5/5	0.0043	-356
O-370/7/8	0.0066	-328
O-410/3/5	0.0081	-382
O-410/5/8	0.0046	-349
O-410/7/2	0.0098	-389
O-450/3/8	0.0072	-378
O-450/5/2	0.0092	-384
O-450/7/5	0.0049	-382

screen plasma nitriding treatment maintains or even slightly improves the good corrosion resistance of the stainless steel. The improvement of corrosion resistance can also be indicated from the cross-sectional SEM image after etching (Figure 4.2.4). After immersing in the etchant, the 316 SS substrate suffers severe corrosion, while no corrosion takes place on the S-phase layers. However, it is also noted that the current density of the treated samples (in particular 410 ℃ and 450 ℃ treated samples) during the passive stage is higher than that of untreated materials (Figure 4.2.12).

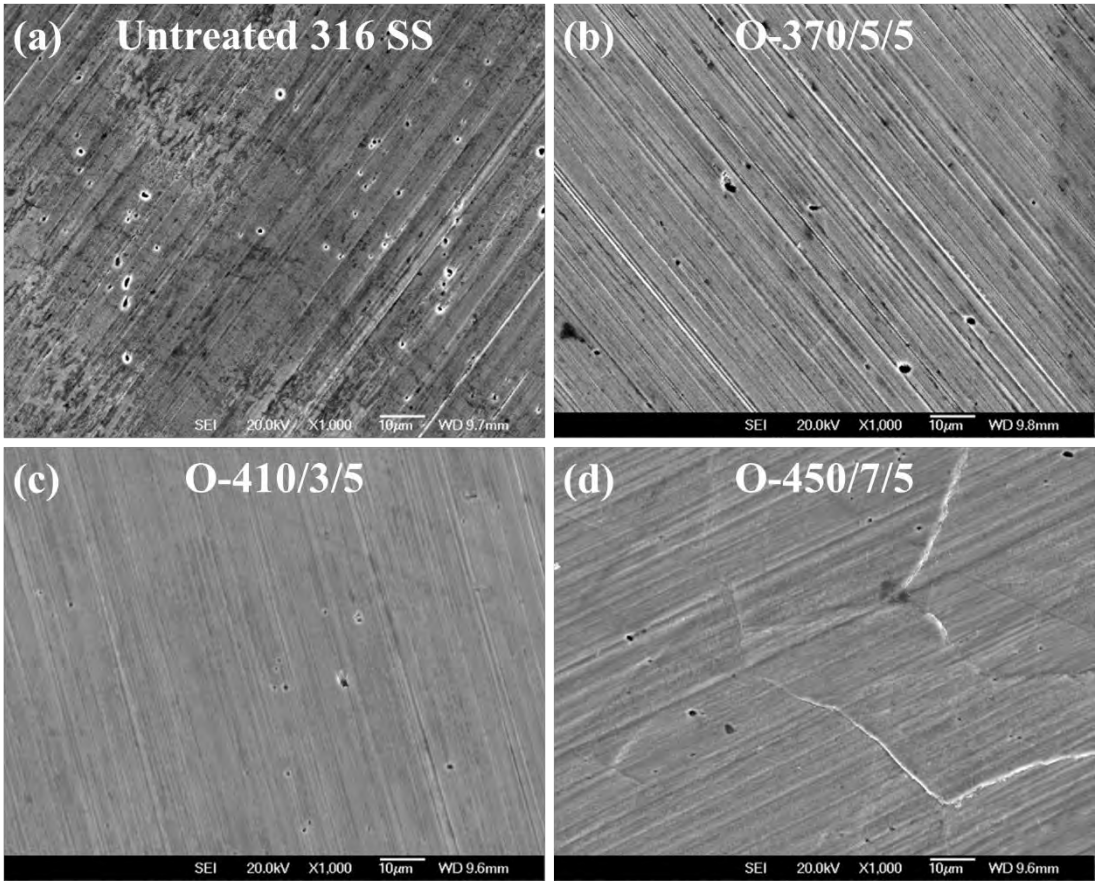

Figure 4.2.13 SEM observation of samples after polarisation tests
(a) untreated 316 SS (b) O-370/5/5 (c) O-410/3/5 (d) O-450/7/5

The surfaces morphologies of samples after polarisation tests were examined by SEM. The typical corrosion morphologies of each temperature group are shown in Figure 4.2.13. It can be seen from Figure 4.2.13 (a) that the untreated 316 stainless steel suffers severe pitting corrosion with a high density of pits and general corrosion. In contrast, the density of pits and the extent of general corrosion found on the ASPN treated surface are very low. Clearly, the active screen plasma nitriding has changed the dominant corrosion mechanisms of 316 stainless steel from severe pitting corrosion to very mild general corrosion. It can be seen that the high temperature (450 ℃) treated O-450/7/5 (Figure 4.2.13(d)) exhibits mild intergranular corrosion, which might be related to the surface relief observed in Figure 4.2.3. With the increase of nitriding temperature and duration, the intergranular corrosion becomes much more severe, which might lead to the deterioration of corrosion resistance.

4.2.8 Further investigations

Some further investigations were conducted to better understand the influence of ASPN treatments on the corrosion resistance and surface electrical conductivity of 316 stainless steel.

4.2.8.1 ASPN vs DCPN

In order to show the advantages of ASPN treatments over conventional DCPN treatments, the surface conductivity and corrosion behaviour of the 316 stainless steel DCPN treated at 450 ℃ for 7 h (DCPN-450/7) were also measured and compared with O-450/7/5 sample.

The ICR values of 450 ℃ /7 h DCPN and ASPN treated samples are shown in Figure 4.2.14. The ICR value of the DCPN treated sample is marginally lower than that of the ASPN treated sample, which might be related to the relatively high surface

roughness of the DCPN treated sample (0.185 μm) than the ASPN treated sample (0.133 μm).

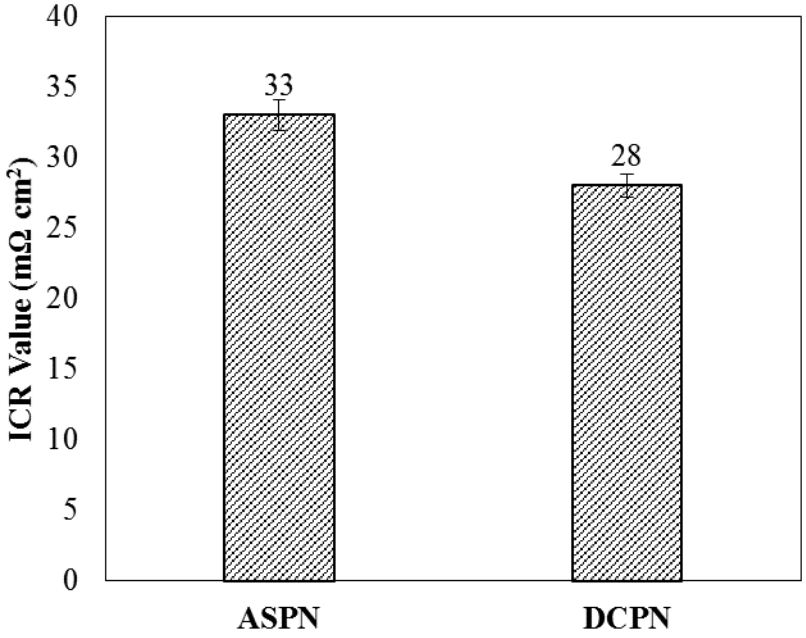

Figure 4.2.14 The ICR values of ASPN and DCPN treated 316 stainless steel (450 °C for 7 h)

The potentiodynamic polarisation tests of the 450 °C/7 h DCPN treated samples were conducted, and the results are listed in Table 4.3. It can be seen that the corrosion current density of DCPN treated samples is more than 7 times larger than that of the ASPN treated samples, and the corrosion potential of DCPN treated samples is more negative than that of the ASPN treated samples. The results indicate that the corrosion behaviour of the DCPN treated samples is much worse than that of the ASPN treated samples.

Table 4.3 Corrosion potential and corrosion current density of ASPN and DCPN

Sample	I_{corr} (mA/cm^2)	E_{corr} (mV) vs Ag/AgCl
ASPN	0.0049	-382
DCPN	0.0341	-401

4.2.8.2 The influence of deposition layer

As discussed in Section 4.2.7, compared with the untreated materials, the ASPN treated samples possess a remarkably reduced corrosion current density (I_{corr}) and a slightly increased corrosion potential (E_{corr}). However, the passive current density for the ASPN treated samples is higher than that of the untreated material. So some further work was done to find out the reason for the relatively high passive current density of the ASPN treated sample.

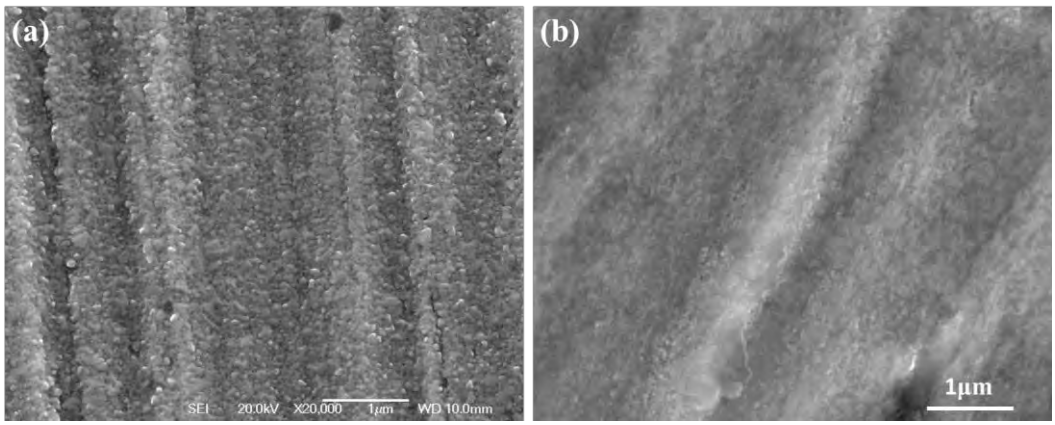

Figure 4.2.15 The surface morphologies of O-410/7/2
(a) before polarisation test (b) after polarisation test

The surface morphology of ASPN treated O-410/7/2 sample before and after polarisation test were observed using SEM. From the comparison of high magnification SEM images (Figure 4.2.15), a significant change can be observed that the surface deposition layer is completely removed after polarisation test. As mentioned in literature [229], this deposition layer is sputtered from the metal screen, which is made of carbon steel, and deposited onto the sample surface during treatment. The corrosion resistance of the material sputtered from the carbon steel screen is poor and easily corroded, which might be the reason for the relatively high passive current density of the ASPN treated samples.

In order to investigate the effect of the deposition layer on the corrosion behaviour of ASPN treatment samples, O-410/7/2 sample was gently polished to only remove the deposition layer. The corrosion behaviour and surface conductivity of the polished O-410/7/2 sample were evaluated using potentiodynamic polarisation and compared with the un-polished one.

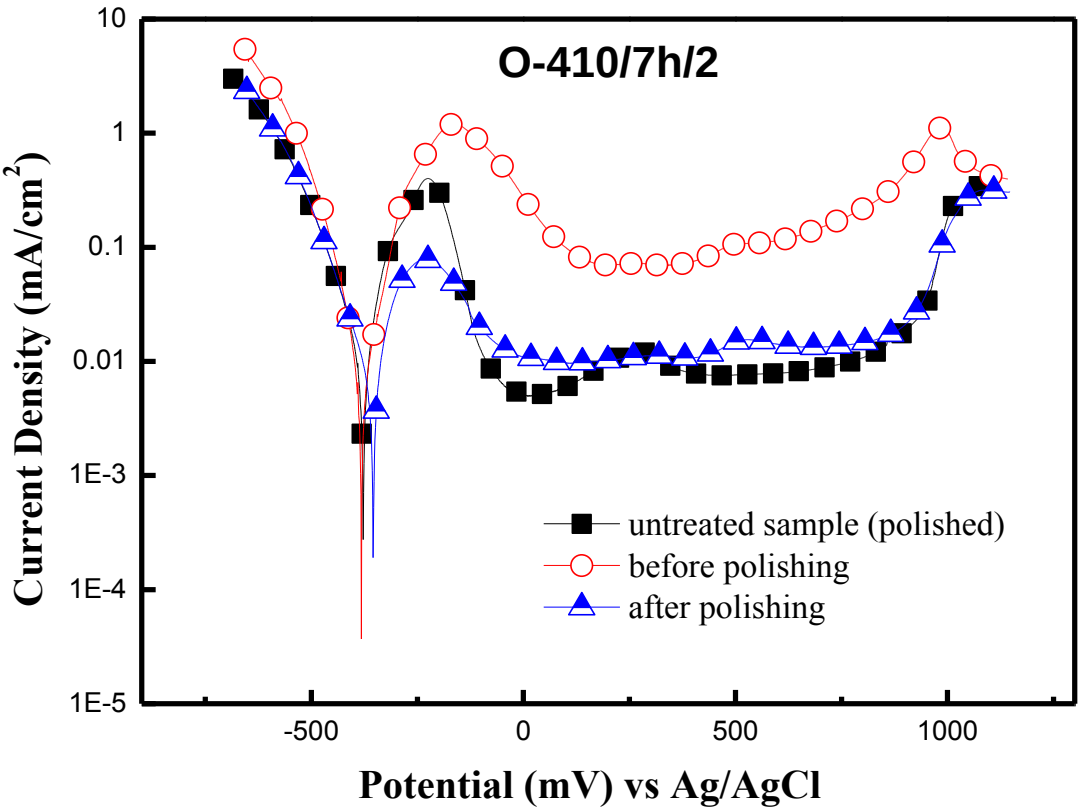

Figure 4.2.16 Polarisation curves of O-410/7/2 sample before and after polishing

Figure 4.2.16 shows the polarisation curves of O-410/7/2 sample before and after polishing as well as the polished (but without surface treatment) 316 stainless steel. It can be seen that after polishing, the passive current density reduces significantly down to the same level as that of the untreated sample. In addition, the corrosion current density reduces and the corrosion potential increases, which indicates the improved corrosion resistance after polishing. The improvement can also be demonstrated from

the surface morphology after the corrosion tests (Figure 4.2.17). The number of pits on polished O-410/7/2 sample is reduced significantly compared with the untreated sample and mild general corrosion can be found on the surface of polished O-410/7/2 sample. Again, it proves that the S-phase has changed the dominant corrosion mechanisms from pitting corrosion to general corrosion.

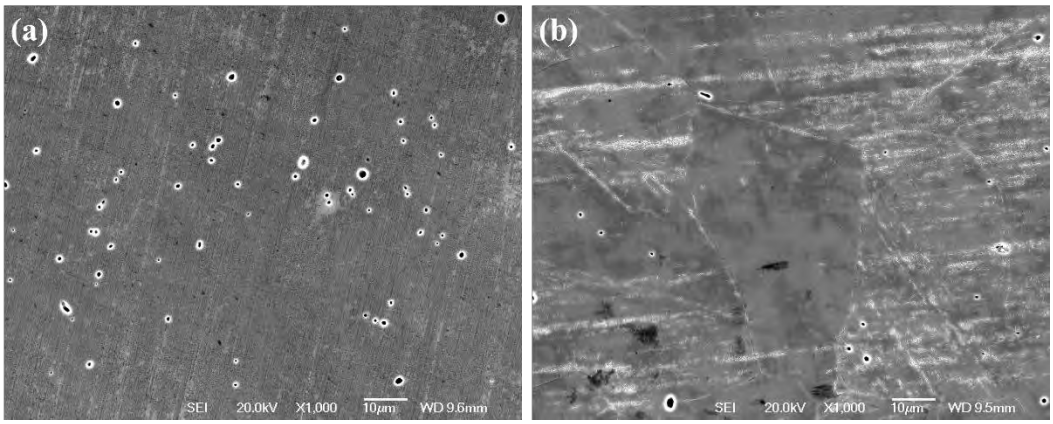

Figure 4.2.17 Corrosion morphologies of (a) untreated and (b) O-410/7/2 sample after polishing

The ICR values of O-410/7/2 sample before and after polishing together with polished and ground untreated 316 SS are shown in Figure 4.2.18. The roughness of all samples is also shown. The ICR value of the polished O-410/7/2 sample is lower than that of the polished untreated 316 stainless steel although both have similar roughness. However, the ICR value of the polished O-410/7/2 sample increases to more than 12 times than that of the as-treated O-410/7/2 sample. Compared with the as-treated O-370/3/2, the polished O-410/7/2 sample has a similar surface roughness, but shows 7 times higher ICR value. It can be concluded that the surface deposition layer is essential in reducing ICR although it may increase the surface roughness and reduce the electrochemical corrosion resistance.

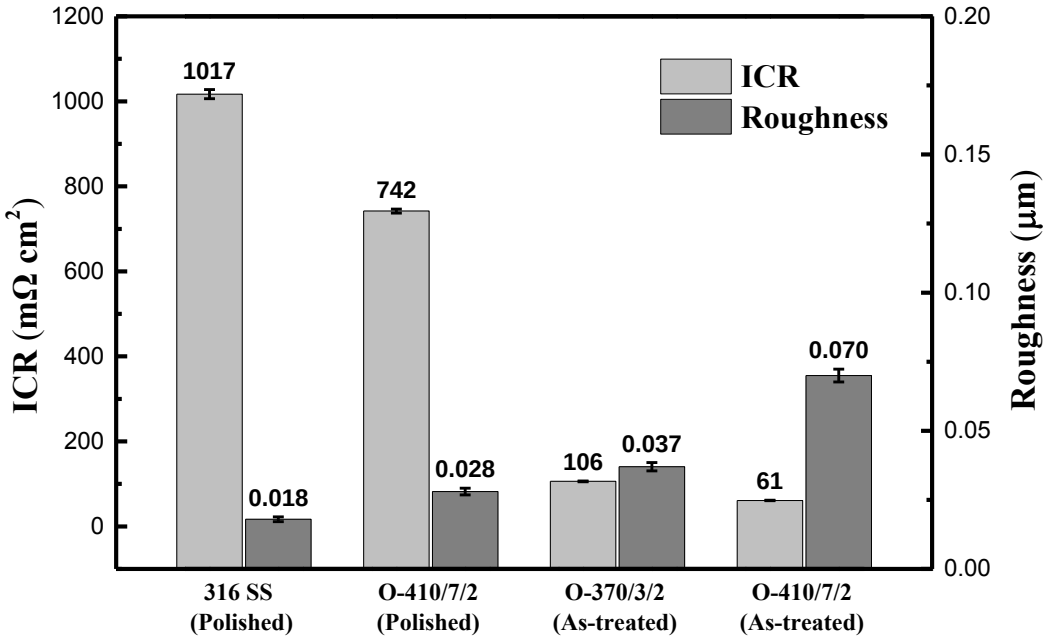

Figure 4.2.18 ICR value and surface roughness of samples before and after polishing

4.2.8.3 Effect of active screen materials

From the results of the above Section 4.2.8.2, the deposition layer is important in improving surface conductivity but negatively affects the corrosion behaviour. A potential solution that could balance these two performances is to produce a deposition layer with good corrosion resistance on the surface of treated 316 stainless steel.

It has been mentioned that the deposition layer comes from the metal screen used in active-screen plasma treatment, and therefore, using a screen made of good corrosion resistance material might produce a deposition layer with good corrosion resistance and meanwhile maintain the low ICR value.

In order to investigate the influence of screen materials on the surface properties of ASPN treated 316 SS, carbon steel screen (CS-450/7) and 316 stainless steel screen

(SS-450/7) were employed in the ASPN treatments at 450 °C for 7 h using a laboratory scale active screen set-up within the DC Klöckner Ionon 60 kVA plasma furnace (similar to Figure 3.2.3 without Ag addition).

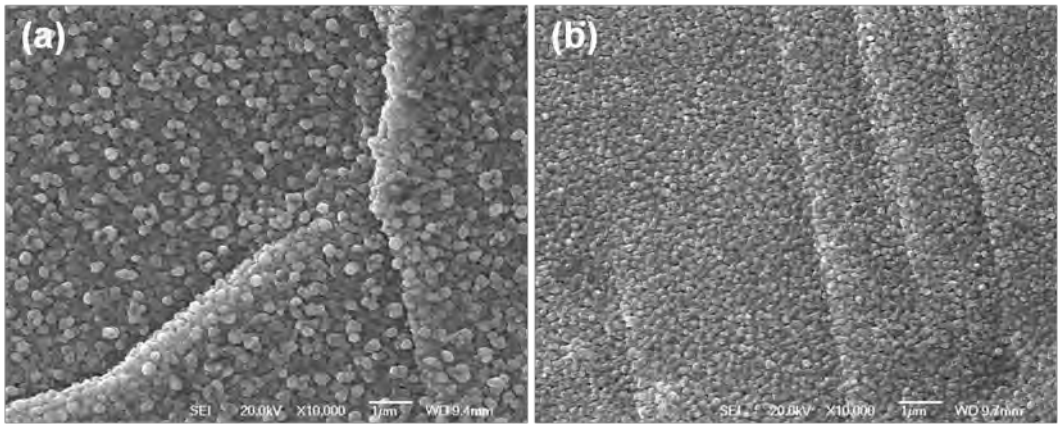

Figure 4.2.19 Surface morphology of active screen plasma nitrided samples with different screen material (a) CS-450/7 (b) SS-450/7

The surface morphologies of the ASPN treated samples with different screens are shown in Figure 4.2.19. It can be clearly seen that, the size of deposited particles is much smaller when using the stainless steel screen (200 nm) than using the carbon steel screen (400 nm). In addition, the deposition layer formed using stainless steel screen is denser than that formed using carbon steel screen, which might be less harmful for corrosion resistance. Although the surface morphology is slightly different when using different screens, the surface roughness and S-phase layer thickness formed are very similar, around 0.12 μm and 8 μm, respectively.

The surface EDS results of these two ASPN treated samples using different screens are listed in Table 4.4. It can be seen that the amount of alloying elements, such as Cr, Ni and Mo, in the SS-450/7 sample is much higher than that in the CS-450/7 sample. The relative amount of the major alloying elements within the surface of the SS-450/7 sample seems slightly lower than that in 316 stainless steel screen. This is mainly due

to the diluting effect of nitrogen introduced by ASPN treatments. The relatively high (vs carbon steel) amount of such alloying elements as Cr, Ni & Mo could be detected from the CS sample surface, which is caused by the fact that the thickness of the deposition layer is much thinner than the penetration depth of EDS electron beam and the element of the stainless steel substrate contributed to the results.

Table 4.4 Surface EDS results of samples (wt %)

Sample	C	N	O	Cr	Mn	Fe	Ni	Mo
Bare 316 SS	3.20	—	0.11	16.89	1.54	65	10.88	2.37
CS-450/7	2.52	5.53	1.35	9.61	0.78	74.17	5.19	0.86
SS-450/7	2.87	5.23	1.74	14.04	1.46	62.78	10.1	1.78

From the XRD results shown in Figure 4.2.20, the difference in phase constituents between the CS and SS samples can be identified. Firstly, apart from the peaks of S-phase, the peaks of Fe_4N and Fe_3N are also detected from the CS-450/7 sample but absent in the SS-450/7 sample. The presence of such iron nitrides is the results of the iron sputtered from the carbon steel screen reacted with nitrogen, formed iron nitrides and deposited on the surface [198]. Secondly, the intensity of the S-phase peaks from the CS-450/7 sample is much lower than that from the SS-450/7 sample, which could be attributed to the formation of the iron nitrides on the surface of the CS-450/7 sample.

The potentiodynamic polarisation curves of the untreated and ASPN treated samples using different screen materials are drawn in Figure 4.2.21. In terms of the passive current density, in general, the CS-450/7 and the SS-450/7 are in the same level, which is slightly higher than that of the untreated one. Specifically, in the potential range from -130 mV to 240 mV the current density of the SS-450/7 sample is lower than that of the CS-450/7 sample, and the current densities of those two samples are almost identical in the rest potential range.

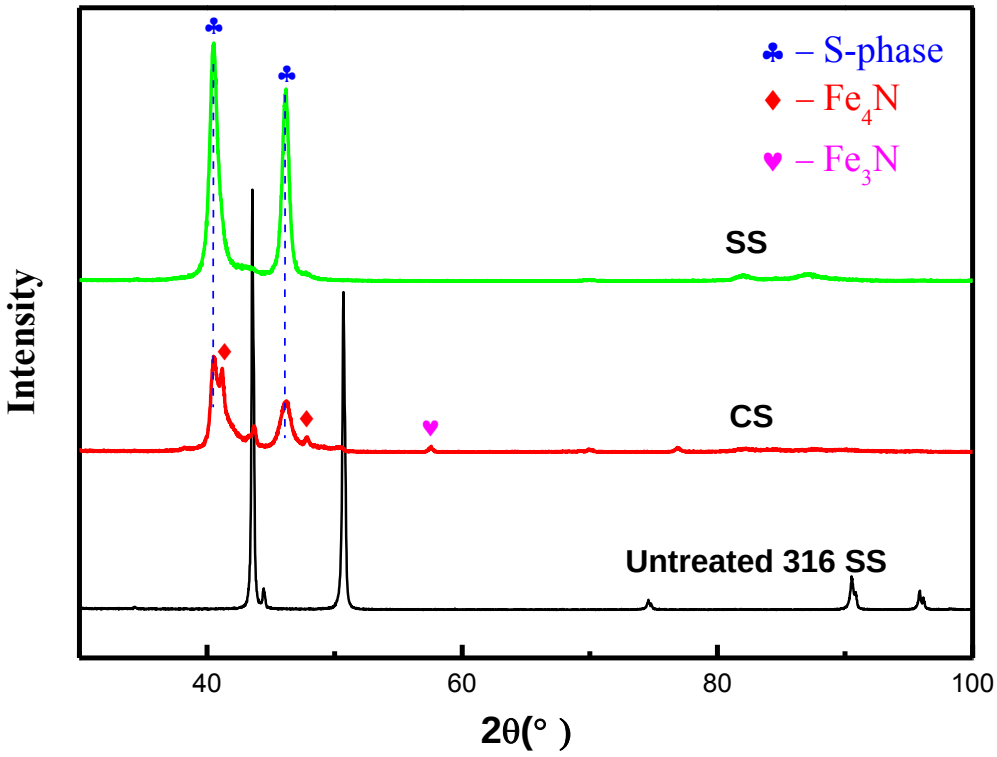

Figure 4.2.20 XRD results of different samples

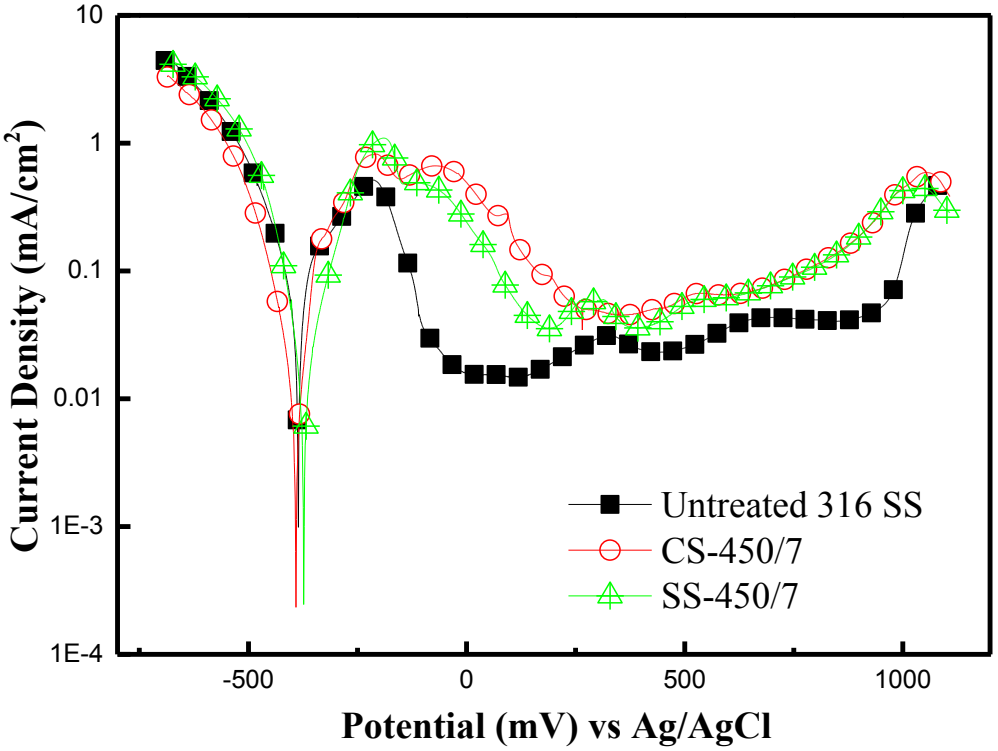

Figure 4.2.21 The potentiodynamic polarisation curves of different material screen treated samples

The corrosion current density and corrosion potential of these two samples are shown in Table 4.5. The corrosion current densities of the CS-450/7 samples is close to that of the untreated sample, while the SS-450/7 sample shows only one fourth that of the CS-450/7 samples. The corrosion potential of the CS sample is more negative than that of the untreated one; in contrast, the SS sample shows more positive corrosion potential than that of the untreated one. Clearly, the CS-450/7 sample possesses a worse corrosion resistance than that of the SS-450/7 sample, mainly due to the relatively low film density and the deposition of iron nitrides.

Table 4.5 Results of corrosion tests of ASPN treated samples with different screen

Sample	I_{corr}(mA/cm^2)	E_{corr} (mV) vs Ag/AgCl
Untreated 316 SS	0.085	-386
CS-450/7	0.080	-391
SS-450/7	0.018	-373

The ICR values of the ASPN treated sample using two different screens are shown in Figure 4.4.22, and the ICR value of the untreated 316 stainless steel with similar roughness is also presented for reference. After ASPN treatment, the ICR value reduces to one-seventh that of the untreated material. It can be seen that the ICR values of CS-450/7 and SS-450/7 sample are close to each other. Taking the experimental error into account, the ICR value of those two samples should be in the same level.

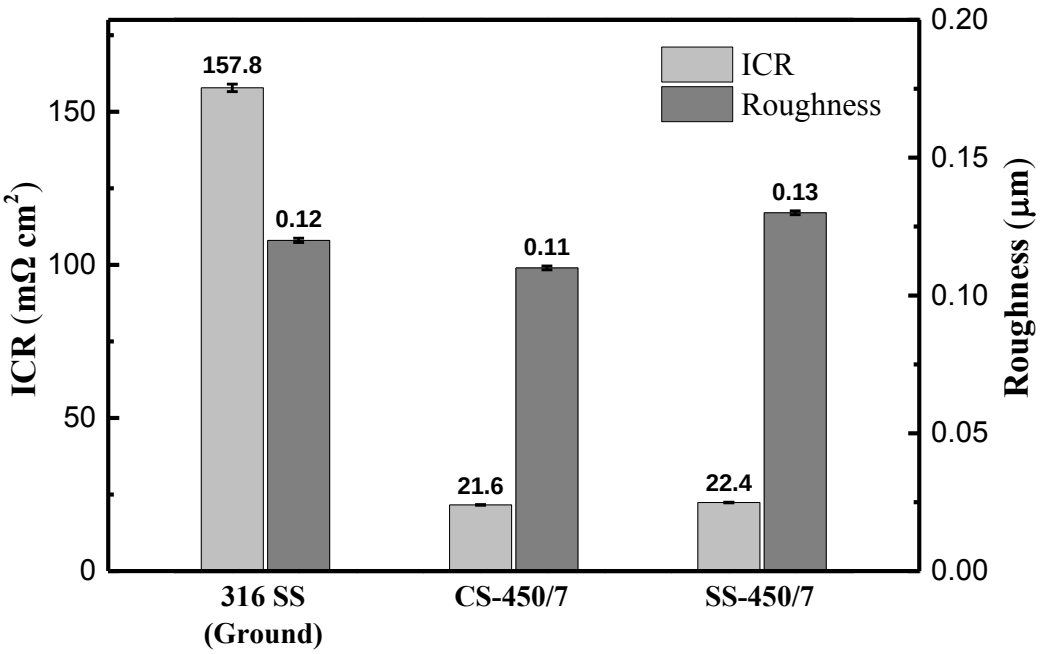

Figure 4.2.22 The ICR value of ASP treated samples with different mesh material

As reported in literature [230], it is possible to alloy the surface of austenitic stainless steel with both interstitial elements (such as N and C) and substitutional elements (such as Ag and Cu) using a composite screen for ASPN treatment. Therefore, by modifying the materials of the screen, the corrosion resistance of the active screen plasma nitrided surface could be tailored by active screen plasma co-alloying with both N to form S-phase and alloying elements to modify corrosion properties and/or surface conductivity. The results of active screen plasma alloying with different alloy elements are reported in the latter chapters.

4.2.9 Summary

From the results shown above, the low temperature ASPN treatment can effectively reduce the ICR value of 316 stainless steel, but it is still much higher than the DoE target (10 mΩ cm^2); the low temperature ASPN treatment could increase corrosion

potential and improve the pitting corrosion resistance of 316 stainless steel in 0.05M sulphuric acid, but also raise the passive current density.

Further investigations have revealed that, the deposition layer formed on the ASPN treated surface greatly affects the surface conductivity and corrosion behaviour. By changing the material of the active screen, the corrosion behaviour and surface conductivity of ASPN treated 316 stainless steel can be tailored.

4.3 Active screen plasma alloying with nitrogen and silver (ASPA(N&Ag))

From the results of Section 4.2, by modifying the active screen material, the surface properties of ASPN treated 316 stainless steel can be tailored. Based on this, sliver was selected as the alloying element to be added to the lid of the active screen. The lid was fabricated by hot isostatic pressing (HIP) technique with the final composition of 5 wt % Ag and 95 wt % 316 stainless steel (in weight percentage). The active screen plasma alloying with nitrogen and silver (ASPA(N&Ag)) treatments were conducted in the DC Klöckner Ionon 60 kVA plasma furnace with lab-scale active screen setting (Figure 3.2.3). The treated surfaces were first ground and then polished to mirror finish. The treatment parameters were set as temperature – 450 ℃ , pressure – 4 mbar, gas mixture – 25 % N_2 + 75 % H_2, based on the previous results in our group. The treatment durations were set as 7 h (Ag-450/7), 10 h (Ag-450/10) and 15 h (Ag-450/15). The normal ASPN treatments were also conducted in the same furnace using 316 stainless steel lid for comparison.

4.3.1 Surface morphology and chemical composition

The surface morphology of ASPA(N&Ag) treated samples was observed by SEM. The low magnification SEM images of the samples are presented in Figure 4.3.1 (a) (c) (e). Surface relief could be found from all three samples. The morphology of the deposition layer on the surface of the ASPA(N&Ag) treated samples seems different among these three samples. The difference could be easily observed from high magnification SEM images, which are shown in Figure 4.3.1 (b) (d) (f). The deposition layer on 7 h treated Ag-450/7 sample (Figure 4.3.1 (b)) looks uniform and consists of small particles with a similar size of 150 nm in diameter. For 10 h treated

Ag-450/10 sample (Figure 4.3.1 (d)), the size of the particles obviously increases ranging from 100 nm to 300 nm. For 15 h treated Ag-450/15 sample (Figure 4.3.1 (f)), the surface seems denser than other two samples.

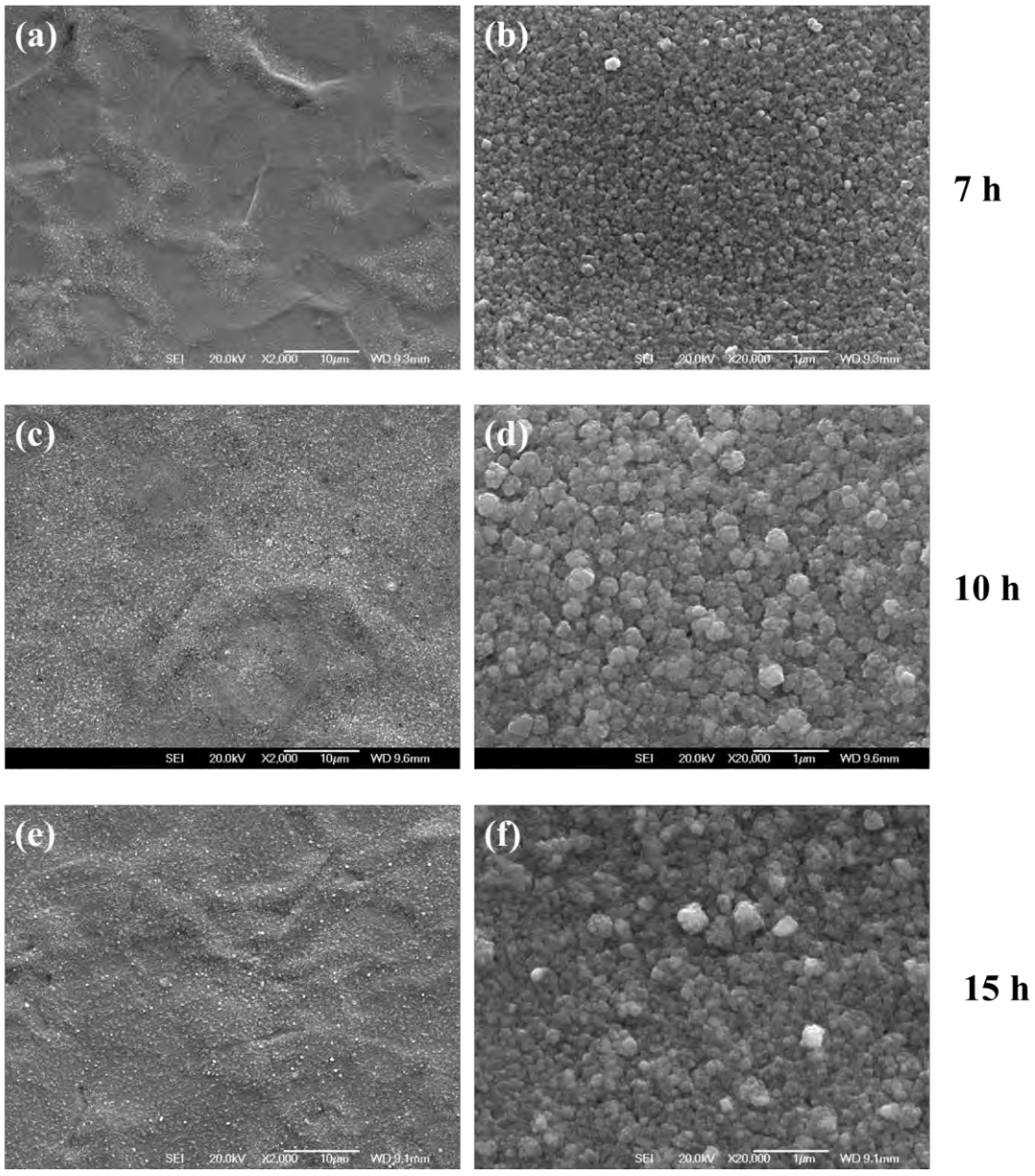

Figure 4.3.1 low and high magnification SEM images of the surface morphology (a) (b) Ag-450/7 (c) (d) Ag-450/10 (e) (f) Ag-450/15

The surface roughness of the ASPA(N&Ag) treated samples are shown in Figure 4.3.2. After ASPA(N&Ag) treatments, the surface roughness (≥ 0.13 μm) is much higher than that of the as-polished untreated surface (0.02 μm) and comparable with

that of the #240 grit ground 316 SS (0.12 μm). In general, the surface roughness increases with the increase of treatment duration mainly due to the intensified surface relief, and a large increase in surface roughness is observed when increasing the treatment duration from 10 h to 15 h. This finding is in agreement with the surface morphology observations. In addition, for the same treatment duration, the ASPA(N&Ag) treated samples have a similar surface roughness to that of the ASPN treated sample.

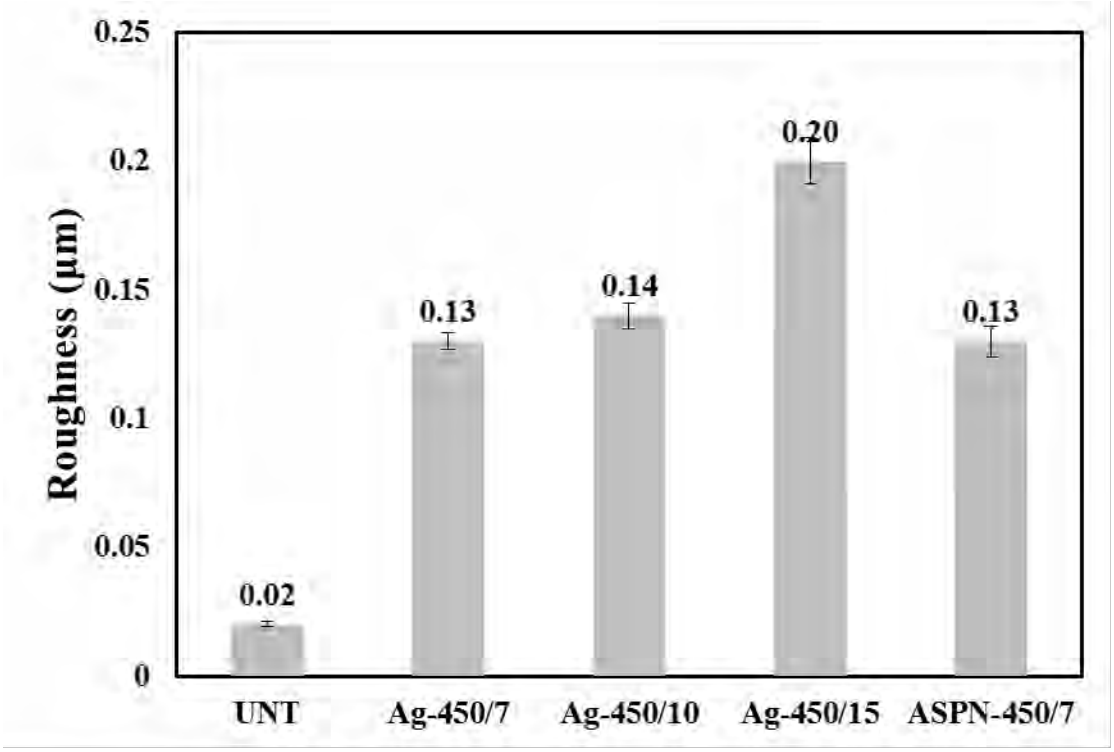

Figure 4.3.2 surface roughness of ASPA(N&Ag) samples

The weight percentage of element Ag on the ASPA(N&Ag) treated surfaces was measured by EDS and the results are charted in Figure 4.3.3. It can be seen that Ag has been successfully introduced into the surface of 316 SS through the ASPA(N&Ag) treatments, and the content of the Ag increases with the increase of treatment duration.

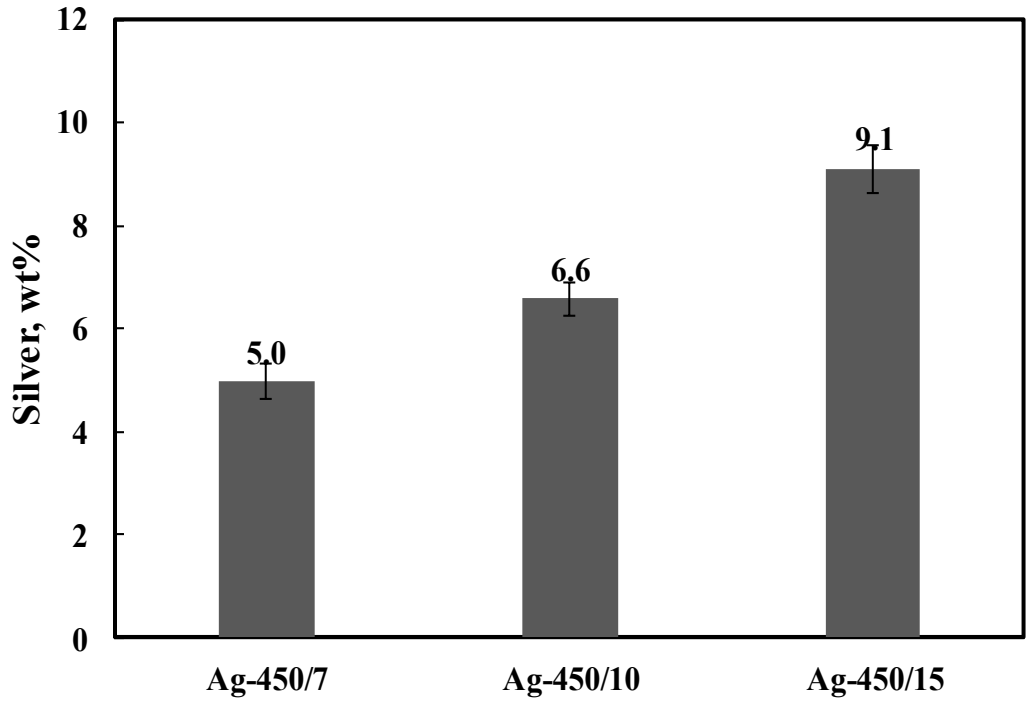

Figure 4.3.3 Weight percentage of Ag and Fe on the treated surface

The high magnification backscattered electron image of Ag-450/15 sample is shown in Figure 4.3.4 (a). From the different contrasts of the image, it can be seen that there are two different materials deposited on the surface, namely bright and grey materials. According to the principle of backscattered electron, the bright contrast means high atomic mass. The comparison of the EDS spectra collected from the areas with different contrasts are shown in Figure 4.3.4 (b), which reveals that the bright material has higher signal of silver than the grey material. Considering the spatial resolution of EDS (few microns) is much larger than the size of the bright particles (only 200 nm), the EDS signal of elements, such as Fe, Cr and Ni, might come from the surrounding area. Therefore, these bright particles might be metallic Ag particles.

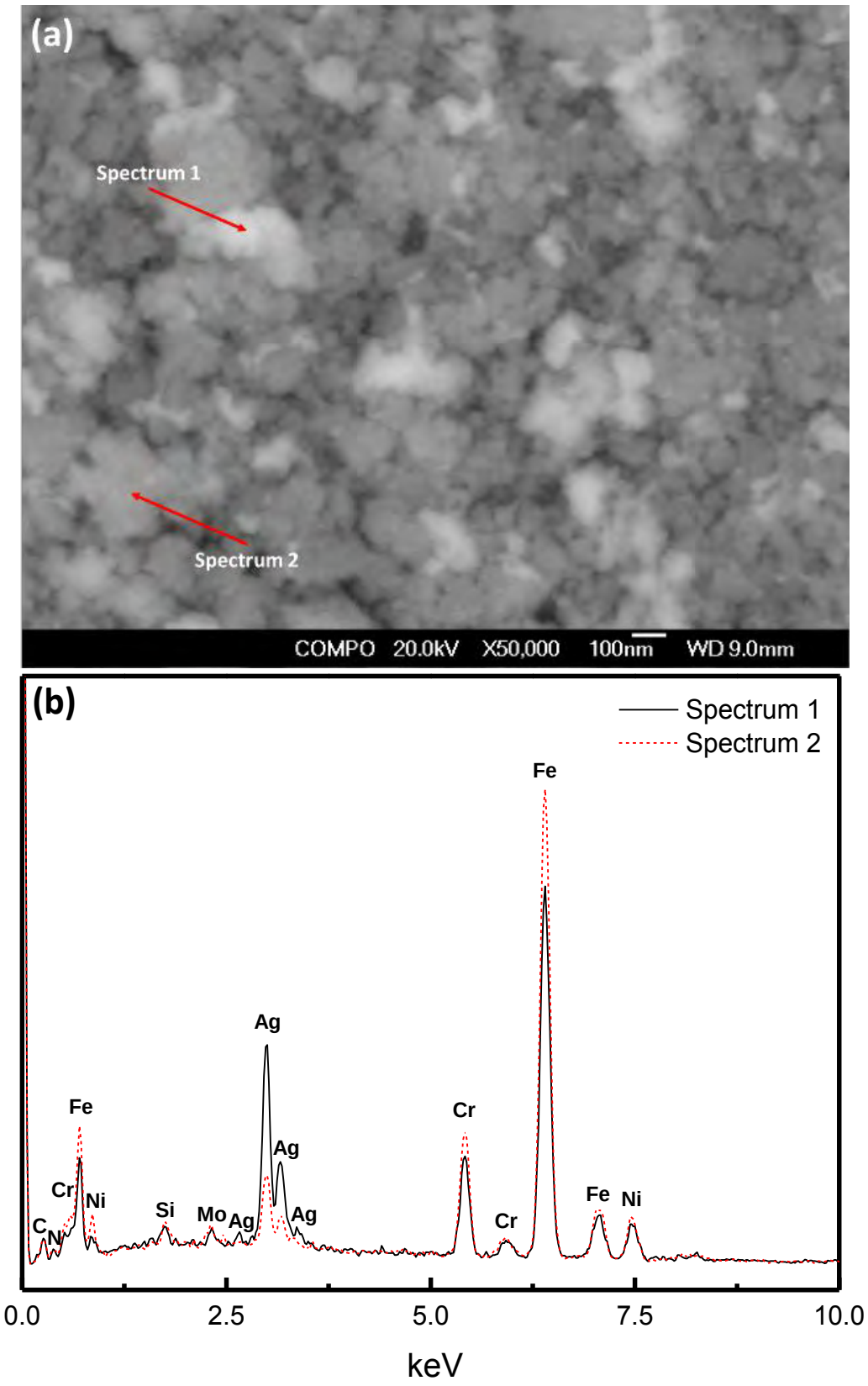

Figure 4.3.4 Analysis of Ag-450/15 under high magnification

(a) Surface backscatter image (b) EDS spectra of two points

4.3.2 Phase identification

The phase constituent of ASPA(N&Ag) treated samples were analysed by XRD. The diffraction patterns of all samples are plotted in Figure 4.3.5. Typical peaks of S-phase, similar to that formed in ASPN treated samples (Figure 4.2.7), can be seen from all the ASPA(N&Ag) treated samples. Apart from S-phase, the peaks of Ag and 316 SS could also be found from all the spectra of the ASPA(N&Ag) treated samples. The peaks of iron nitrides can be also found from the XRD patterns of Ag-450/10 and Ag-450/15 samples. With the increase in the treatment duration, the peak intensity of both iron nitrides and Ag increases, while the peaks for S-phase reduces, and the reason of this phenomenon will be discussed in Section 4.3.3.2.

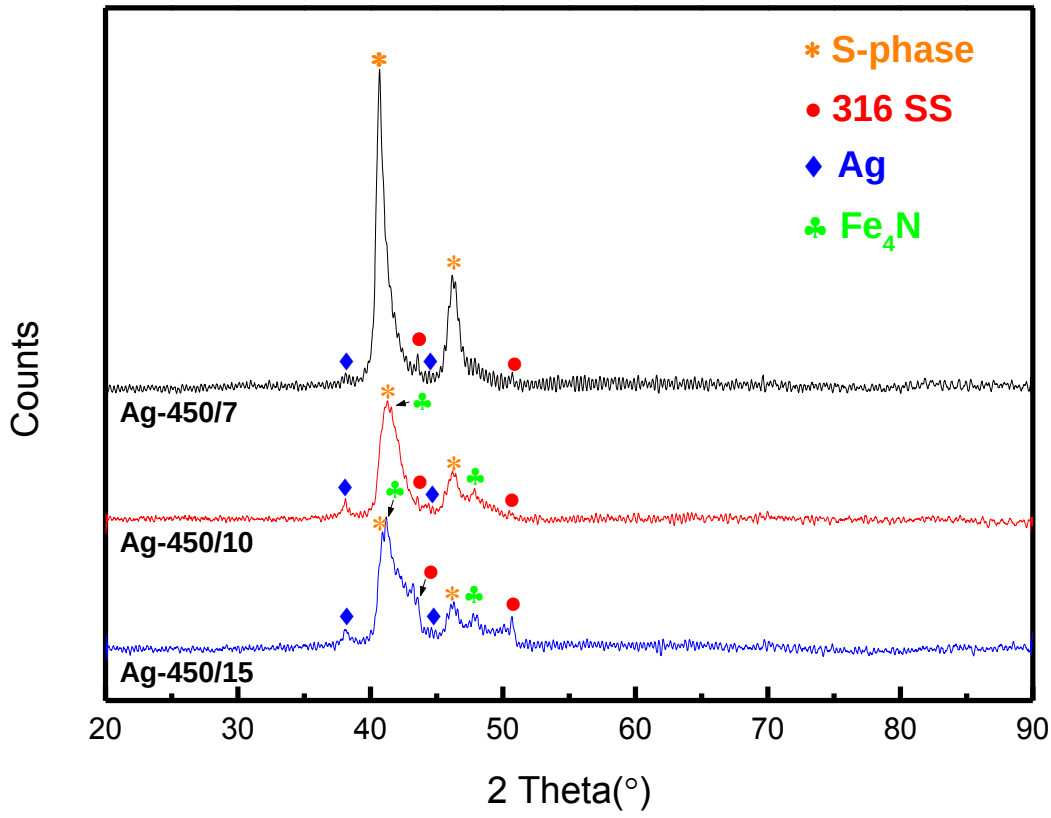

Figure 4.3.5 XRD patterns of ASPA(N&Ag) samples

The ASPA(N&Ag) treatments were also conducted on Si wafers simultaneously with the Ag-450/15 sample. By using Si wafer as substrate, any mass transformation between deposition layer and the stainless steel substrate could be avoided, and thus the composition of the deposition layer could be investigated without the influence of the stainless steel substrate.

The XRD spectra of 15 h ASPA(N&Ag) treated Si wafers are drawn in Figure 4.3.6. Apart from the peaks of Si substrate, the peaks of Ag and Fe_4N could be found from the XRD pattern but no peaks of S-phase can be found. From the XRD results, it follows that the main components of the deposition layer are Ag and iron nitride.

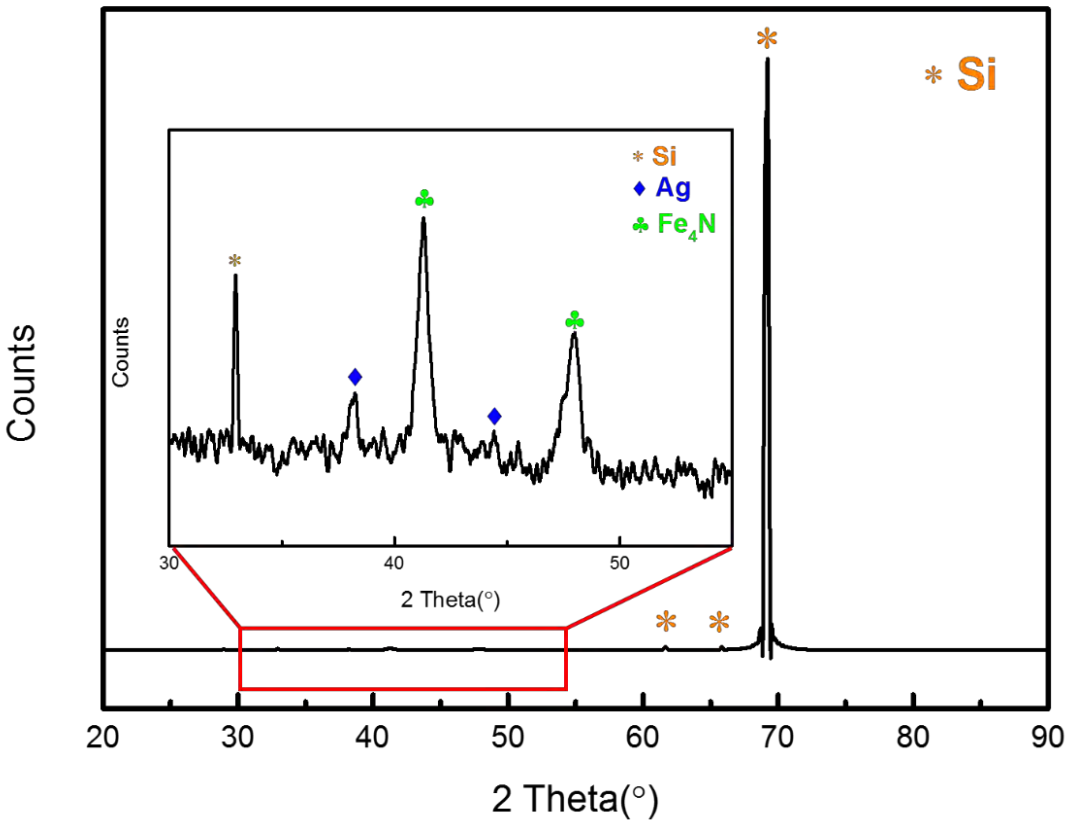

Figure 4.3.6 XRD patterns of Si wafer under 15h ASPA(N&Ag) treatment

4.3.3 Layer structure

4.3.3.1 GDS

The nitrogen profiles against the depth were obtained by GDS, and the results are shown in Figure 4.3.7. All the nitrogen profiles exhibit a similar trend, a sharp drop can be seem in first several hundred nano-meters below the surface, followed by a slow decrease and finished with a relatively rapid decline. In addition, the nitrogen content in those layers increases with the treatment duration.

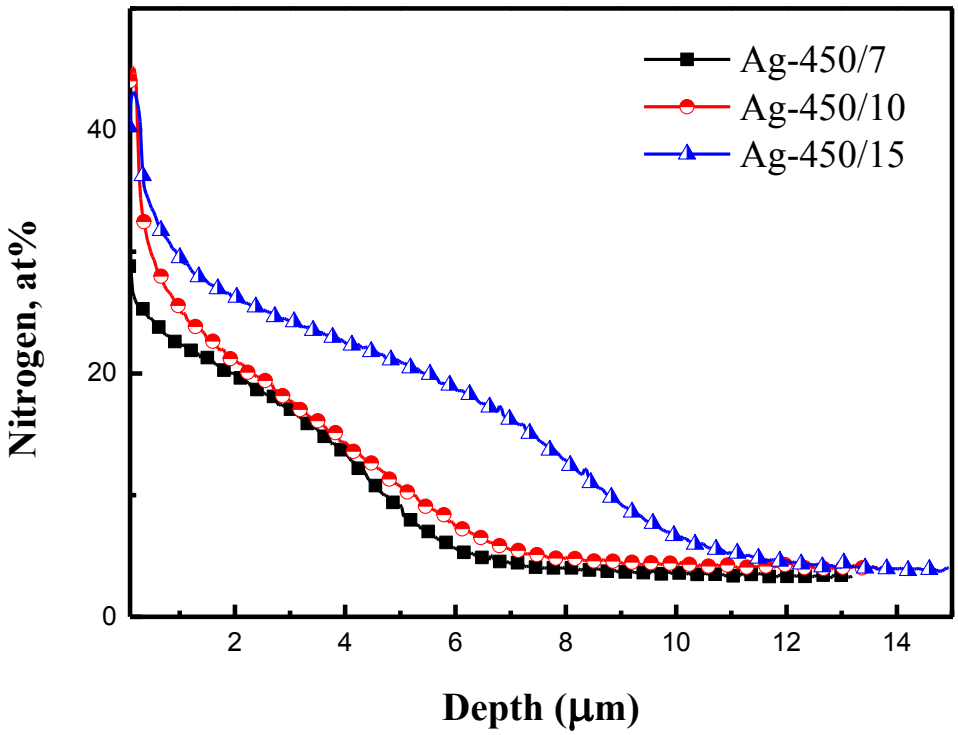

Figure 4.3.7 Nitrogen depth profiles of ASPA(N&Ag) samples

The Ag profile against depth was also obtained by GDS and the results are plotted in Figure 4.3.8. All Ag profiles show a remarkably decrease from the very surface, which is followed by a plateau before it drops again. It is interesting to find that there is a peak at the end of plateau for all the profiles. Those peaks might be related to the

arcing on the Ag containing lid at the beginning of the ASPA(N&Ag) treatments, thus leading to relatively rapid sputtering. The depth of Ag-rich region increases with the increasing treatment duration.

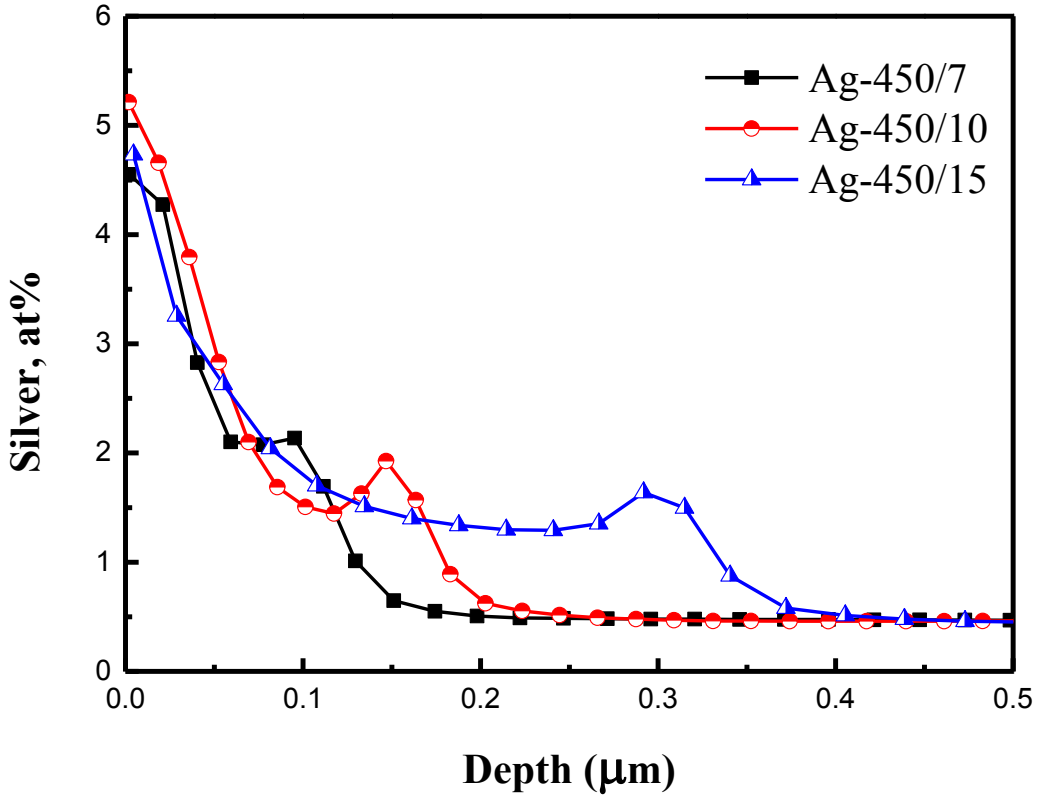

Figure 4.3.8 Ag depth profiles of ASPA(N&Ag) samples

4.3.3.2 SEM

The cross sectional SEM images of different samples are shown in Figure 4.3.9. Feature-less layers with different thicknesses can be observed on the surface of each sample. Those feature-less layers are similar to the layers shown in the SEM images of ASPN treated sample (Figure 4.2.4 (a) (c) (e)). From the XRD results in Figure 4.3.5 and the GDS results in Figure 4.3.7, the feature-less layers can be identified as S-phase layers. The high magnification cross-sectional SEM images near the surface are also presented in Figure 4.3.9 (b) (d) (f). Very thin deposition layers can be found

on the very surface of the S-phase layers. These layers are uniform, dense and tightly bonded with the underneath S-phase layer. Judging from the EDS analysis, the XRD patterns and the GDS results, these deposition layers are the Ag-rich layers.

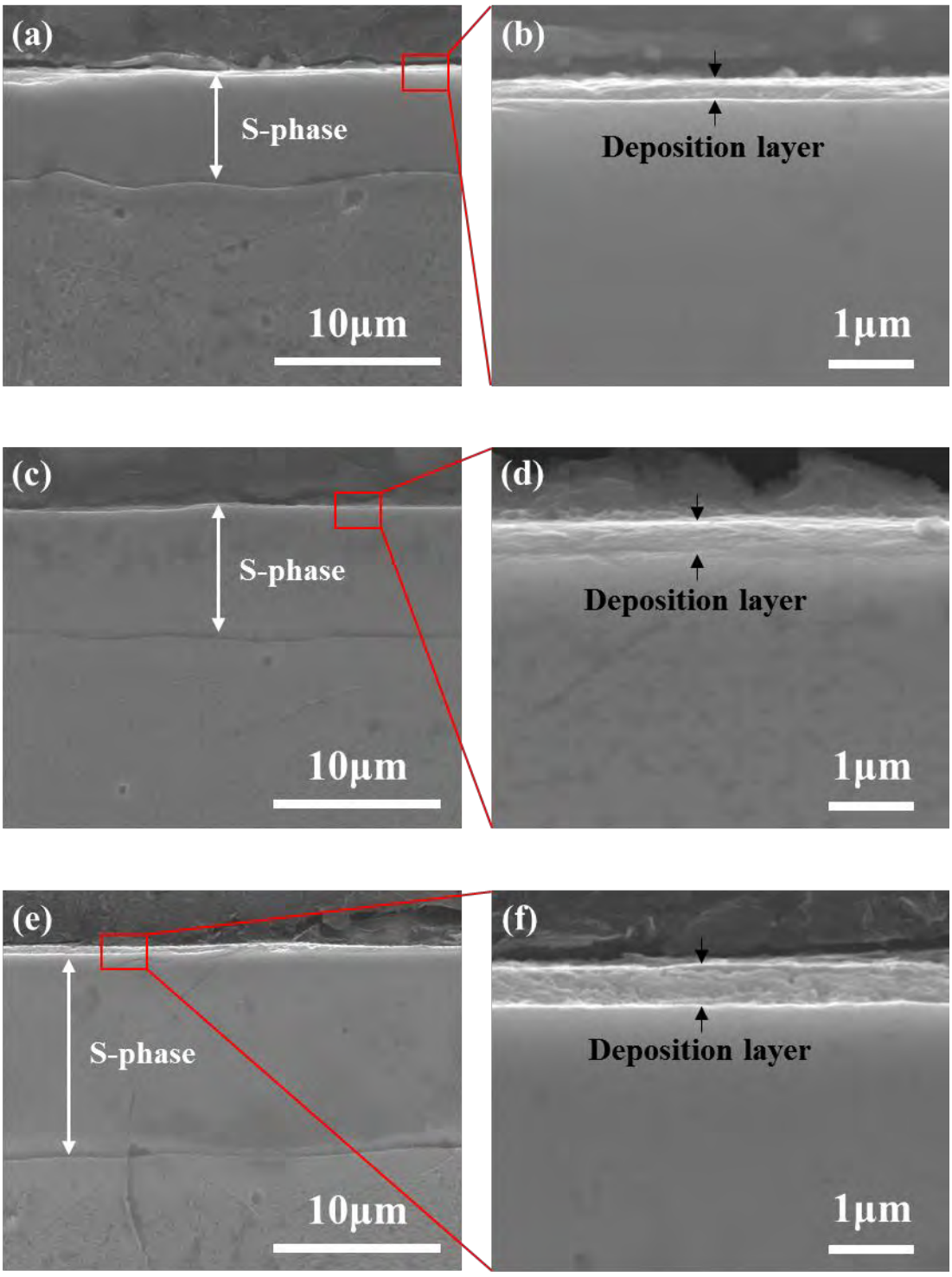

Figure 4.3.9 Low and high magnification Cross-sectional SEM images of ASPA(N&Ag) treated samples (a) (b) Ag-450/7 (c) (d) Ag-450/10 (e) (f) Ag-450/15

The thickness of the S-phase layers and the deposition layers on different samples were measured from the corresponding SEM images and are charted in Figure 4.3.10. It can be seen that the layer thickness of S-phase and deposition layer increases with the increase of treatment time. The S-phase thickness of the Ag-450/7 sample (6.5 μm) is thinner than that of ASPN treated sample (8 μm) when treated under the same nitriding conditions, this phenomenon will be explained in the Section 5.2.1. The thickness of those S-phase layers and Ag-rich deposition layers is in agreement with the depth of the high-nitrogen and Ag-rich region obtained by GDS (Figure 4.3.7 and Figure 4.3.8).

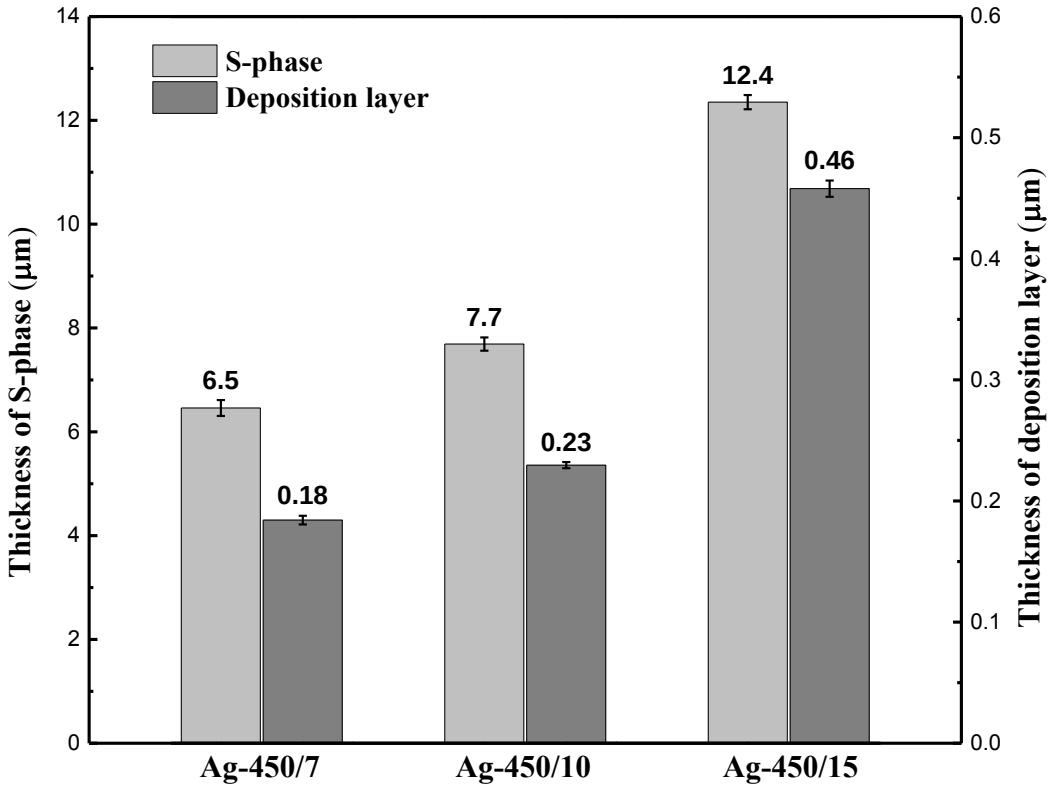

Figure 4.3.10 Thickness of S-phase layer in different ASPA(N&Ag) samples

4.3.4 Surface electrical conductivity

The interfacial contact resistance (ICR) values of ASPA(N&Ag) treated samples for different durations are given in Figure 4.3.11. The ICR value for ground untreated 316 SS with similar surface roughness and 450 °C/7 h ASPN sample treated in the same experiment setup are also presented for comparison. It can be seen from the figure that the ICR values of all the ASPA(N&Ag) treated samples are around 20 mΩ cm^2, which is about one order of magnitude lower than that of the untreated one and also lower than that of the ASPN treated sample (24.4 mΩ cm^2). The ICR results indicate that the introduction of highly conductive Ag element can further enhance the surface conductivity of ASPN treated 316 stainless steel.

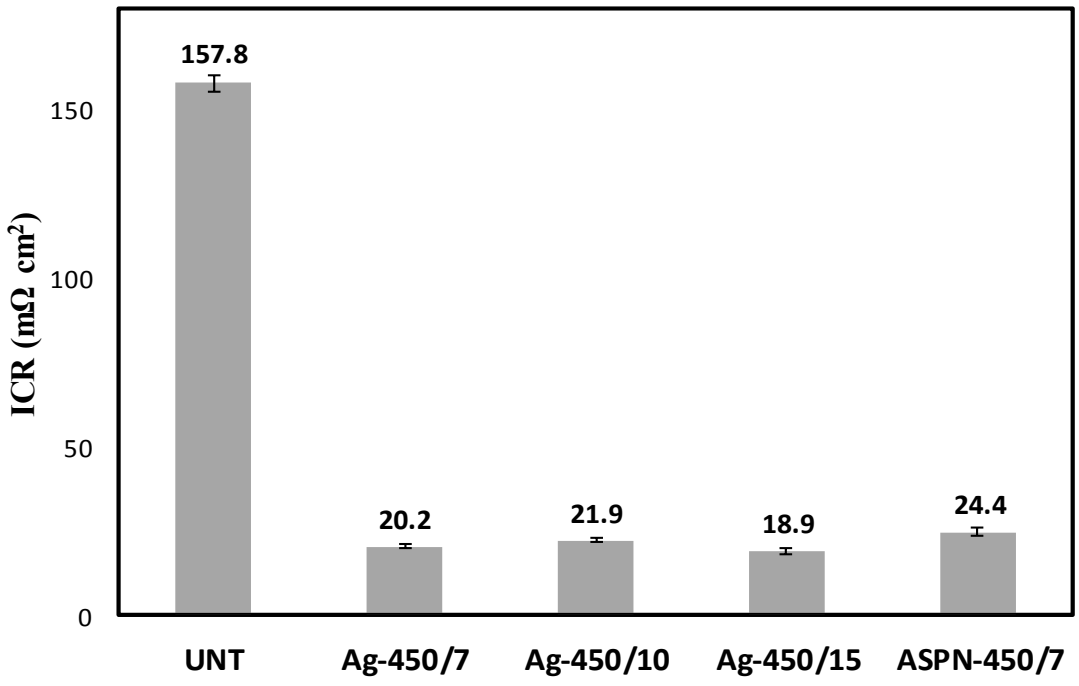

Figure 4.3.11 ICR values of ASPA(N&Ag) samples

4.3.5 Corrosion behaviour

The corrosion performance of ASPA(N&Ag) treated 316 SS was evaluated by potentio-dynamic polarisation tests. Their polarisation curves are plotted in Figure 4.3.12 together with the results of untreated 316 SS and ASPN treated sample for comparison. The corrosion potential and corrosion current density were calculated from the polarisation curves and summarised in Table 4.6.

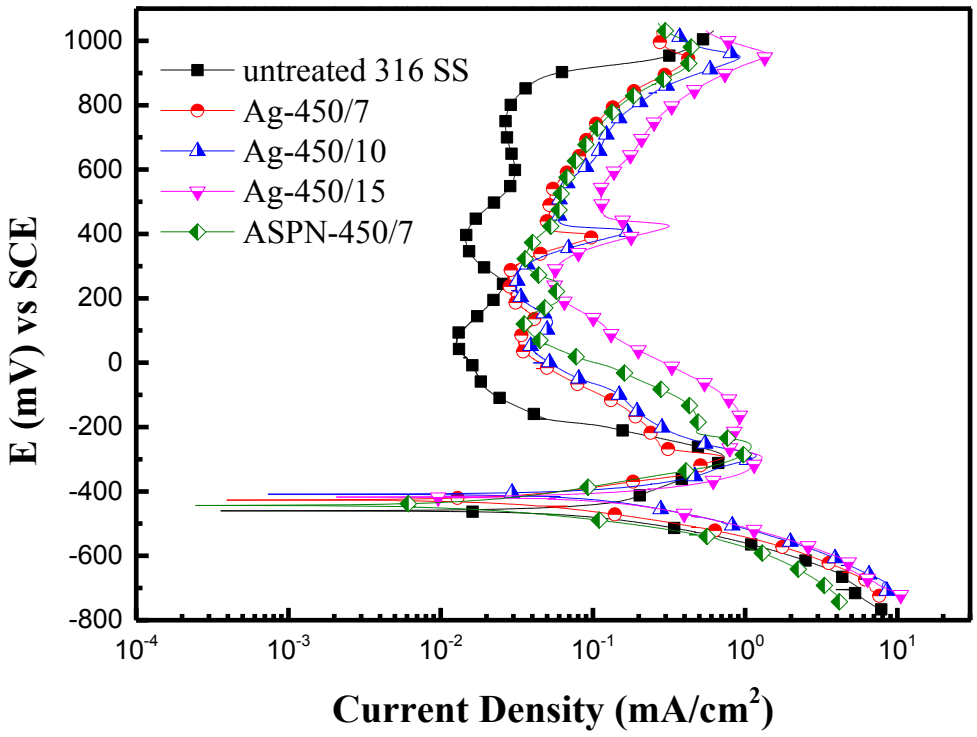

Figure 4.3.12 Potentiodynamic polarisation curves of ASPA(N&Ag) samples

From the corrosion potential point of view, the ASPA(N&Ag) treated samples exhibit more positive value than that of the untreated sample, which means the reduction of corrosion tendency. The corrosion potential of the ASPA(N&Ag) treated samples increases first with the treatment duration, peaks for the 10 h treated sample and then decreases when further increasing the treatment time to 15 h (Table 4.6). The increase of the corrosion potential from 7 h to 10 h is mainly due to the increase of Ag content

in the plasma alloyed surface. For the 15 h treated sample, although the Ag content is higher than the others, the high degree of surface relief results in more defects on the surface, leading to the decrease of corrosion potential. The corrosion current densities of the ASPA(N&Ag) treated samples are lower than that of the untreated one, with the Ag-450/7 sample exhibiting an order of magnitude lower corrosion current density than that of the untreated one.

Table 4.6 Corrosion results of ASPA(N&Ag) samples

sample	corrosion potential (mV vs SCE)	corrosion current density (mA/cm^2)
UNT	-460	0.114
Ag-450/7	-427	0.021
Ag-450/10	-409	0.086
Ag-450/15	-417	0.097
ASPN-450/7	-443	0.088

Comparing the ASPA(N&Ag) samples with the ASPN sample treated under the same treatment conditions, the former shows more positive corrosion potential, lower corrosion current density and lower passive current density than the latter. Hence, the corrosion resistance of the ASPA(N&Ag) treated 316 stainless steel is better than that of the ASPN treated one.

However, from the passive current density point of view, all treated samples show a higher passive current density than that of the untreated stainless steel. The passive current density is in the order of Ag-450/15 > Ag-450/10 > ASPN-450/7 > Ag-450/7. The high passive current density of the plasma treated samples could be attributed to the increased surface roughness (Figure 4.3.2) due to the formation of S-phase and the resulted surface relief.

4.3.6 Summary

From the results reported above, the ASPA(N&Ag) treatments can significantly reduce the ICR value from 157.8 mΩ cm^2 for the untreated 316 SS down to around 20 mΩ cm^2. In addition, the corrosion potential of all the ASPA(N&Ag) treated samples are more positive than that of the untreated 316 stainless steel and the corrosion current densities are lower than that of the untreated 316 stainless steel. Comparing the ASPA(N&Ag) treated samples with the ASPN treated samples, the former exhibits superior surface conductivity and corrosion resistance than the latter. Therefore, the active screen plasma co-alloying treatment with both N and Ag does improve the surface conductivity and corrosion resistance (in terms of corrosion potential and corrosion current density) of 316 stainless steel samples. However, the reduced ICR values are still higher than that of the DoE target, which is 10 mΩ cm^2, and the problem of high passive current density after treatments has not been solved. Therefore, it is necessary to conduct more co-alloying treatments with different alloying treatments.

4.4 ASP co-alloying with N and Nb (ASPA(N&Nb))

Because of the excellent corrosion resistance and electrical conductivity, as mentioned in Section 2.4.1, niobium was selected as the element to modify the surface of 316 stainless steel by means of active screen plasma co-alloying. Different from the alloying method for ASPA(N&Ag) which used a Ag doped 316 SS lid produced by hot isostatic pressing (HIP) technique, the lid of the active screen of ASPA(N&Nb) was specially designed with niobium wires hung on the 316 SS mesh lid as the alloying source (Figure 3.2.4). In addition, the ASPA(N&Nb) treatments were conducted in the AS Plasma Metal 75 kVA + 15 kVA industrial scale plasma furnace (Figure 3.2.4). Based on the results reported in Section 4.2, the treatment temperature was set as 450 ℃ for all ASPA(N&Nb) treatments.

4.4.1 Influence of treatment duration

The treatment temperature, applied bias and pressure were set as 450 ℃ , 5 % and 0.75 mbar, respectively, and the length of niobium wire was 1mm. The treatment durations were set as 7 h (Nb-450/7/5-1mm), 10 h (Nb-450/10/5-1mm), 15 h (Nb-450/15/5-1mm) and 20 h (Nb-450/20/5-1mm).

4.4.1.1 Surface morphology and chemical composition

The surface morphology of ASPA(N&Nb) treated samples with 1 mm Nb wires for different durations are shown in Figure 4.4.1. From the low magnification SEM images, surface relief can be clearly observed from the surface of all treated samples and the extent of surface relief intensifies with the treatment duration. It is interesting to find that on the surface of Nb-450/10/5-1mm (Figure 4.4.1 (c)), two areas with different contrasts can be observed, namely bright area and grey area (marked by dot line). It seems like the territory of the grey areas matches well with the grains. Similar

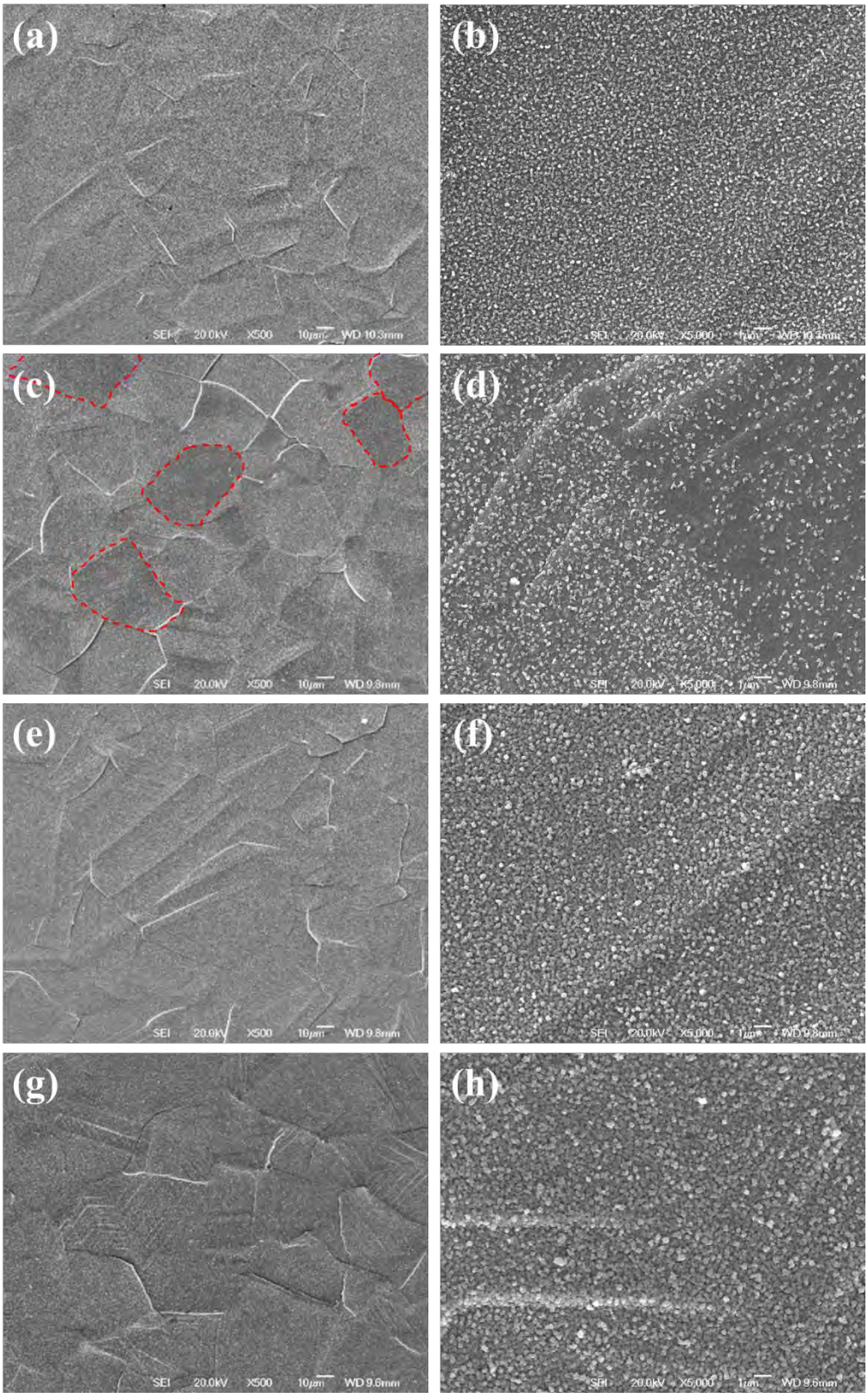

Figure 4.4.1 Low and high magnification of surface morphologies SEM images of 1mm Nb ASPA(N&Nb) treatments

(a) (b) Nb-450/7/5-1mm (c) (d) Nb-450/10/5-1mm

(e) (f) Nb-450/15/5-1mm (g) (h) Nb-450/20/5-1mm

findings were reported before for ASP nitrided austenitic stainless steel [229], which was caused by the anisotropic diffusion of nitrogen in grains with different crystallographic orientations. The high magnification surface SEM images show that all the treated surfaces are covered by many nano-particles and their size increases with the increase of treatment duration.

The surface roughness results of the 1 mm Nb ASPA(N&Nb) treated samples are shown in Figure 4.4.2. With the increase in treatment duration, the roughness of the treated surface increases. This is in line with the results of the ASPA(N&Ag) treated samples reported in Section 4.3.

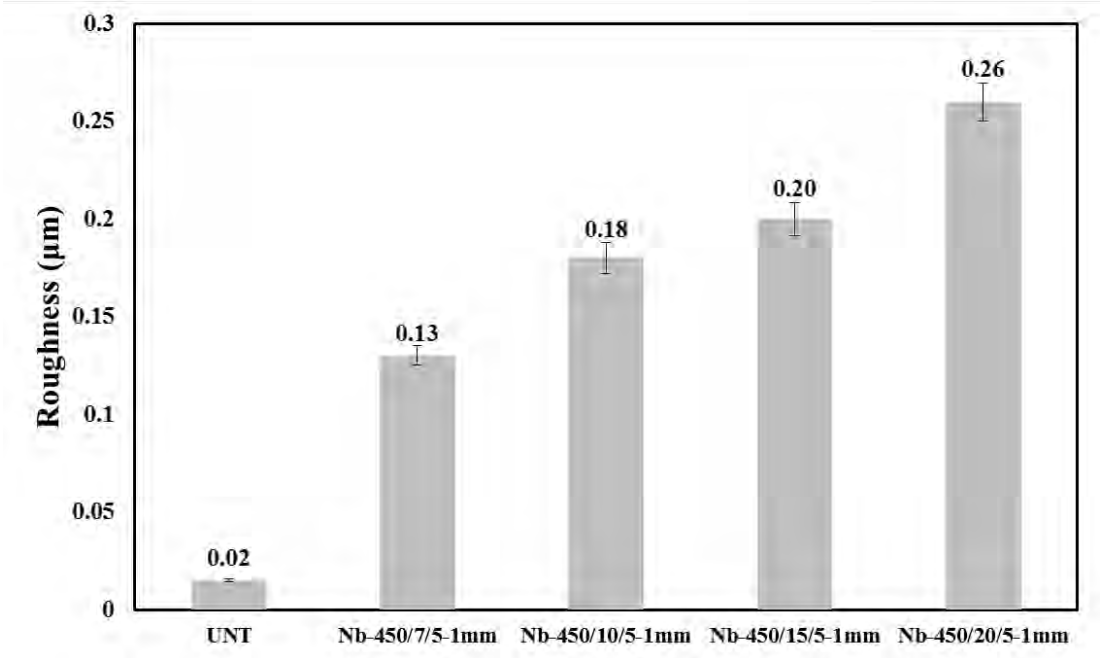

Figure 4.4.2 Surface roughness of 1 mm Nb ASPA(N&Nb) and normal ASPN treated samples for different durations

The surface nitrogen and niobium content of 1 mm Nb ASPA(N&Nb) treated samples are shown Figure 4.4.3. The content of nitrogen increases with the treatment duration. The niobium can been detected from the treated surfaces, and the content also

increases with the increase of the treatment duration. However, the niobium content is lower than 0.6 wt%.

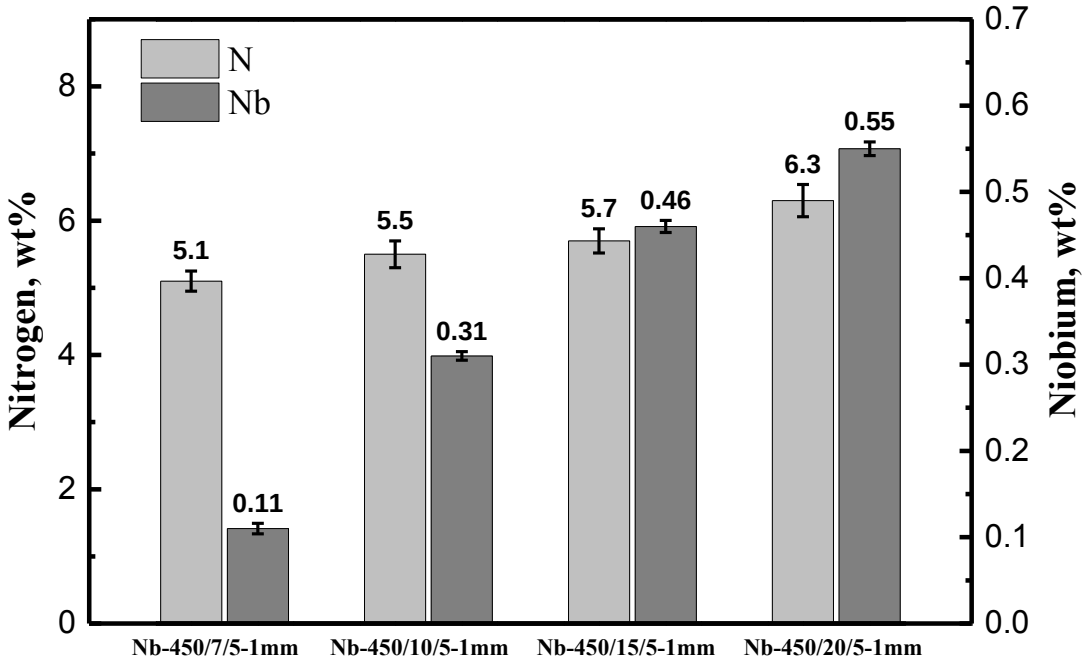

Figure 4.4.3 Nitrogen and niobium weight percentage of 1 mm Nb ASPA(N&Nb) treated samples

4.4.1.2 Phase and layer structures of treated surfaces

The XRD patterns of 1 mm Nb ASPA(N&Nb) treated samples are shown in Figure 4.4.4. The characteristic peaks of S-phase can be detected from all treated surfaces. With the increase of treatment duration, the position of the remaining S-phase peaks shifts to a lower angle, which will be explained latter. No other peaks can be found from all the treated surfaces.

The SEM images of cross-sectional 1 mm Nb ASPA(N&Nb) samples are presented in Figure 4.4.5. According to the results of XRD, the top layer on each sample can be identified as S-phase layer. The thickness of the S-phase layer of different samples is listed in Figure 4.4.6, which increases with the treatment duration.

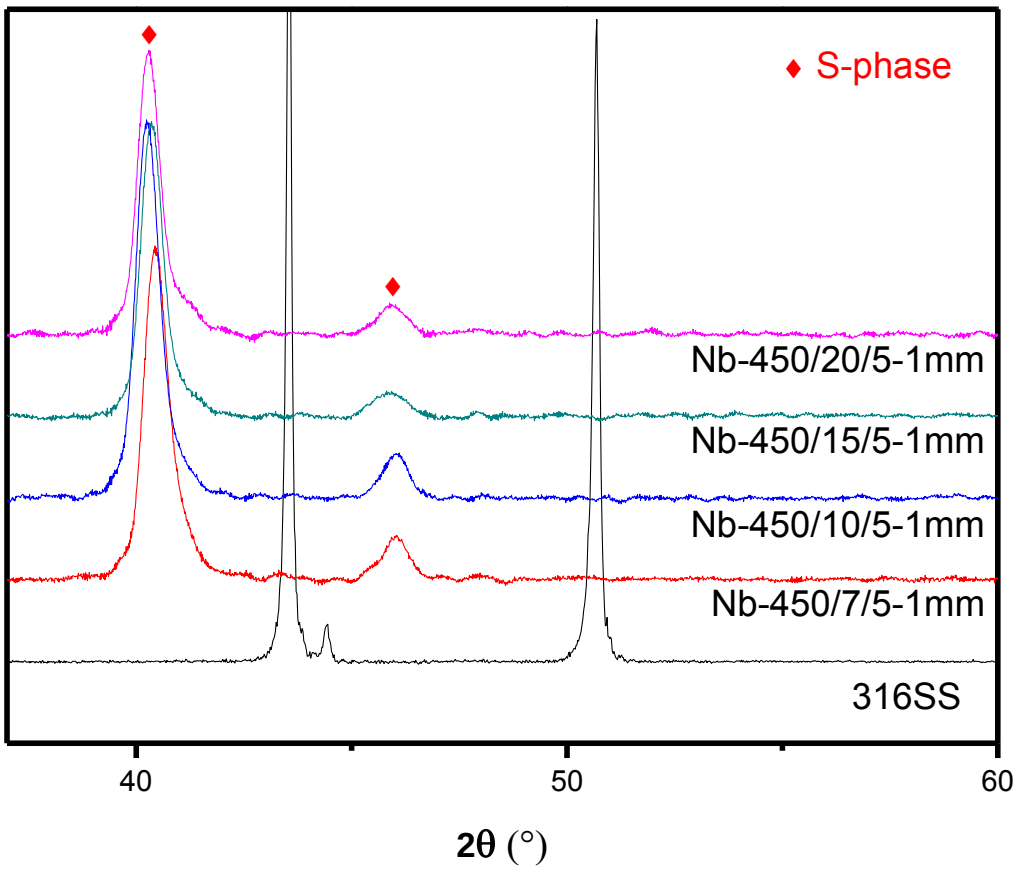

Figure 4.4.4 XRD patterns of 1 mm Nb ASPA(N&Nb) and ASPN treated samples

The GDS nitrogen depth profiles of 1 mm Nb ASPA(N&Nb) treated samples are plotted in Figure 4.4.7. Both the nitrogen content and the penetration depth increase with the increase of the treatment duration. The high nitrogen content in the S-phase leads to great grain expansion and left-shift of XRD peaks (Figure 4.4.4). The trace amount of niobium cannot be detected using the GDS technique.

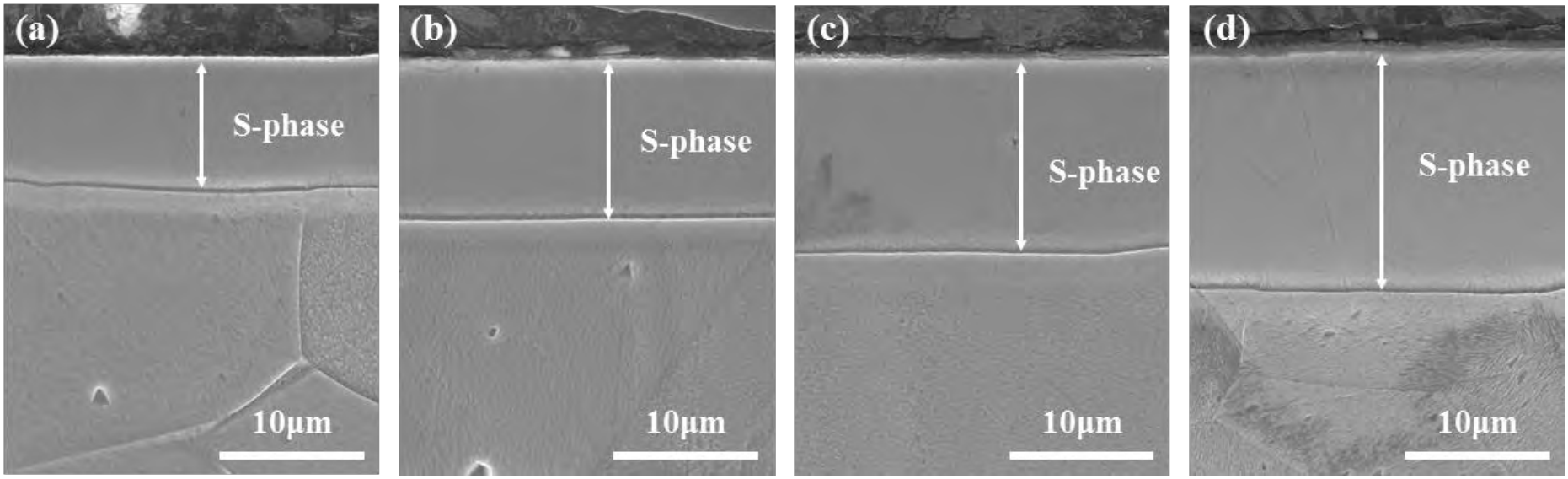

Figure 4.4.5 Cross-sectional SEM images of 1 mm Nb ASPA(N&Nb) treated samples
(a) Nb-450/7/5-1mm (b) Nb-450/10/5-1mm
(c) Nb-450/15/5-1mm (d) Nb-450/20/5-1mm

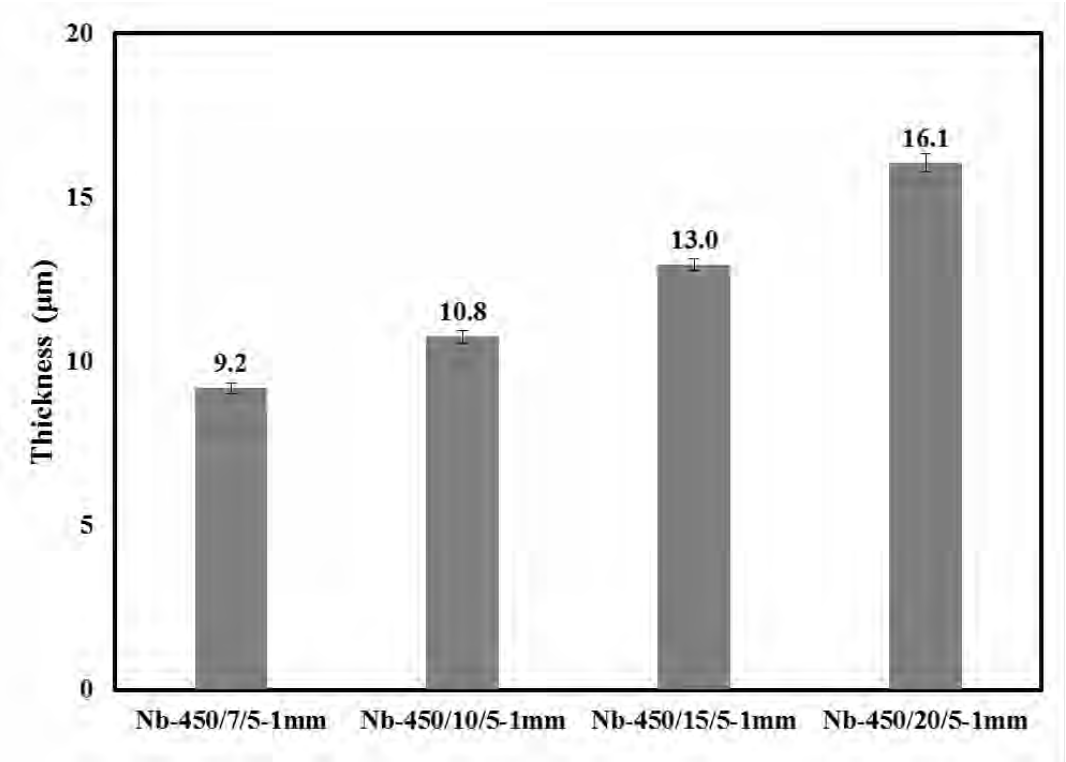

Figure 4.4.6 S-phase thickness of 1 mm Nb ASPA(N&Nb) treated samples

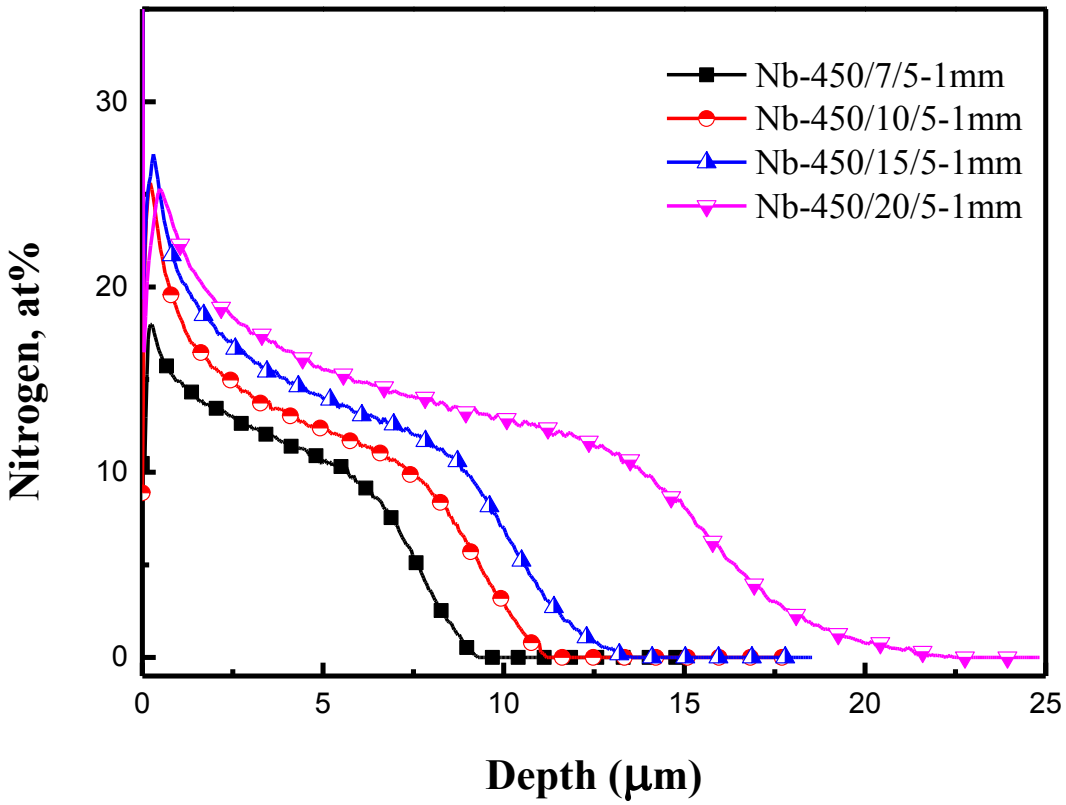

Figure 4.4.7 GDS nitrogen depth profiles of 1 mm Nb ASPA(N&Nb) treated samples

4.4.1.3 Surface conductivity

The ICR values of 1 mm Nb ASPA(N&Nb) treated samples are shown in Figure 4.4.8. The ICR values of Nb-450/7/5-1mm sample and Nb-450/10/5-1mm sample are close to each other (around 14.5 mΩ cm^2). When further increasing the treatment time to 15 hour or above, the ICR value suddenly jumps to around 17.5 mΩ cm^2.

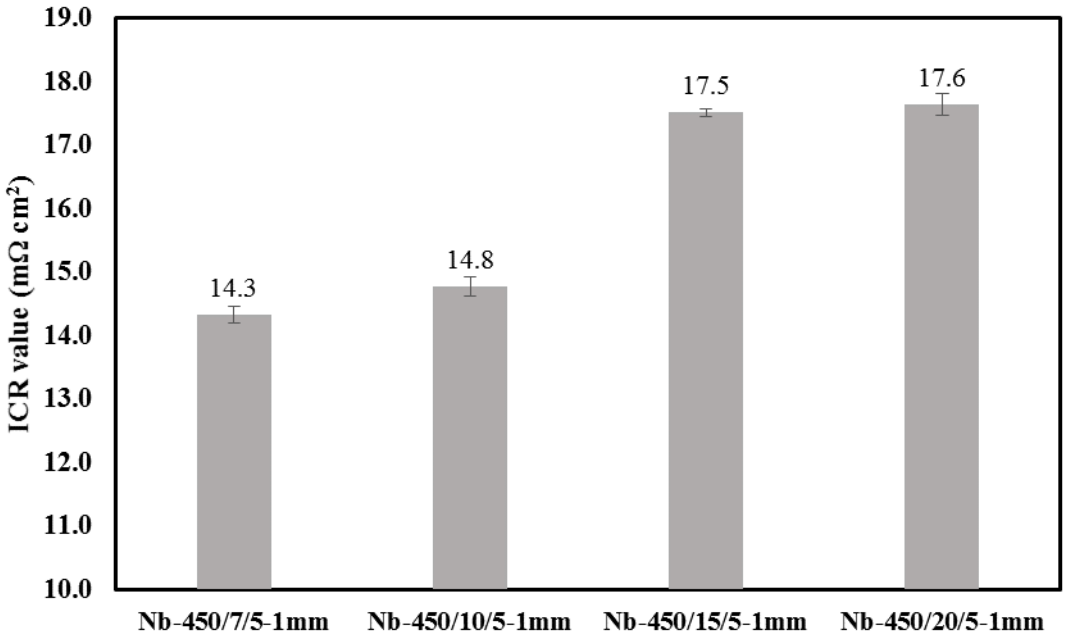

Figure 4.4.8 ICR values of 1 mm Nb ASPA(N&Nb) treated samples

From the results of the surface composition, Nb can be introduced into the surface by mean of active screen plasma co-alloying with both nitrogen and niobium and successfully reduce the ICR value to around 14.5 mΩ cm^2. But the amount of niobium in the surface is too low when 1 mm Nb wires were used as the alloying source. To increase the niobium amount in the alloyed surfaces, longer Nb wires were employed in the following section. Basing on the ICR results of 1 mm Nb ASPA(N&Nb) treated and the corrosion results of ASPA(N&Ag) treatments in Section 4.3.5, the treatment duration was selected as 10 h for further investigation and optimisation of parameters.

4.4.2 Influence of the length of Nb wires

In order to investigate the influence of Nb wire length on the ASPA(N&Nb) treated surface, different lengths of Nb wires were applied onto the 316 SS mesh lid. The treatment temperature, duration, pressure and applied bias were set as 450 ℃ , 10 h, 0.75 mbar and 5 %, respectively. The length of Nb wires was selected as 2 mm (Nb-450/10/5-2mm), 5 mm (Nb-450/10/5-5mm), 7 mm (Nb-450/10/5-7mm) and 10 mm (Nb-450/10/5-10mm).

4.4.2.1 Surface morphology and chemical composition

The macro appearance and the surface roughness of the ASPA(N&Nb) treated samples with different lengths of Nb wires are shown in Figure 4.4.9. The surface of Nb-450/10/5-2mm sample (Ra = 0.18 μm) is dark grey and clearly roughed after treatment, and hence no mirror reflection can be seen from its surface. The surface of Nb-450/10/5-5mm sample (Ra = 0.07 μm) is slightly roughed, and the reflection on the surface is not so clear as the polished 316 SS. Except for the surface colour changes to light brown, the surface morphology of Nb-450/10/5-7mm (Ra = 0.02 μm) and Nb-450/10/5-10mm (Ra = 0.03 μm) samples looks similar to the polished 316 stainless steel (Ra = 0.01 μm) with the reflection being clearly seen from the surfaces.

The low magnification SEM surface images of all the treated samples with different lengths of Nb wires are presented in Figure 4.4.10. Surface relief can be easily seen from Nb-450/10/5-2mm sample (Figure 4.4.10(a)). Although surface relief can also be found from Nb-450/10/5-5mm sample (Figure 4.4.10(c)), the intensity reduces remarkably. On the other hand, no surface relief can be seen from the surface of Nb-450/10/5-7mm and Nb-450/10/5-10mm samples (Figure 4.4.10 (e) (g)). High magnification SEM images of the treated surface are also shown in Figure 4.4.10. On

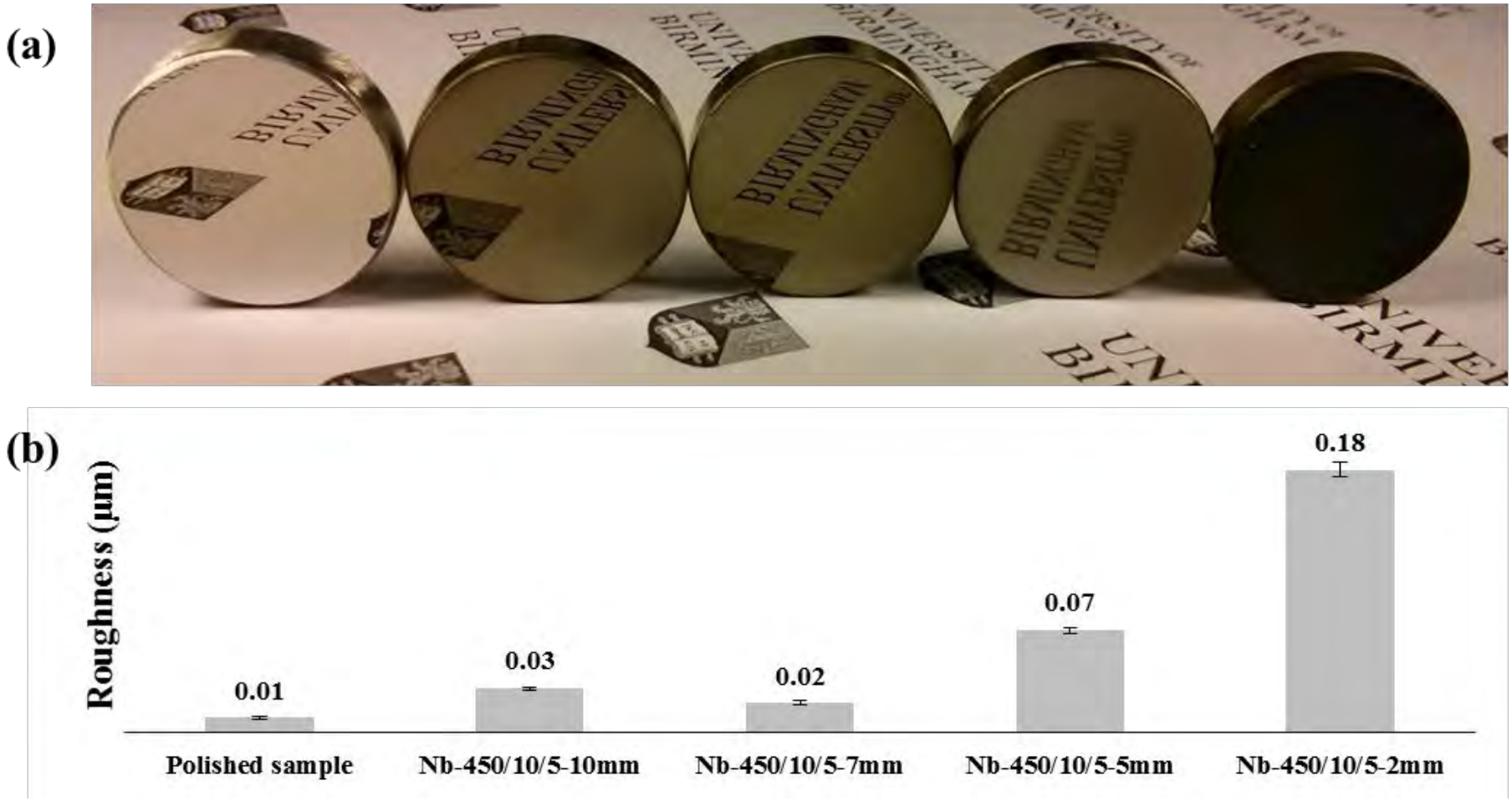

Figure 4.4.9 The macro morphology of ASPA(N&Nb) treated sample with different length of alloying wires

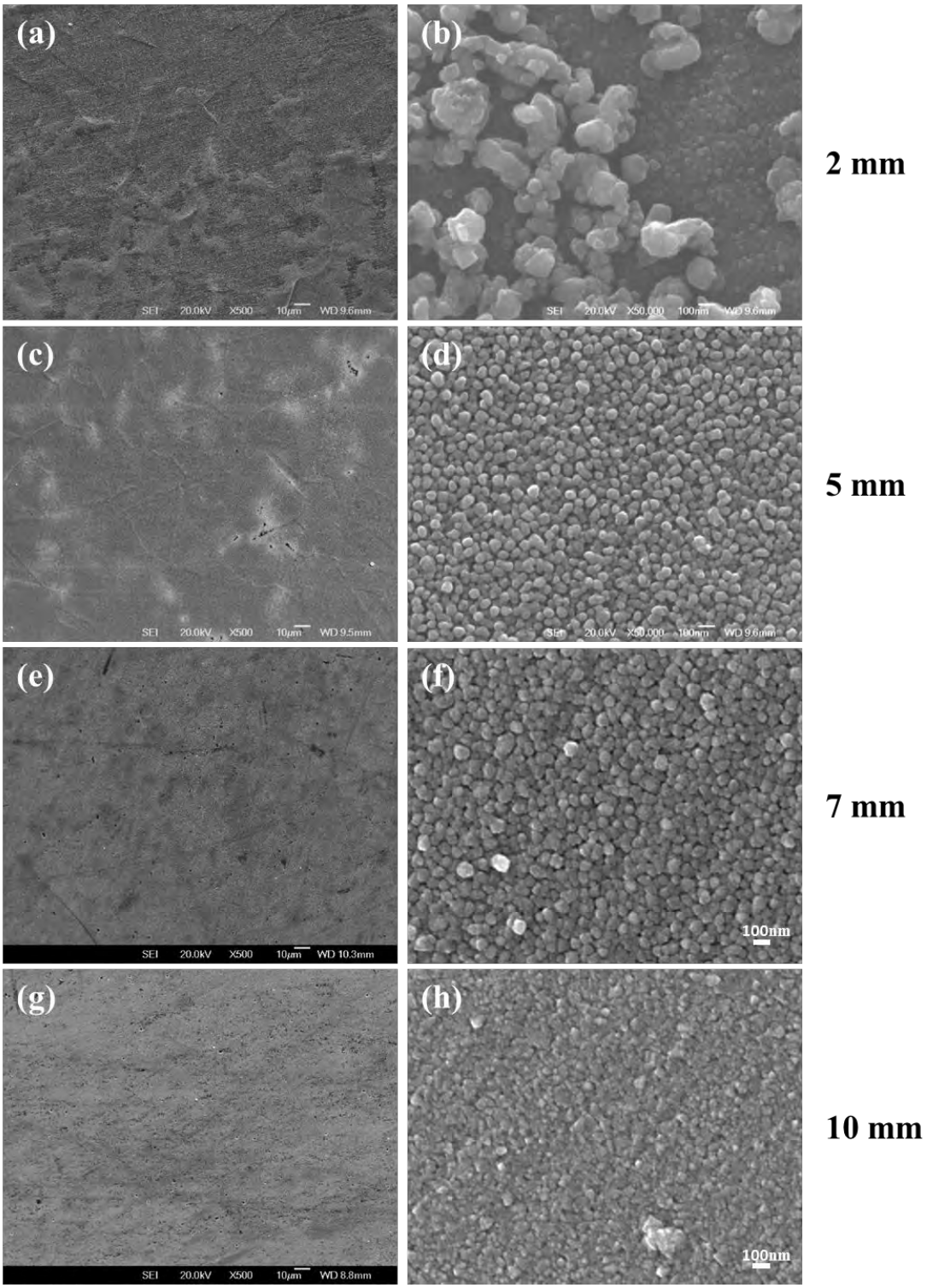

Figure 4.4.10 Low and high magnification SEM images of ASPA(N&Nb) treated sample with different length of alloying wires

(a) (b) Nb-450/10/5-2mm (c) (d) Nb-450/10/5-5mm

(e) (f) Nb-450/10/5-7mm (g) (h) Nb-450/10/5-10mm

the surface of Nb-450/10/5-2mm sample (Figure 4.4.10 (b)), some large particles of 200-400 nm in diameter can be seen on the top of a dense layer consisting of small particles (30-50 nm in diameter). Large particles are absent from other surfaces, replaced by small round shape particles about 100 nm in diameter (Figure 4.4.10 (d)&(f)). For Nb-450/10/5-10mm sample (Figure 4.4.10 (h)), the boundary of each individual particle cannot be identify clearly. In general, the density of particle layer increases with the Nb wire length.

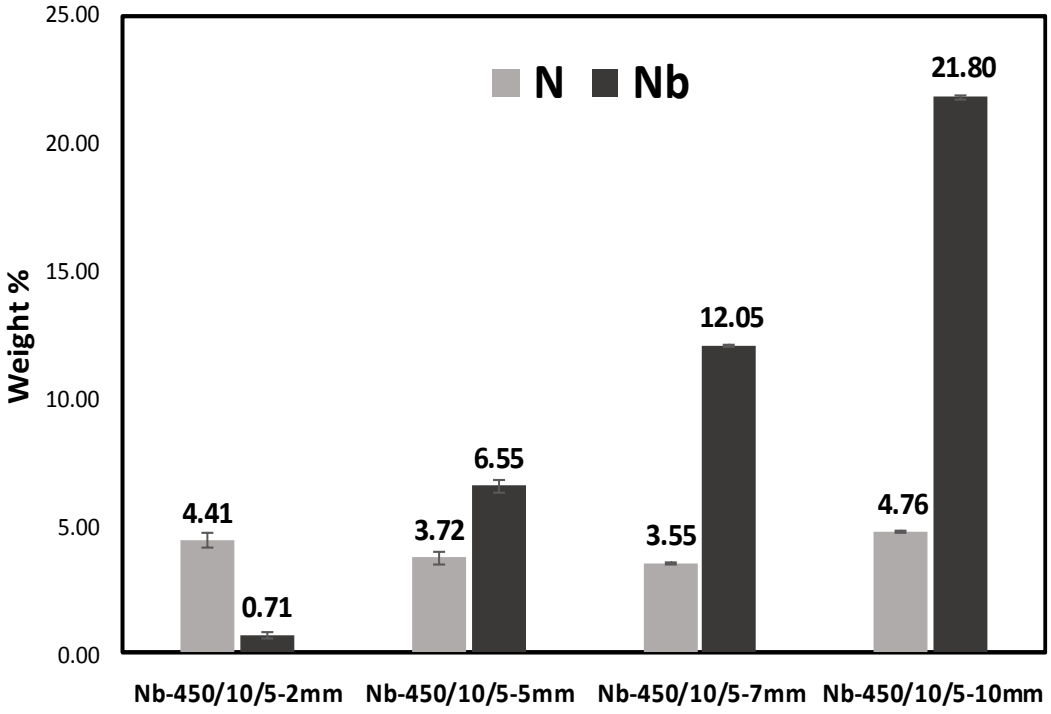

Figure 4.4.11 Surface composition of ASPA(N&Nb) treated sample with different length of alloying wires

The surface chemical compositions were measured by EDS and the content of nitrogen and niobium are shown in Figure 4.4.11. The niobium content increases monotonically with the length of Nb wire. While the nitrogen content decreases from 4.41 wt% for Nb-450/10/5-2mm to 3.55 wt% for Nb-450/10/5-7mm sample before it increases to 4.76 wt% for the Nb-450/10/5-10mm sample. The decrease of nitrogen

content against the wire length is related to the diluting effect of niobium. In fact, the weight percentage ratio between N and Fe increased monotonously from 0.072 to 0.104 when increasing Nb wire length from 2 to 10 mm, which demonstrates that the absolute nitrogen content also increases with the Nb wire length.

4.4.2.2 Phase and layer structures of treated surfaces

XRD

The XRD patterns of the samples treated using different lengths of Nb alloying wires are shown in Figure 4.4.12. The Nb-450/10/5-2mm sample shows a set of peaks in the position of 2θ = 40.6° and 46.3°, which are characteristic peaks of S-phase. For Nb-450/10/5-5mm sample, the peaks of austenite substrate can be clearly observed, and in addition, broaden peaks attached to the corresponding austenite peaks are also found. Although the shift of peaks is less than that of the Nb-450/10/5-2mm sample, these peaks are also from the S-phase and more evidence will be shown latter.

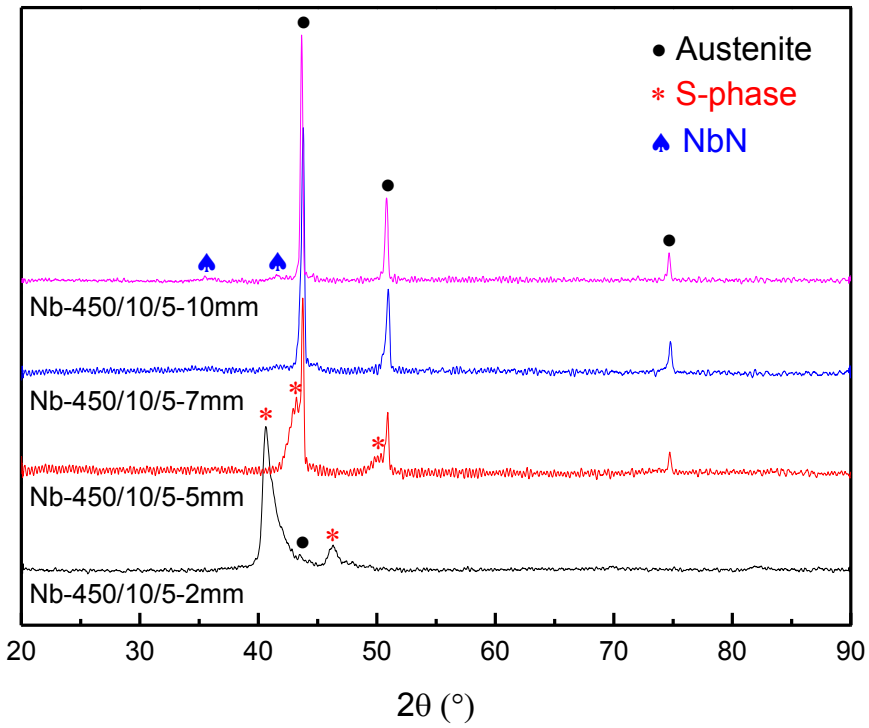

Figure 4.4.12 XRD patterns of samples treated using different wire length

For Nb-450/10/5-7mm and Nb-450/10/5-10mm samples, strong peaks of austenite substrate can be found. In addition, very weak peaks of NbN can be found in the position around 2θ = 36° and 42° from the pattern of the Nb-450/10/5-10mm sample.

GDS

The element depth profiles of nitrogen and niobium are shown in Figure 4.4.13. The nitrogen depth profile of ASPN treated 316 stainless steel under the same nitriding conditions is also plotted in Figure 4.4.13(a) as reference. The Nb-450/10/5-2mm and Nb-450/10/5-5mm samples show a relatively high nitrogen content and this high nitrogen region extends to the depth of about 8 and 4.5 μm, respectively. This high nitrogen content implies the formation of S-phase in these two samples. The difference in nitrogen content in the S-phase layer results in the different degrees of angle shifting of the XRD peaks (Figure 4.4.12). In contrast, the Nb-450/10/5-7mm and Nb-450/10/5-10mm samples show lower nitrogen profiles than that of the Nb-450/10/5-2mm and Nb-450/10/5-5mm samples and the depth is less than 1 μm. It is also interesting to find that the nitrogen content of all the ASPA(N&Nb) treated samples is lower than that of the ASPN treated samples and the depth of high nitrogen region is also thinner than the ASPN treated sample.

Unlike the 1 mm Nb ASPA(N&Nb) treated samples reported in Section 4.4.1, the depth profiles of niobium can be measured by GDS, which implies the increased niobium content when longer (> 1 mm) niobium wires were applied. It can be seen from Figure 4.4.13 (b) that both the content and the depth of niobium increase with the increase of Nb wire length.

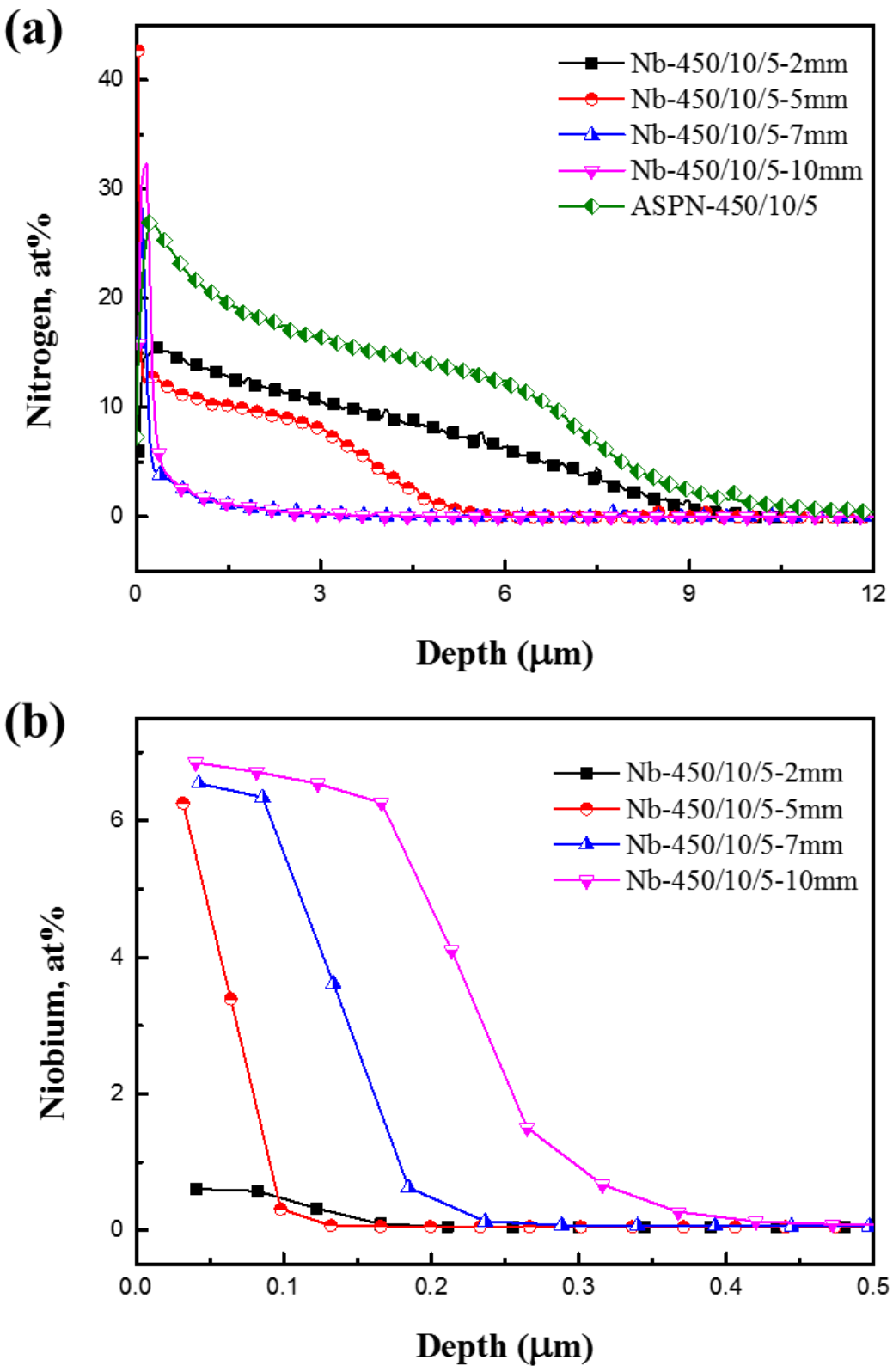

Figure 4.4.13 Element depth profile of ASPA(N&Nb) treated sample with different length of alloying wires (a) nitrogen (b) niobium

SEM

The cross sectional SEM images of the ASPA(N&Nb) treated samples as a function of the Nb wire length used are shown in Figure 4.4.14. Featureless layers with different thicknesses can be observed from Nb-450/10/5-2mm (Figure 4.4.14 (a)) and Nb-450/10/5-5mm (Figure 4.4.14 (c)) samples, but no such layer could be seen in Nb-450/10/5-7mm (Figure 4.4.14 (e)) and Nb-450/10/5-10mm (Figure 4.4.14 (g)) samples. Based on the XRD and GDS results above, the feature-less layer can be identify as S-phase. From the high magnification cross-sectional SEM images of the very surface (Figure 4.4.14 (b) (d) (f) (h)), except Nb-450/10/5-2mm sample, deposition layers with different thicknesses can be seen from other samples. From the results of GDS niobium profiles, these deposition layers should be rich in niobium. However, only Nb-450/10/5-10mm samples exhibit niobium related XRD peaks (NbN), because the deposition layers on the other samples are too thin to be detected by XRD.

Combining the results of SEM, XRD and GDS, the layer structure of the ASPA(N&Nb) treated surfaces can be identified, which is an niobium nitride deposition layer on the top of an S-phase layer. The thickness of the S-phase and deposition layer of each sample are compared in Figure 4.4.15. It can be seen that the thickness of the S-phase layer decreases with the increase of the Nb wire length; in contrary, the thickness of the deposition layer increases with the increase of the Nb wire length. The S-phase layer thickness of Nb-450/10/5-2mm sample (8.4 μm) is thinner than the normal ASPN treated sample under the same nitriding conditions (10.5 μm).

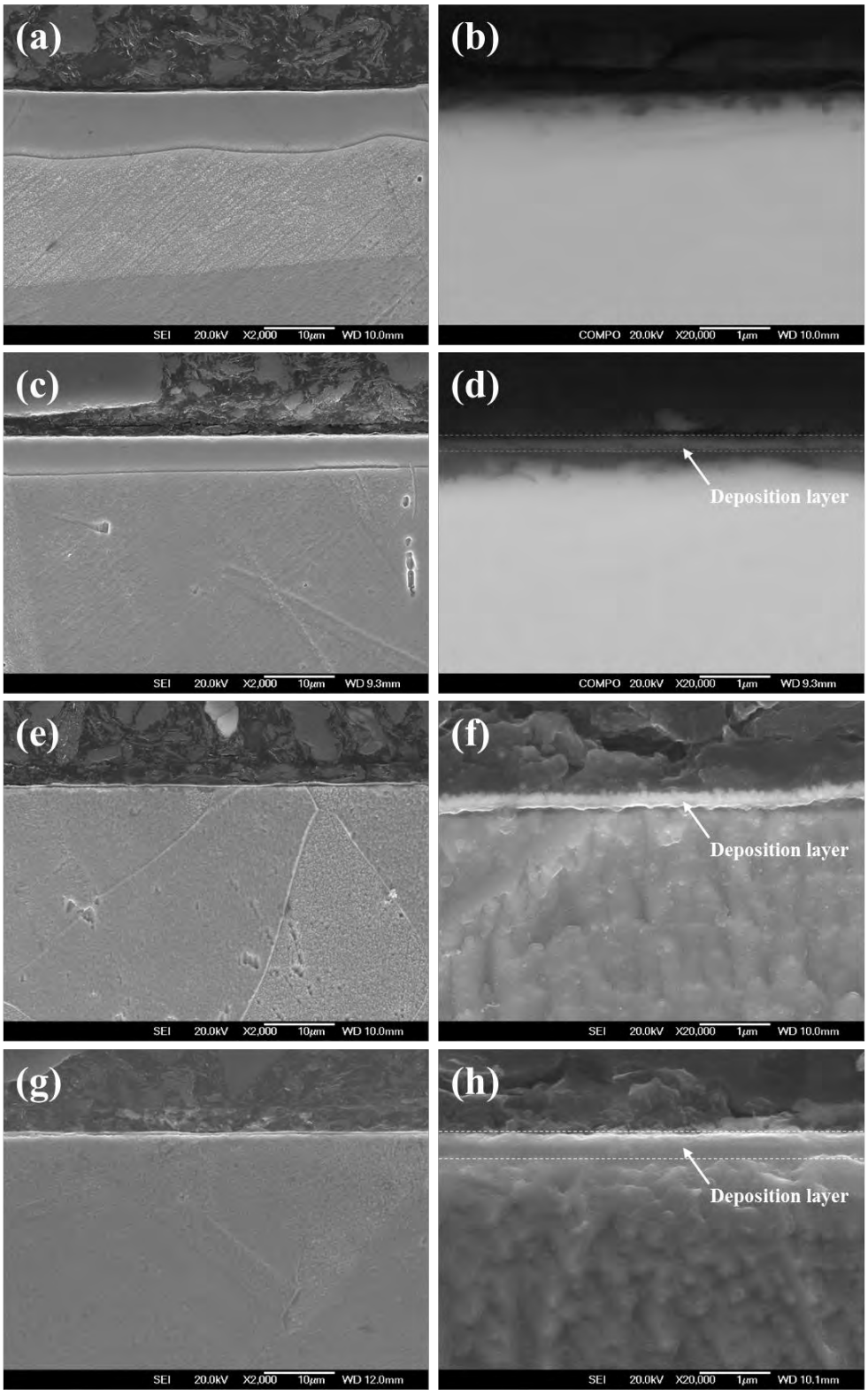

Figure 4.4.14 Low and high magnification cross sectional images of ASPA(N&Nb) treated sample with different length of alloying wires

(a) (b) Nb-450/10/5-2mm (c) (d) Nb-450/10/5-5mm

(e) (f) Nb-450/10/5-7mm (g) (h) Nb-450/10/5-10mm

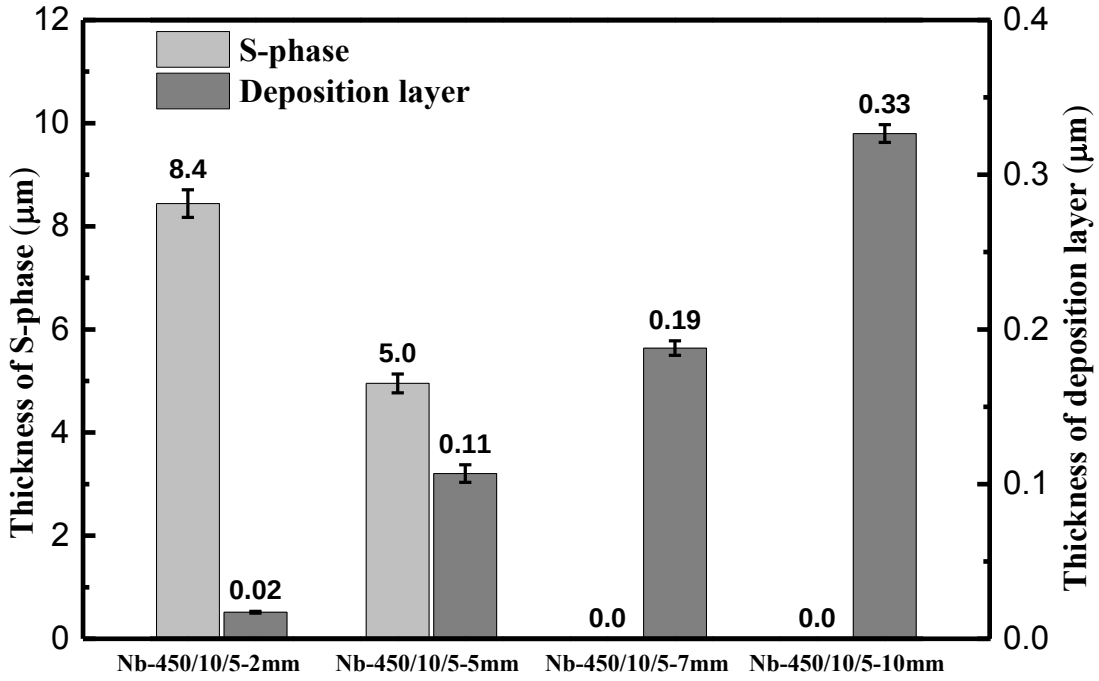

Figure 4.4.15 Thickness of S-phase and deposition layer of ASPA(N&Nb) treated sample with different length of niobium wires

4.4.2.3 Surface conductivity

The ICR values of ASPA(N&Nb) treated sample with different lengths of Nb alloying wires are presented in Figure 4.4.16 with the results of ASPN treated samples for comparison. A reduction of ICR about one order of magnitude can be seen after the ASPA(N&Nb) treatments. It is of interest to note that the Nb-450/10/5-5mm sample exhibits the lowest ICR value among all the ASP treated samples. Nb-450/10/5-7mm and Nb-450/10/5-10mm samples show a higher ICR value than Nb-450/10/5-2mm and Nb-450/10/5-5mm samples but still lower than that of the ASPN treated sample.

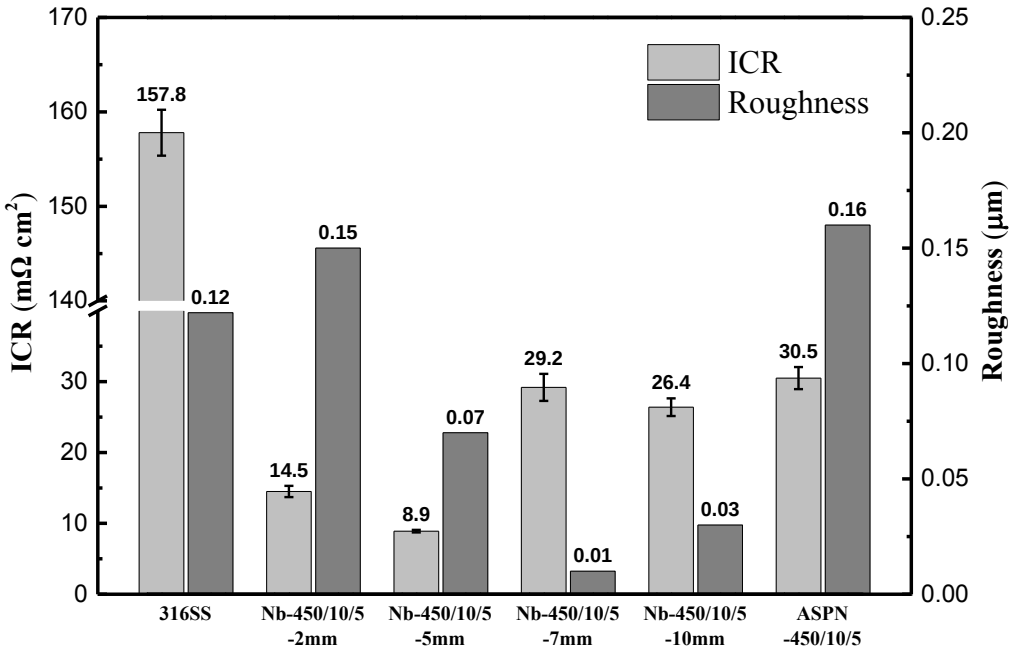

Figure 4.4.16 ICR values of ASPA(N&Nb) treated sample with different length of alloying wires

4.4.2.4 Corrosion performance

The potentio-dynamic polarisation curves of ASPA(N&Nb) treated sample with different lengths of Nb alloying wires are plotted in Figure 4.4.17 (a) with the curves of polished 316 stainless steel and ASPN treated sample for reference and the part near the corrosion potential is enlarged and shown in Figure 4.4.17 (b). The results of corrosion potential and corrosion current density of all the samples are summarised in Table 4.7.

All the ASPA(N&Nb) treated samples exhibit a more positive corrosion potential and lower corrosion current density than that of the untreated and normal ASPN treated samples. In terms of the passive current density, the ASPA(N&Nb) treated samples is much lower than that of the normal ASPN sample and very close to that the untreated 316 stainless steel. In general, the passive current density decreases with the increase of niobium wire length.

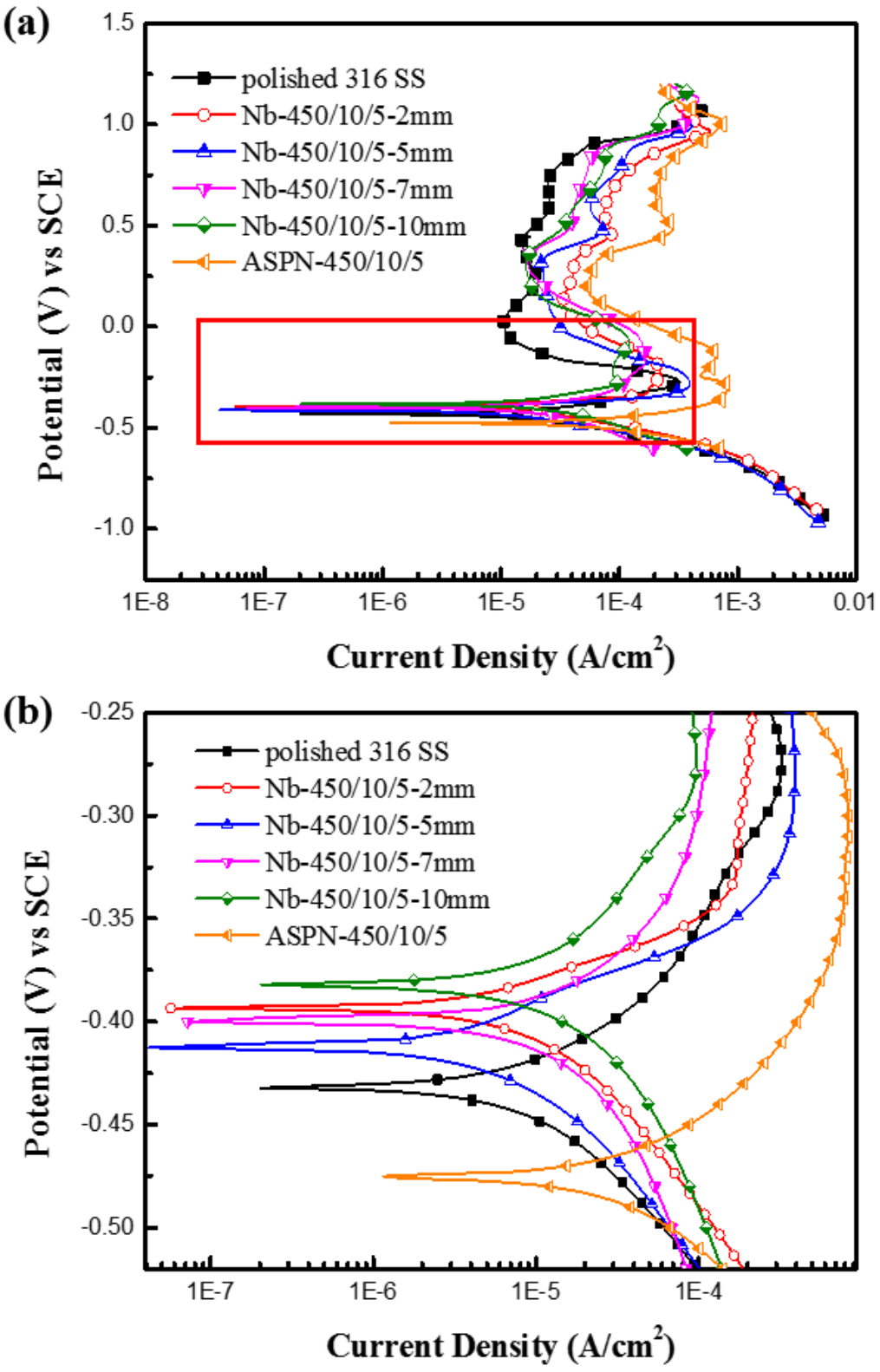

Figure 4.4.17 Potentio-dynamic polarisation curves of ASPA(N&Nb) treated samples with different length of niobium wires

Table 4.7 corrosion potential and corrosion current density of ASPA(N&Nb) treated samples with different length of alloying wires

Sample	E(mV) vs SCE	Current density ($\mu A/cm^2$)
Polished 316 SS	-432	26.587
Nb-450/10/5-2mm	-380	11.905
Nb-450/10/5-5mm	-412	9.028
Nb-450/10/5-7mm	-400	11.290
Nb-450/10/5-10mm	-382	11.468
ASPN-450/10/5	-476	74.750

Judging from the results of surface conductivity and corrosion performance, the 5 mm Nb ASPA(N&Nb) treated sample exhibits the best surface performance in terms of the lowest surface conductivity and similar corrosion behaviour with other ASPA(N&Nb) treated samples. Hence, the Nb alloying wire of 5 mm in length was selected for further investigation.

4.4.3 Influence of applied bias

In order to investigate the influence of applied bias on the ASPA(N&Nb) treated surface, three different applied bias levels were chosen as 5 % (Nb-450/10/5-5mm), 10 % (Nb-450/10/10-5mm) and 15 % (Nb-450/10/15-5mm). Other treatment parameters were set as following: temperature 450 ℃ , length of Nb alloying wire 5 mm, treatment duration 10 h and pressure 0.75 mbar. Although the treatment parameter of the 5 % applied bias sample in this section is identical to that of the sample in the previous section, the treatment was repeated to minimize the influence of experimental error.

4.4.3.1 Surface morphology

The surface morphology of the ASPA(N&Nb) treated samples as a function of the applied bias are shown in Figure 4.4.18. It can be seen that the surface morphology is

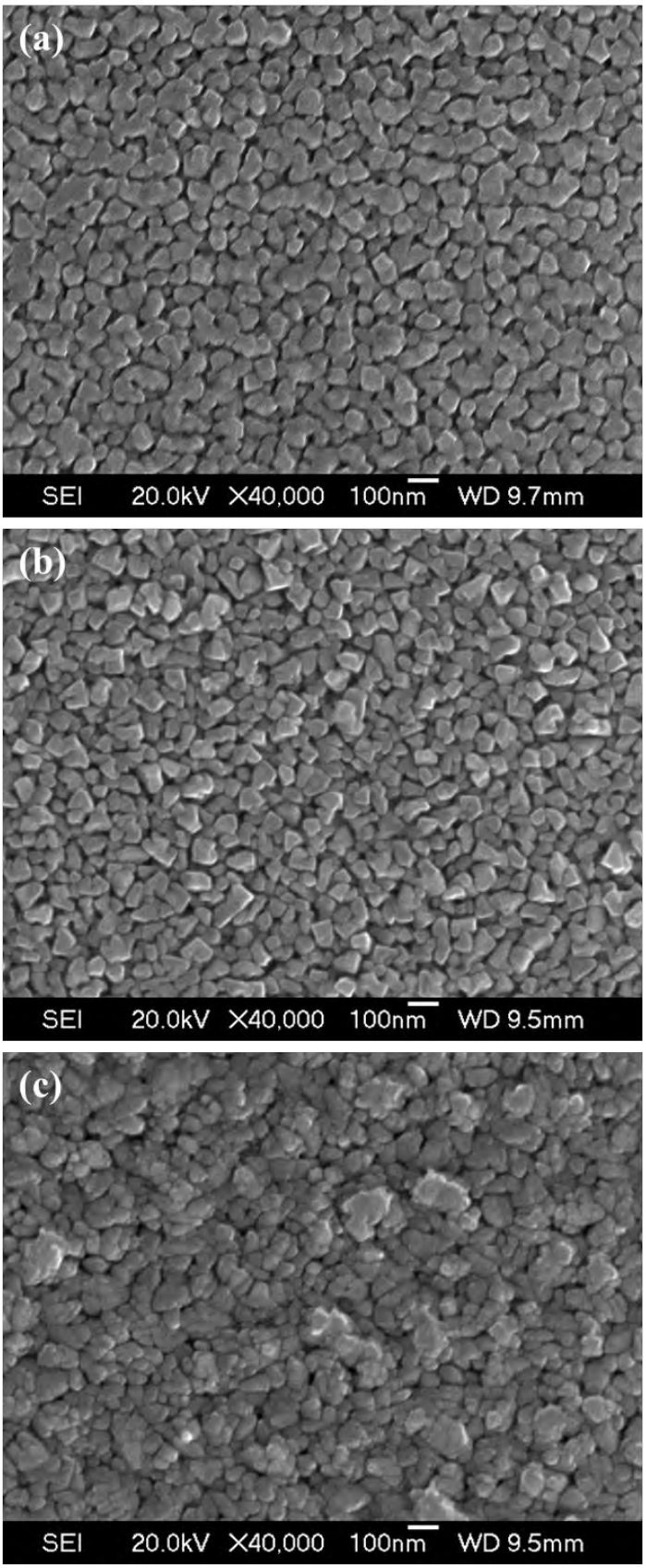

Figure 4.4.18 Surface morphology of the ASPA(N&Nb) treated samples under different applied bias: (a) Nb-450/10/5-5mm (b) Nb-450/10/10-5mm (c) Nb-450/10/15-5mm

similar for the samples treated under 5 % (Figure 4.4.18 (a)) and 10 % bias (Figure 4.4.18 (b)), consisting of particles with a similar size of about 100 nm. However, when increasing the applied bias to 15 %, the size of surface particles becomes uneven with very small particles and relatively larger clusters but the density of the surface layer is improved with reduced number of pinholes. The surface composition of the three ASPA(N&Nb) treated samples under different biases is shown in Figure 4.4.19. It can be seen that the content of the alloyed Nb increases markedly with the increase of the applied bias; in contrary, the content of Cr, Ni and Fe decreases with the increase of the bias used. The light elements were measured using XPS and the results are reported latter.

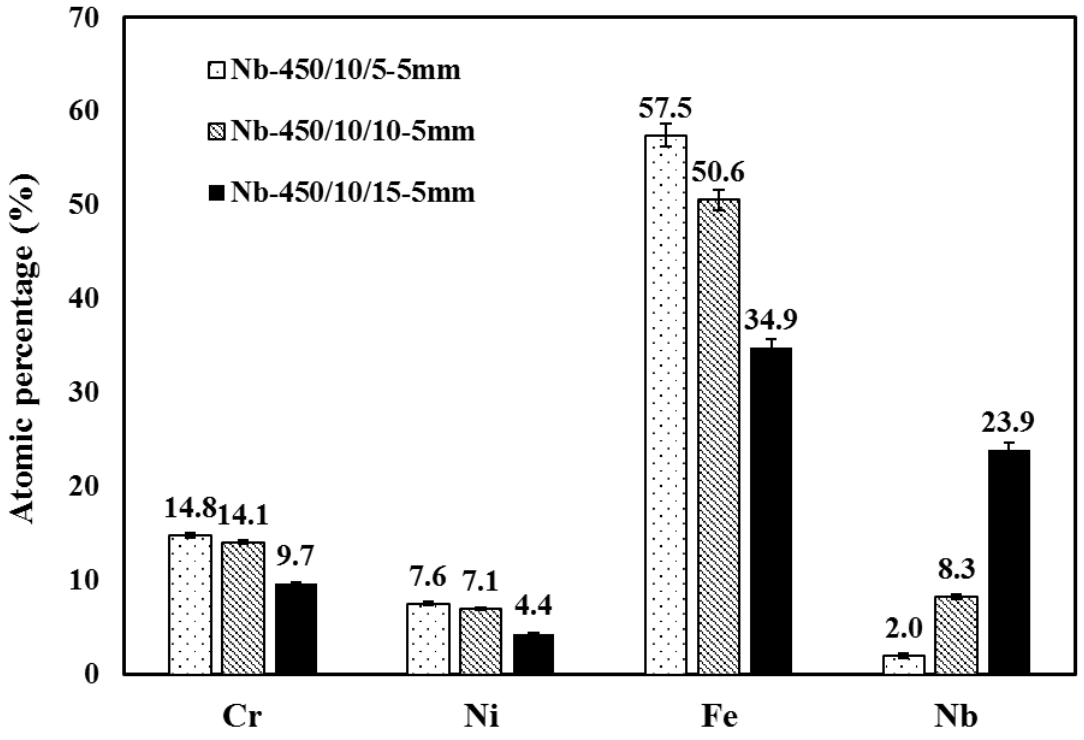

Figure 4.4.19 Surface composition of ASPA(N&Nb) treated samples under different applied bias

4.4.3.2 Phase constitute and layer structures of the treated surfaces

XRD

The XRD patterns of ASPA(N+Nb) treated samples under different applied biases are plotted in Figure 4.4.20. It can be seen from the XRD pattern of the Nb-450/10/5-5mm sample that an additional set of peaks can be observed apart from the peaks from the austenitic stainless steel substrate. Comparing with the peaks of the substrate, those additional peaks move to a lower angle and are broaden to some extent. These are characteristic features of the S-phase formed in low-temperature plasma nitrided austenitic stainless steel [231]. However, comparing with the XRD pattern in Section 4.2.3, the angle shifting of the Nb-450/10/5-5mm sample is relatively smaller, which

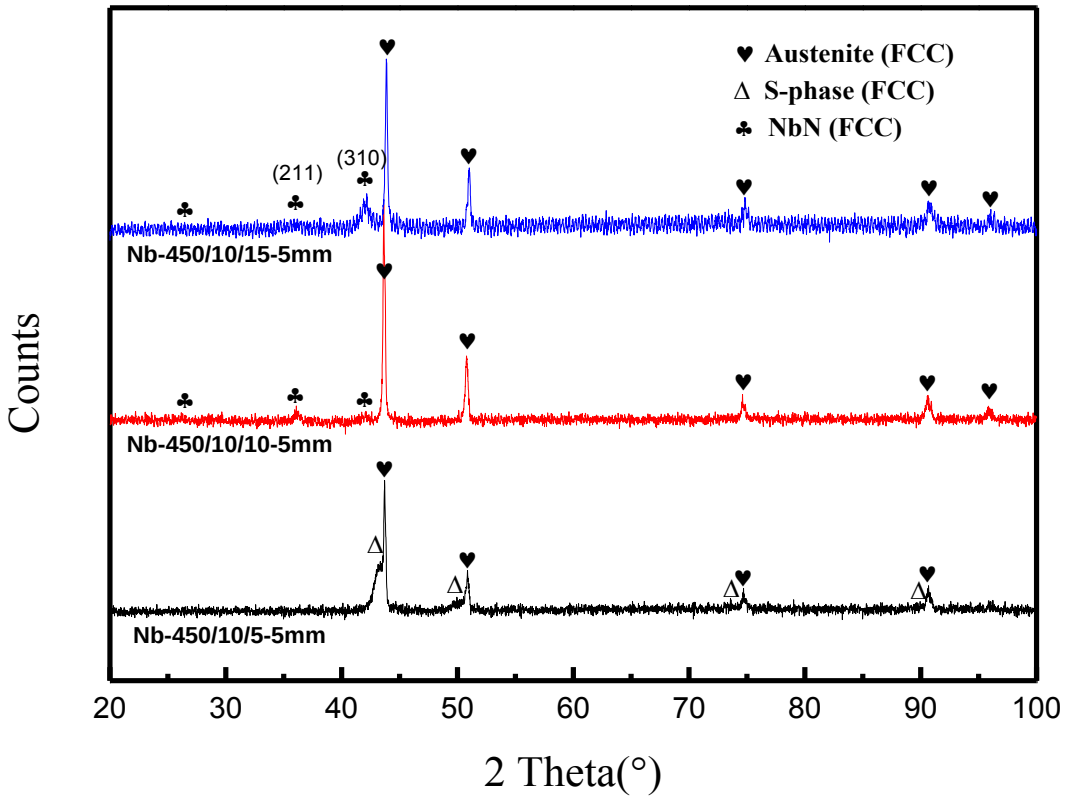

Figure 4.4.20 XRD of ASPA(N&Nb) treated samples under different applied bias

will be discussed latter. No peaks of niobium nitride could be found from the XRD pattern of Nb-450/10/5-5mm sample. For the samples treated by 10 % and 15 % biases, apart from the peaks of the substrate, the peaks of NbN can also be detected. The dominated orientation of NbN changed from (211) for the Nb-450/10/10-5mm sample to (310) for the Nb-450/10/15-5mm sample. No peaks of S-phase can be found from the XRD patterns of these two samples.

XPS

The chemical states of Fe, Nb and N in ASPA(N+Nb) treated samples were analysed by XPS and the spectra obtained after argon ions sputtering for 60 s, 180 s, 360 s and 540 s are shown in Figure 4.4.21. The XPS spectra of N 1s and Nb 3d for Nb-450/10/5-5mm are given in Figure 4.4.21 (a) and (b). It can be seen from these XPS spectra that the binding energy of N 1s and Nb 3d does not change significantly with the sputtering time (or depth). The binding energy of N 1s was determined to be 397 eV, which is lower than that of the standard binding energy of N 1s (398.4 eV). The binding energy of Nb 3d was identified as 203.4 eV and 206.3 eV, which are higher than the corresponding standard binding energy of metallic niobium (202.3 eV and 205 eV). Such deviation from the standard binding energy of Nb 3d and N 1s implies the formation of niobium nitride. The obtained values of the binding energy of Nb 3d and N 1s are in good agreement with the results reported by other researchers (Nb 3d: 203.3 eV and 206.2 eV; N 1s: 397.1 eV) [232]. Other conclusions can also be drawn from Figure 4.4.21 (a) and (b) are that the intensity of the Nb 3d and N 1s spectra decrease with the increase of the sputtering time, and that the peak of Nb 3d totally vanishes but N 1s still remains after sputtering for 540 s. Taking the relatively low sputtering rate of XPS into account, the niobium nitride layer formed on the Nb-450/10/5-5mm sample must

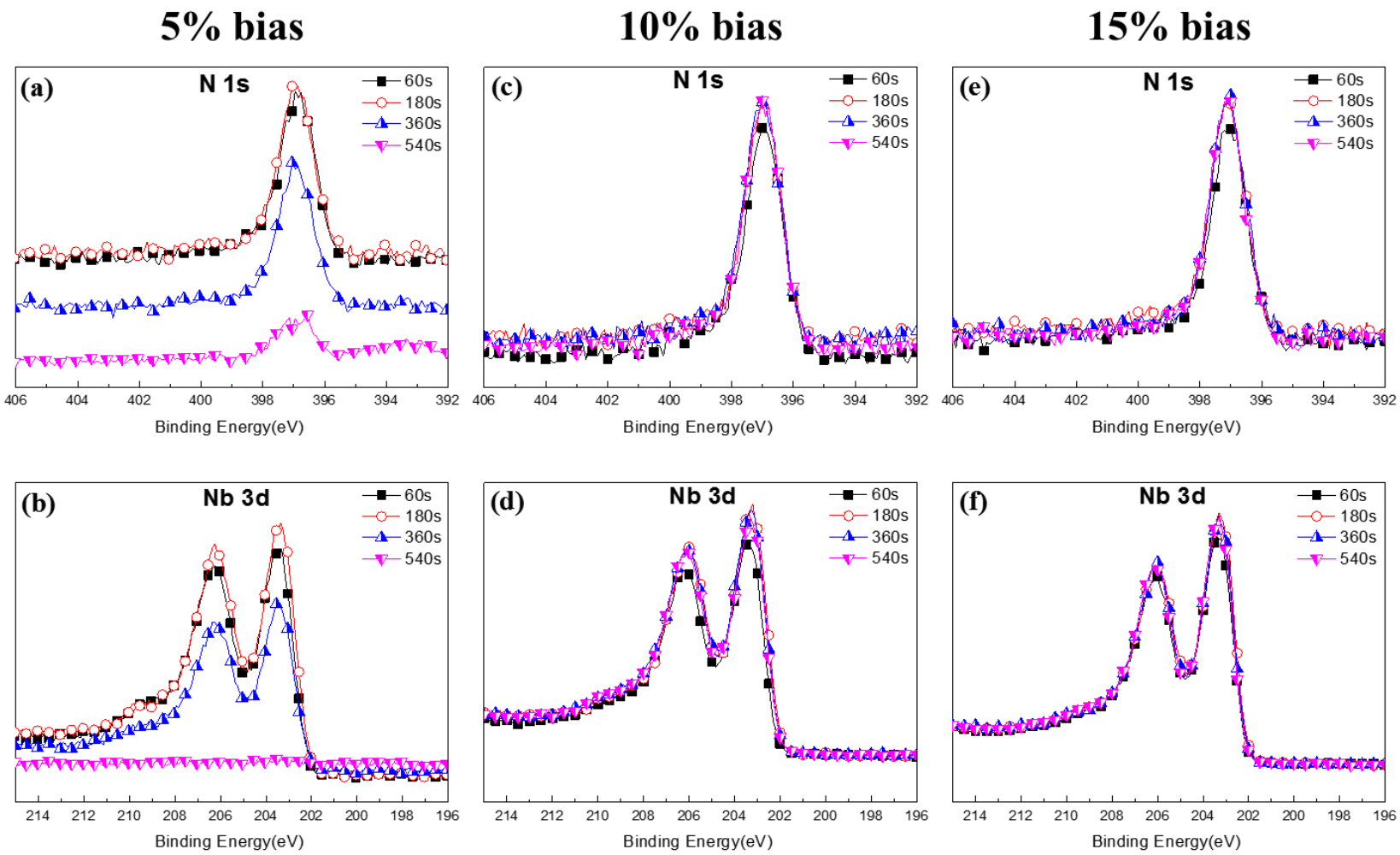

Figure 4.4.21 The N1s and Nb3d XPS spectra of ASPA(N&Nb) treated samples under different applied bias

(a) (b) Nb-450/10/5-5mm (c) (d) Nb-450/10/10-5mm (e) (f) Nb-450/10/15-5mm

be very thin. Such a thin niobium nitride layer is difficult to be detected by XRD, resulting in the absence of niobium nitride peaks in the XRD pattern of the Nb-450/10/5-5mm sample (Figure 4.4.20).

The N and Nb spectra of Nb-450/10/10-5mm and Nb-450/10/15-5mm samples are given in Figure 4.4.21 (c)&(d), and (e)&(f), respectively. It can be seen that the N and Nb spectra obtained from the Nb-450/10/10-5mm sample are the same as those from the Nb-450/10/15-5mm sample. Except for the spectra of 60s-sputtered surface, other spectra of 180 s, 360 s and 540 s sputtered surfaces exhibit almost identical profiles. The binding energy of N 1s and Nb 3d identified from the surfaces of the Nb-450/10/10-5mm and the Nb-450/10/15-5mm samples is the same as that determined from the Nb-450/10/5-5mm sample. Therefore, the XPS results of the Nb-450/10/10-5mm and the Nb-450/10/15-5mm samples also indicate the formation of a niobium nitride layer on the surface of these two samples and the niobium nitride layers are thicker than that formed on the surface of the Nb-450/10/5-5mm sample as these spectra are independent of the sputtering time up to 540 s.

The spectra obtained after argon irons sputtering for 360 s were quantitatively analysed and the results are summarised in Figure 4.4.22. It can be cleanly seen that the atomic percentage of N and Nb increases with the increase of the applied bias. The identification of NbN peaks from the XRD patterns (Figure 4.4.20) is in agreement with the quantification analysis of the XPS spectra. The atomic ratio of N/Nb for the 15%Bs sample is around 1.23, which is close to that of the NbN (1.00).

Apart from niobium and nitrogen, iron was also detected by XPS. The binding energy of iron was determined to be 706.7 eV and the peak position does not change after different sputtering durations (Figure 4.4.23). By the reference [233] [234], the

binding energy values of Fe 2p indicates that the iron exists as an γ-Fe_4N in the modified surface, and the intensity of the Fe 2p peaks reduces gradually with the increase of the applied bias. A very low amount of chromium and nickel was found by XPS as well and identified as nitride. Most probably, they were sputtered from the stainless steel cage, reacted with active nitrogen in the plasma and then deposited onto the plasma treated surfaces.

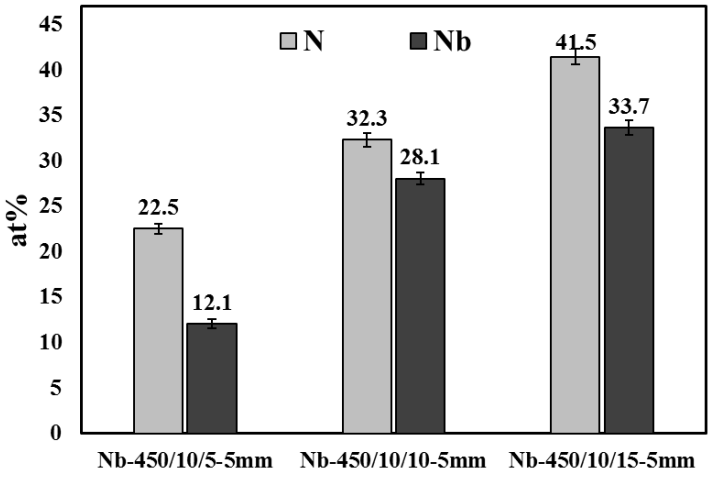

Figure 4.4.22 The quantification analysis of XPS spectra of ASPA(N&Nb) treated samples under different applied bias

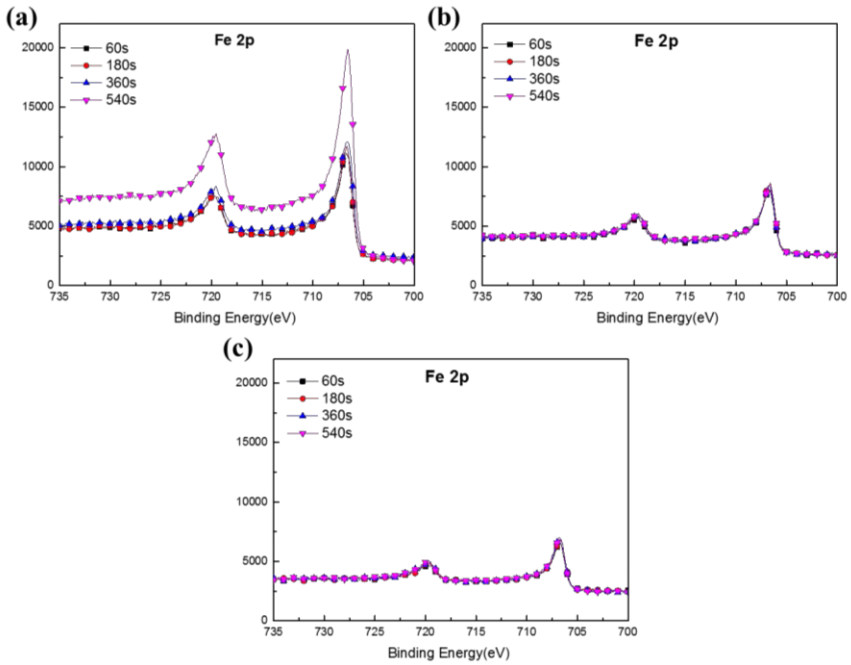

Figure 4.4.23 The Fe 2p XPS spectra of ASPA(N+Nb) samples

(a) Nb-450/10/5-5mm (b) Nb-450/10/10-5mm (c) Nb-450/10/15-5mm

SEM

The cross-sectional images of ASPA(N+Nb) treated samples are shown in Figure 4.4.24. The samples observed under low magnification were etched, while the samples observed under high magnification were not etched to optimally reveal the microstructural features.

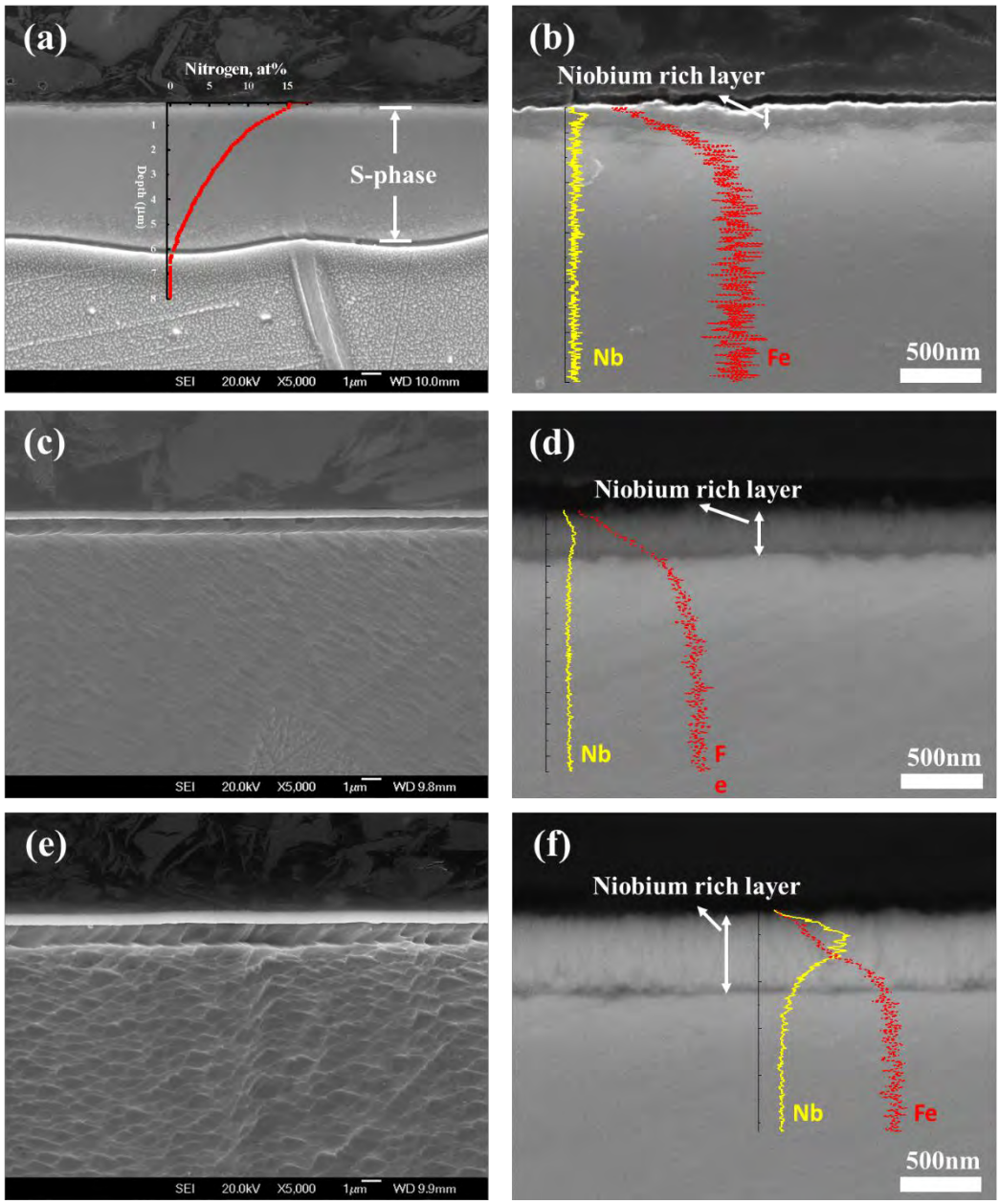

Figure 4.4.24 Low and high magnification of cross-sectional images of ASPA(N&Nb) samples under different applied bias

(a) (b) Nb-450/10/5-5mm (c) (d) Nb-450/10/10-5mm (e) (f) Nb-450/10/15-5mm

For the sample treated with 5% bias (i.e. Nb-450/10/5-5mm), a featureless layer can be found on the top of the surface in low magnification SEM image (Figure 4.4.24 (a)). The GDS nitrogen depth profile as inlet in Figure 4.4.24 (a) indicates the high nitrogen content in this featureless layer with a maximum content of 15 at% at the surface. Referring to the typical features observed in the previous sections and taking the XRD results (Figure 4.4.20) into account, this layer can be identified as S-phase. Under high magnification, a dark thin layer was observed on the top of the S-phase layer formed on Nb-450/10/5-5mm sample (Figure 4.4.24 (b)). The EDS element line-scan indicates that this thin dark layer is rich in niobium.

For Nb-450/10/10-5mm and Nb-450/10/15-5mm samples, a white dense layer can be found on the top of the severely corroded substrate and no S-phase layer can be found from those two samples (Figure 4.4.24 (c)&(e)). In addition, a groove can be observed between the white layer and the substrate. The formation of the groove is most probably due to the huge difference in corrosion resistance between the top Nb nitride layer and the substrate to the etchant, which is similar with the discussion in Section 4.2.1.

From the high magnification backscattered electron (BSE) images of the Nb-450/10/10-5mm and Nb-450/10/15-5mm samples (Figure 4.4.24 (d)&(f)), it can be seen that the top layer is dense and columnar structured, which is in agreement with the surface morphology observed under SEM (Figure 4.4.18). The EDS line-scan also proves that the surface layer contains a high level of niobium. Taking the results of SEM, XPS and XRD into account, the niobium rich layer on the surface could be deduced as a NbN dominant layer.

The thickness of the niobium nitride layer and the S-phase layer is compared in Figure 4.4.25 as a function of the bias used. It can be seen that the thickness of the niobium nitride layer increases with the increase of the applied bias.

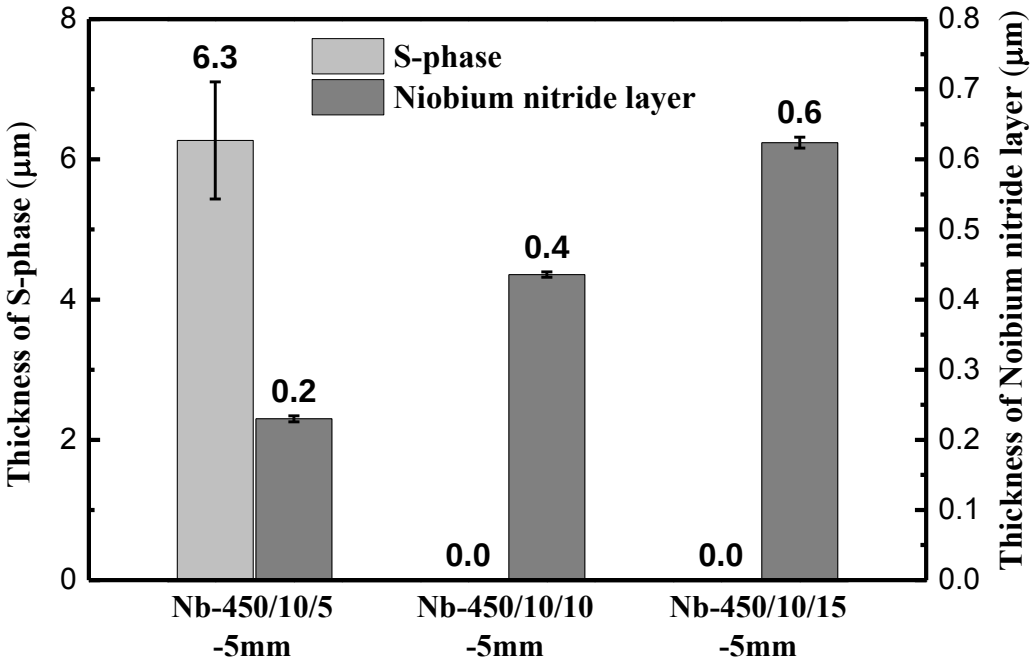

Figure 4.4.25 The thickness of S-phase and deposition layer of ASPA(N&Nb) treated samples under different applied bias

4.4.3.3 Surface conductivity

The results of ICR measurements are shown in Figure 4.4.26. Compared with the ICR results of ASPN samples reported before (Section 4.2.6), the ICR value is further reduced to below the DoE target (10 mΩ cm^2) by simultaneously introducing N and Nb (i.e. ASPA(N&Nb)). The Nb-450/10/5-5mm sample possesses the lowest average ICR value, which might be related to the duplex surface structure with a combination of S-phase and the Nb containing deposition layer.

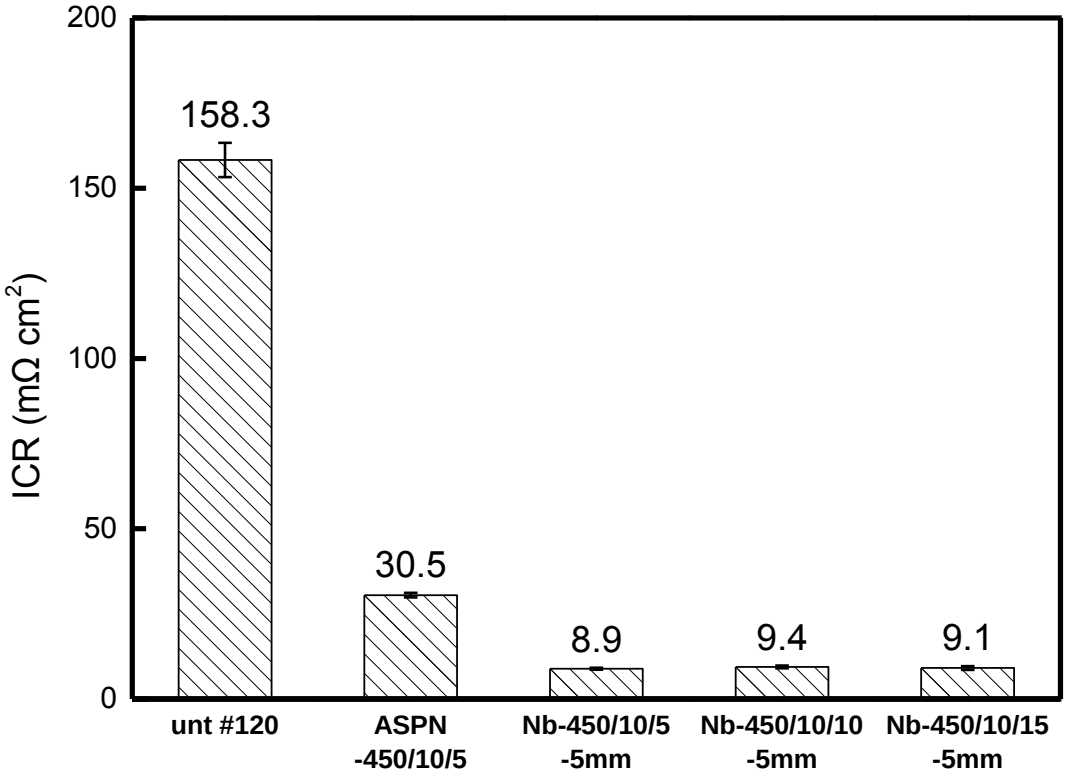

Figure 4.4.26 The ICR values of ASPA(N&Nb) samples under different applied bias

4.4.3.4 Corrosion behaviour

The potentiodynamic polarisation curves of ASPA(N&Nb) treated samples are drawn in Figure 4.4.27. It can be seen clearly that the ASPA(N&Nb) treated samples exhibit more positive corrosion potential than that of the untreated sample and typical ASPN treated sample. The passive current density of the ASPA(N&Nb) treated samples is higher than that of the untreated sample but lower than that of the ASPN treated sample. It is also noted that in general the passive current density reduces with the increase of the applied bias. In particular, the Nb-450/10/15-5mm sample shows the lowest passive current density, almost one order of magnitude lower than that of the normal ASPN treated sample.

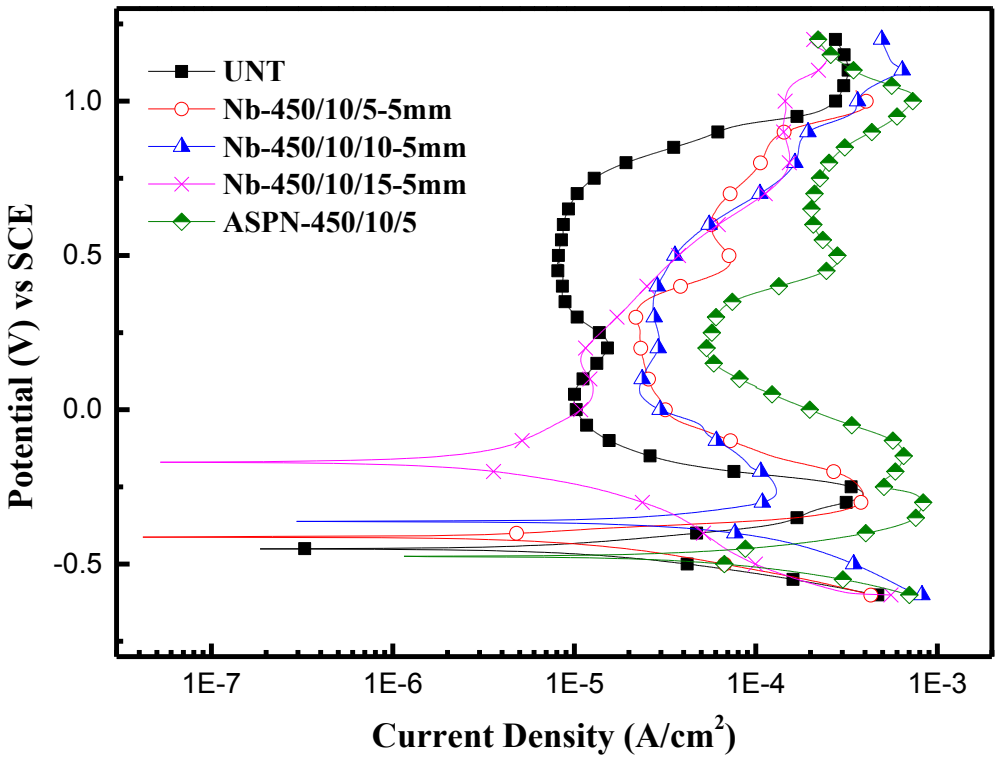

Figure 4.4.27 Potentiodynamic polarisation curves of ASPA(N&Nb) treated samples under different applied bias

Table 4.8 Corrosion potential and corrosion current density of ASPA(N&Nb) treated samples under different applied bias

Sample	E_{corr} (mV) vs SCE	I_{corr} (μA/cm^2)
Untreated	-450	10.3
Nb-450/10/5-5mm	-412	9.0
Nb-450/10/10-5mm	-362	20.8
Nb-450/10/15-5mm	-170	3.2
ASPN-450/10/5	-476	74.8

The corrosion potential (E_{corr}) and corrosion current density (I_{corr}) of all samples were quantitatively calculated from the potentiodynamic polarisation curves and the results are summarised in Table 4.8. It can be seen that the corrosion potential of ASPA(N&Nb) treated sample increases with the applied bias and much higher than

that of the untreated and the normal ASPN treated sample. It is obvious from Table 4.8 that the Nb-450/10/15-5mm sample exhibits the best corrosion resistance in terms of the highest corrosion potential and the lowest corrosion current density.

Due to the best potentiodynamic performance, the Nb-450/10/15-5mm sample was selected for further potentiostatic polarisation tests. The potentiostatic polarisation results of the untreated sample and the Nb-450/10/15-5mm sample under -0.1 V and 0.6 V are plotted in Figure 4.4.28. When -0.1 V (vs SCE) is applied (Figure 4.4.28 (a)), the current density of the 15%Bs sample gradually increases during the whole test duration; however, the current density of the untreated sample increases in the first 2000 s and then decreases in the rest of the test. Accordingly, the current density of the Nb-450/10/15-5mm sample is lower than that of the untreated sample within the first 8500 s, and then becomes larger in the rest of the test. When 0.6 V (vs SCE) is applied (Figure 4.4.28 (b)), the Nb-450/10/15-5mm sample stabilises more quickly than the untreated sample. However, after stabilisation the current density of the Nb-450/10/15-5mm sample (2.21×10^{-6} A/cm^2) is slightly higher than that (1.63×10^{-6} A/cm^2) of the untreated sample. Both of the two samples show higher current density than that of the DoE target (1×10^{-6} A/cm^2). It is worth noting that after 11000 s, the current density of the untreated sample fluctuates strongly, which indicates the failure of the passive protect film. In contrary, the current density of the Nb-450/10/15-5mm sample is stable during the entire test, which indicates the better long-term stability of the niobium nitride layer.

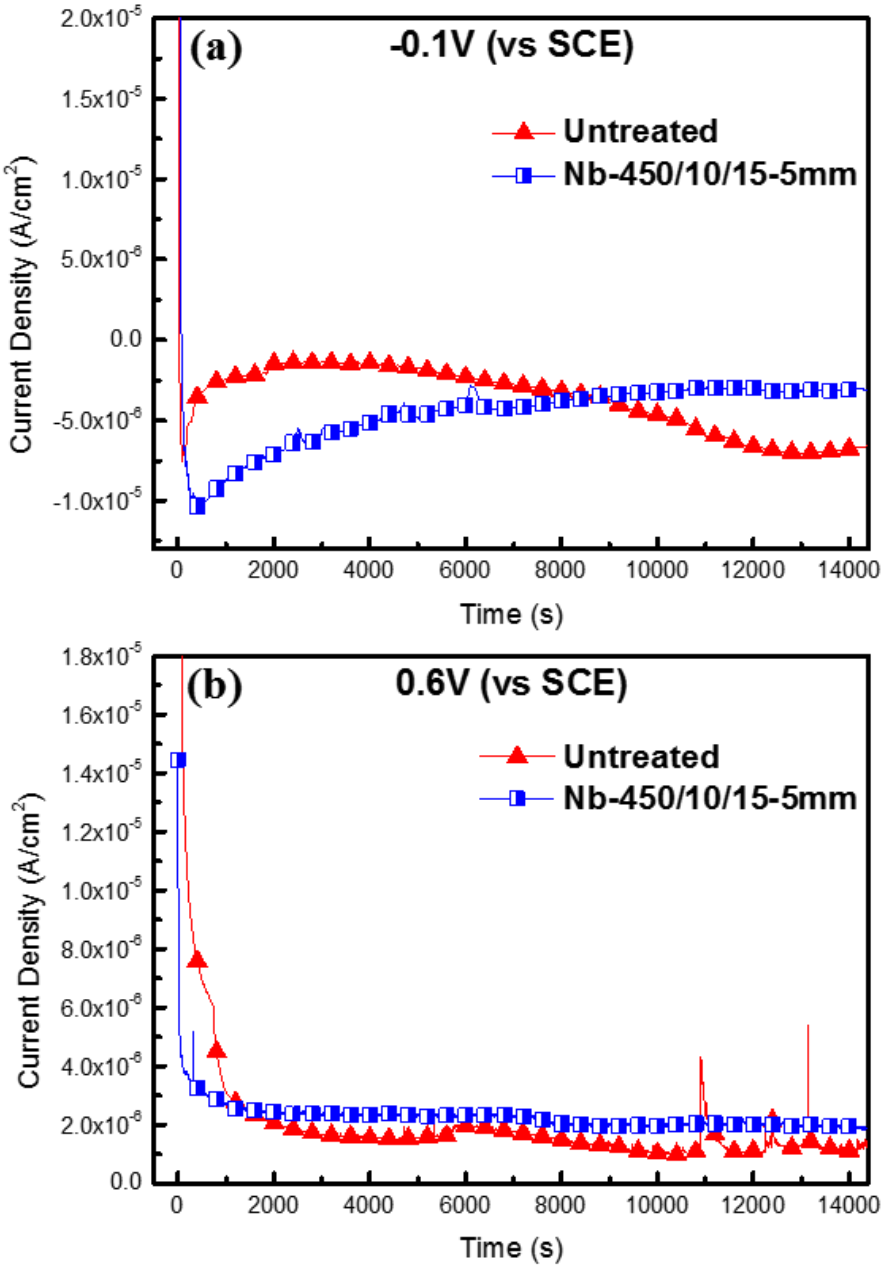

Figure 4.4.28 The potentiostatic polarisation results of the untreated sample and the Nb-450/10/15-5mm sample

(a) under -0.1 V (b) under 0.6 V

From the results reported in this section and previous section, the multi-layer structured samples, consisting of an S-phase layer and a niobium rich deposition layer, exhibits improved surface properties in terms of high interfacial conductivity and good corrosion resistance. A further increase in the thickness of niobium rich deposition layer might offer even better corrosion resistance. In view of this, a

specially designed multi-step ASPA(N&Nb) process with varying applied bias was conducted, and the results are reported in the following section.

4.4.4 Multi-step process with varying bias

Multi-step active screen plasma co-alloying (with nitrogen and niobium) processes were conducted to produce an S-phase sublayer and thick niobium rich surface deposition layer, simultaneously. From the results discussed in Section 4.4.3, an S-phase sublayer can be formed when the applied bias is lower than 5 %. So in the first step, 0 % and 5 % was selected as the applied bias; in the second step, 10 % applied bias was chosen. Two treatments with different parameter settings were conducted: (1) 0 % bias for 10 h plus 10 % bias for 10 h (Nb-450/20/(0+10)-5mm); (2) 5 % bias for 10 h plus 10 % bias for 10 h (Nb-450/20/(5+10)-5mm). The other parameters were set as follows: temperature 450 ℃, length of alloying wire 5 mm and pressure 0.75 mbar.

4.4.4.1 Surface morphology and composition

The low magnification surface morphology SEM images of the ASPA(N&Nb) treated sample with varying bias are shown in Figure 4.4.29 (a) (c). It can be seen that the Nb-450/20/(0+10)-5mm sample does not show any surface relief. In contrast, some surface relief (denoted by arrows) can be found from the surface of Nb-450/20/(5+10)-5mm sample. The difference in surface morphology can be confirmed by the surface roughness of these two samples. The surface roughness of Nb-450/20/(0+10)-5mm sample is 0.01 μm, which is similar to that of the polished surface. While for Nb-450/20/(5+10)-5mm sample, its roughness is around 0.11 μm, which is much larger than that of the former. The high magnification surface morphology SEM images of the ASPA(N&Nb) treated sample with varying bias are also shown in Figure 4.4.29 (b) (d). The surface of both samples is covered by fine

particles. Judging from the bright contrast, those white contrasted particles (denoted by arrows) outstand from the surfaces. Difference is difficult to find from the comparison of the surface morphology of these two samples.

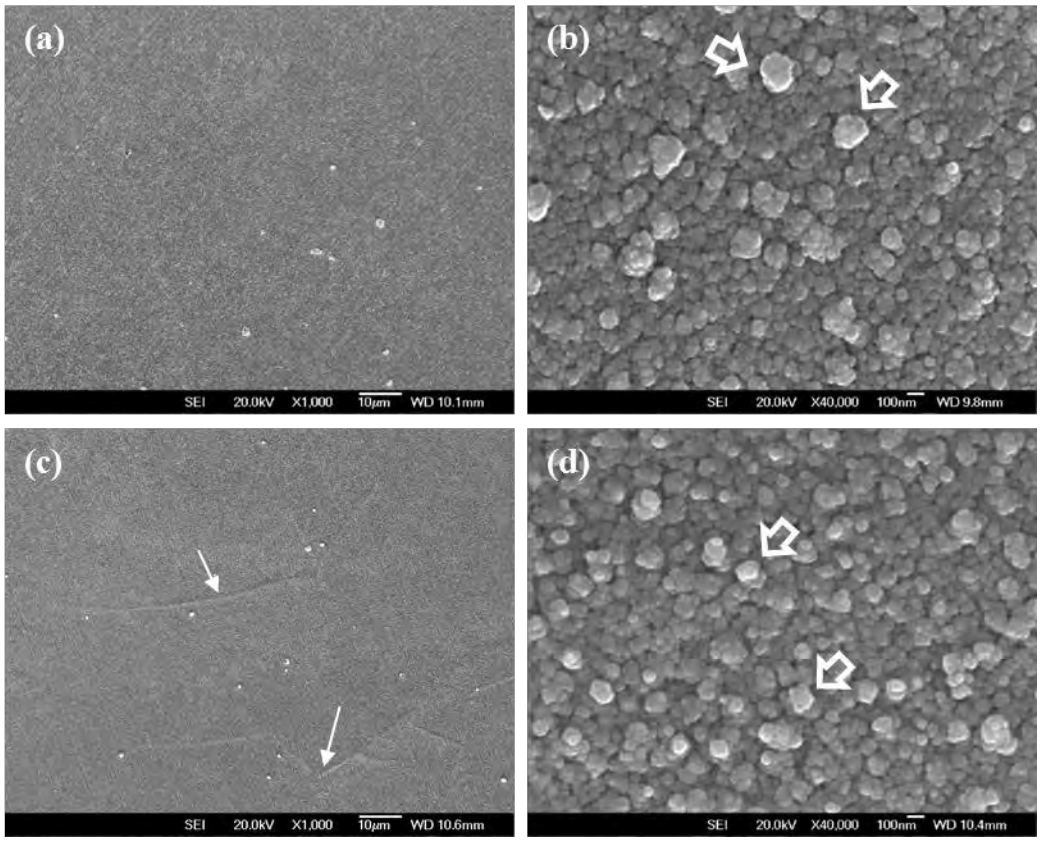

Figure 4.4.29 Low magnification surface morphology SEM images of ASPA(N&Nb) treated sample with varying bias

(a) (b) Nb-450/20/(0+10)-5mm (c) (d) Nb-450/20/(5+10)-5mm

The surface composition of the ASPA(N&Nb) treated sample with varying bias is presented in Figure 4.4.30. The nitrogen and niobium contents of Nb-450/20/(5+10)-5mm samples are obviously higher than that of the Nb-450/20/(0+10)-5mm sample, due to the higher applied bias in the first step for the former than for the latter.

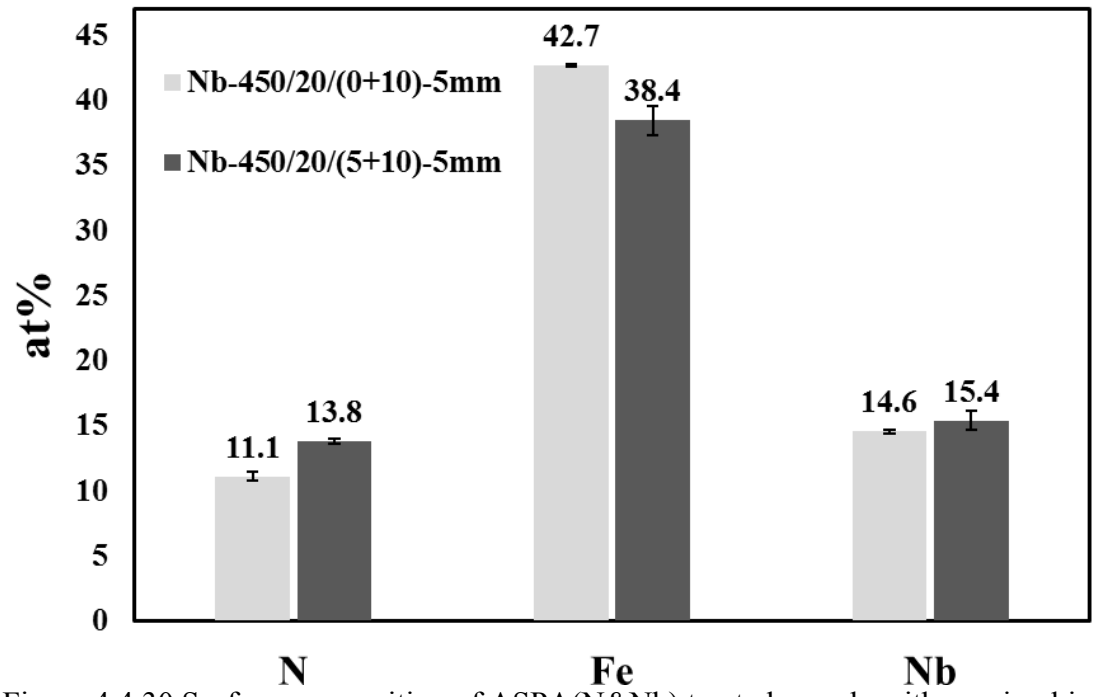

Figure 4.4.30 Surface composition of ASPA(N&Nb) treated sample with varying bias

4.4.4.2 Phase and layer structures of treated surfaces

XRD

The XRD patterns of Nb-450/20/(0+10)-5mm and Nb-450/20/(5+10)-5mm samples are plotted in Figure 4.4.31. The peaks of austenitic substrate can be clearly found from the two samples. A few weak peaks could be indexed to niobium nitride (NbN) from both samples. For Nb-450/20/(0+10)-5mm sample, no peaks of S-phase can be identified. In contrast, apart from the peaks of substrate, another set of broaden peaks, locating in the lower angle than the corresponding peaks of substrate, can be seen from the pattern of Nb-450/20/(5+10)-5mm. These new peaks possess the characteristic of S-phase.

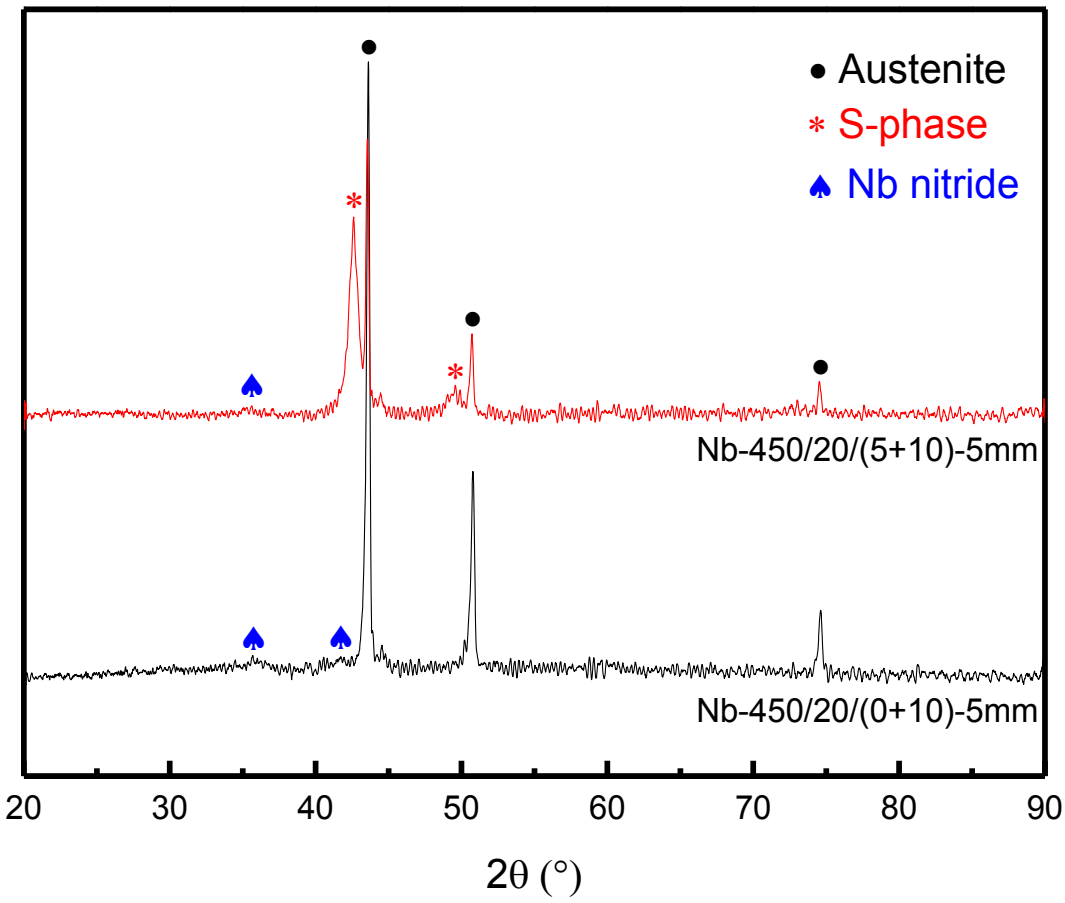

Figure 4.4.31 XRD patterns of ASPA(N&Nb) treated sample with varying bias

GDS

The GDS element depth profiles shown in Figure 4.4.32 show that the surface region (< 500 nm) of those two samples are rich in nitrogen and niobium. However, some differences are observed from the depth profiles of N and Nb for these two samples. The Nb-450/20(0+10)-5mm sample contains slightly higher N content but lower Nb content in the near surface region (about 250 nm from the surface) as compared with Nb-450/20(5+10)-5mm sample. In addition, more N diffused into the subsurface layer in the latter than in the former. The relatively high nitrogen content implies the formation of S-phase layer on the surface of the Nb-450/20(5+10)-5mm treated sample.

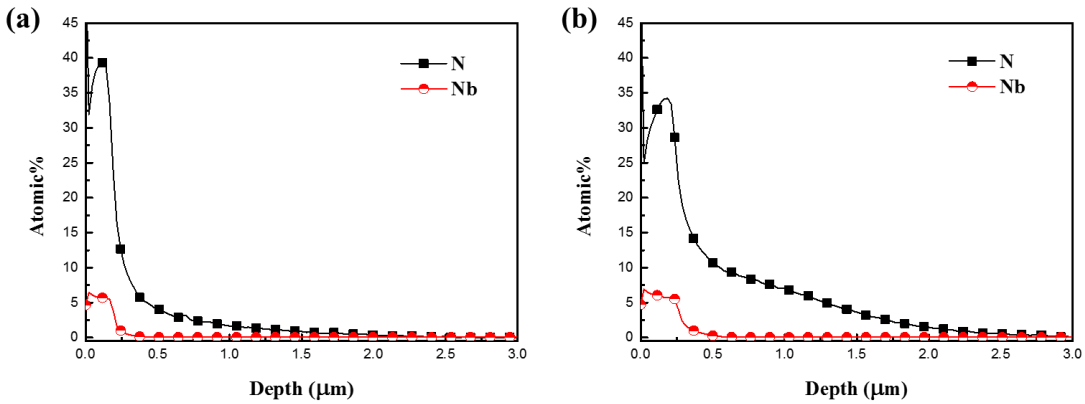

Figure 4.4.32 Nitrogen and niobium depth profiles of ASPA(N&Nb) treated sample with varying bias: (a) 0%+10% (b) 5%+10%

SEM

The cross-sectional SEM images of ASPA(N&Nb) treated sample with varying bias are shown in Figure 4.4.33. For Nb-450/20/(0+10)-5mm sample, only a deposition layer, having a columnar structure, is found, and the thickness of this layer is in agreement with the niobium and nitrogen rich layer shown in the GDS results (Figure 4.4.32). In conjunction with the XRD results shown in Fig.4, this layer could be identified as NbN. For the Nb-450/20/(5+10)-5mm sample, a duplex layer structure can be observed, consisting a surface deposition layer and a featureless layer underneath. Based on the XRD and GDS results, these two layers can be identified as NbN and S-phase, respectively. The thickness of the NbN deposition layer and S-phase layer of those two samples are listed in Figure 4.4.34.

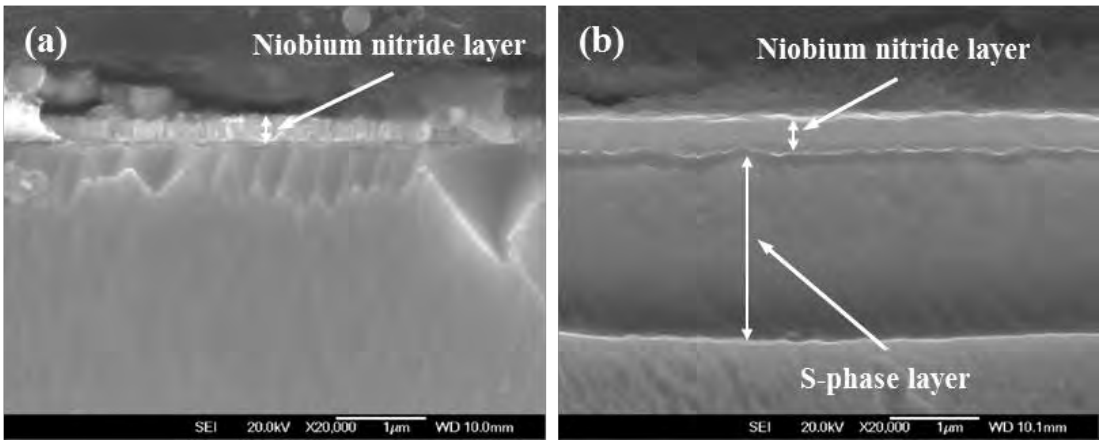

Figure 4.4.33 Cross-sectional SEM images of ASPA(N&Nb) treated sample with varying bias (a) Nb-450/20/(0+10)-5mm (b) Nb-450/20/(5+10)-5mm

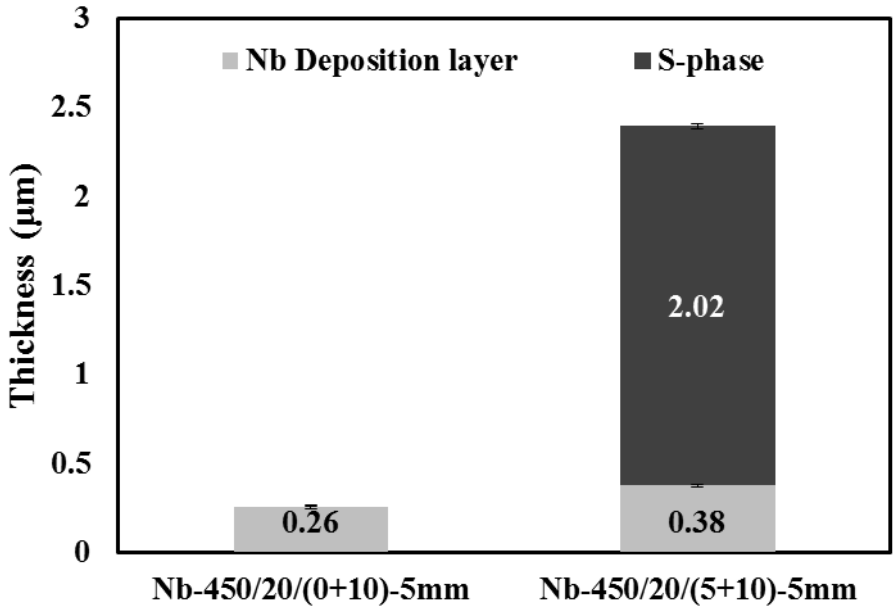

Figure 4.4.34 S-phase and deposition layer thickness of ASPA(N&Nb) treated sample with varying bias

4.4.4.3 Surface conductivity

The ICR values of ASPA(N&Nb) treated sample with varying bias are given in Figure 4.4.35. The ICR values for both samples are lower than 10 mΩ cm^2. The 5%+10% (i.e. Nb-450/20/(5+10)-5mm) sample which possesses a duplex layer

structure, exhibits a lower ICR value than the 0%+10% (i.e. Nb-450/20/(0+10)-5mm) sample which has a single layer structure. The finding strongly confirms that the duplex layer structure shows better surface conductivity.

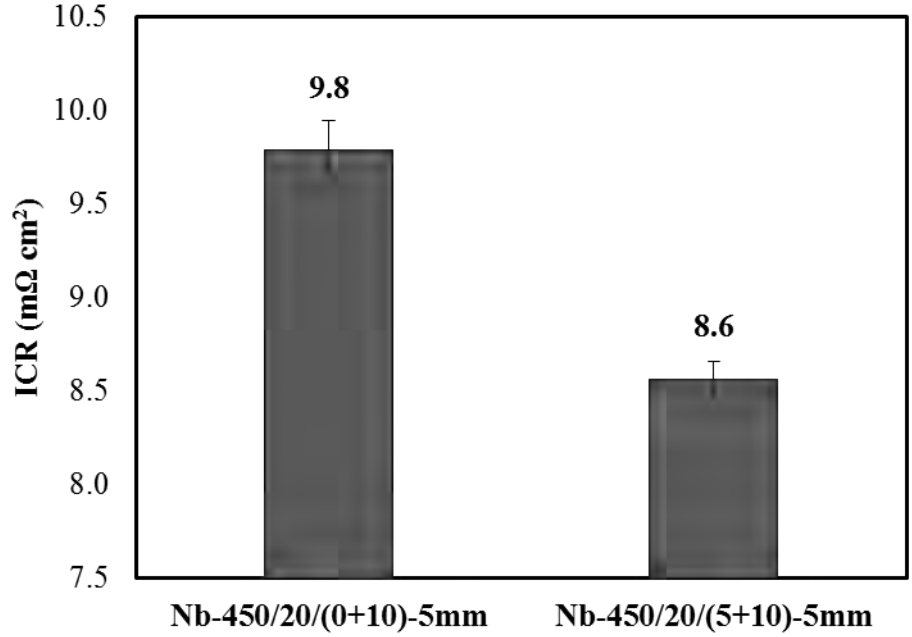

Figure 4.4.35 ICR values of ASPA(N&Nb) treated sample with varying bias

4.4.4.4 Corrosion behaviour

The potentio-dynamic polarisation curves of ASPA(N&Nb) treated sample with varying bias are plotted in Figure 4.4.36, and the corresponding corrosion potential and corrosion current density are listed in Table 4.9.

It can be seen that the corrosion potential of these two treated samples are more positive than that of the untreated sample, and the corrosion current density of the treated samples is lower than that of the untreated sample. Although, the passive current density of the treated samples is still higher than but close to that of the untreated sample.

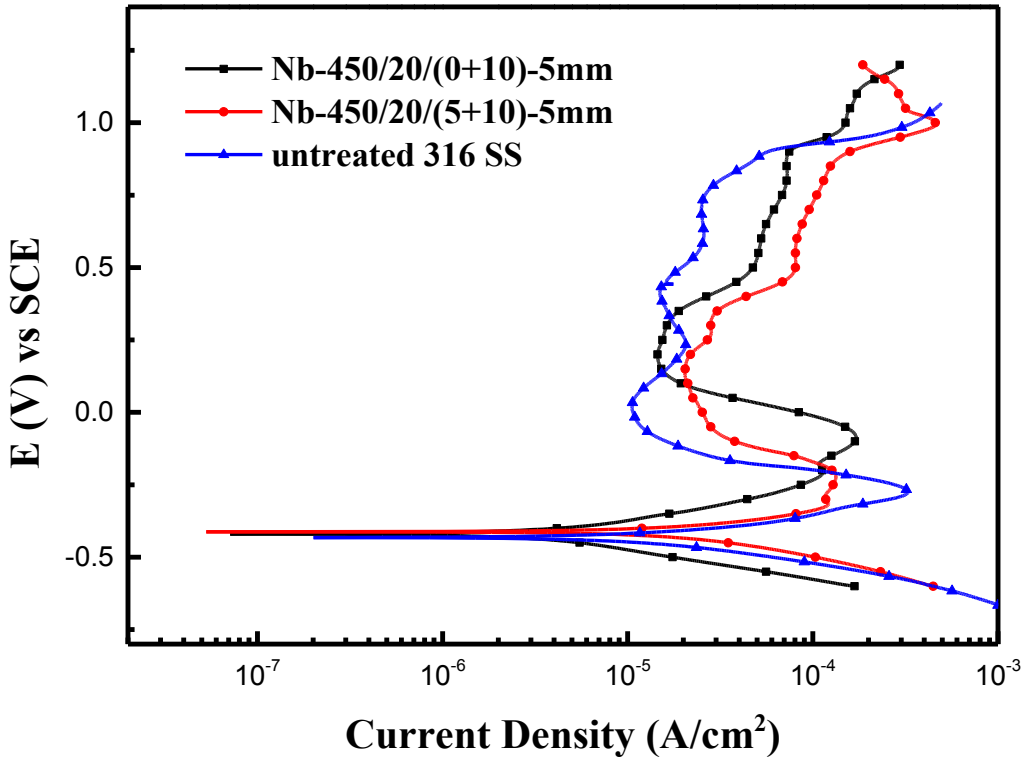

Figure 4.4.36 Potentio-dynamic polarisation curves of ASPA(N&Nb) treated sample with varying bias

Table 4.9 Corrosion potential and corrosion current density of ASPA(N&Nb) treated sample with varying bias

sample	corrosion potential (mV) vs SCE	corrosion current density (μA/cm^2)
UNT	-432	26.587
Nb-450/20/(0+10)-5mm	-420	6.94
Nb-450/20/(5+10)-5mm	-428	12.6

4.4.5 Summary

In this section, the influence of different parameters of ASPA(N&Nb) treatments on the treated surfaces have been investigated. From the systematic analyses, some of the parameters have been optimised, such as the treatment duration (10 h) and length of Nb alloying wires (5 mm). In terms of the applied bias, low bias produced a duplex

layer structure consisting of a niobium nitride surface layer and an S-phase layer, while high bias produced only a relatively thick niobium nitride layer.

By means of ASPA(N&Nb) treatments, niobium element can be introduced into the treated surface mainly as niobium nitride. The results of corrosion tests and ICR measurement have revealed that the introduction of niobium could improve the corrosion resistance, reduce the passive corrosion current density (comparing with previous active screen plasma alloying treatments) and significantly reduce the ICR value. However, from the potentio-static tests, the performance of the ASPA(N&Nb) treated samples is still worse than that of the untreated sample. Hence, the element should be replaced by other alloying elements to further improve the corrosion behaviour and/or surface electrical conductivity.

4.5 ASP co-alloying with N and Pt (ASPA(N&Pt))

As reported in the previous section, active screen plasma co-alloying with nitrogen and niobium (ASPA(N&Nb)) treatments have shown promising results in modifying the surface of 316 stainless steel for bipolar plates. The interfacial contact resistance (ICR) values of the ASPA(N&Nb) treated samples are reduced significantly to below the DoE target of 10 mΩ cm^2; the results of potentiodynamic tests indicate that the corrosion potential of ASPA(N&Nb) treated samples is more positive and the current density is lower than that of the untreated 316 stainless steel and the normal ASPN treated samples. However, the current density of the ASPA(N&Nb) treated sample in potentiostatic tests is still higher than that of the untreated sample and also higher than the target of DoE (1×10^{-6} A/cm^2). To this end, platinum was selected as an alloying element to further improve the corrosion behaviour of the 316 SS surface.

Based on the optimisation results of previous sections, only the influence of applied bias was investigated for active screen plasma co-alloying with both nitrogen and platinum (ASPA(N&Pt)).

4.5.1 The influence of applied bias

The applied bias was selected as 5 % (Pt-450/10/5), 10 % (Pt-450/10/10) and 15 % (Pt-450/10/15), and the rest treatment parameters were set as follows: temperature 450 ℃ , length of alloying wire 5 mm, treatment duration 10 h and pressure 0.75 mbar.

4.5.1.1 Surface morphology and composition

The surface morphologies of the ASPA(N&Pt) samples treated under different applied biases are shown in Figure 4.5.1. All the three treated surfaces are completely

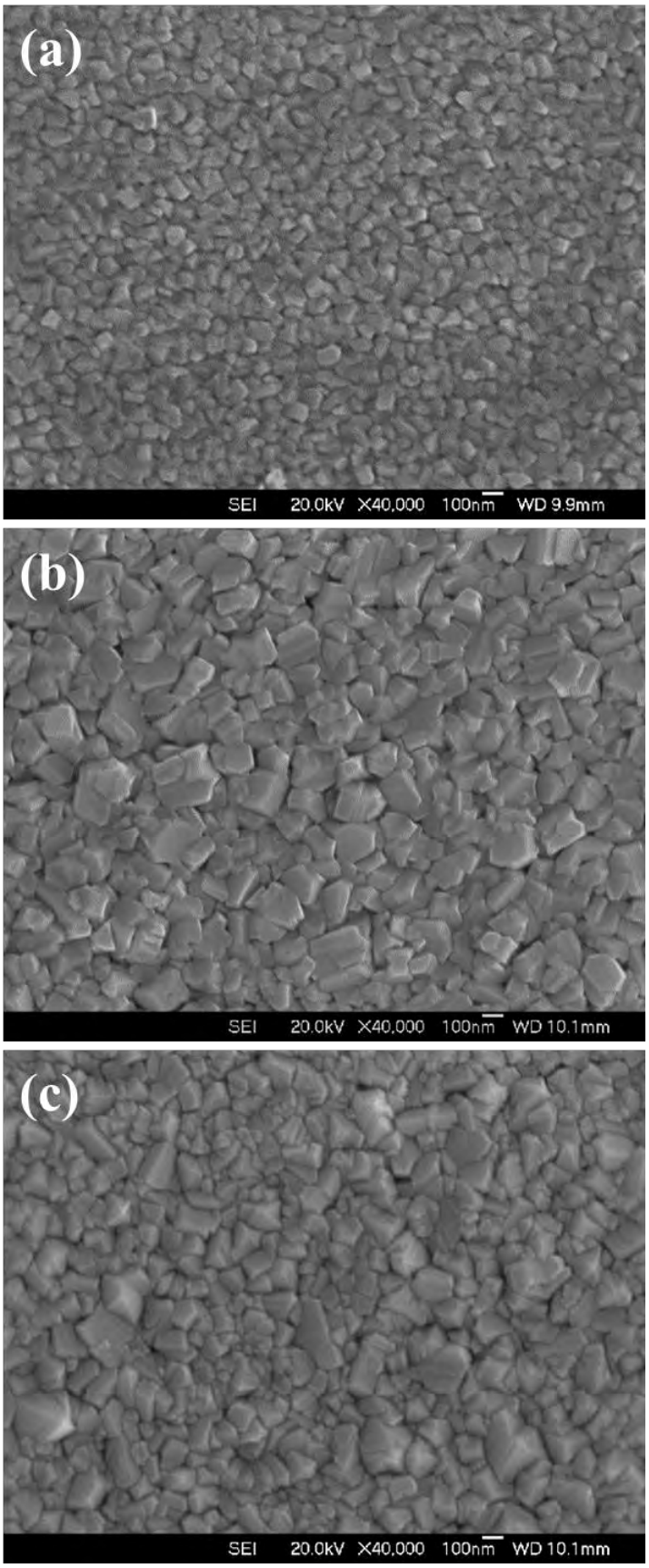

Figure 4.5.1 Surface morphology of ASPA(N&Pt) treated samples under different applied bias (a) Pt-450/10/5 (b) Pt-450/10/10 (c) Pt-450/10/15

covered by small polygonal granular particles, an indication of crystal facets. For Pt-450/10/5 sample (Figure 4.5.1 (a)), the diameter of the particles is around 100 nm. When the applied bias increased to 10 % (Figure 4.5.1(b)), much larger particles with the diameter of above 200 nm are observed. The number of large particles seems to reduce when the bias was further increased to 15 % (Figure 4.5.1(c)), and the surface is covered by both small particles (100 nm) and large particles (250 nm).

The surface composition of ASPA(N&Pt) samples under different biases was obtained by EDS and results are charted in Figure 4.5.2. It can be clearly seen that Pt dominates all the treated surfaces and the content of Pt increases with the increase of applied bias. The elements in 316 austenitic stainless steel, such as Fe, Cr and Ni, can also be detected, which were most possibly sputtered from the stainless steel screen, and the content of those elements decreases with the increase of applied bias. The content of nitrogen was measured by XPS and will show latter.

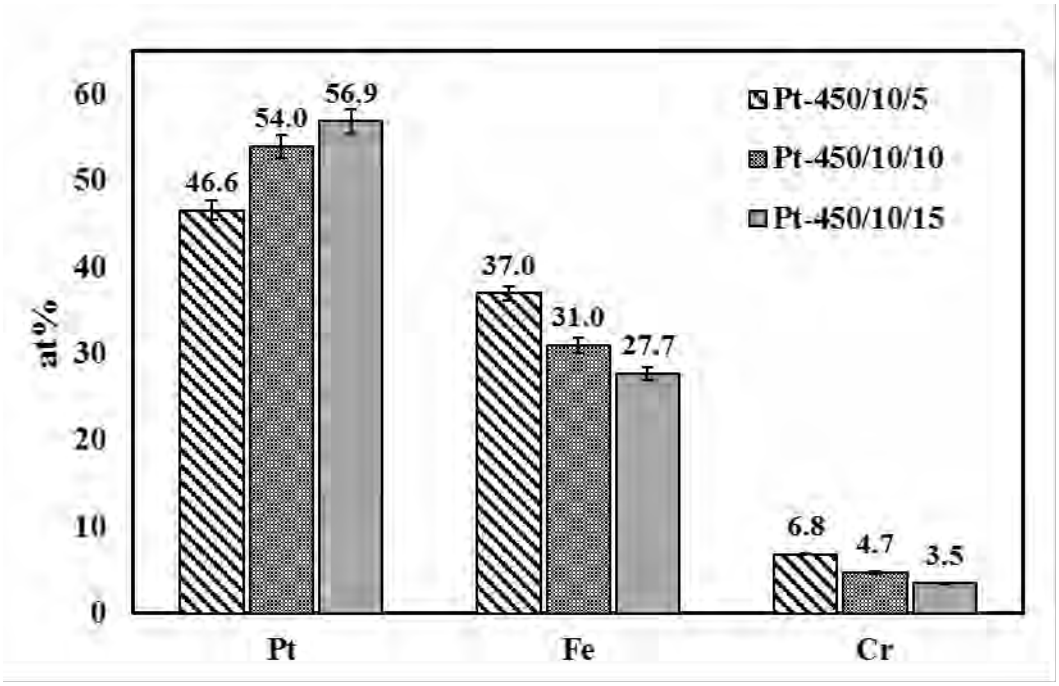

Figure 4.5.2 EDS results of ASPA(N&Pt) treated samples under different applied bias

4.5.1.2 Phase and layer structure

XRD

Figure 4.5.3 depicts the XRD results of the ASPA(N&Pt) samples treated under different applied biases. The peaks of Pt_3Fe [235] [236] (ASTM: 00-029-0716) are clearly shown in all three patterns. Careful observation of Pt-450/10/5 sample (Figure 4.5.3 (b)) reveals that there are small peaks adjacent to each platinum iron peak, which are contributed by iron nitride (Fe_4N). Apart from that, the peaks of stainless steel substrate could also be found from all three samples. For Pt-450/10/5 sample, the intensity of austenite peaks is quite strong and comparable to that of the platinum peaks, and the intensity decreases with the increase of applied bias. Comparing the spectra of Pt-450/10/10 and Pt-450/10/15, it is interesting to find that the ratio of peak intensity between (111) and (220) changes from around 2:1 (when 10 % bias applied) to 1:1 (when 15 % bias applied), and the intensity of peak (200) does not show obvious change. This finding suggests that the applied bias governs the preferred orientation of Pt_3Fe.

XPS

The chemical states of different elements on the ASPA(N&Pt) surface were analysed by XPS and the spectra were obtained after each 60 s of Ar sputtering up to 600 s. The spectra of Pt, Fe and N after 60 s and 600 s sputtering are presented in Figure 4.5.4. It can be seen that the spectra are independent of the sputtering time (depth), which indicates the homogeneous chemical composition against the depth. Judging from the binding energy position of Pt and Fe [237], the formation of Pt_3Fe can be confirmed. Small amount of chromium could also be detected from the treated surfaces (spectra not shown), and was identified as metal state.

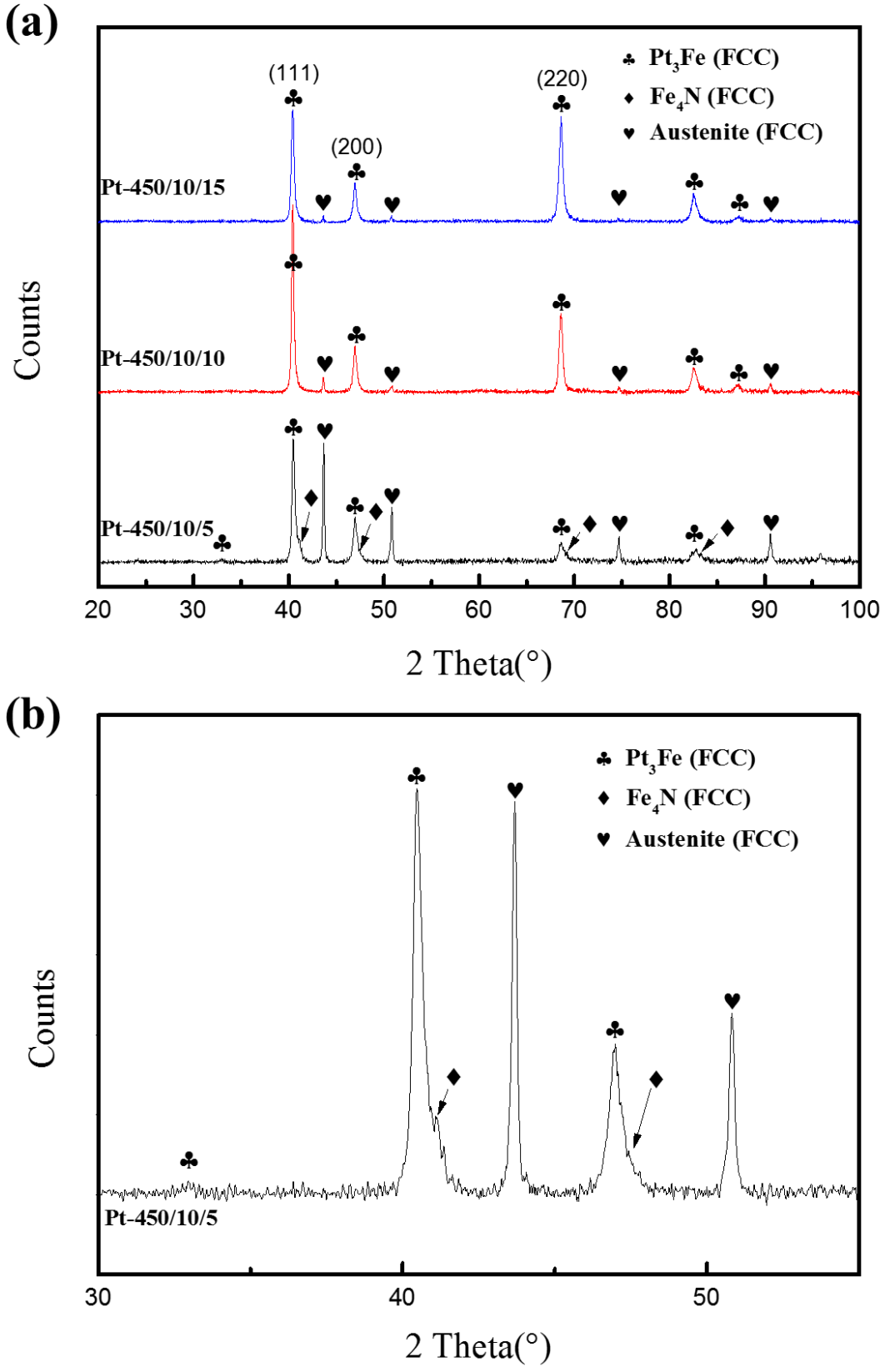

Figure 4.5.3 XRD of ASPA(N&Pt) samples under different applied bias (a) and Pt-450/10/5 (b)

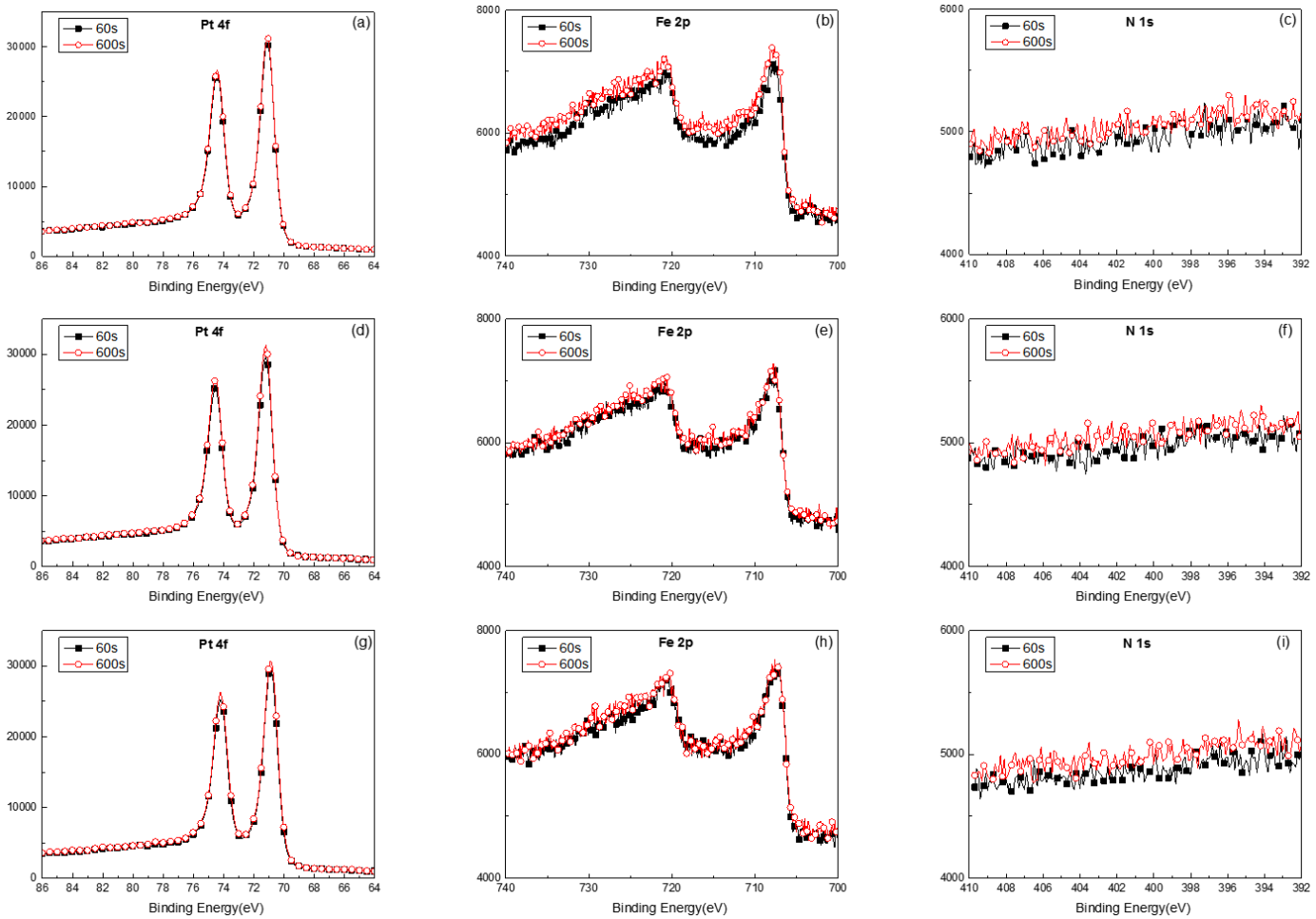

Figure 4.5.4 Pt, Fe and N XPS spectra of ASPA(N&Pt) treated samples under different applied bias

(a) (b) (c) Pt-450/10/5 (d) (e) (f) Pt-450/10/10 (g) (h) (I) Pt-450/10/15

For the element of nitrogen, very weak peaks of N around 397.5 eV could be detected from the 60 s Ar sputtered surface of Pt-450/10/5 sample, but this peak vanishes when sputtering time increased to above 120 s. For the other two samples, no peaks of nitrogen can be detected from any Ar sputtered surfaces.

The quantification analysis of XPS spectra after 360 s Ar sputtering was conducted and the results are shown in Figure 4.5.5. From the quantitative analysis, it can be seen that the content of elements, namely Pt, Fe and Cr, among three samples are close to each other and their difference is within the range of the experimental error, which indicates the chemical composition of the treated surfaces is independent of the applied bias. The atomic ratio of Pt/(Fe+Pt) is around 0.63, which is within the chemical variation of the Pt_3Fe phase (0.6 ~ 0.8) in the Pt-Fe phase diagram [238]. This finding also confirms the identification of Pt_3Fe phase in Figure 4.5.3.

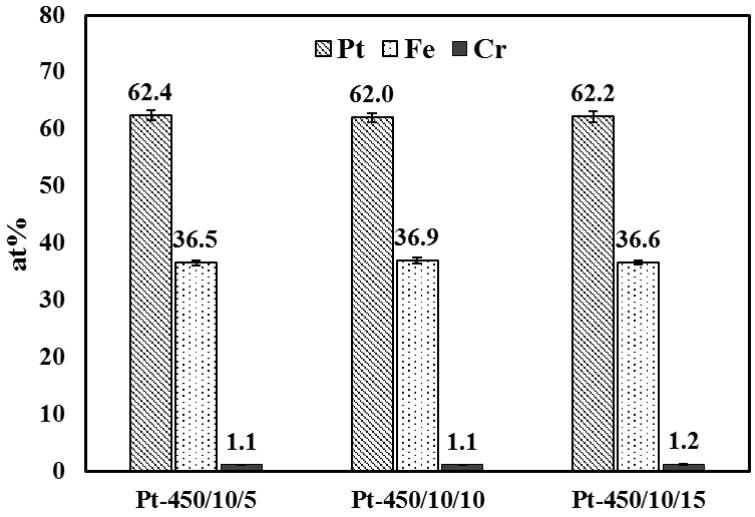

Figure 4.5.5 Quantification analysis of XPS spectra of ASPA(N&Pt) different bias treated surface

SEM

The cross-sectional structures of the ASPA(N+Pt) treated surfaces were observed by high magnification SEM. In order to clearly reveal the layer structures, cross sections

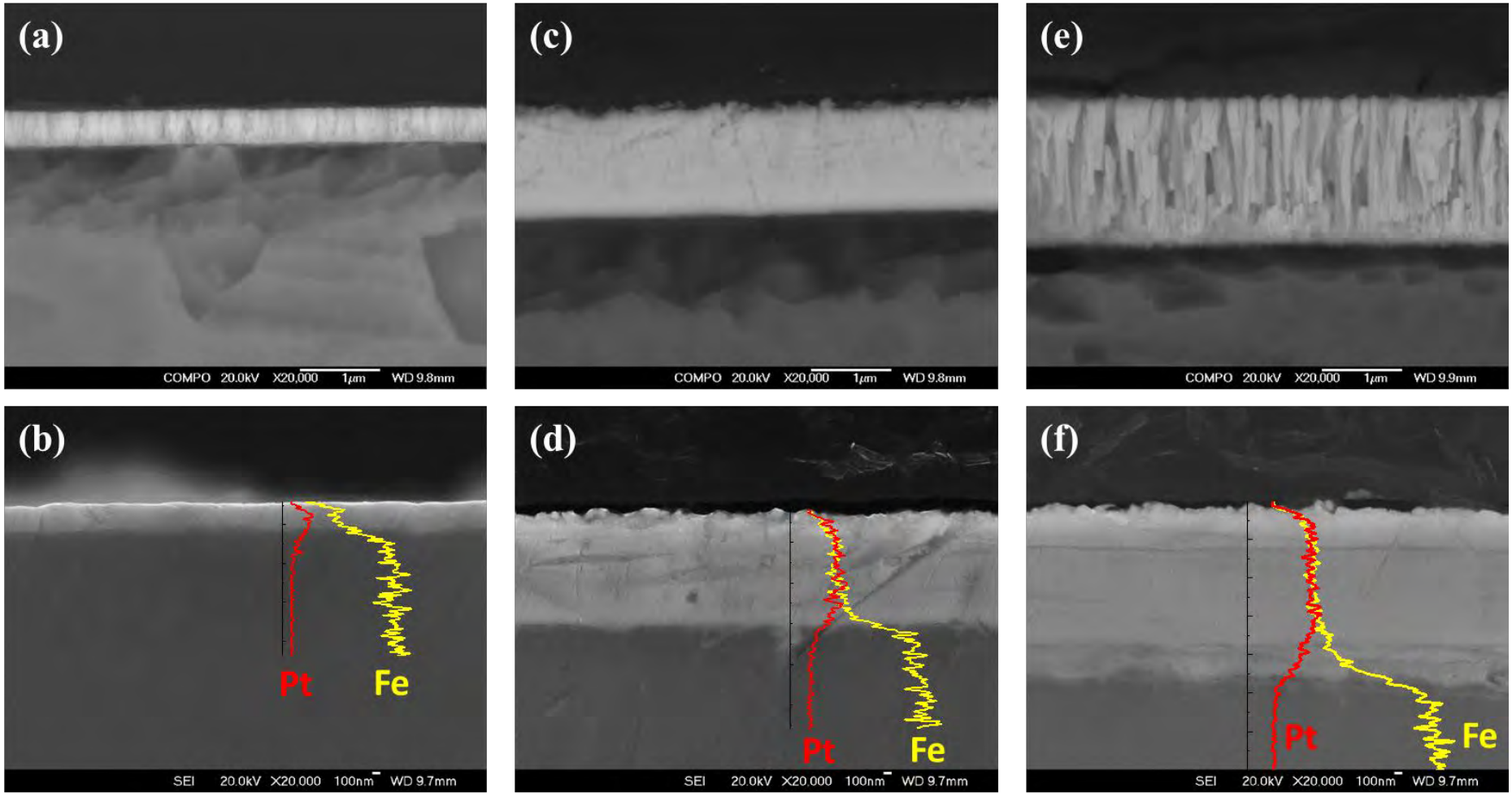

Figure 4.5.6 Cross-sectional SEM images of ASPA(N&Pt) treated samples under different applied bias

(a) (b) Pt-450/10/5 (c) (d) Pt-450/10/10 (e) (f) Pt-450/10/15

were etched and back-scattered electron analysis was employed (Figure 4.5.6(a)(c)(e)). The cross-sectional element line-scan was conducted on the un-etched cross-sections to optimally reveal the chemical composition against depth (Figure 4.5.6 (b) (d) (f)). A white dense surface layer can be seen on the top of each sample. All the white layers exhibit a columnar structure. The thickness of the white layer increases with the increase of applied bias (Pt-450/10/5: 0.28 μm, Pt-450/10/10: 1.20 μm and Pt-450/10/15: 1.76 μm), thus leading to the reduced XRD peak intensity of the substrate (Figure 4.5.3). The cross-sectional element line-scans confirm that the white surface layer is a Pt-rich layer. Taking the results of XPS and XRD into account, these white surface layers should be dominated by Pt_3Fe.

4.5.1.3 Interfacial contact resistance

The ICR values of the ASPA(N+Pt) treated samples under different applied bias are presented in Figure 4.5.7 with the untreated 316 SS as reference. The surface roughness of all the ASPA(N+Pt) treated samples shown in Figure 4.5.7 is about 0.01 μm. The ICR values of all the ASPA(N&Pt) treated samples are closed to each other (6.4-6.9 mΩ cm^2), and the difference is within the range of the experimental error. In addition, the ICR value of ASPA(N+Pt) treated samples is two order of magnitudes lower than that of the untreated sample (158.3 mΩ cm^2) and lower than that of the DOE 2020 target (10 mΩ cm^2) [239]. Comparing with the ICR results of ASPA(N&Nb) treated samples reported in the previous section (around 9 mΩ cm^2), the ASPA(N&Pt) treated samples exhibit even lower ICR. The results of ICR values have indicated that the introduction of a Pt_3Fe deposition layer can significantly enhance the surface electrical conductivity of 316 SS.

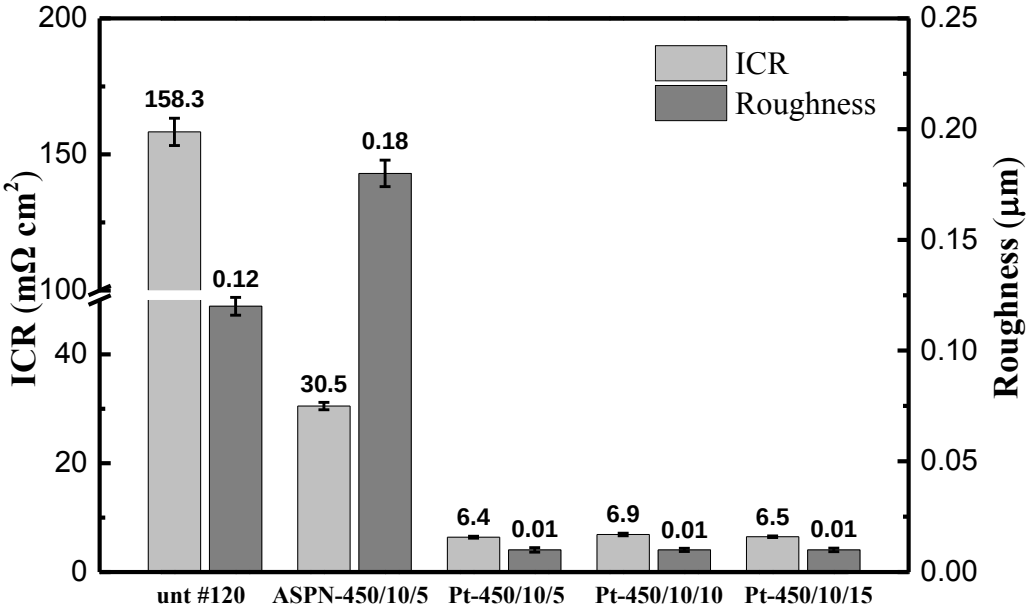

Figure 4.5.7 ICR results and surface roughness of ASPA(N&Pt) treated samples under different applied bias

4.5.1.4 The corrosion behaviour of ASPA(N&Pt) samples

Potentio-dynamic polarisation tests were conducted to compare corrosion behaviour of the ASPA(N&Pt) treated samples with that of the untreated and normal ASPN treated samples (Figure 4.5.8). It is clear from Figure 4.5.8 that the corrosion potential of all the ASPA(N+Pt) samples is almost identical and much more positive than that of the untreated and ASPN treated samples. In general, the passive current density decreases with the increase of applied bias. For Pt-450/10/5 and Pt-450/10/10 samples, the passive current density is much lower than that of the ASPN treated sample, but still higher than that of the untreated sample. The passive current density of Pt-450/10/15 sample is lower than that of the untreated sample in the potential range from -110 mV to 340 mV.

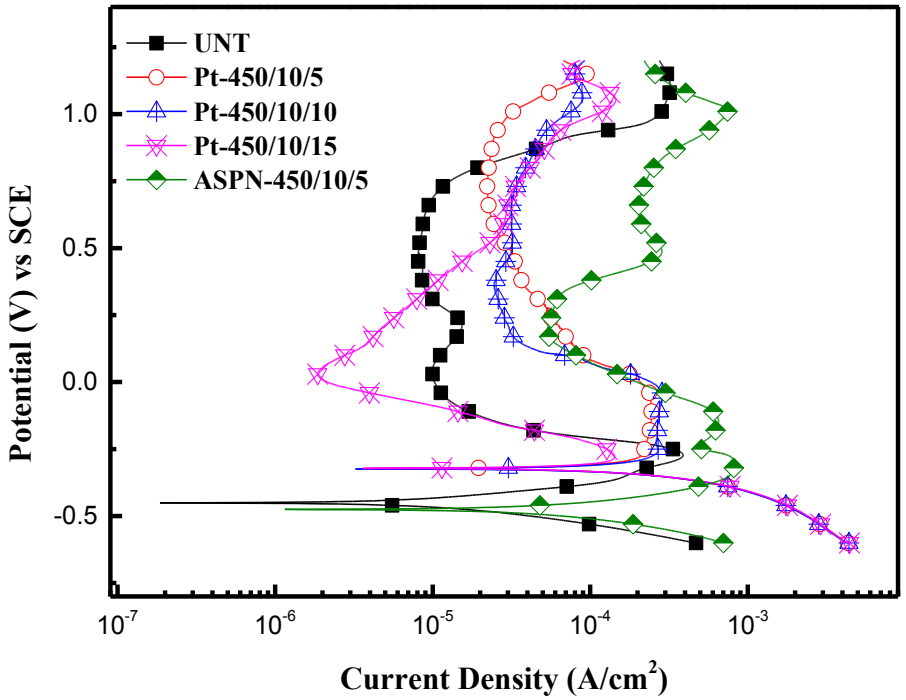

Figure 4.5.8 The potentio-dynamic polarisation curves of ASPA(N&Pt) treated under different applied bias

The corrosion potential and corrosion current density of all the samples were calculated from the corresponding polarisation curves and are listed in Table 4.10. As can be seen from the results, the corrosion potential of ASPA(N&Pt) treated sample (-322 mV) is much higher than that of the untreated sample (-450 mV), the current density is in the same order of magnitude as the untreated sample and lower than that of the normal ASPN treated sample. Among the ASPA(N&Pt) treated samples, the Pt-450/10/15 sample shows the lowest corrosion current density.

Table 4.10 Corrosion potential and corrosion current density of ASPA(N&Pt) treated samples under different applied bias

Sample	E_{corr} (mV) vs SCE	I_{corr} (μA/cm^2)
UNT	-450	10.3
Pt-450/10/5	-322	47.9
Pt-450/10/10	-324	55.7
Pt-450/10/15	-322	24.5
ASPN-450/10/5	-476	74.75

Based on the performance in the potentio-dynamic polarisation tests, the Pt-450/10/15 sample showing the best corrosion resistance was chosen for further potentiostatic polarisation tests under the potential of -0.1 V and 0.6 V (Figure 4.5.9). When a potential of -0.1 V was applied (Figure 4.5.9 (a)), the current density of untreated 316 SS reduces immediately from positive side and stabilises in negative side after 500 s. After stabilisation, the current density of the untreated sample ranges from -6.72×10^{-6} A/cm^2 to -1.45×10^{-6} A/cm^2. For the ASPA(N&Pt) treated Pt-450/10/15 sample, throughout the whole test the current density is negative, specifically, the current density increases significantly before 1500 s and then gradually increases in the rest of the test. The negative current density is due to the reduction of H^+ ions to H_2, which can provide cathodic protection for the measured samples [166]. The current density of Pt-450/10/15 sample varied from -2.62×10^{-5} A/cm^2 to -1.45×10^{-5} A/cm^2, which is about one order of magnitude lower than that of the untreated one. When a potential of 0.6 V was applied (Figure 4.5.9 (b)), the current density of both samples drop significantly at the beginning. The Pt-450/10/15 sample takes a shorter time (about 360 s) than the untreated sample (about 2400 s) to get stable. Within the stabilisation region, the current density of Pt-450/10/15 sample (3.4×10^{-8} A/cm^2) is about two order of magnitudes lower than that of the untreated one (1.54×10^{-6} A/cm^2). In addition, the current density of untreated sample shows strong fluctuation after 10000 s; in contrast, the current density of Pt-450/10/15 is very stable in the whole test.

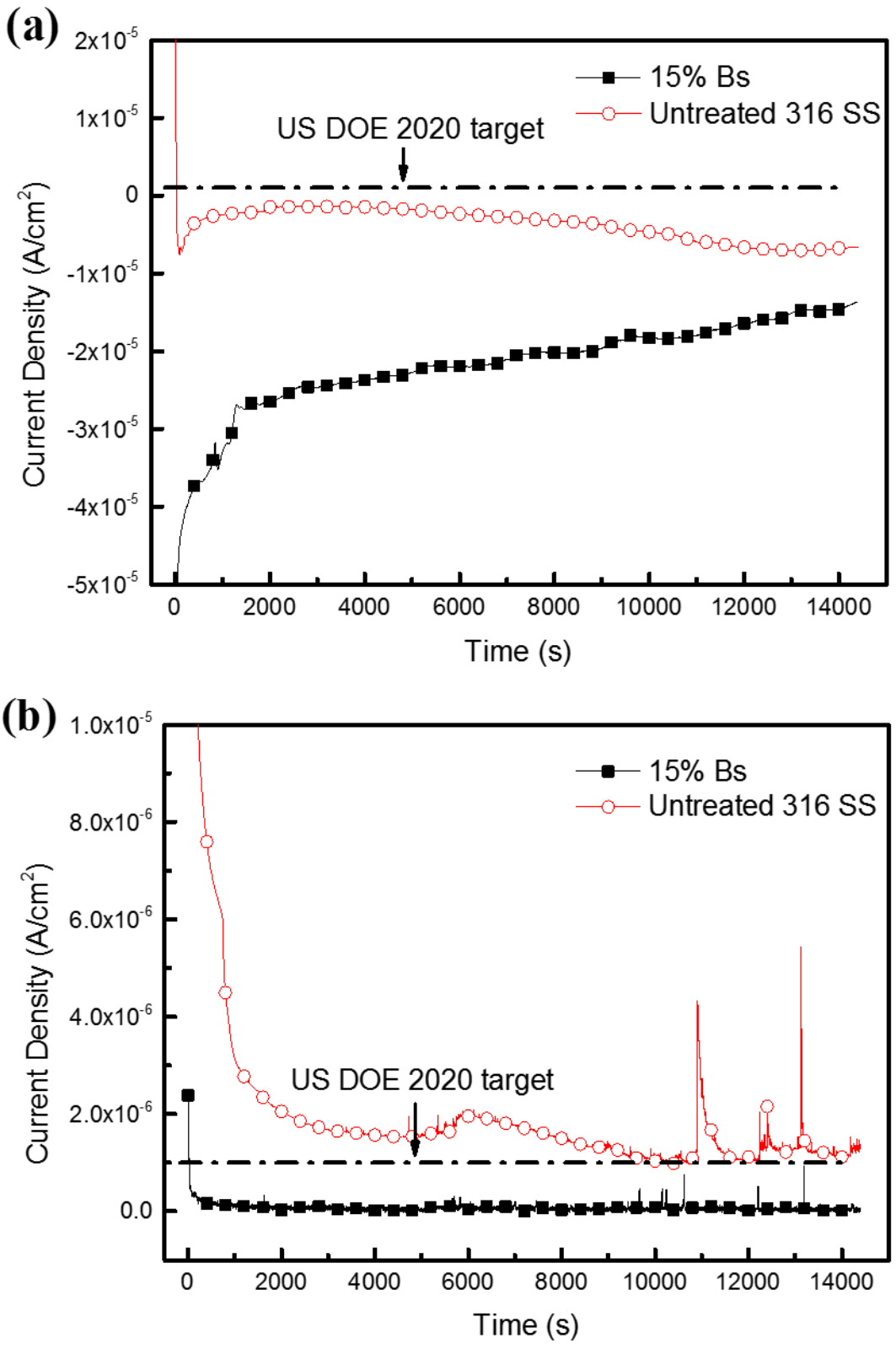

Figure 4.5.9 Potentiostatic polarisation results of Pt-450/10/15 and untreated sample under different potential: (a) -0.1 V (b) 0.6 V

Judging by the results of potentiostatic polarisation, it follows that the Pt-450/10/15 sample exhibits better long-term stability in both of the simulated PEMFC anode and cathode working environment with the current density being lower than that of the DOE 2020 target (1×10^{-6} A/cm^2) [239].

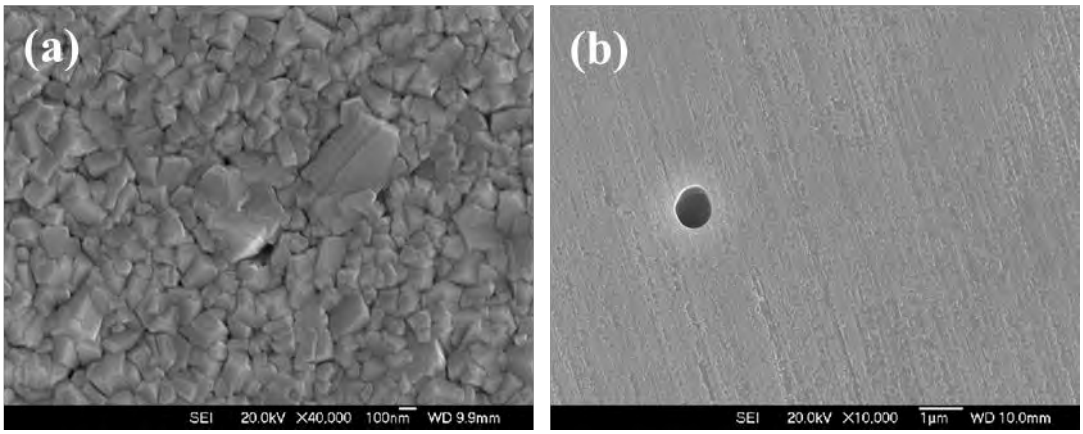

Figure 4.5.10 Surface morphology of different sample after 4h potentiostatic polarisation test (0.6 V): (a) Pt-450/10/15 (b) untreated 316 SS

The surface morphology of samples after 4 h potentio-static test at the potential of 0.6 V were observed by SEM and images are presented in Figure 4.5.10. The surface morphology of Pt-450/10/15 sample in the high magnification image shows no evidence of corrosion and it is almost identical to that of the as-treated samples (Figure 4.5.1 (c)). However, for the untreated sample, both general corrosion and pitting corrosion can be observed on the corrosion tested surface.

4.5.2 The influence of varying bias

It is know from the results of previous section that under 5 – 15 % bias, only a surface Pt deposition layer could be produced without S-phase sublayer. However, from the results of ASPA(N&Nb) treatments (Section 4.4.4), the duplex layer structure could be produced and outperformed the single layered surfaces. Hence, in order to produce

duplex layer structure using ASPA(N&Pt) treatments, ASPA(N&Pt) treatments with varying bias were conducted: (1) the bias was set as 0 % for the first 10 h plus 10 % for the second 10 h (Pt-450/20/(0+10)), and (2) 5 % for the first 10 h plus 10 % for the second 10 h (Pt-450/20/(5+10)). The rest treatment parameters were set as follows: temperature 450 ℃ , length of alloying wire 5 mm and pressure 0.75 mbar.

4.5.2.1 Surface morphology and composition

The low magnification surface morphology of Pt-450/20/(0+10) and Pt-450/20/(5+10) samples are shown in Figure 4.5.11 (a) and (c). The surfaces of both the samples are covered by a dense layer. For Pt-450/20/(0+10) sample (Figure 4.5.11 (a)), some large particles can be observed from the surface. While for Pt-450/20/(5+10) sample (Figure 4.5.11 (b)), the size of particles are even, and no large particles could be found from its surface. The difference in surface morphology between those two samples can be easily seen from the high magnification SEM image shown in Figure 4.5.11 (b) and (d). The small particles on both the samples are random convex polyhedrons, with the size of 100 – 300 nm in diameter. The large particles in Pt-450/20/(0+10) seem to be agglomerations of many small ones, which can be concluded from the grain boundaries on the surface of the large particles. The size of the large particles is around 500 nm in diameter.

The surface composition of the ASPA(N&Pt) treated samples with varying bias is shown in Figure 4.5.12. It can be seen that the high applied bias in the first step increases the content of Pt, as well as nitrogen and iron.

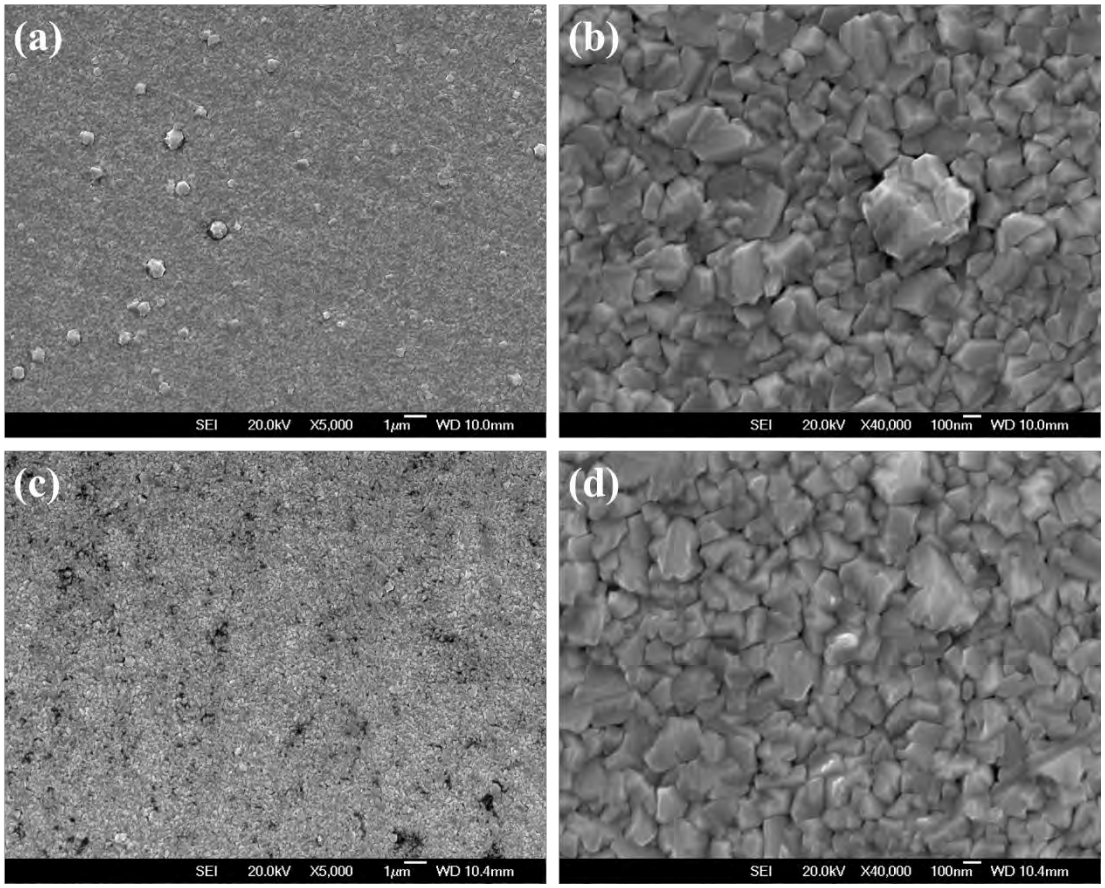

Figure 4.5.11 Low and high magnification surface SEM images of ASPA(N&Pt) treated samples with varying bias: (a) (b) Pt-450/20/(0+10) (c) (d) Pt-450/20/(5+10)

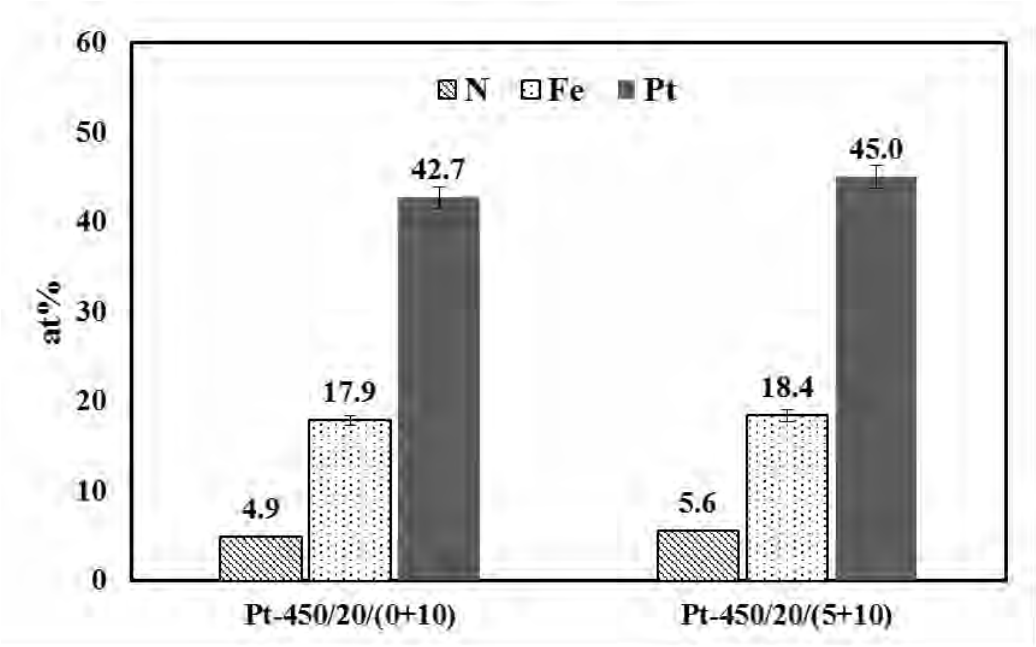

Figure 4.5.12 EDS results of ASPA(N&Pt) treated samples with varying bias

4.5.2.2 Phase and layer structure

XRD

The XRD patterns of multi-step ASPA(N&Pt) treated samples are shown in Figure 4.5.13. For the Pt-450/20/(0+10) sample, the peaks of platinum iron and austenite substrate can both be detected, and the intensity of platinum iron peaks is much higher than that of the substrate. Regarding Pt-450/20/(5+10) sample (Figure 4.5.13(b)), several differences can be found: firstly, although the peak intensity of platinum iron is still stronger than that of the substrate, the difference between these two peaks reduced; the most important difference is that a set of weak peaks attached to the corresponding austenite peak in the position of $2\theta = 43.7°$ and $50.4°$ are detected, which are most possibly contributed by S-phase.

GDS

The GDS nitrogen depth profiles of ASPA(N&Pt) treated samples with varying bias are plotted in Figure 4.5.14. For Pt-450/20/(0+10) sample, the depth of high nitrogen region is about 1 μm. For the nitrogen profile of Pt-450/20/(5+10) sample, it exhibits two peaks: the centre of first peak is in the same position as that of the Pt-450/20/(0+10) sample, but showing a higher N content; the second peak shows relatively high nitrogen content and has a long tail extending to the depth of around 4 μm. The relatively high and deep nitrogen content together with the weak XRD peaks close to the peaks of substrate indicate the formation of S-phase in the Pt-450/20/(5+10) sample.

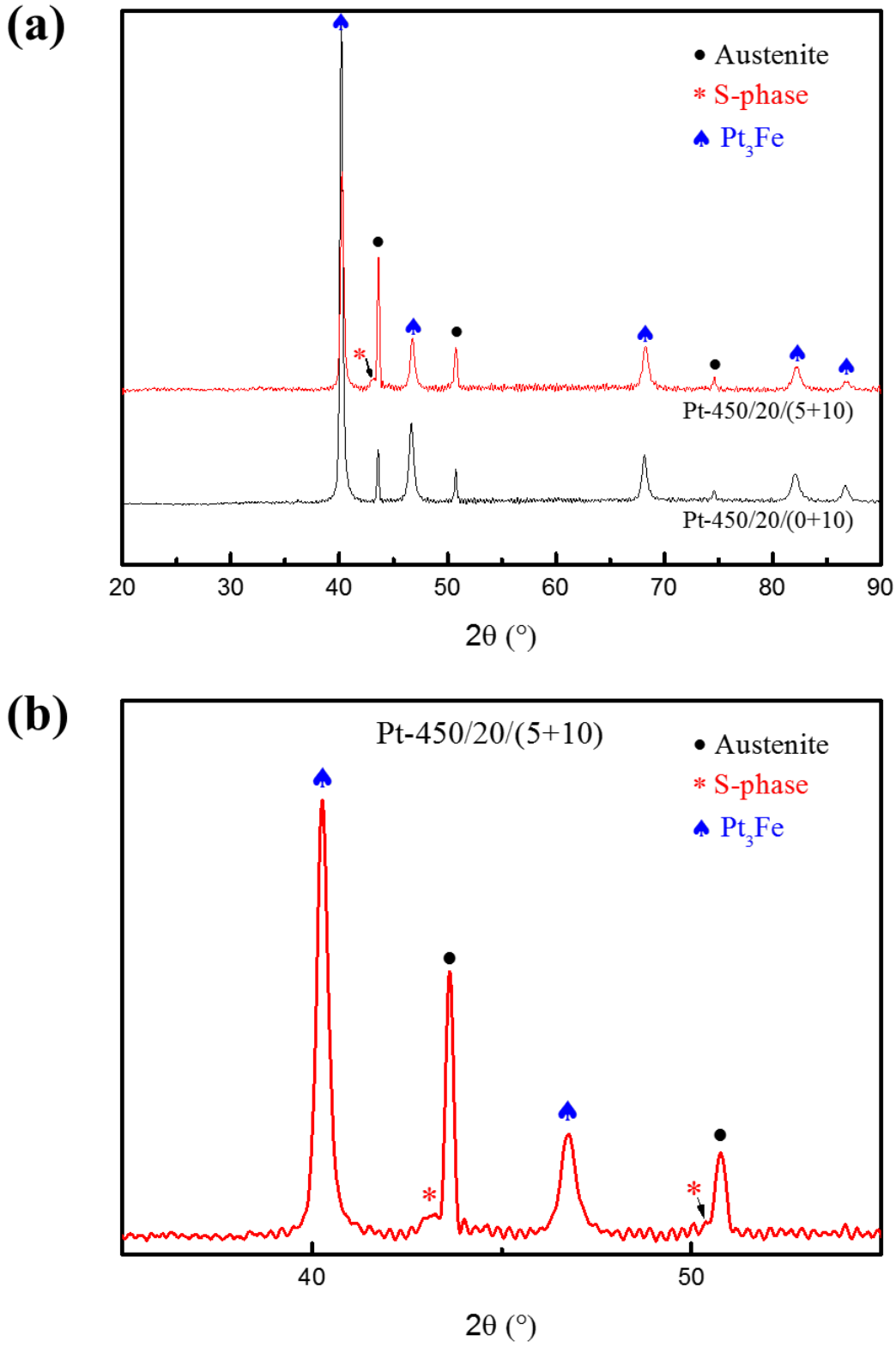

Figure 4.5.13 XRD patterns of varying bias treated samples

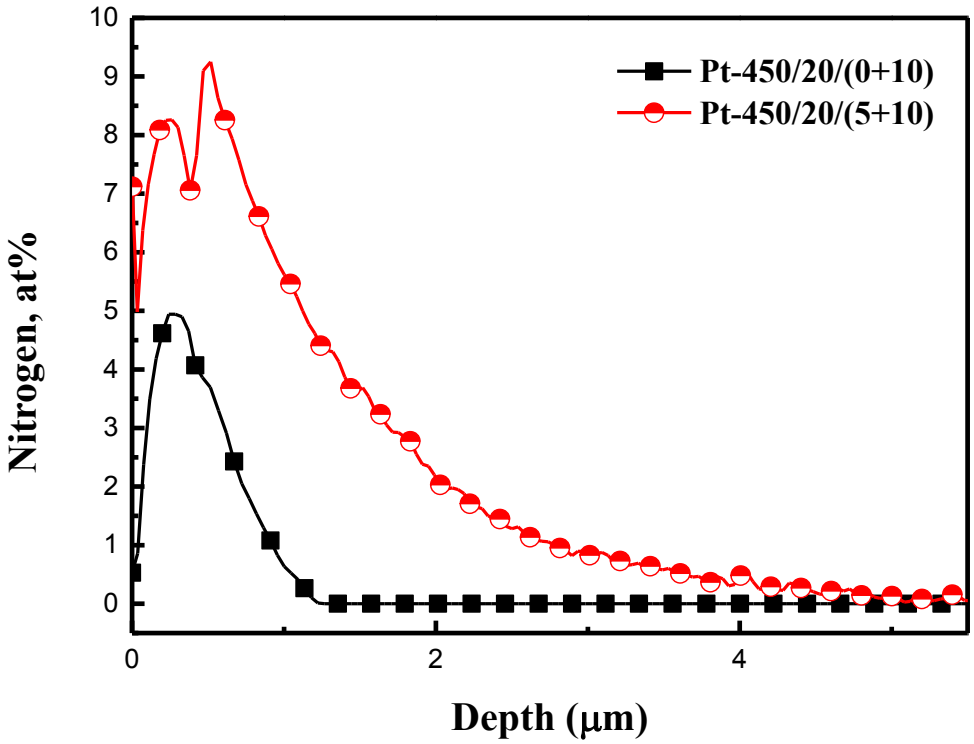

Figure 4.5.14 GDS nitrogen profile of ASPA(N&Pt) treated samples with varying bias

SEM

The cross-sectional SEM images of ASPA(N&Pt) treated samples with varying bias are shown in Figure 4.5.15. For Pt-450/20/(0+10) sample (Figure 4.5.15 (a)), only a single layer can be found on the surface of the substrate, which is dense and uniform. The EDS element line-scan shown in the high magnification SEM image (Figure 4.5.15 (b)) indicates the high Pt content of this layer.

For Pt-450/20/(5+10) sample (Figure 4.5.15 (c)), a duplex layer structure is observed, consisting of a dense layer on top and a featureless layer underneath. The EDS line-scans shown in the high magnification cross-sectional SEM images (Figure 4.5.15 (d)) also indicates the high Pt content in the white surface layer. The thickness of the featureless layer matches with the depth of the high nitrogen region shown in Figure 4.5.14. Therefore, this featureless layer could be identified as S-phase.

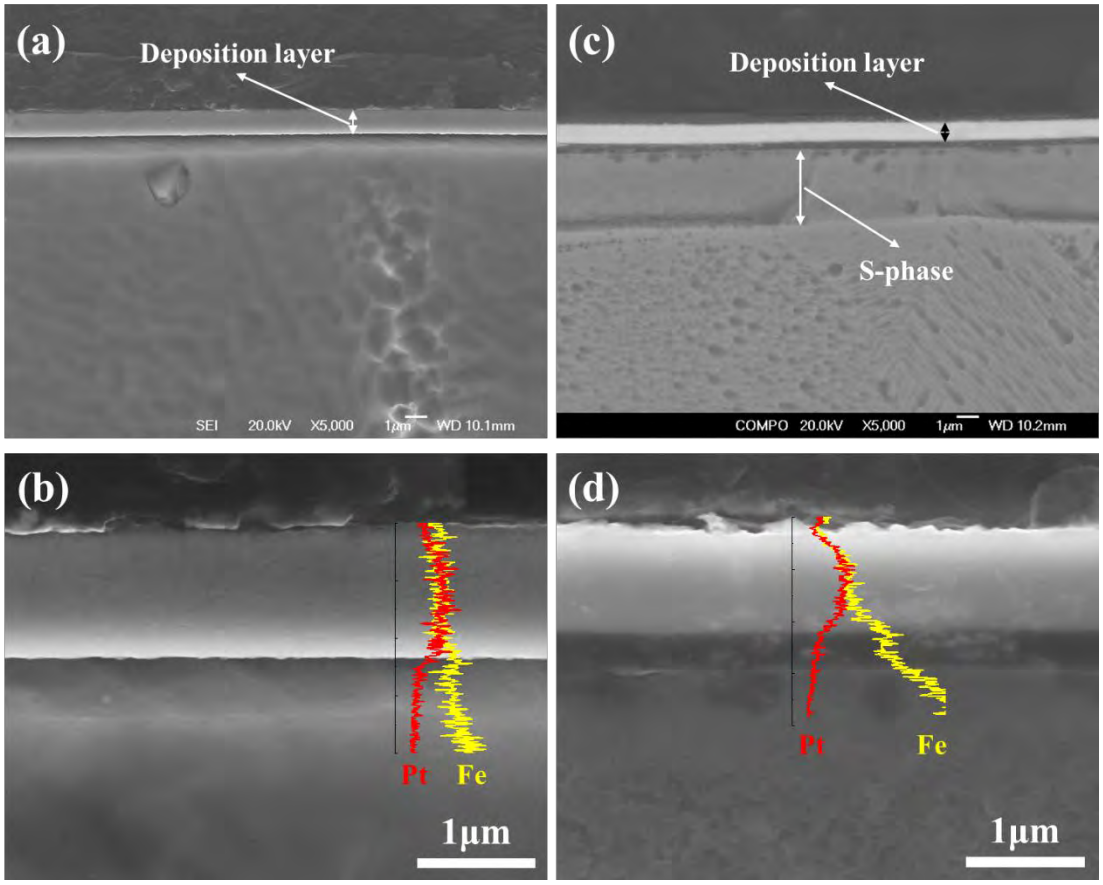

Figure 4.5.15 Low magnification cross-sectional SEM images of ASPA(N&Pt) treated samples with varying bias (b) Pt-450/20/(0+10) (c) (d) Pt-450/20/(5+10)

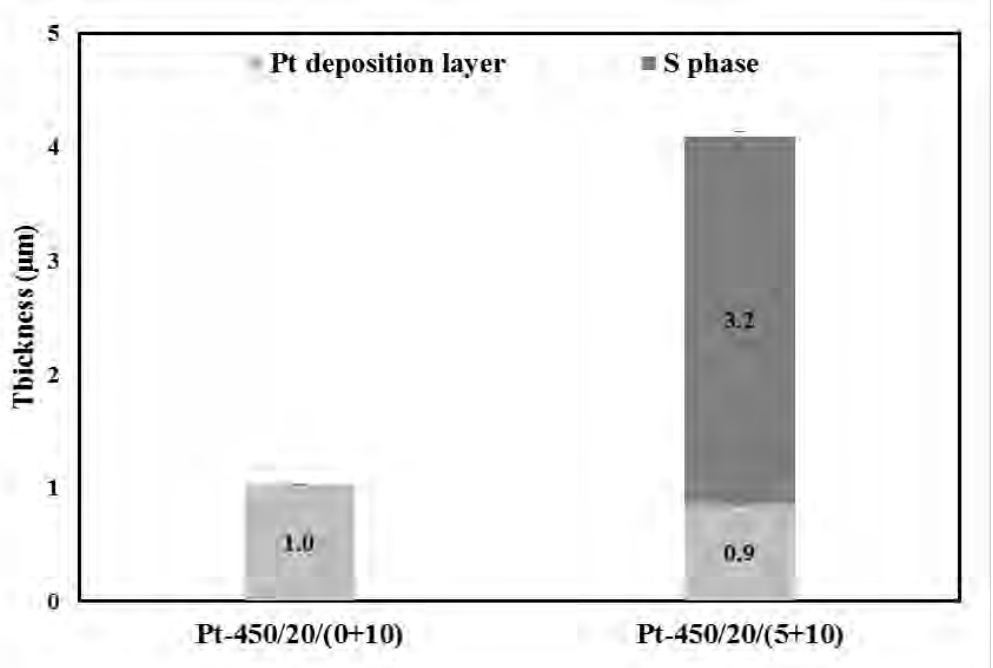

Figure 4.5.16 The thickness of deposition layer and S-phase of ASPA(N&Pt) treated samples with varying bias

The thickness of the deposition layers and the S-phase of the ASPA(N&Pt) treated samples with varying bias are compared in Figure 4.5.16. It can be seen that the thickness of the Pt deposition layer are closed for those two samples.

4.5.2.3 Interfacial contact resistance

The ICR values of ASPA(N&Pt) treated samples with varying bias are shown in Figure 4.5.17. The ICR values of the two samples are lower than 9 mΩ cm^2, and the Pt-450/20/(5+10) sample shows a slightly lower ICR value than that of the Pt-450/20/(0+10). Considering the similar surface roughness and the thickness of Pt deposition layer, the formation of S-phase should have contributed to the further reduction of ICR value.

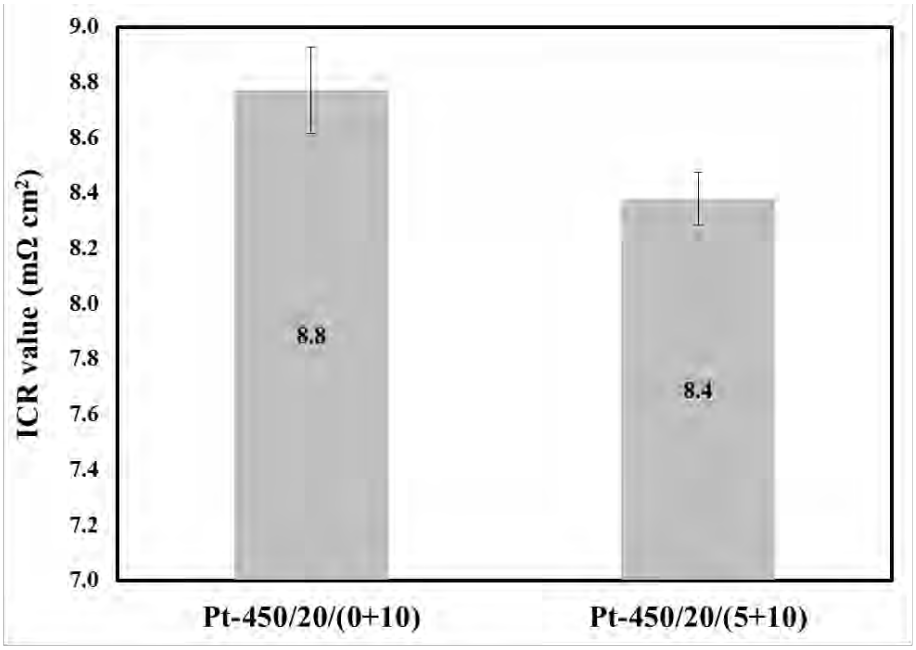

Roughness (μm)	0.03	0.04

Figure 4.5.17 The ICR values of ASPA(N&Pt) treated samples with varying bias

4.5.2.4 Corrosion behaviour

The corrosion behaviour of ASPA(N&Pt) treated samples with varying bias was evaluated using potentiodynamic polarisation tests and the polarisation curves are shown in Figure 4.5.18. The ASPA(N&Pt) with varying bias treated samples show significantly improved corrosion potential compared with the untreated samples. From -0.6 V to -0.3 V, the polarisation curves of the two ASPA(N&Pt) treated samples almost overlapped with each other. However, in the passive region, the passive current density of Pt-450/20/(0+10) sample is about one order of magnitude lower than that of the Pt-450/20/(5+10) sample, and the passive current density of the former is in the same level as the untreated 316 SS.

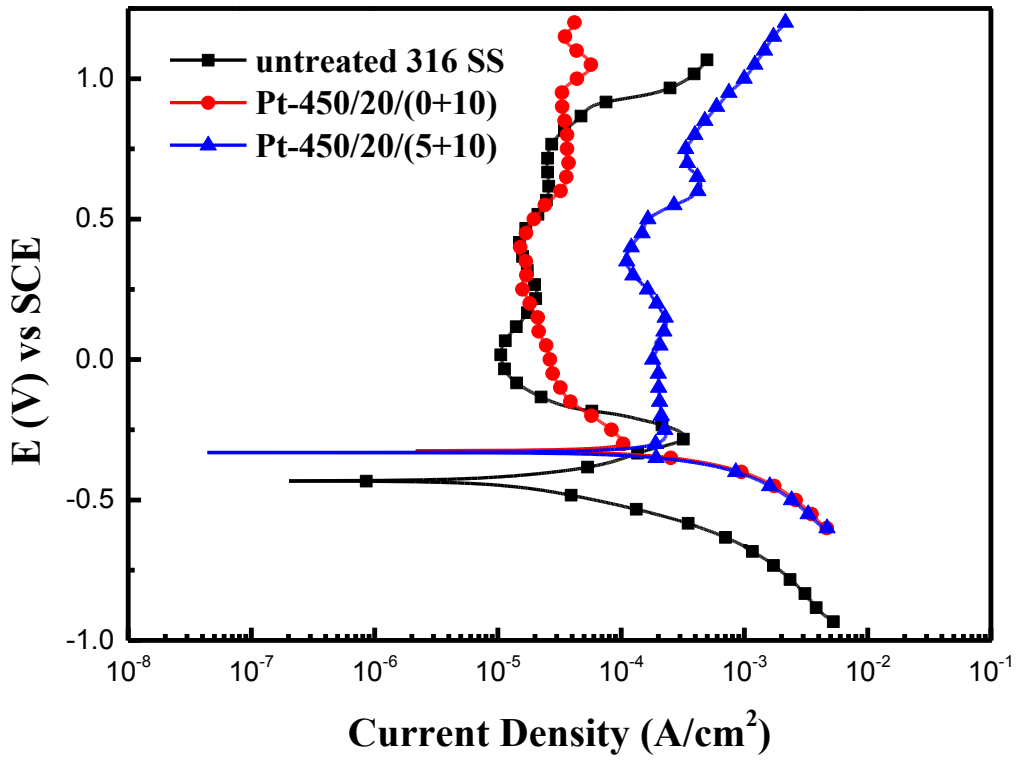

Figure 4.5.18 The potentiodynamic polarisation curves of ASPA(N&Pt) treated samples with varying bias

The corrosion potential and corrosion current density of the untreated 316 SS and ASPA(N&Pt) varying bias treated samples are listed in Table 4.11. The corrosion potential of ASPA(N&Pt) treated samples is close to each other and more positive than that of the untreated sample. However, the corrosion current density of those treated samples is higher than that of the untreated one.

Table 4.11 corrosion potential and corrosion current of ASPA(N&Pt) treated samples with varying bias

Sample	Corrosion potential (mV) vs SCE	Corrosion current density ($\mu A/cm^2$)
UNT	-450	10.3
Pt-450/20/(0+10)	-325	40.6
Pt-450/20/(5+10)	-331	65.6

4.5.3 Summary

In this section, platinum has been selected as the alloying element in active screen plasma alloying treatments. By adjusting the treatment parameter, namely the applied bias, two different layer structures could be produced, a single Pt_3Fe deposition layer or a duplex layer consisting of a Pt_3Fe deposition layer followed by an S-phase layer.

The ICR measurement reveals that the addition of platinum could further reduce the ICR value to around 7 $m\Omega \cdot cm^2$. The corrosion tests demonstrate that the corrosion resistance is greatly improved (compared with ASPA(N&Nb)) after the ASPA(N&Pt) treatments, not only in the terms of corrosion potential, but also the long-term performance in potentio-static tests. Based on the results, the introduction of platinum by means of active screen plasma alloying is a promising method for the surface modification of 316 stainless steel for the application of PEMFC bipolar plates.

Chapter 5. Discussion

As reported in Chapter 4, the new plasma surface alloying technologies developed from this research including active screen plasma alloying with nitrogen (i.e. nitriding) and active screen plasma co-alloying (i.e. ASPA(N&Ag), ASPA(N&Nb) and ASPA(N&Pt)) can improve the surface properties (especially reduce ICR value) of 316 austenitic stainless steel. In order to understand the mechanisms involved, in this chapter the mass transfer during active-screen plasma treatments are discussed first in Section 5.1, then the surface layer formation mechanisms are proposed in Section 5.2 and finally the surface properties of the plasma treated surfaces systems are compared.

5.1 The mass transfer in active screen plasma treatments

As discussed in Section 2.5.2, the mechanism of active screen plasma nitriding (ASPN) has been studied by some researchers [197] [198] [204] [210] and a model of "sputtering and deposition" was proposed by Zhao et al. to understand the ASPN of austenitic stainless steels. Some evidence has been reported to support the hypothesis that the deposition layer on the surface is sputtered from the screen, which acts as nitrogen carriers, and the decomposition of that deposited materials releases nitrogen to diffuse into the surface and form the S-phase if the treatment temperature is low. However, there is still no direct evidence to demonstrate the nitrogen mass transfer between the deposition layer and the substrate; the mechanism for the new plasma co-alloying processes developed has not been fully studied yet. To this end, some additional experiments have been designed and conducted using different substrates (bare 316 SS, Au coated 316 SS and Si wafer) to investigate the nitrogen mass transfer in active screen plasma alloying. This is mainly because Au is widely used in

surface engineering and oxidation to study surface layer formation; it is known that the solid solubility of nitrogen in Si wafer is very low and hence the as-deposition layer could be retained on the surface of Si wafer.

5.1.1 N mass transfer in ASPN

The surface of 316 stainless steel samples was polished to mirror-finish (down to 1 μm diamond paste). Some part of the surface was coated with Au in a vacuum gold-coater for 3 min, and the rest part of the surface was left uncoated. These partly coated samples were treated in the industrial AS unit with the experiment setting shown in Figure 3.2.4 using a normal 316 stainless steel lid without alloying wire. The treatment duration was set as 15 h, 20 h and 30 h. Other parameters were set as follow: temperature 450 ℃, applied bias 5 % and pressure 0.75 mbar. Si wafers were also placed on the surface of some samples and treated simultaneously.

The low magnification SEM images of the ASPN treated uncoated and Au-coated surfaces for different durations are shown in Figure 5.1.1. Under low magnification, the surface morphology of ASPN treated Si wafer is very similar to that of the ASPN treated Au-coated surface, and thus is not shown here. The uncoated samples treated for 15 h, 20 h and 30 h are labelled as 15h, 20h and 30h, respectively. The Au coated samples treated for 15 h, 20 h and 30 h are labelled as Au-15h, Au-20h and Au-30h, respectively.

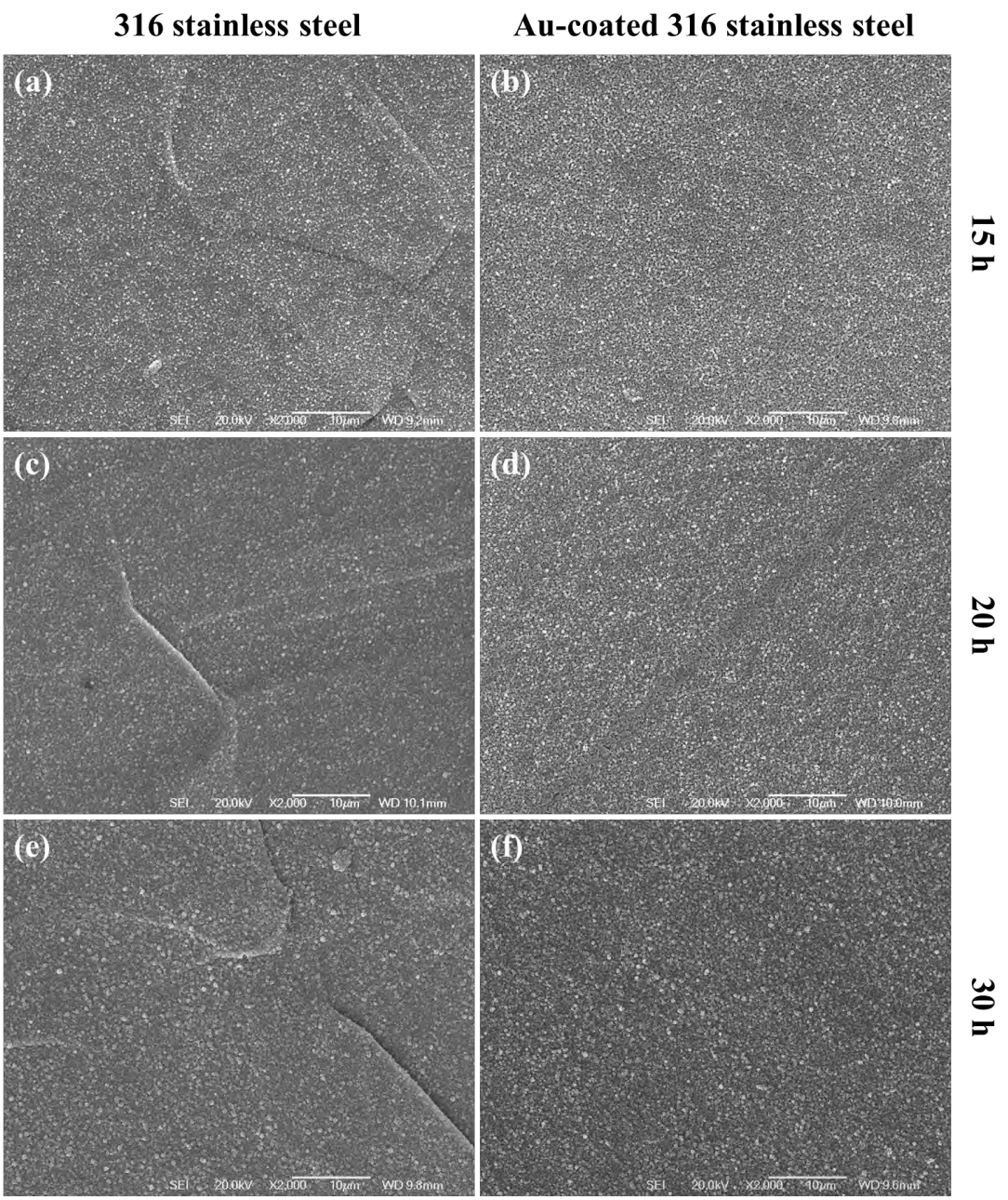

Figure 5.1.1 The low magnification surface morphology SEM images of samples
(a) 15h (b) Au-15h (c) 20h (d) Au-20h (e) 30h (f) Au-30h

It can be seen from Figure 5.1.1 that for the ASPN treated uncoated surfaces, surface relief can be easily seen and the extent is intensified with the increase of treatment duration. On the other hand, no surface relief can be observed from the surface of ASPN treated Au coated surfaces, even after 30h treatment.

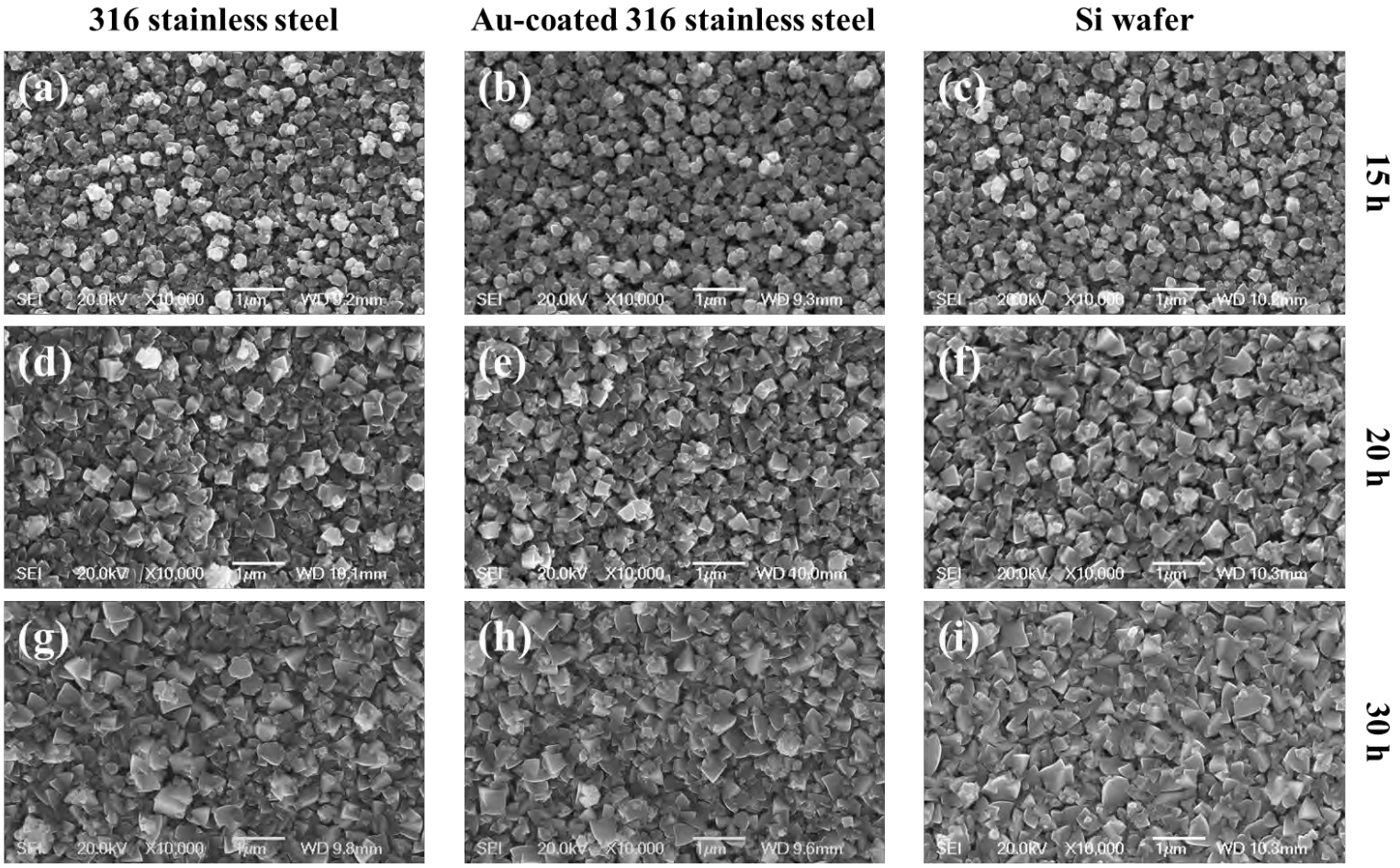

Figure 5.1.2 The high magnification surface morphology SEM images of samples

(a) 15h (b) Au-15h (c) Si-15h (d) 20h (e) Au-20h (f) Si-20h (g) 30h (h) Au-30h (i) Si-30h

The high magnification surface SEM images of ASPN treated bare surfaces, Au-coated surfaces and Si wafer surfaces (Si-15h, Si-20h and Si-30h) are shown in Figure 5.1.2. All the surfaces are covered by nano-sized particles and the size of the particle and the density of the surface layer increase with the increase of treatment duration. For the same treatment duration, the size of the particles formed on the three surfaces is similar. However, for 15h and 20h ASPN treated surfaces, the deposition layer formed on the uncoated bare surfaces is denser than that formed on the Au-coated surfaces and Si wafer surfaces. When treated for 30h, the surface morphology of the three different surfaces is almost identical.

The GDS nitrogen depth profiles of the ASPN treated bare surfaces and Au-coated surfaces are shown in Figure 5.1.3. It is obvious that after the same ASPN treatment the nitrogen content of the ASPN treated bare surfaces is much higher than that of the ASPN treated Au-coated surfaces and the depth of high nitrogen region of the former is also much larger than the latter.

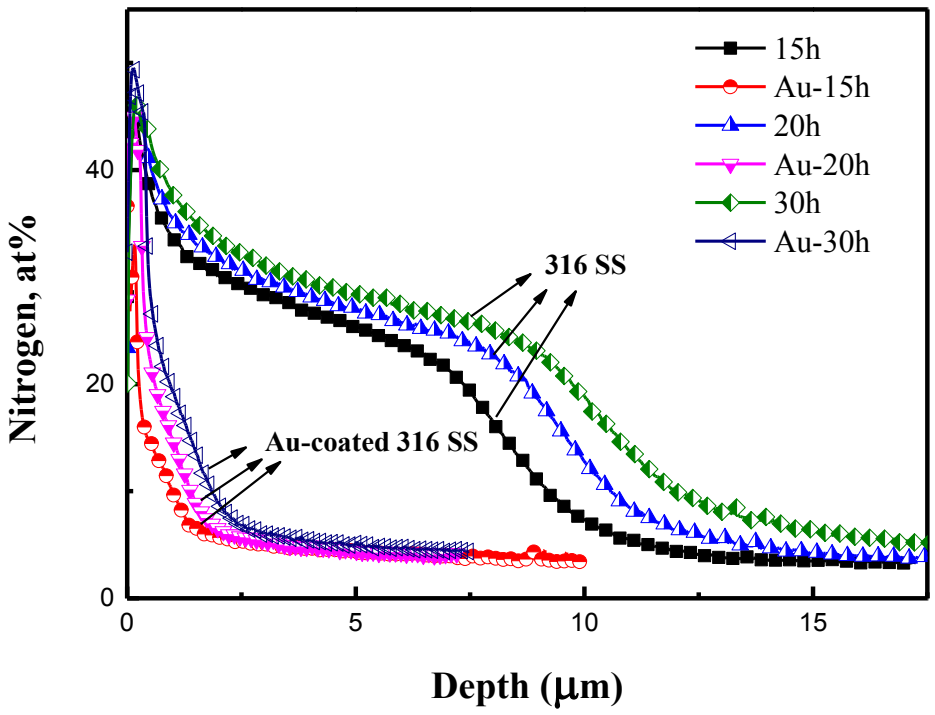

Figure 5.1.3 Nitrogen depth profiles of samples

The low magnification cross-sectional SEM images of the ASPN treated bare surfaces and Au-coated surfaces are shown in Figure 5.1.4. A featureless layer can be found from all the treated surface, which could be identified as S-phase layers due to their very high nitrogen content (Figure 5.1.3). Although the thickness of the S-phase layer formed on bare and Au-coated surfaces increases with treatment duration, the thickness of the S-phase layer is significantly thinner on the latter. The huge difference in S-phase thickness between the ASPN treated bare surfaces and the Au-coated surfaces can be clearly seen in Figure 5.1.5.

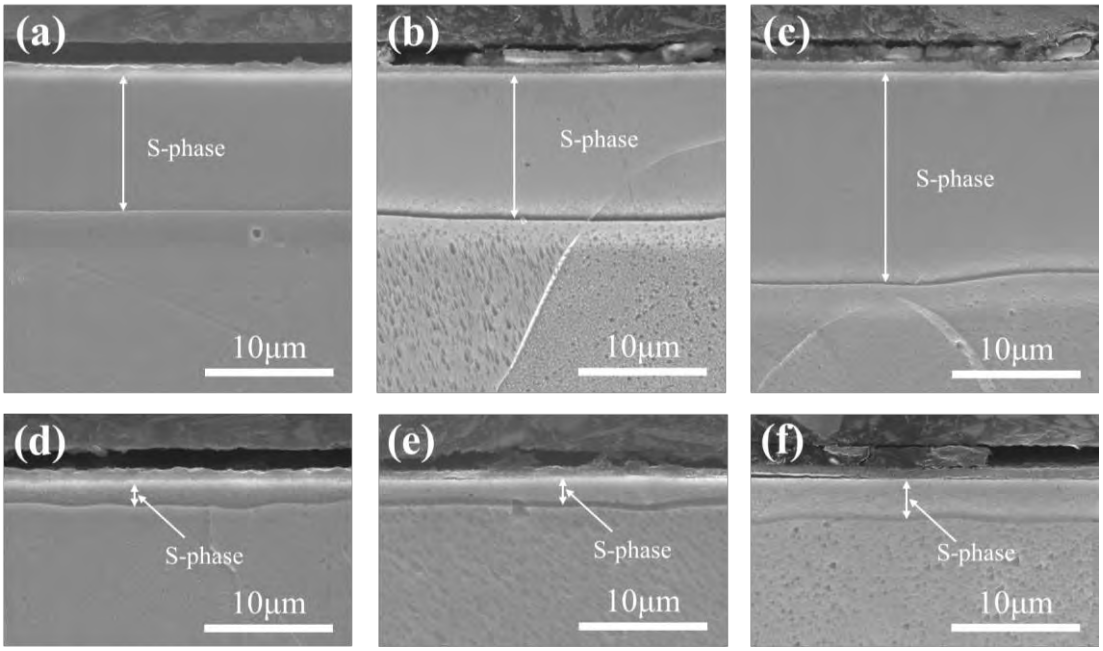

Figure 5.1.4 The cross-sectional SEM images of samples (a) 15h (b) 20h (c) 30h (d) Au-15h (e) Au-20h (f) Au-30h

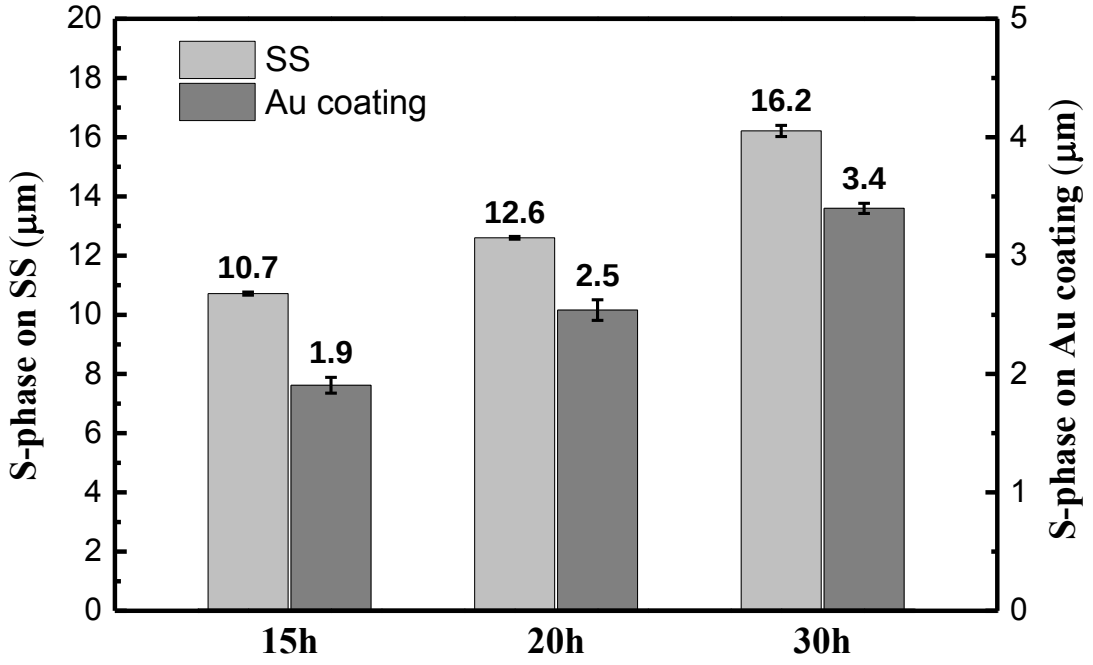

Figure 5.1.5 S-phase thickness of ASPN treated un-coated and Au-coated 316 stainless steel surfaces

The high magnification cross-sectional SEM images of the surface area of all the treated surfaces are shown in Figure 5.1.6. A deposition layer marked by arrows can be observed on each surface. It can be seen that for each surface, the thickness of the deposition layer increases with the increase of treatment duration.

The EDS element line-scanning of Au as shown in the middle column of Figure 5.1.6 indicates the location of the original Au coating, and it can be seen that a deposition layer was formed on the top of the originally coated Au layer. The deposition layers formed on the uncoated and Au-coated surfaces are uniform and dense. However, the structure of the deposition layer on the Si wafer surfaces is different, consisting of many small particles with a clear boundary.

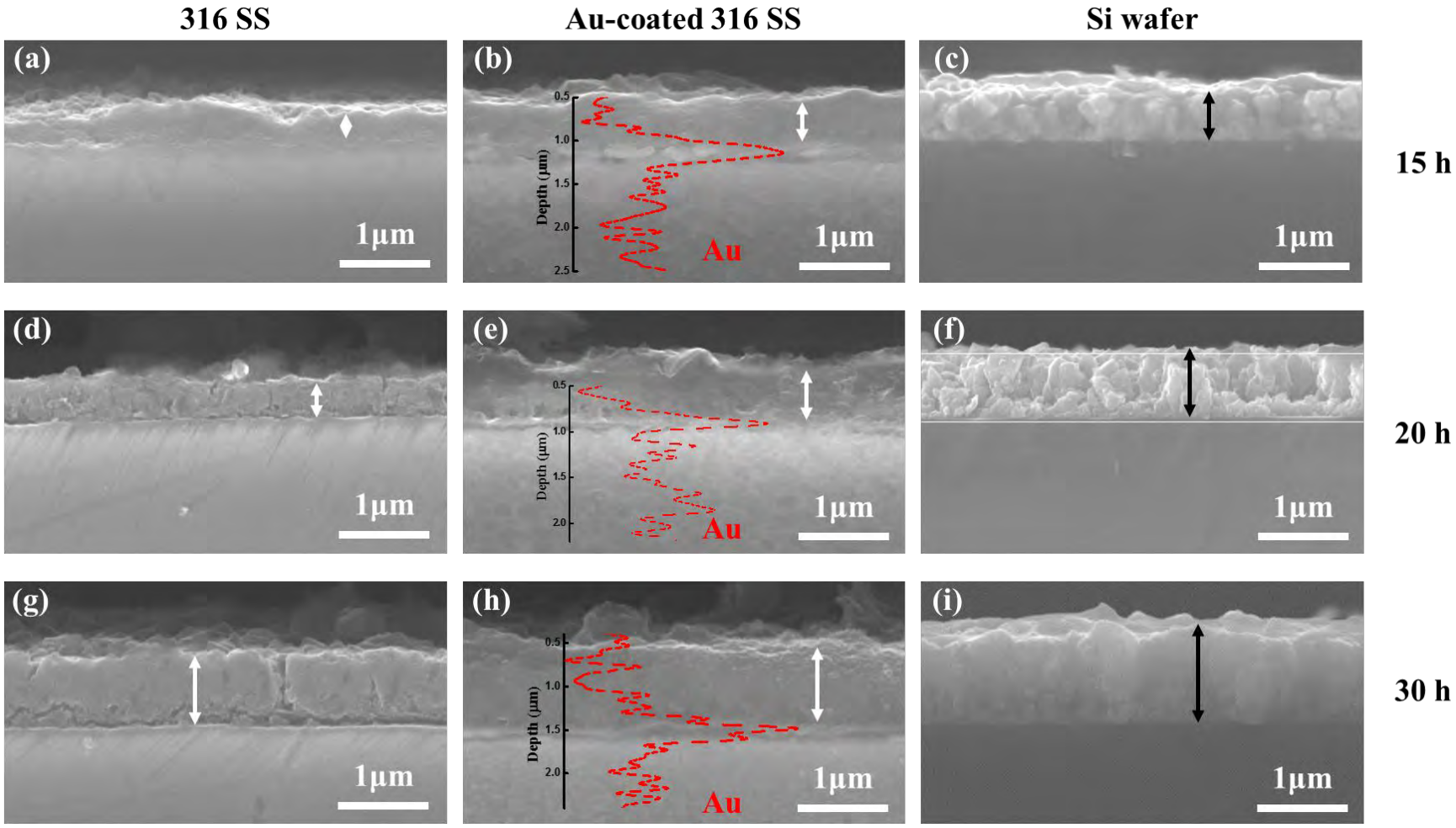

Figure 5.1.6 The cross-sectional SEM images of the deposition layers on different substrates for different treatment duration

(a) 15h (b) Au-15h (c) Si-15h (d) 20h (e) Au-20h (f) Si-20h (g) 30h (h) Au-30h (i) Si-30h

As shown in Figure 5.1.7, the deposition layer thickness is in the order of the Si wafer surfaces > the Au-coated surfaces > the un-coated surface.

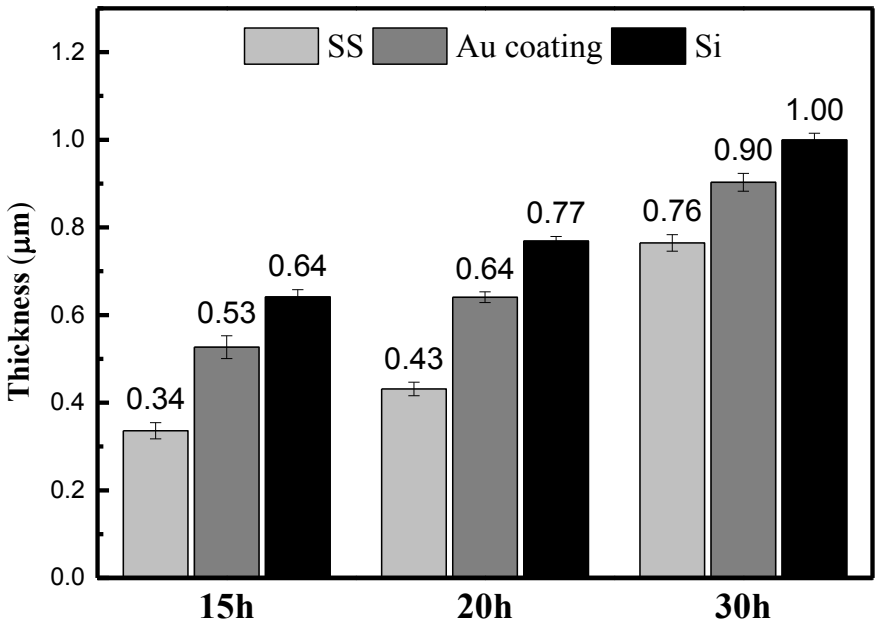

Figure 5.1.7 The thickness of deposition layer on different substrates for different treatment durations

The XRD pattern of 30 h ASPN treated Si wafer is plotted in Figure 5.1.8. The peaks of Fe_4N can be easily found from the XRD pattern. However, no peaks from FeN as reported in literature [210] could be identified, when a glass slide was used as the substrate.

In summary, a deposition layer can be formed during ASPN on bare 316 SS, Au-coated 316 SS and Si wafer surfaces, its thickness increases with treatment duration from 15 to 30 h. When treated for the same conditions, the thickness of the deposition layer increases from un-coated 316 SS through Au-coated 316 SS and to Si wafer but an opposite trend is observed for the thickness of S-phase sublayer: un-coated 316 SS > Au-coated 316 SS > Si wafer surfaces (indeed no S-phase formation).

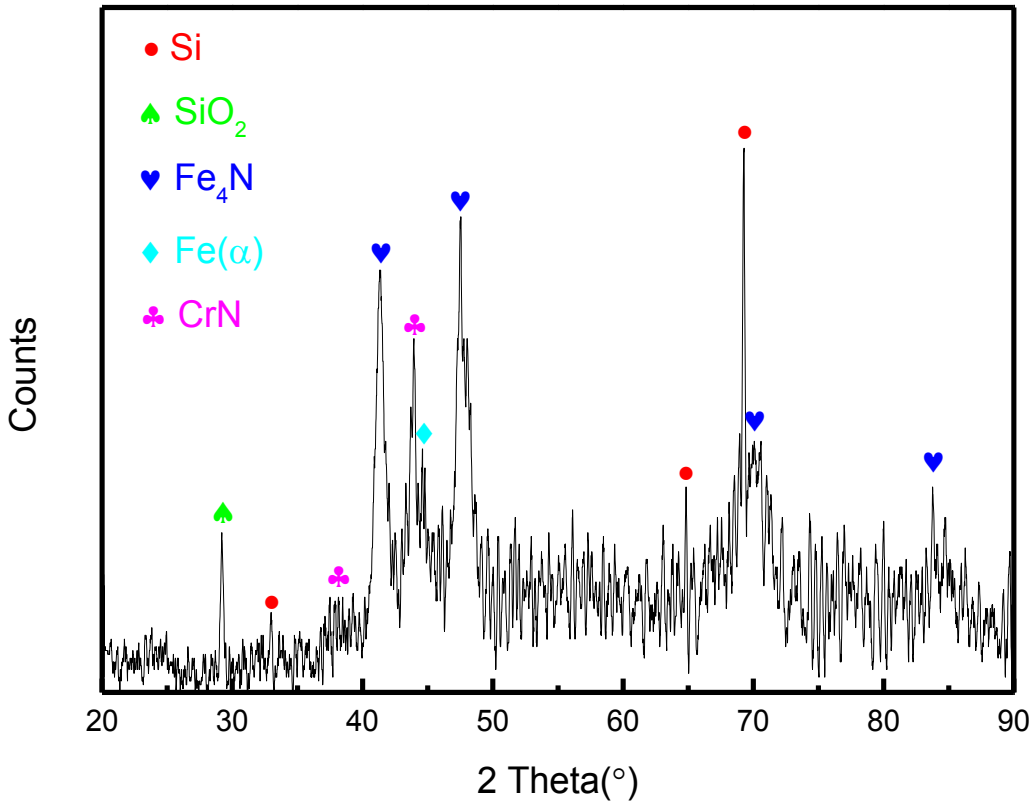

Figure 5.1.8 XRD pattern of Si wafer ASPN treated for 30 h

5.1.2 ASPA(N&Nb)

The mass transfer between the deposition layer and the substrate during active screen plasma co-alloying was investigated using ASPA(N&Nb) as an example. Part of the polished 316 stainless steel surface was coated with gold and ASPA(N&Nb) treated together with Si wafers and the treatment conditions were the same for the additional ASPN treatments discussed in the last section: treatment duration 15 h, 20 h and 30 h, temperature 450 ℃， applied bias 5 %, pressure 0.75 mbar and the length of niobium alloying wire 5 mm.

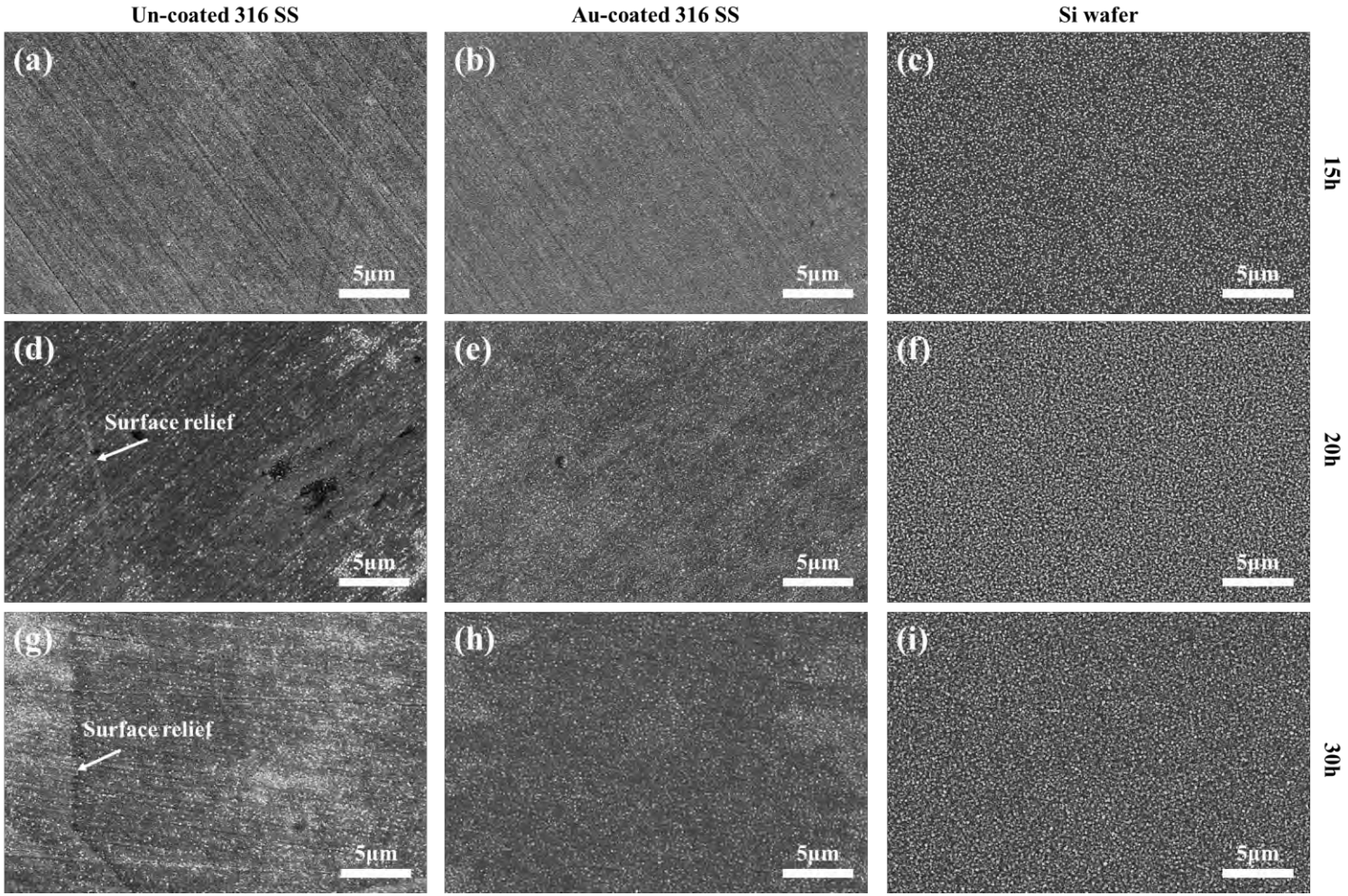

Figure 5.1.9 The low magnification surface morphology SEM images of ASPA(N&Nb) samples

(a) 15h(Nb) (b) Au-15h(Nb) (c) Si-15h(Nb) (d) 20h(Nb) (e) Au-20h(Nb) (f) Si-20h(Nb) (g) 30h(Nb) (h) Au-30h(Nb) (i) Si-30h(Nb)

The low magnification surface SEM images of bare surfaces (15h(Nb), 20h(Nb) and 30h(Nb)), Au-coated surfaces (Au-15h(Nb), Au-20h(Nb) and Au-30h(Nb)) and Si wafer surfaces (Si-15h(Nb), Si-20h(Nb) and Si-30h(Nb)) as a function of ASPA(N&Nb) treatments duration are shown in Figure 5.1.9. Surface relief can be observed from the surface of 20h(Nb) and 30h(Nb) treated bare 316 SS samples, which is intensified with treatment duration. In contrast, no surface relief can be seen from the Au-coated surfaces and Si wafer surfaces even after 30h ASPA(N&Nb) treatments. For the Au-coated surfaces, the initial polishing marks gradually disappear with the increase of treatment duration due to the increase of deposition layer thickness. After treatment, the surfaces of the Si wafer are covered by homogenous fine particles.

It can be seen from the high magnification surface morphology SEM images presented in Figure 5.1.10 that when treated under the same treatment conditions, the particles on the surface of Si wafer are the largest, followed by Au-coated surface and bare 316 stainless steel surface. On the other hand, the density of deposition layer on the bare 316 stainless steel surface is the highest, followed by Au-coated surface and Si wafer surfaces, which follows the opposite trend to the particle size.

The weight percentage ration of N/Nb on different surfaces after 15h ASPA(N&Nb) treatment is shown in Figure 5.1.11. Clearly, when treated under the same conditions, the Si wafer surface exhibits the highest N/Nb ratio, followed by the Au-coated 316 surface, and the bare 316 SS surface reveals the lowest N/Nb ratio. The 20 h and 30 h treated surfaces followed the same trend.

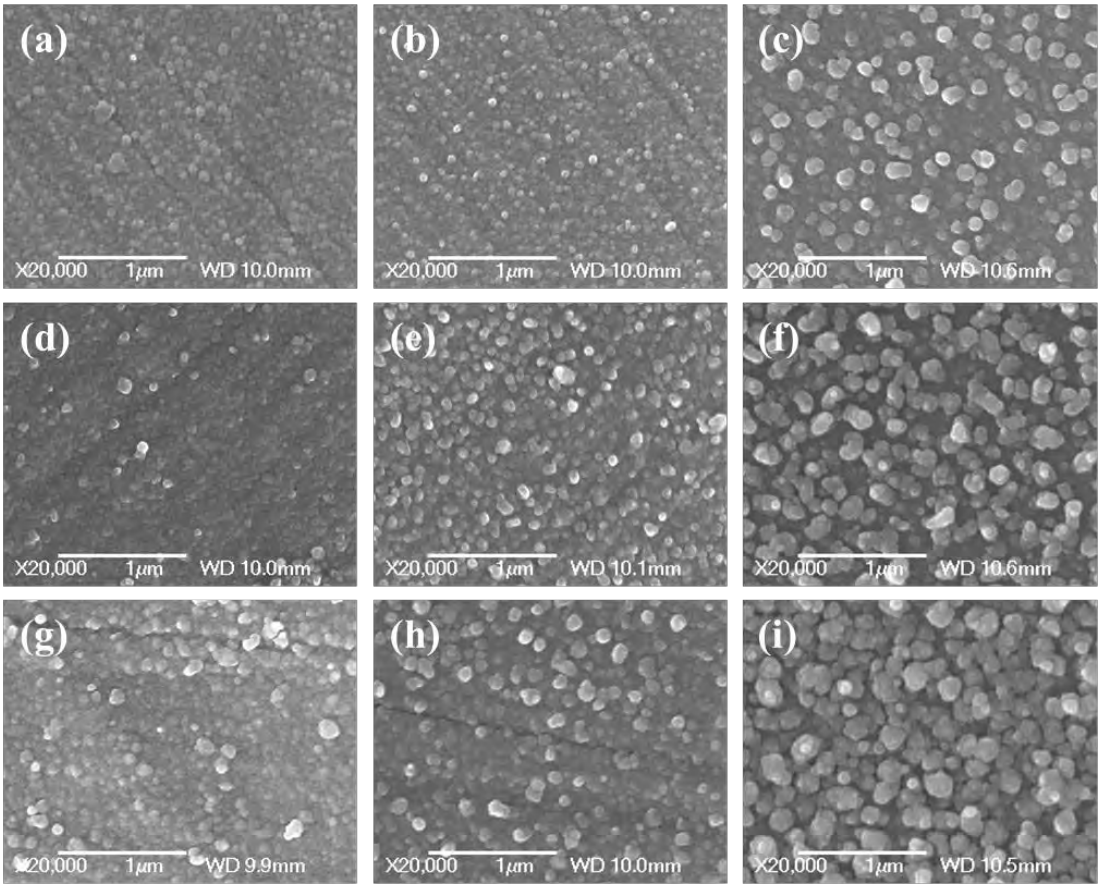

Figure 5.1.10 The high magnification surface morphology SEM images of samples (a) 15h(Nb) (b) Au-15h(Nb) (c) Si-15h(Nb) (d) 20h(Nb) (e) Au-20h(Nb) (f) Si-20h(Nb) (g) 30h(Nb) (h) Au-30h(Nb) (i) Si-30h(Nb)

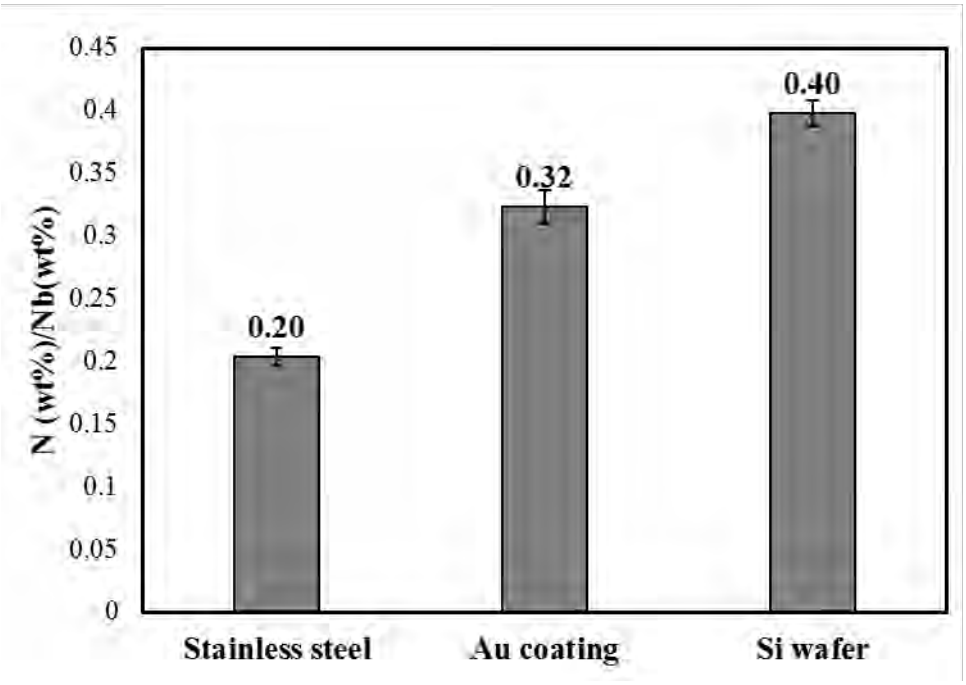

Figure 5.1.11 The weight percentage ration of N/Nb on different surface under 15h

The low magnification cross-sectional SEM images of the un-coated 316 stainless steel surfaces and the Au-coated surfaces are shown in Figure 5.1.12. Expect for Au-15h(Nb) sample, a clear surface layer with different morphology (marked by red arrows) from the substrate can be observed. Referring to the SEM images shown in the previous section, this layer can be identified as S-phase layers. For both bare and Au-coated 316 SS surfaces, the thickness of the S-phase increases with the increase of the treatment duration but the bare 316 SS surfaces show a much thicker S-phase than the Au-coated surfaces when ASPA(N&Nb) treated under the same conditions.

The high magnification cross-sectional SEM images of the deposition layer formed on different substrates are shown in Figure 5.1.13. A deposition layer (marked by black arrows) with a varying thickness can be found from these ASPA(N&Nb) treated samples. For the bare 316 SS surfaces, the deposition layer is very dense and uniform. EDS element line-scannings conducted on the Au-coated surfaces demonstrate the high content of niobium in the deposition layer and identify the location of the Au coatings. The morphology of the deposition layers formed on the Au-coated surfaces differ from that formed on the bare surfaces with uniform thickness and clearly seen particle boundaries. The thickness of the deposition layer formed on the Si wafer surfaces is un-uniform with larger particles than that formed on the Au-coated surfaces.

The thickness of the S-phase formed during ASPA(N&Nb) on different substrates are listed in Figure 5.1.14, which increases with treatment duration for both the uncoated bare surfaces and the Au-coated surfaces. However, the S-phase layer formed on the bare surface is much thicker than that formed on the Au-coated surfaces.

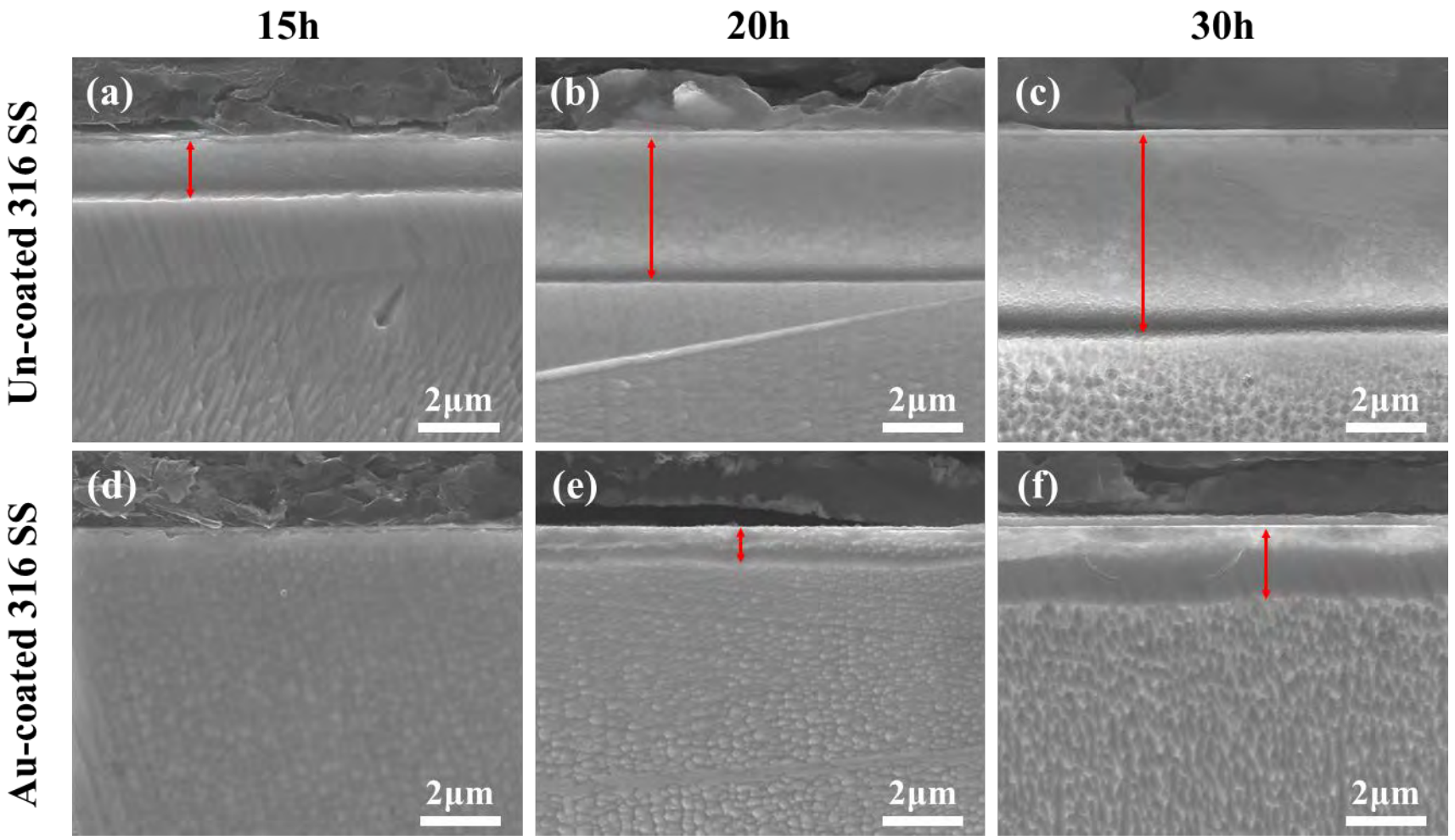

Figure 5.1.12 The low magnification cross-sectional SEM images of S-phase layers

Un-coated surfaces (a) 15h(Nb) (b) 20h(Nb) (c) 30h(Nb); Au-coated surfaces (d) Au-15h(Nb) (e) Au-20h(Nb) (f) Au-30h(Nb)

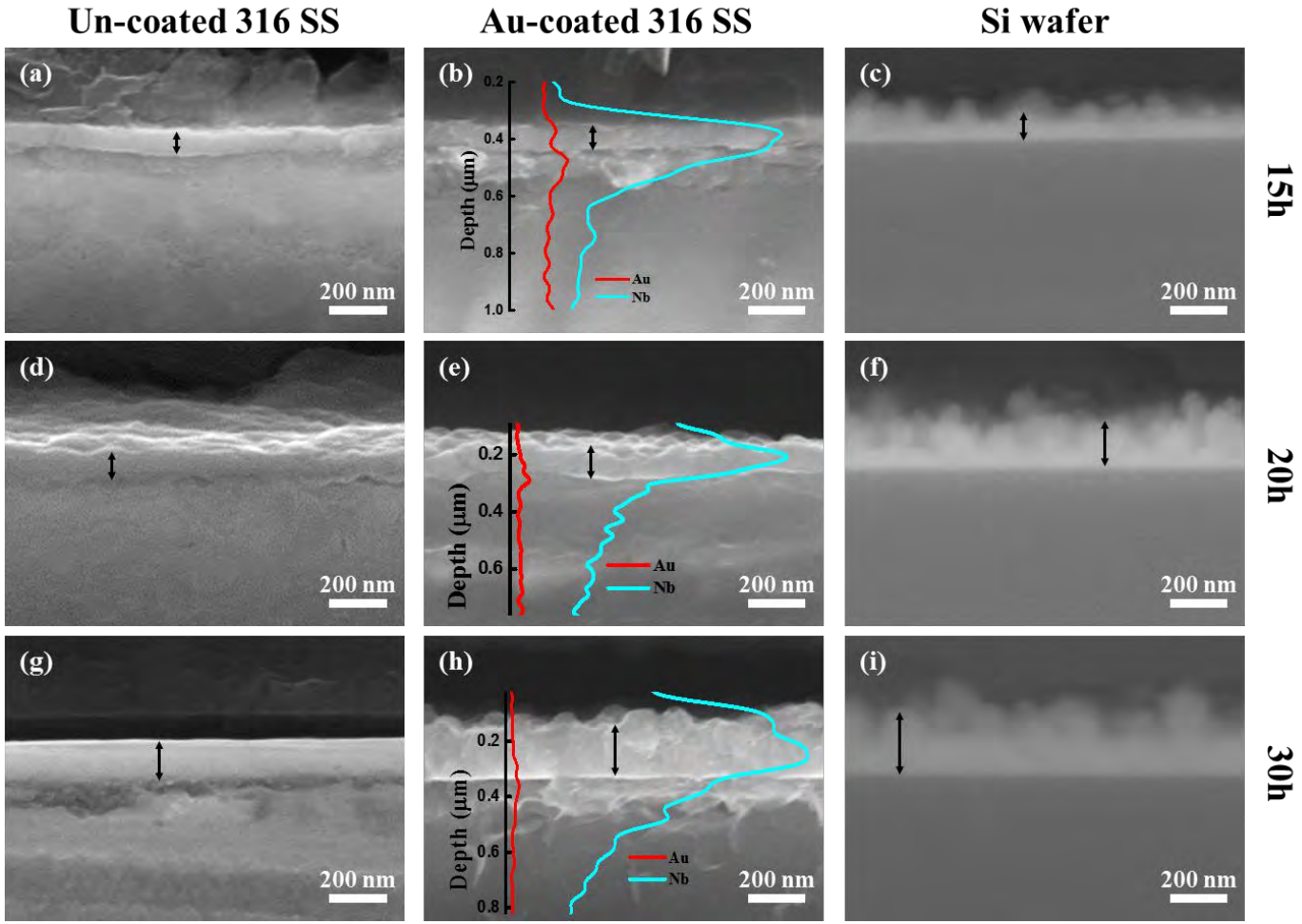

Figure 5.1.13 The high magnification cross-sectional SEM images of the deposition layers

(a) 15h(Nb) (b) Au-15h(Nb) (c) Si-15h(Nb) (d) 20h(Nb) (e) Au-20h(Nb) (f) Si-20h(Nb) (g) 30h(Nb) (h) Au-30h(Nb) (i) Si-30h(Nb)

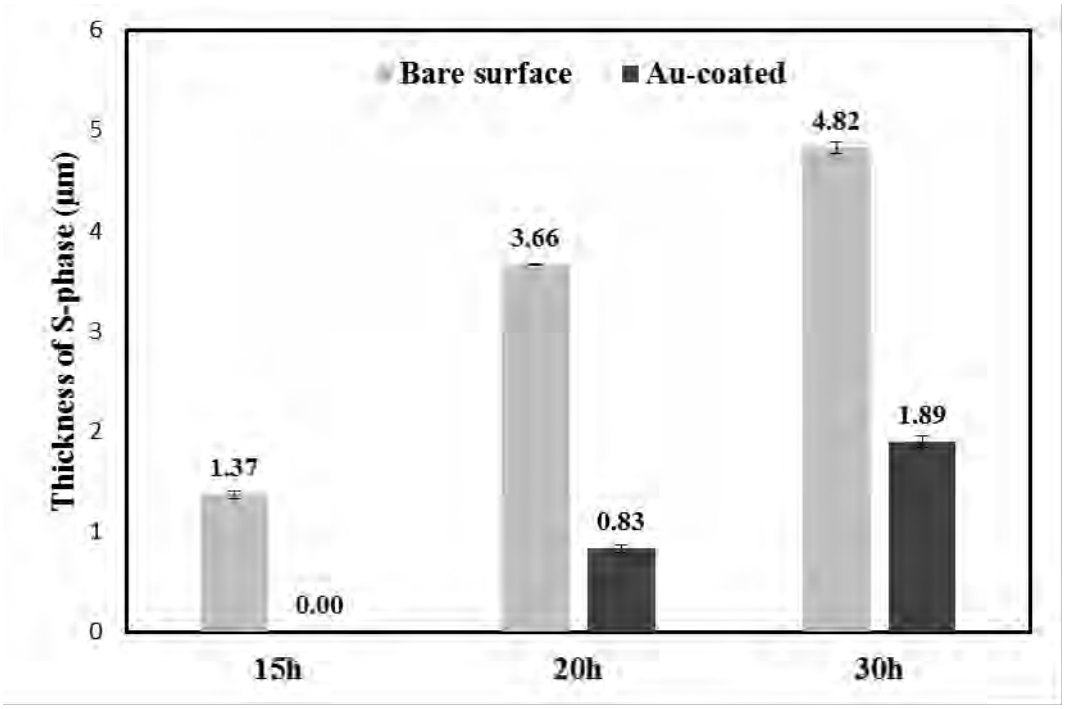

Figure 5.1.14 The S-phase thickness formed on different substrates as a function of treatment duration

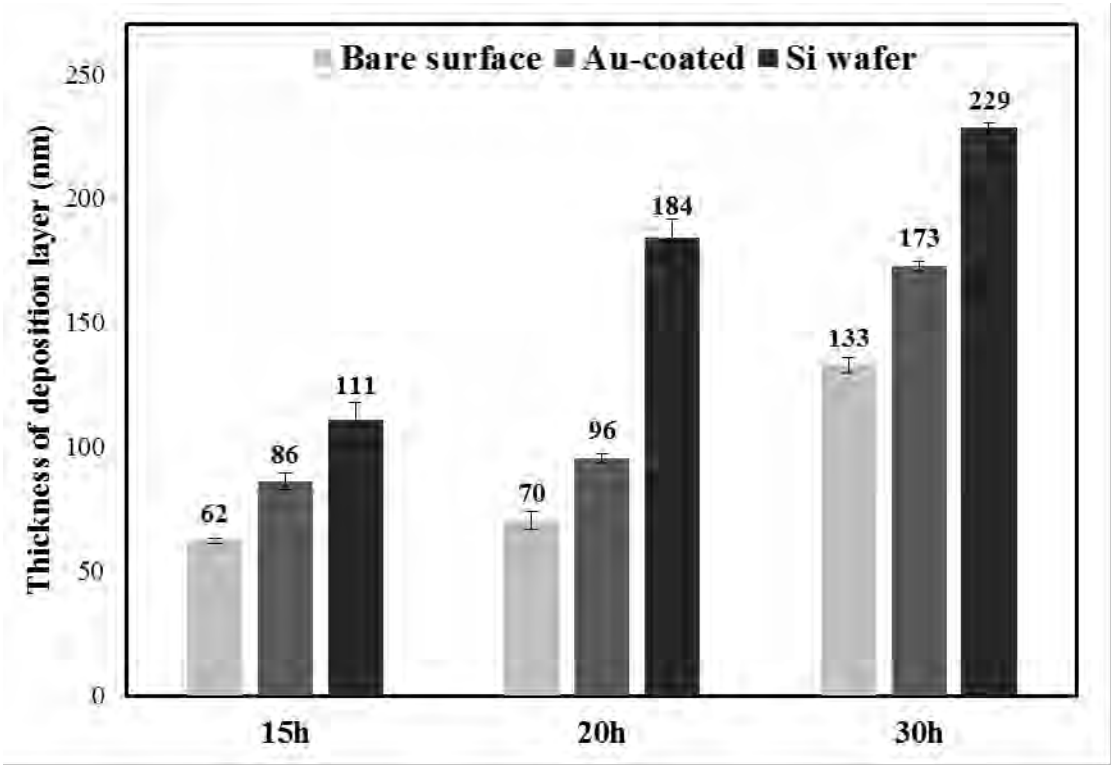

Figure 5.1.15 The thickness of deposition layer on different substrates as a function of treatment duration

The thickness of the deposition layers formed is compared in Figure 5.1.15. In general, the thickness of the deposition layer increases with the treatment duration for all three surfaces. When treated under the same duration, the deposition layer formed on the Si wafer surfaces is the thickest, followed by that formed on the Au-coated surface, and the deposition layer formed on the bare surface is the thinnest.

In summary, when treated under the same conditions using the same substrate, similar surface layer structure and treatment duration effect were observed in both ASPA(N&Nb) and ASPN. Both the surface deposition layers (Figure 5.1.7 vs Figure 5.1.15) and the S-phase layer (Figure 5.1.5 vs Figure 5.1.14) are thicker when formed by ASPN than by ASPA(N&Nb).

5.1.3 Effect of substrate on layer formation

It can be seen from the additional results presented above in Sections 5.1.1 and 5.1.2 that when treated under the same conditions using the same substrate, the two different treatments, namely the ASPN and the ASPA(N&Nb), produced the same surface layer structures: a surface deposition layer only formed on Si wafer but a duplex structure (a deposition layer followed by a S-phase layer) formed on 316 SS (whether it is coated or not); the surface deposition layer is much thicker when formed on the surface of Si wafer than on Au-coated surface and bare 316 SS surface.

The difference in deposition layer thickness can be explained by the different responses of the substrate surfaces to the diffusion of nitrogen. It is known that the solid solubility of nitrogen in Si is extremely low (9×10^{-6} at%) [240]. Therefore, no appreciable diffusion layer will be formed in Si wafer surface when treated at such low temperatures; hence, Si wafer surface completely blocked the diffusion of active nitrogen between the deposition layer and the Si substrate, thus all the deposited

materials remaining on the surface without any mass transfer. Therefore, the deposition layer thickness is the highest on the Si wafer surface.

The Au-coating on the stainless steel surface could retard the diffusion of active nitrogen but cannot completely block the mass transfer between the deposition layer and the substrate. This is proved by the formation of S-phase underneath the surface deposition layer; however, the S-phase layer is much thinner when formed on the Au-coated than uncoated bare 316 SS surfaces. Therefore, the thickness of the deposition layer on Au-coated 316 surface is thinner than that on the Si wafer surface but thicker than that on the bare surface where the active nitrogen could easily diffuse into the bare substrate without any retardation.

The above discussion on mass transfer and substrate effect is fully supported by ASPN (Figure 5.1.7) and ASP co-alloying with N and Nb i.e. ASPA(N&Nb) (Figure 5.1.15).

Not only is the thickness of the deposition layer but also the content of nitrogen affected by the different substrate. As can be seen from the surface EDS results shown Figure 5.1.11, the ratio of N and Nb, which are introduced to the surface simultaneously during ASPA(N&Nb) treatment, on different surfaces is in the order of Si wafer > Au-coating > bare surface. This indicates that the relative content of nitrogen left in the surface deposition layer is also in the same order. The reduction of nitrogen content is related to the decomposition of the deposited material and the inward diffusion of the released nitrogen atoms. This mechanism is strongly supported by the nitrogen diffused into the substrate. As shown in Figure 5.1.3, a much larger amount of nitrogen as evidenced by the larger area below the nitrogen depth profiles was introduced into the uncoated 316 SS than into the Au-coated 316

SS surface, thus forming a thicker S-phase layer with a high nitrogen content in the former than in the latter (Figure 5.1.5 and Figure 5.1.14).

Based on the above results, one conclusion can be drawn that nitrogen mass transfer takes place between the deposition layer and the substrate by the decomposition of the nitrides in the deposition layer and the subsequent inward diffusion of active nitrogen atoms. This mass transfer leads to the reduction of layer thickness and nitrogen content of the surface deposition layer, and the formation of S-phase sublayer in the substrate.

5.2 Surface layer forming mechanisms

In this work, in addition to nitrogen three different kinds of alloying elements were selected to conduct the active screen plasma co-alloying (ASPA) treatments, namely silver, niobium and platinum. In this section, the potential mechanisms involved are discussed by comparing with that of ASPN because the latter is better understood than the former.

5.2.1 ASPA(N&Ag)

The S-phase thickness of ASPN and ASPA(N&Ag) samples, treated under the same nitriding conditions, are compared in Figure 5.2.1. The S-phase layer of the ASPN sample is thicker than that of the ASPA(N&Ag) sample. In addition, the nitrogen depth profile shown in Figure 5.2.2 reveals that the nitrogen content in the S-phase of the ASPN sample is also higher than that of the ASPA(N&Ag) sample.

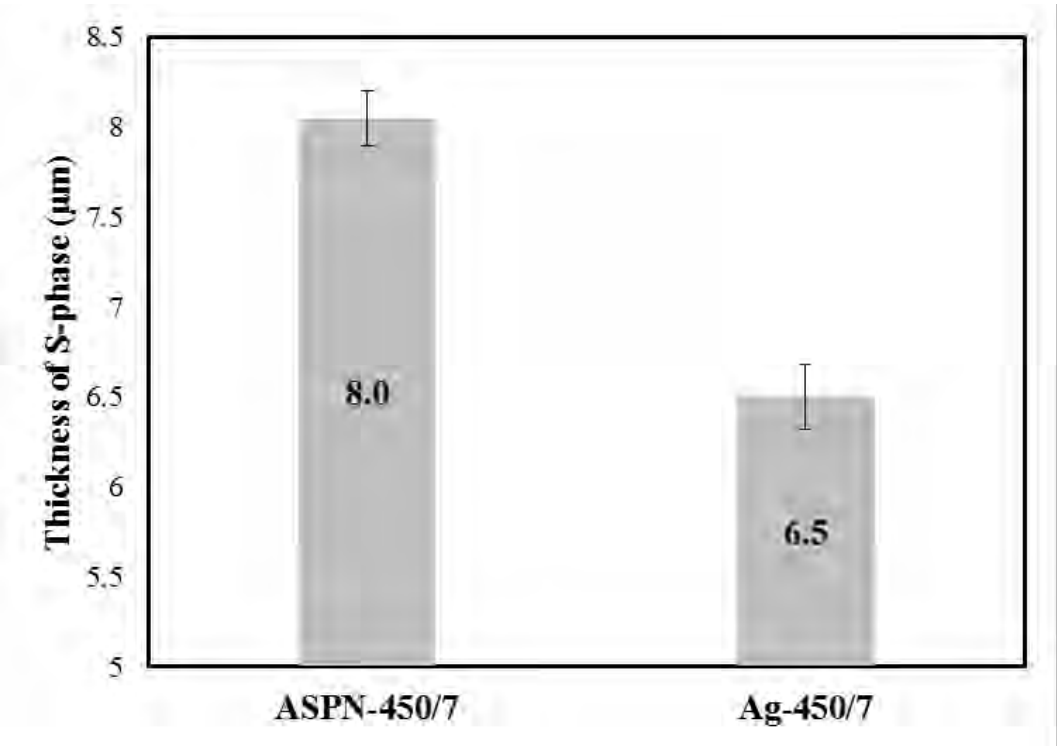

Figure 5.2.1 S-phase thickness of ASPN and ASPA(N&Ag) samples

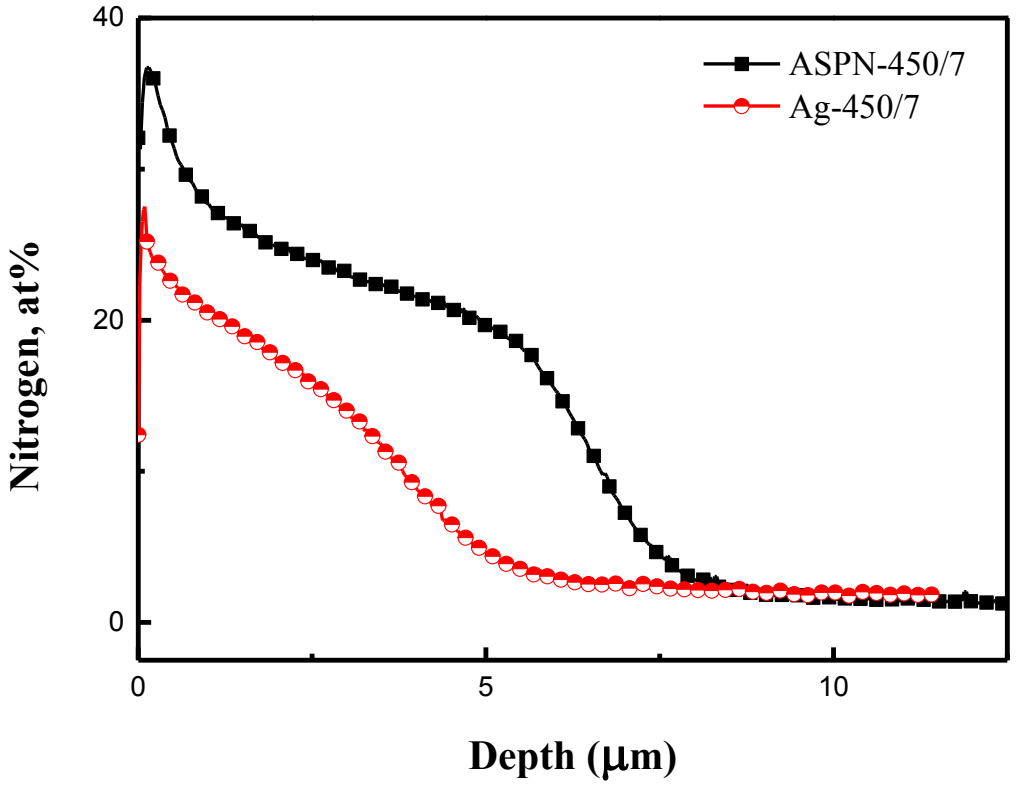

Figure 5.2.2 The GDS nitrogen depth profiles of ASPN and ASPA(N&Ag) samples

The XRD patterns of ASPN and ASPA(N&Ag) are plotted in Figure 5.2.3. As discussed in Section 4.3.2, not only S-phase peaks, but also silver peaks can be detected from the ASPA(N&Ag) pattern. Comparing the S-phase peaks of the ASPN sample and the ASPA(N&Ag) sample reveals that the peak intensity of the former is stronger than that of the latter. Apart from that, the S-phase peak position of the ASPN sample is slightly shifted to lower angle than that of the ASPA(N&Ag) sample. The difference in the S-phase XRD peaks might be related to the relatively lower nitrogen content in the S-phase of the ASPA(N&Ag) sample shown Figure 5.2.2.

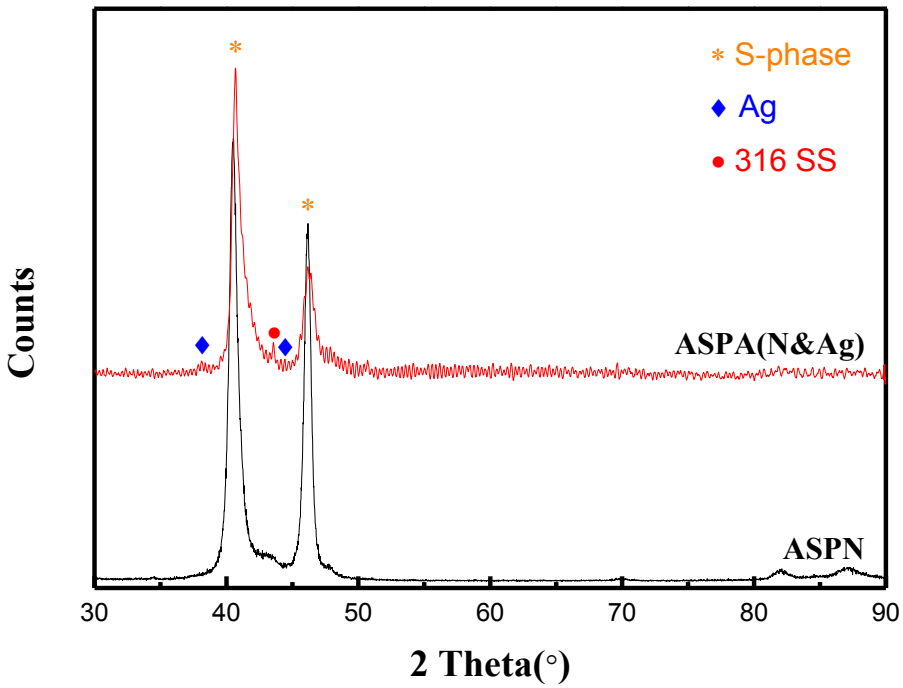

Figure 5.2.3 The XRD patterns of ASPN and ASPA(N&Ag) samples

The cross-sectional TEM observation of the deposition layer on the surface of ASPA(N&Ag) sample was conducted to better understand the microstructure of the deposition layer (Figure 5.2.4). A dense multi-grain columnar deposition layer can be found on the surface with a well-defined interface. The analysis of the SAD patterns from the deposition layer (Figure 5.2.4 (b)) reveals that, the discontinuous rings can be identified as fcc structured Ag (ASTM No. 01-087-0719) and Fe_4N-like M_4N (M =

Fe, Cr, Ni) contributes to the bright arc rings, indicating a group of grains with a similar crystal orientation. Underneath the deposition layer, fcc structured S-phase pattern is identified, as can be seen in Figure 5.2.4 (c).

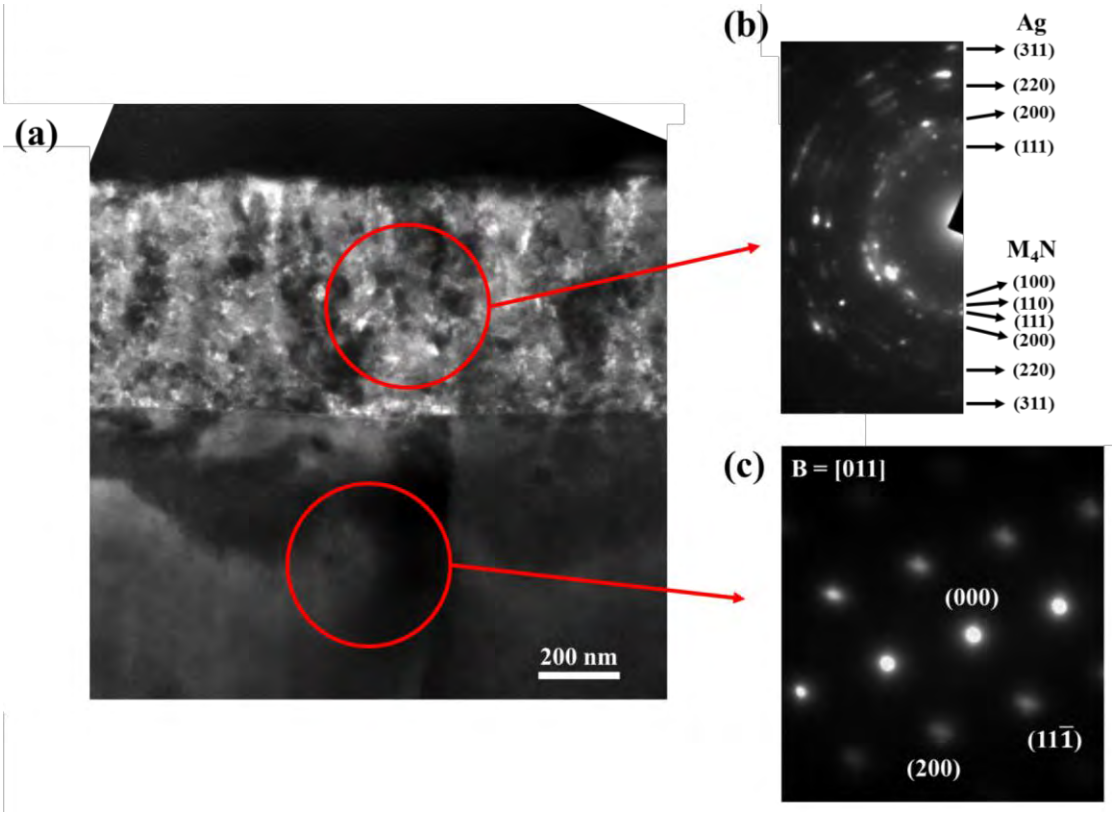

Figure 5.2.4 (a) Cross-sectional TEM microstructure of Ag-450/15 sample and corresponding SAD patters of (b) the deposition layer and (c) the substrate

In order to investigate the distribution of the silver grains, EDS analysis was conducted during TEM observation (Figure 5.2.5). The spectra from the polygon grains (such as "1" and "3" in Figure 5.2.5 (a)), uniformly distributed in the deposition layer, shows higher intensity of Ag (point "1" 26.6 at%, point "3" 40.25 %) than the ones from point "2" (10.7 at%), where mainly contains M_4N grains with Ag particles embedded.

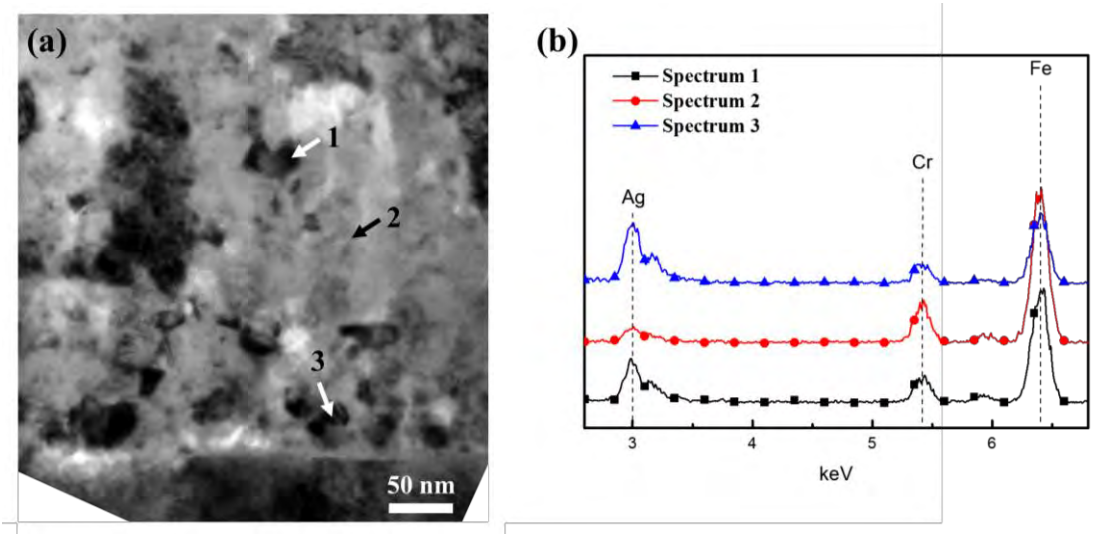

Figure 5.2.5 EDS analysis of Ag-450/15 sample (a) TEM image (b) EDS spectra from spots 1, 2 and 3 in (a)

From the TEM analysis, it is clear that the deposition layer of ASPA(N&Ag) composes of nano-crystalline M_4N and uniformly distributed silver particles.

As discussed in Section 5.1, in order to investigate the microstructure and composition of surface deposition layer without the influence of the stainless steel substrate, Si wafers were treated together with 316 SS samples using the same ASPA(N&Ag) treatment parameters. This is because by using Si wafer as a substrate, the mass transfer between the deposition layer and the stainless steel substrate could be avoided or minimised.

The SEM surface morphology of Si wafers after ASPA(N&Ag) treatment as a function of treatment duration are shown in Figure 5.2.6, with the high magnification SEM images as inlet. After 7 h treatment (Figure 5.2.6 (a)), many small lumps with a diameter of 800 nm could be observed on the surface consisting of a fine deposited particles. When increasing the treatment duration to 10 h, the boundary of the lumps

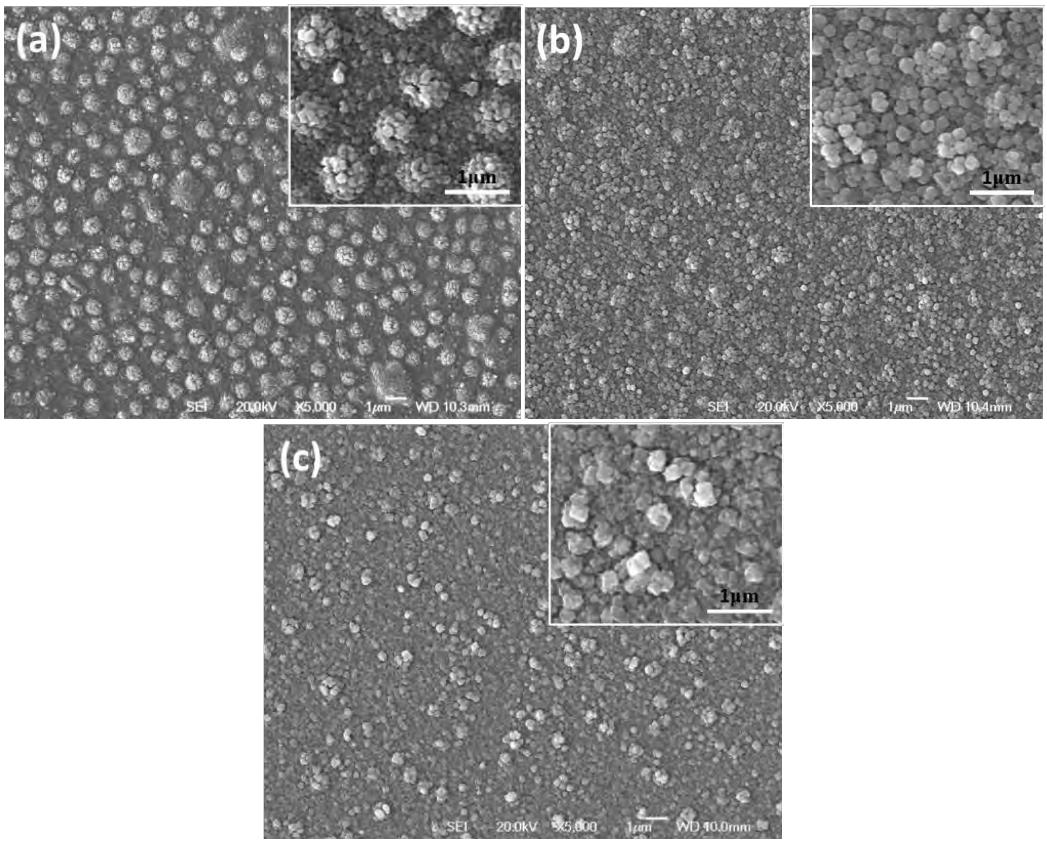

Figure 5.2.6 Surface SEM images of ASPA(N&Ag) treated Si wafer as a function of treatment duration (a) 7h, (b) 10h and (c) 15h

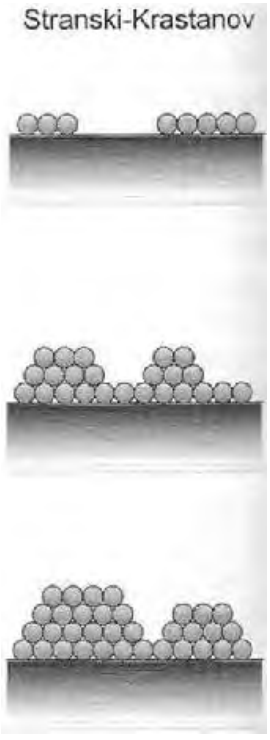

Figure 5.2.7 The schematic diagram of Stranski-Krastanov mode [241]

becomes blurry (Figure 5.2.6(b)) and these lumps almost disappear after the 15 h treatment (Figure 5.2.6(c)). The change of the surface morphology with the treatment duration implies that the growth of deposition layer follows the layer plus island or Stranski-Krastanov mode (Figure 5.2.7) [241], which is similar with the ASPN treatment [197].

The cross-sectional SEM images of the deposition layer on Si wafer after ASPA(N&Ag) treatment are exemplified in Figure 5.2.8. It can be seen from the cross-sectional microstructures that the deposition layer consists of small particles, which is in agreement with the Stranski-Krastanov mode. The thickness of deposition layer formed on the 316 SS and Si wafer surface under the same ASPA(N&Ag) conditions are compared in Figure 5.2.9. Similar to the deposition layer on the surface of stainless steel, the layer thickness on Si wafer surfaces increases with the increase of treatment duration, but thicker than that of the former.

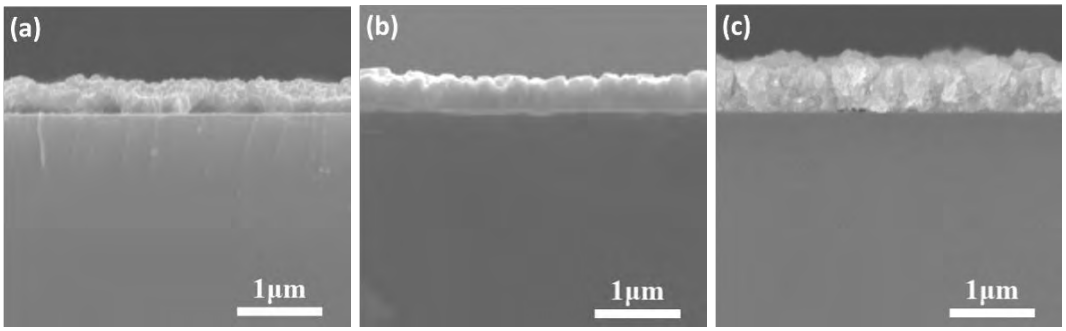

Figure 5.2.8 Cross-sectional SEM images of Ag deposition layer on Si wafer
(a) 7h (b) 10h (c)15h

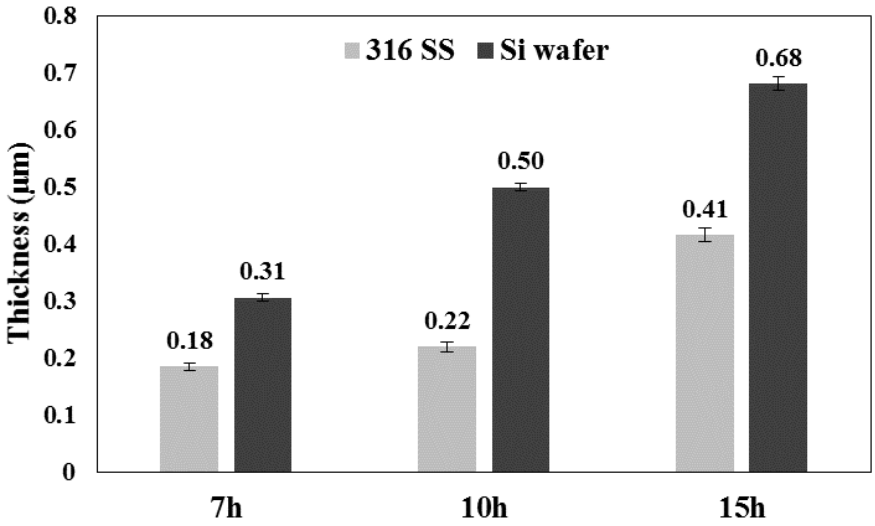

Figure 5.2.9 The comparison of the thickness of deposition layer formed on different substrates during ASPA (N&Ag)

The XRD spectra collected from the ASPA(N&Ag) treated Si wafers are drawn in Figure 5.2.10. Apart from the peaks from the Si substrate, some peaks of Ag and Fe_4N could be identified from the XRD spectra of all the treated Si wafers, and the intensity of those peaks increases with treatment duration. This finding is in agreement with the TEM analysis (Figure 5.2.4 and Figure 5.2.5).

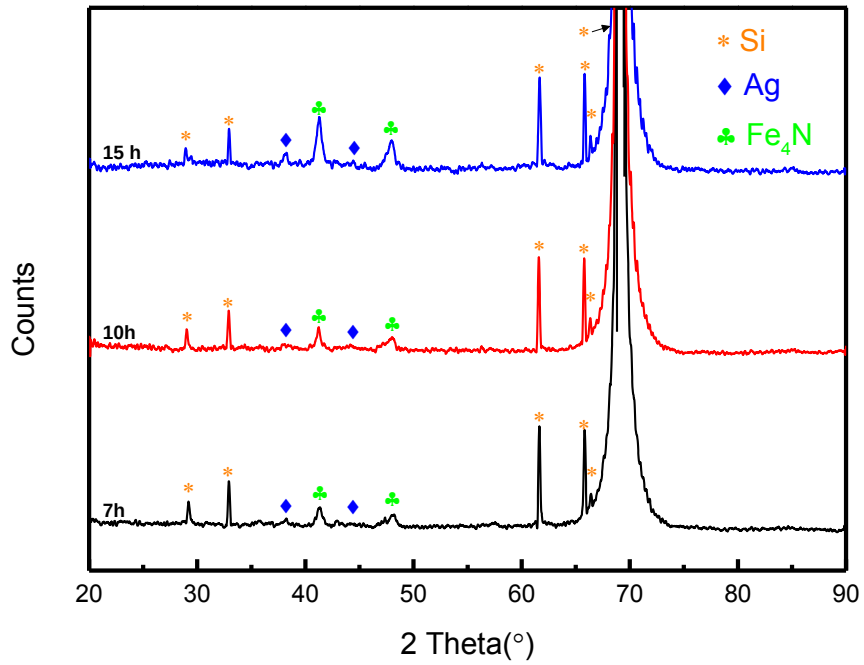

Figure 5.2.10 XRD patterns of ASPA(N&Ag) treated Si wafer

It can be deduced from the above results that iron nitrides and silver are sputtered from the screen and co-deposited onto the surface of treated samples during the ASPA(N&Ag) treatment. As discussed in Section 2.5.2, the iron nitrides in the deposition layer is unstable and tends to be decomposed to release active nitrogen atoms. When deposited on austenitic stainless steel, these active nitrogen atoms will diffuse inward to the substrate to form S-phase. This leads to the reduction of deposition layer thickness (Figure 5.2.9), which is in full agreement with the results in Section 5.1. From the comparison between ASPN and ASPA(N&Ag) treatment, the latter treatment produces thinner and lower-nitrogen content S-phase, which is caused by the addition of silver particles in the deposition layer.

The effect of silver addition on the surface layer forming of ASPA(N&Ag) treatment can be explained by the proposed mechanism shown in Figure 5.2.11. Compared with the ASPN, the deposited silver particles sputtered from the Ag-containing lid occupy some sites on the surface and retard the diffusion of released nitrogen into the substrate. The silver particles embedded in the deposition layer also retard the diffusion of nitrogen, released from the deposition layer above. Hence, less nitrogen could diffuse into the matrix lattice, leading to the thinner S-phase layer (Figure 5.2.1) and lower nitrogen content in the S-phase (Figure 5.2.2).

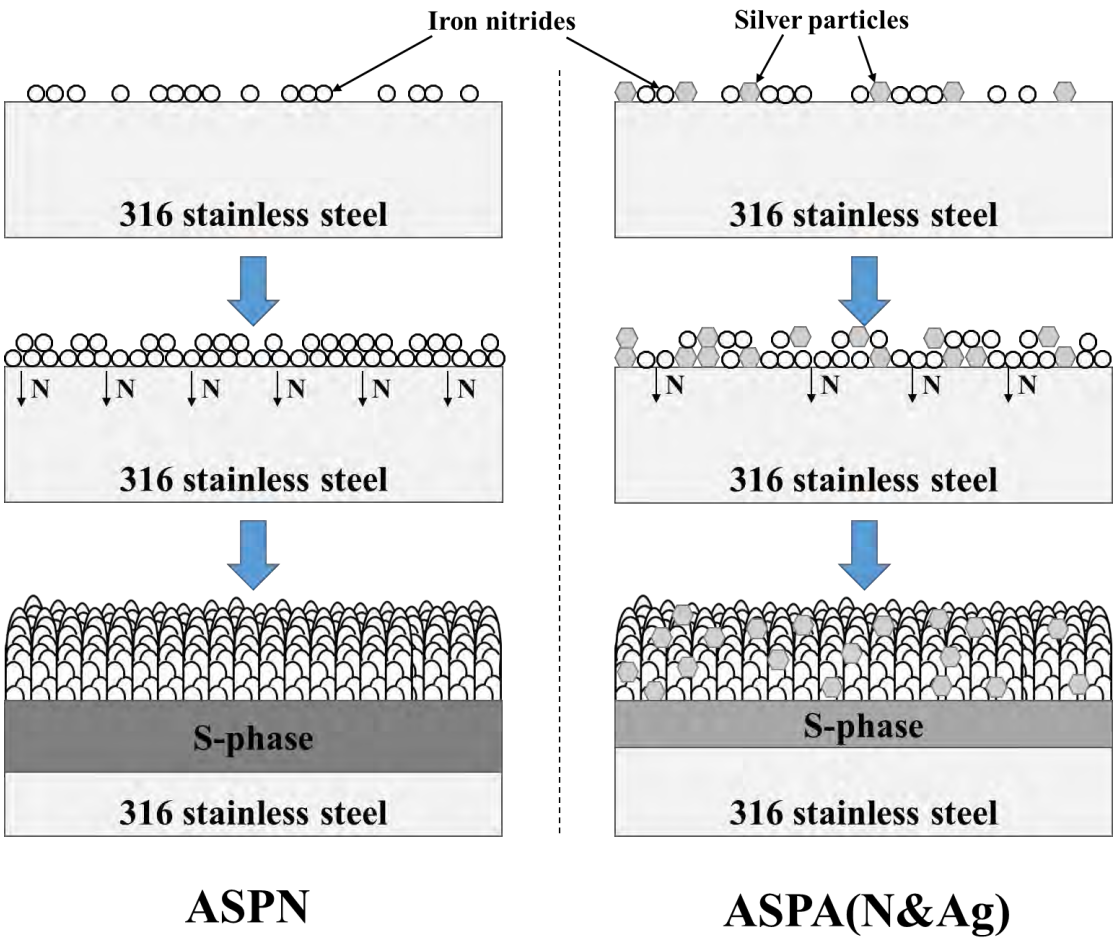

Figure 5.2.11 Schematic mechanisms of ASPN (left-hand side) and ASPA(N&Ag) (right-hand side)

5.2.2 ASPA(N&Nb)

In order to better understand the surface layer forming mechanism of the ASPA(N&Nb) treatments, the ASPN sample (ASPN-450/10/5) and the ASPA(N&Nb) sample (Nb-450/10/5-5mm) treated with an alloying wire length in 5 mm under the same conditions (450 °C, 10 h, 0.75 mbar, 5 % bias) are compared.

The cross-sectional SEM images and the S-phase thickness of the ASPN-450/10/5 sample and the Nb-450/10/5-5mm sample are shown in Figure 5.2.12 and Figure 5.2.13, respectively. It can be clearly seen that both the ASPN treatment and the ASPA(N&Nb) treatment produced a S-phase layer on the top of the plasma treated

samples (Figure 5.2.12); however, the thickness of the S-phase layer formed on the ASPN-450/10/5 sample is around twice as that formed on the Nb-450/10/5-5mm sample. Not only is the S-phase thickness different for those two samples, the nitrogen content profiles (Figure 5.2.14) against depth also show a great difference. As compared in Figure 5.2.14, the nitrogen content of the ASPN treated sample is much higher than that of the ASPA(N&Nb) treated sample. These findings are similar with that of ASPA(N&Ag).

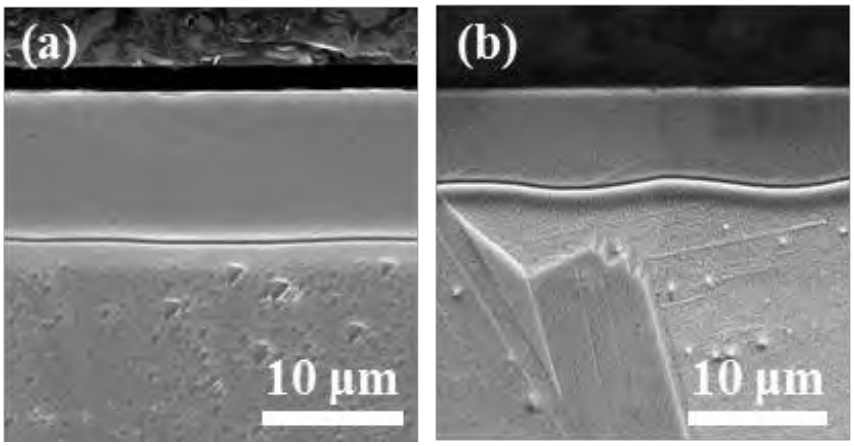

Figure 5.2.12 The cross-sectional SEM images of ASPN sample and ASPA(N&Nb) sample treated at 450 ℃ for 10 h with 5 % bias

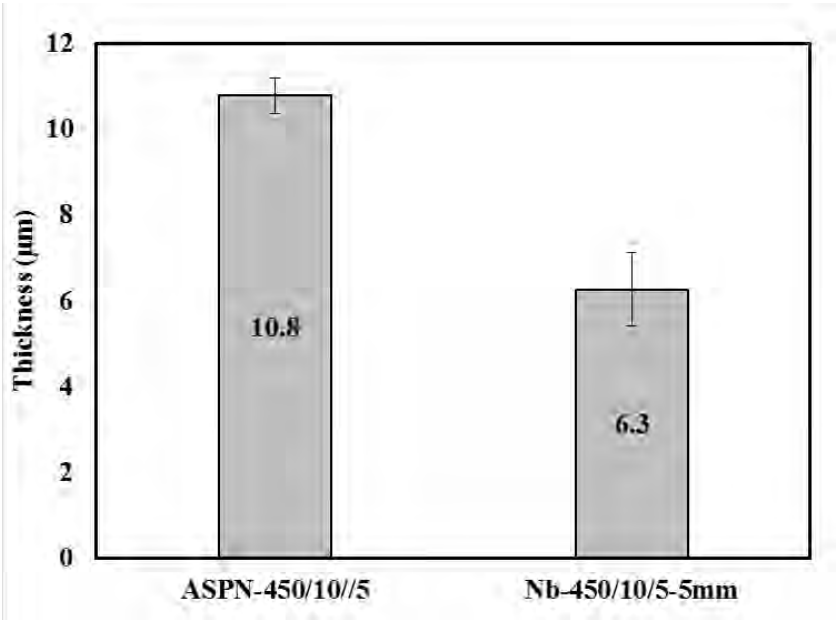

Figure 5.2.13 The S-phase thickness of ASPN and ASPA(N&Nb) samples treated at 450 ℃ for 10 h with 5 % bias

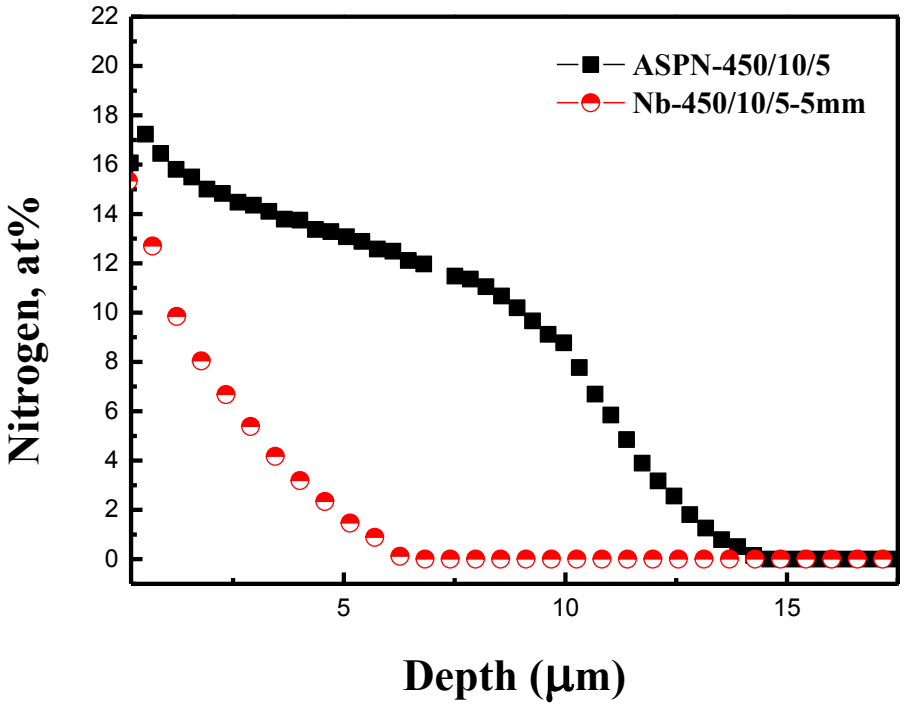

Figure 5.2.14 The atomic percentage of nitrogen profile against depth of ASPN and ASPA(N&Nb) samples treated at 450 ℃ for 10 h with 5 % bias

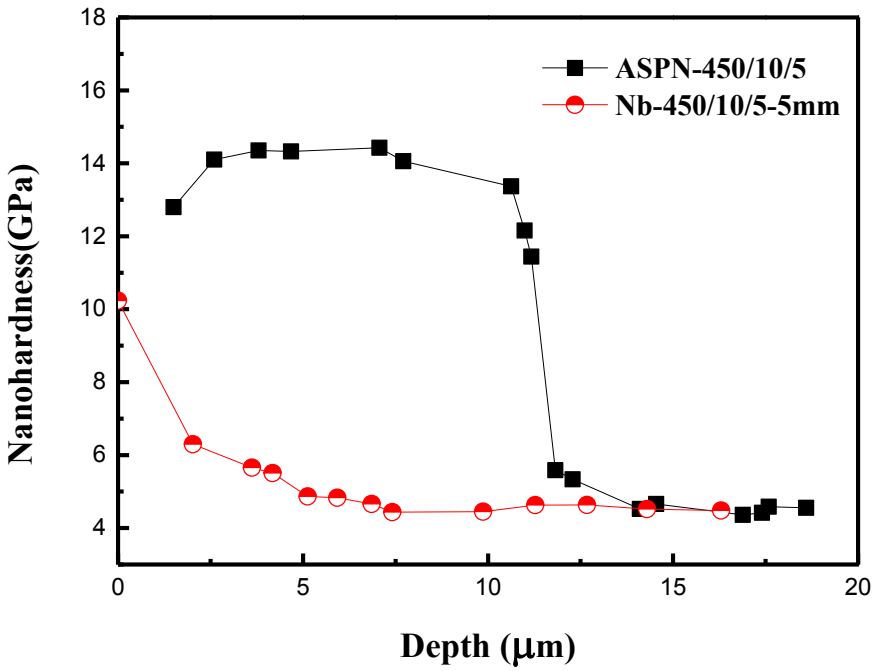

Figure 5.2.15 The nano-hardness profiles of ASPN and ASPA(N&Nb) samples treated at 450 ℃ for 10 h with 5 % bias

The comparison of nano-hardness depth profiles of ASPN sample and ASPA(N&Nb) sample is showed in Figure 5.2.15. The nano-hardness profiles show a similar trend as that of the nitrogen profile shown in Figure 5.2.14. The hardness of the S-phase case in ASPN-450/10/5 is about 14 GPa and the high hardness region is extended to a depth around 10 μm. Whilst the hardness of S-phase in the Nb-450/10/5-5mm sample is only around 6 GPa and it decreases continuously with the depth to the substrate value at about 5 μm below the surface.

Clearly, more nitrogen is introduced into the ASPN treated sample than into the ASPA(N&Nb) treated sample when treated under the same conditions. The major different in nitrogen mass transfer should be attributed to the Nb introduced during the ASPA(N&Nb) treatment as a Nb-containing active-screen lid was used. It is known that niobium has a high affinity with nitrogen as it is a strong nitride former [242], and during the ASPA(N&Nb) treatments most of the nitrogen would react with niobium to form niobium nitrides (Figure 4.4.21 and Figure 4.4.24).

In order to better understand the influence of niobium nitrides on the surface layer forming of ASPA(N&Nb) treatment, TEM analysis of ASPA(N&Nb) treated sample was conducted. It can be seen from Figure 5.2.16 (a), a dense, columnar structured deposition layer is formed on the surface. On the top surface, a few small hillocks (marked by arrows), composed of nano-crystalline, can be found, which are the white contrasted particles observed in surface SEM images (Figure 4.4.29). SAD pattern (Figure 5.2.16 (c)) taken from the deposition layer (Figure 5.2.16 (b)) shows a dominant set of fcc structured rings, and the d-spacing values are close to the nitride of NbN. A few weak diffraction spots, with the d-spacing of Fe_4N, were also identified (marked by arrows). SAD pattern shown in Figure 5.2.16 (d) was taken from the interface between the deposition layer and the substrate. A [$\bar{1}$12] fcc pattern

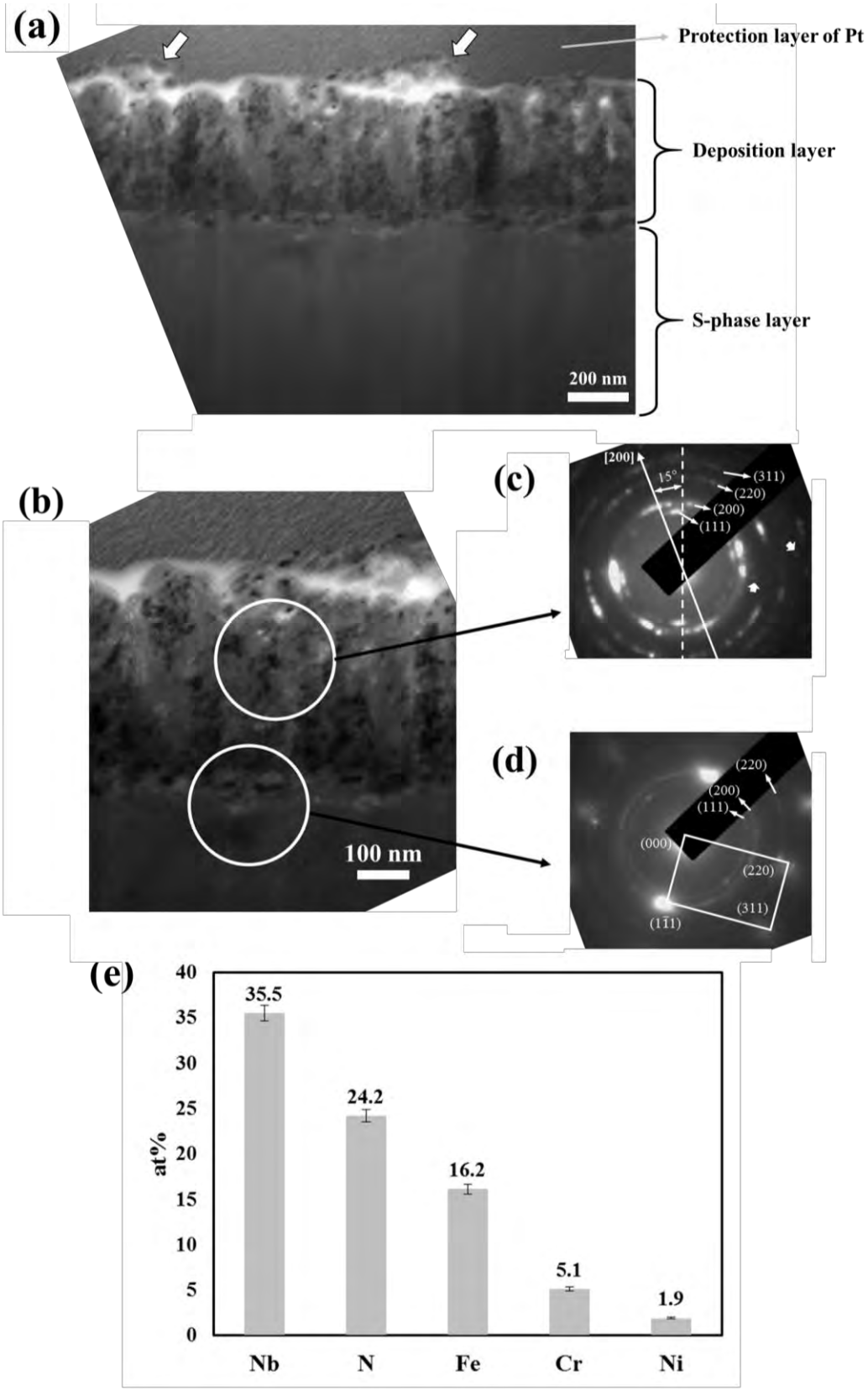

Figure 5.2.16 TEM analysis of Nb-450/20/(5+10)-5mm sample (a) low magnification cross-sectional TEM image (b) high magnification cross-sectional TEM image (c) SAD pattern of deposition layer (d) SAD pattern of interface (e) EDS results of deposition layer

from the substrate and a set of fcc rings from the top layer, can be indexed. The d-spacing calculation of [$\bar{1}$12] pattern confirmed that the surface of the substrate was transformed to S-phase during the treatment and the d-spacing of the rings in Figure 5.2.16 (d) are similar to the d-spacing of NbN in Figure 5.2.16 (c). Compare the Figure 5.2.16 (c) with Figure 5.2.16 (d), the rings in Figure 5.2.16 (d) are nearly full, fine and diffused, while the rings in Figure 5.2.16 (c) are discontinued, thick and diffused. Figure 5.2.16 (e) is the EDS analysis of the chemical composition of the deposition layer, which shows 35 at% of Nb, followed by 24.2 at% of N and 16.2 at% of Fe, small amount of Cr and Ni can also been detected.

Based on the TEM observation and the EDS analysis, it can be concluded that the dominant phase structure of the deposition layer is an fcc structured, NbN-like MN nitride (M = Nb, Fe, Cr, Ni) or Fe, Cr, Ni replaced some of Nb atom positions in NbN phase. The initially deposited particles were fine and randomly oriented as evidenced by the full and fine diffraction rings observed around the interface (Figure 5.2.16 (d)). When the layer was growing, formed columnar grains with preferred orientations of [200] direction in a included angle of 15° to the surface (see Figure 5.2.16 (c)).

Base on the above results, the mechanism of ASPA(N&Nb) could be schematically presented in Figure 5.2.17. In the case of ASPA(N&Nb) treatments, the main components of the deposition layer are NbN-like nitrides and iron nitrides. When a relatively low bias ($\leq$ 5 %) is applied, the NbN-like nitrides cannot dominate the deposition layer, and the amount of iron nitrides is large enough to release nitrogen to the substrate to form an S-phase layer. But compared with the ASPN, the formed S-phase during ASPA(N&Nb) is much thinner. When a high bias is applied, the NbN-like nitrides dominate the deposition layer, and thus the small amount of iron nitrides cannot yield enough nitrogen to form S-phase on the subsurface.

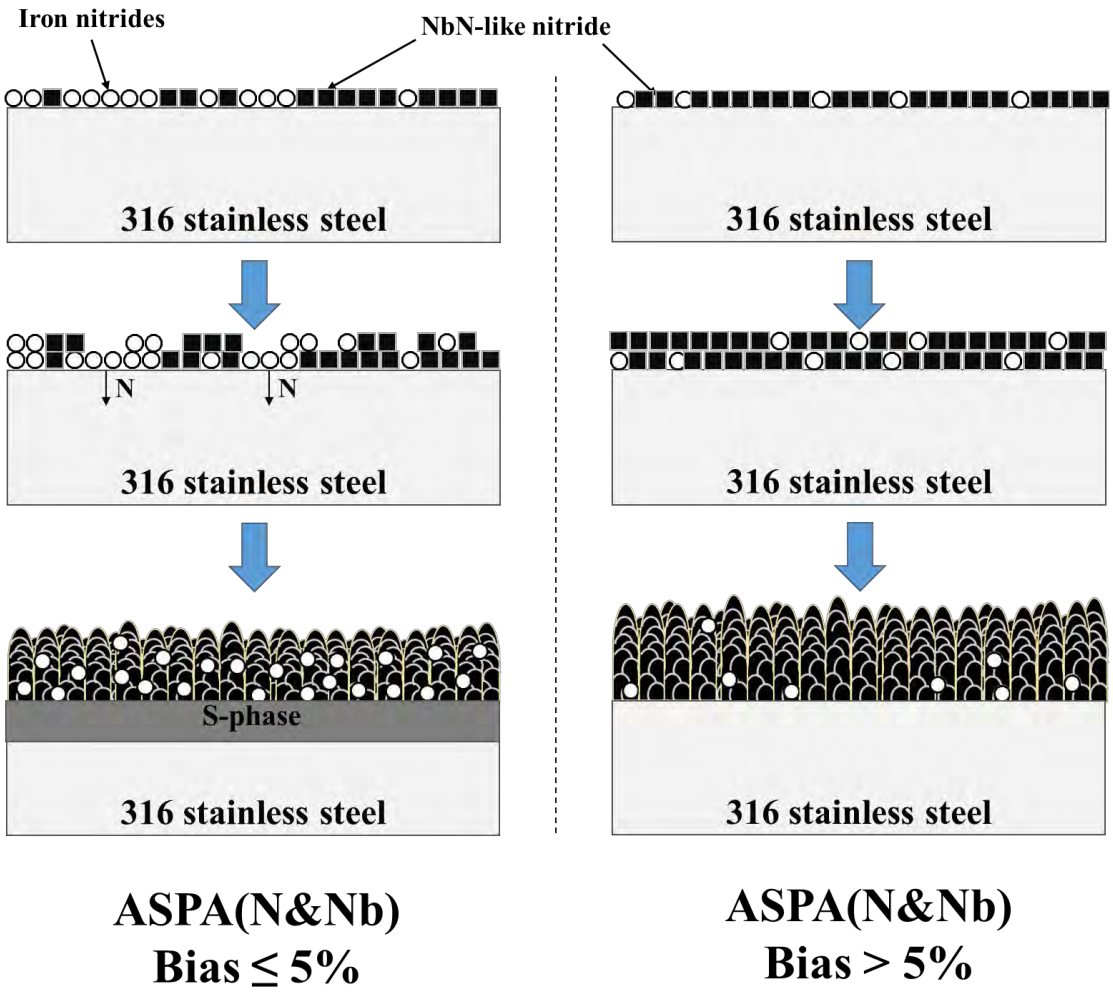

Figure 5.2.17 The schematic mechanism of ASPA(N&Nb)

5.2.3 ASPA(N&Pt)

As have been reported in Sections 4.5, ASPA(N&Pt) treatment can produce even lower ICR than ASPA(N&Nb). This could be attributed to the special microstructure and the associated surface layer forming mechanism.

In the case of ASPA(N&Nb) treatment, as discussed in Section 5.2.2, Nb is a strong nitride forming element. Accordingly, the majority of nitrogen is reacted with niobium to form niobium nitride and limited nitrogen can diffuse into the substrate. However, for ASPA(N&Pt), Pt does not react with nitrogen, due to its noble

properties. From the microstructure reported in Section 4.5.1.2, it can be seen that unlike the ASPA(N&Nb) treated samples, no S-phase can be found even treated under a low applied bias (Figure 4.5.6). This means that the mechanism of the ASPA(N&Pt) is different from that of the ASPA(N&Nb).

The cross-sectional TEM microstructures of the ASPA(N&Pt) treated surface are shown in Figure 5.2.18. A well-developed columnar structured deposition layer was found on the surface of the 316 SS substrate, which is in agreement with the cross-sectional SEM observation (Figure 4.5.6). SAD pattern taken from the layer revealed ring patterns (Figure 5.2.18 (b)) and when small aperture was used to have SAD pattern from a columnar grain (Figure 5.2.19 (a)), spots patterns were shown (Figure 5.2.19 (b)). As can be seen in Figure 5.2.18 (b) and Figure 5.2.19 (b), the diffraction rings and the spots pattern can be indexed to γ-Pt_3Fe [235], which were the phase of the columnar grains of the deposition layer. EDS analysis was conducted at different spots within the layer, and revealed a homogeneous chemical composition over the layer with the atomic ratio of Pt/(Pt+Fe) ≈ 0.69, within the chemical composition variation of the Pt_3Fe (0.6 ~ 0.8), which further confirmed the single phase of Pt_3Fe deposition layer. This is also in agreement with the XPS analysis (Figure 4.5.5). TEM observation at the substrate beneath the deposition layer, revealed no S-phase formation. An austenite fcc pattern, b = [112], taken from just beneath the deposition layer, is evidenced in Figure 5.2.18 (b).

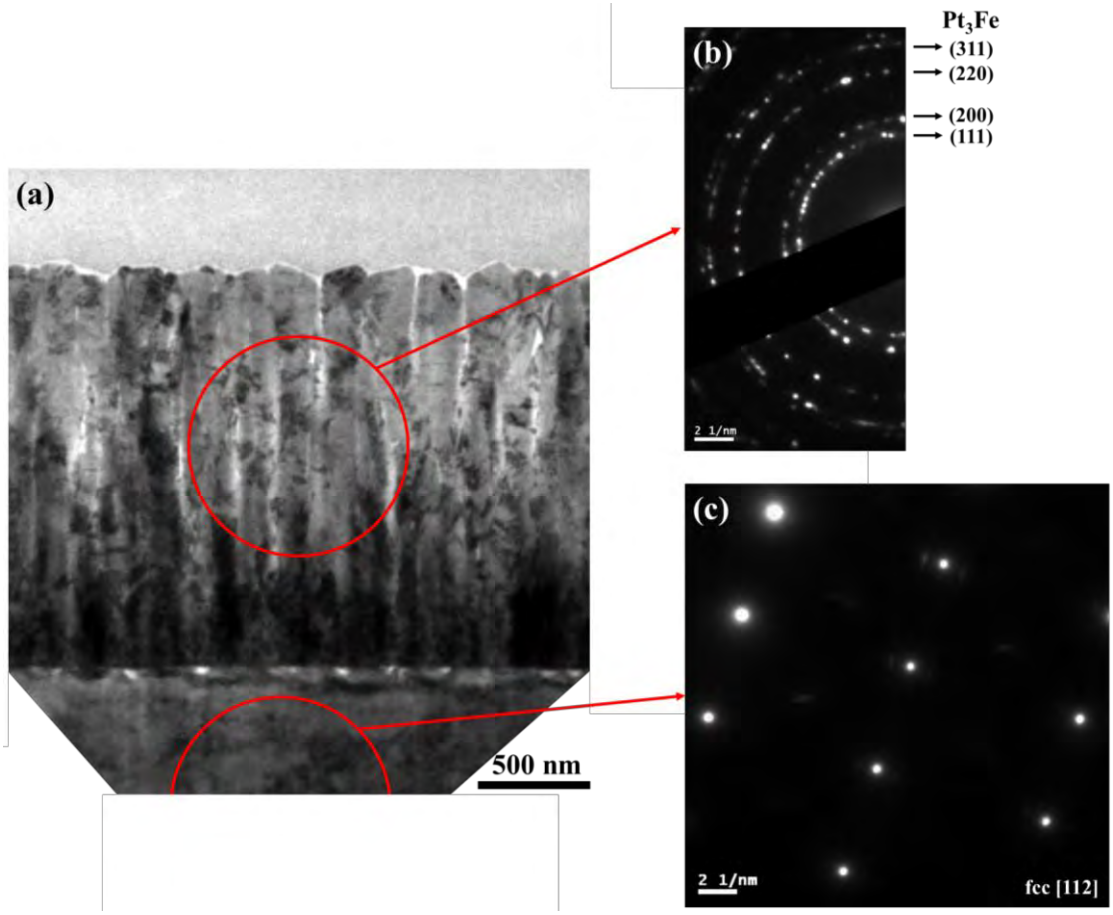

Figure 5.2.18 (a) TEM microstructure and corresponding SAD patterns of (b) the deposition layer and (c) the substrate

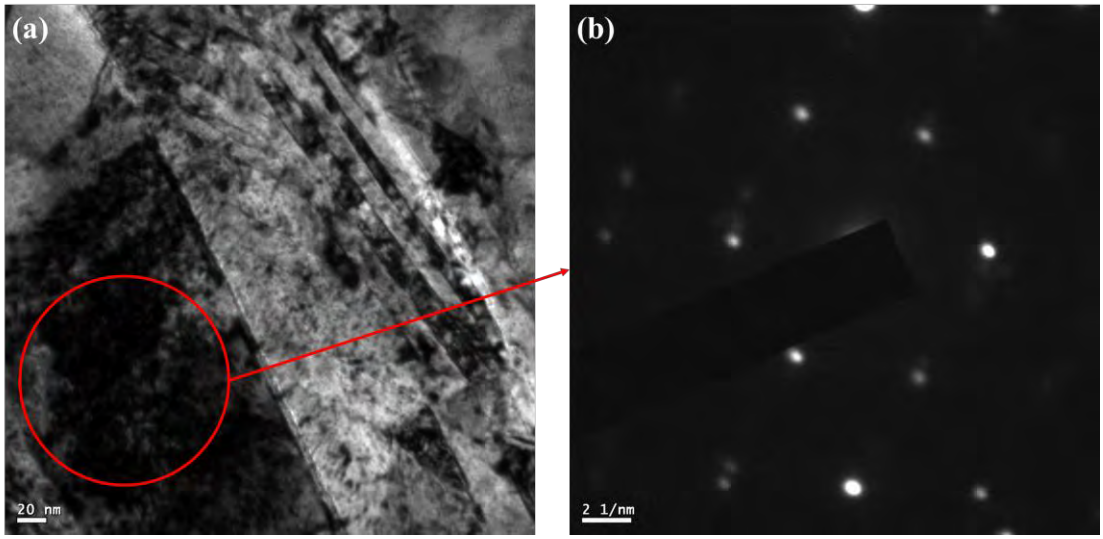

Figure 5.2.19 (a) TEM image of a columnar grain and (b) the corresponding SAD pattern of a Pt_3Fe grain

The dominated amount of Pt (≈ 62 at%, Figure 4.5.5) in the deposition layer formed during the ASPA(N&Pt) might be explained by the relatively high sputtering rate of Pt. It is known that the sputtering rate of Pt is higher than that of the major components of 316 stainless steel, such as Fe and Cr [243]. In addition, the special assembling of Pt wires facilities the rapid sputtering of Pt. This lowered the content of iron nitrides (Figure 4.5.4 (c)) and in the meantime effectively retarded the inward diffusion of nitrogen for the formation of S-phase.

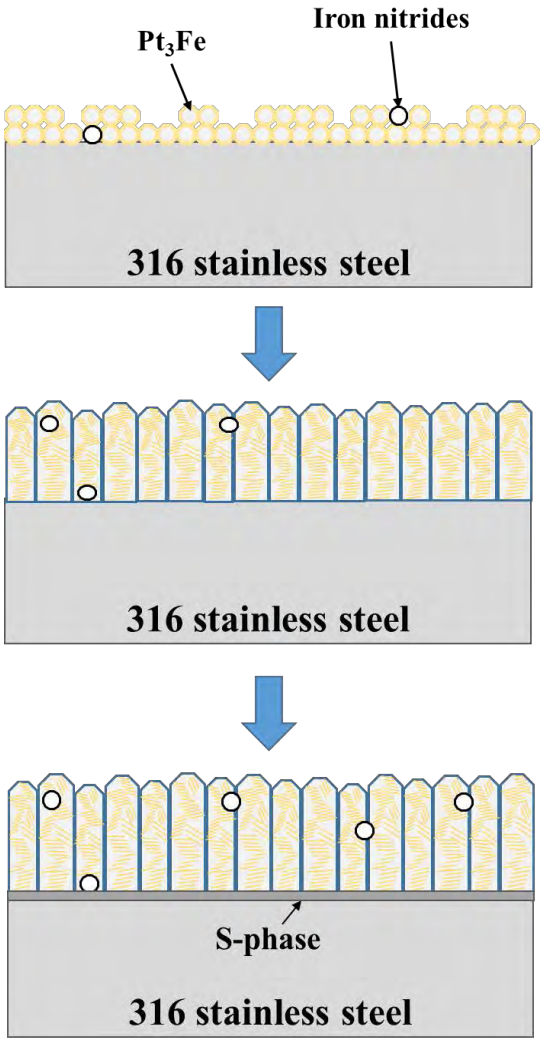

Figure 5.2.20 The schematic of surface layer forming mechanisms for ASPA(N&Pt)

From the above discussion, the mechanism of ASPA(N&Pt) can be summarised in Figure 5.2.20. The effective sputtering of Pt, together with relatively small amount of Fe, leads to a Fe-doped Pt dominated deposition layer, embedded with small amount of iron nitrides, formed on the surface of 316 stainless steel. Although, the Pt_3Fe coating could effectively retard the diffusion of nitrogen, with the extension of treatment duration the released nitrogen could still diffuse inward from the substrate along the defects of the Pt coating to form S-phase (Section 4.5.2.2).

5.3 Improved surface properties

As have reported in Chapter 4, all the ASP treatments including ASPN and ASP co-alloying treatments can improve the surface properties of 316 stainless steel, such as surface electrical conductivity and corrosion behaviour, with different degrees. In this section, the surface properties conferred by different treatments are compared and the reasons behind are discussed.

5.3.1 Surface electrical conductivity

The best ICR value of each treatment is in the order of ASPN (31 mΩ cm^2) > ASPA(N&Ag) (19 mΩ cm^2) > ASPA(N&Nb) (8.6 mΩ cm^2) > ASPA(N&Pt) (6.5 mΩ cm^2). Compared with the ICR of untreated 316 stainless steel with a ground surface (158 mΩ cm^2), the reduction is 80.3 %, 88 %, 94.5 % and 95.9 %, respectively.

5.3.1.1 ASPN

The poor surface conductivity of 316 stainless steel is due to the formation of the oxide passive film on its surface (Section 2.3.4.4). This passive film has a single-layer structure and behaves as n-type semiconductor and the major component of the passive film is Cr oxide [119]. During the heating process of the active screen plasma

treatment, the hydrogen gas is used not only to heat the samples but also to clean the surface to be nitrided. Although the clean effect of ASPN is much weaker than that of the sputtering effect of DCPN [244], part of the oxide film might be removed from the surface of stainless steel. Hence, the thickness of the oxide film would be reduced thus benefiting the improvement of surface conductivity [118]. In addition, the high content of nitrogen might also contribute to thinner oxide layer formed on the stainless steel surface [245].

Another important contributor to the reduced surface electrical conductivity by ASPN treatment is the extremely high (up to 7 GPa) residual compressive stresses in the S-phase layer [227]. The high level of residual compressive stresses is one of the most important features of S-phase. The super-saturation of nitrogen in the austenite matrix results in the lattice expansion but the substrate constrains the expansion, thus leading to the high compressive stresses in the S-phase.

It is know that stress will affect the electrical resistance of metals and alloys. The electrical resistance of a metal under stress can be described by the following equation (Equation 5.3.1) [246]:

$$\rho_p = \rho_0(1 + \phi p) \qquad \text{Equation 5.3.1}$$

in which ρ_p is the electrical resistance under stress, ρ_0 is electrical resistance under vacuum condition without stress, ϕ is the stress coefficient. For iron, the $\phi = 2.34 \times 10^{-6}$ cm^2/kg [246].

Therefore, if the metal is under the compressive stress, the amplitude of lattice vibration will be reduced and hence the scattering of conduction electrons, resulting in the reduction of electrical resistance [247]. Of course, the distortion of the lattice

caused by the supersaturation of nitrogen would, to some extent, counteract the above beneficial effect of residual compressive stress.

5.3.1.2 ASP co-alloying treatments

The microstructure of ASPA(N&Ag) treated samples is similar to that of the ASPN treated samples. The essential difference is the addition of silver particle in the deposition layer. It is well-known that silver is the most electrical conductive metal and the electrical resistance of silver at 20 ℃ is only 15.9 nΩ·m [247].

As discussed in Section 5.2.1, silver particles are sputtered from the Ag-containing lid and then deposited onto the treated surface, which do not react with other elements and exists in an elemental state. Hence, the uniformly distributed silver particles in the deposition layer can act as electrical current paths, facilitating the flow of current and contributing to the reduced ICR value.

However, because of the low silver content in the lid, the amount of silver in the deposition layer is small (Ag = 9.1 wt%, in Figure 4.3.3), compared with Nb = 23.9 at% in ASPA(N&Nb) (Figure 4.4.19) and Pt = 56.9 at% in ASPA(N&Pt) (Figure 4.5.2). Even if the electrical conductivity of silver is better than niobium nitride (570 nΩ·m) [248] and platinum alloys (230~790 nΩ·m) [249], the improvement in surface electrical conductivity by ASPA(N&Ag) is not so large as by ASPA(N&Nb) or ASPA(N&Pt).

The ICR values of the ASPA(N&Nb) and ASPA(N&Pt) treated samples are around 9 and 6.5 $m\Omega \cdot cm^2$, respectively. Although the reduction is only 28 % from ASPA(N&Nb) treated samples to ASPA(N&Pt) treated samples, it is extremely difficulty to reduce the ICR value at this level. The further improvement in surface electrical conductivity is due to the perfect electrical conductivity of Pt and its alloys.

According to the literature, at room temperature the electrical resistivity of platinum and platinum alloys is 105 nΩ·m [250] and 230 ~ 790 nΩ·m [249], respectively; while the electrical resistivity of niobium and niobium nitride is 130 nΩ·m [251] and 570 nΩ·m [248], respectively. The difference in electrical resistivity and alloying element content of these alloying elements could explain the higher surface conductivity of the ASPA(N&Pt) treated samples compared to the ASPA(N&Nb) and ASPA(N&Ag) treated ones.

5.3.2 Corrosion behaviour

Judging from the corrosion potential and passive corrosion current density, in general, the corrosion resistance of ASP alloyed 316 SS is in the order of ASPA(N&Pt) > ASPA(N&Nb) > ASPA(N&Ag) > ASPN. The mechanism for this, is discussed in the following section.

5.3.2.1 ASPN

From the point of view of corrosion potential and corrosion current density, ASPN treatments could improve the corrosion resistance of the 316 stainless steel. In addition, the ASPN treatments have change the dominate corrosion mechanisms from localised corrosion to general corrosion [208]. The mechanism of the improved corrosion resistance of S-phase has been well studied and a theory has been widely accepted [252]. The saturated nitrogen in the S-phase exists as free atoms, and when exposed in an acidic corrosion solution, the free nitrogen atoms would be released from the lattice to react with the hydrogen ions (H^+) by the follow reaction (Equation 5.3.2):

$$[\mathrm{N}] + 4H^+ + 3e^- \rightarrow NH_4^+$$ Equation 5.3.2

The consuming of hydrogen ions retards the decrease of localised pH value, thus preventing pitting corrosion.

Although the corrosion potential and corrosion current density of the ASPN treated 316 stainless steel are slightly better than that of the untreated sample, the passive corrosion current density of the former is even higher than that of the latter. From the results shown in Section 4.2.8.2, the relatively poor corrosion performance is due to the iron nitrides sputtered from the carbon steel screen and deposited on the sample surface. By changing the material of the screen from carbon steel to stainless steel, the passive current density is slightly reduced but is still higher than that of the untreated 316 stainless steel.

5.3.2.2 ASP co-alloying treatments

The ASPA(N&Ag) treated samples possess a better corrosion performance than that of the ASPN treated samples (Table 4.6), due to the introduction of high corrosion resistance silver particles. However, the corrosion resistance of the other components of the deposition layer, such as iron nitride (Section 5.2.1), is much worse than that of the silver. The huge difference in corrosion resistance would lead to galvanic corrosion in the deposition layer, which might have led to the relatively high passive current density of the ASPA(N&Ag) samples (Figure 4.3.12) .

The ASPA(N&Nb) treated samples have shown a much higher corrosion potential and a much lower corrosion current density than that of the ASPA(N&Ag) samples (Table 4.8 vs Table 4.6). This is mainly because the deposition layer formed on the ASPA(N&Ag) treated surface is composed of a mixture or composite of Ag particles and iron nitrides (Figure 5.2.10) but the ASPA(N&Nb) treated surface is completely

covered by a niobium nitride dominated deposition layer (Section 4.4.3.2). Hence, the corrosion potential is improved and the galvanic corrosion observed for the ASPA(N&Ag) treated surface can be reduced. However, the passive corrosion current density and the corrosion current density during the potentio-static tests are still higher than that of the untreated 316 stainless steel (Figure 4.4.27). The possible reasons for the relatively high corrosion current density could be listed as follows. Firstly, the elements from the stainless steel screen, such as iron, chromium and nickel, can be detected by XPS in the niobium nitride single layer (Figure 4.4.23). The difference in corrosion potentials among those elements would still lead to mild galvanic corrosion. Secondly, the defects in the layer might also contribute to the relatively high corrosion current density. The formation of S-phase would yield more defects (such as surface relief) in the top niobium nitride layer (Figure 4.4.29), thus degrading the corrosion behaviour.

For ASPA(N&Pt) treated samples, by optimising the treatment conditions, the corrosion resistance of the treated surfaces in terms of corrosion potential can be effectively enhanced (Table 4.10); meanwhile the passive current density remains in the same level as that of the untreated sample. The superior chemical stability of the ASPA(N&Pt) treated sample has also been observed from the long-duration potentiostatic polarisation tests (Figure 4.5.9). The excellent corrosion resistance of ASPA(N&Pt) treated samples could be related to the great resistance of platinum alloys against aqueous acidic environment [253]. In addition, the relatively high sputtering rate of platinum significantly reduced the amount of the elements from the stainless steel screen (Figure 4.5.5). This is supported by the fact that the atomic ratio of Fe: Nb on the Nb-450/10/15-5mm sample is as high as 1.46 where iron is dominant

in the deposition layer, whilst the atomic ration of Fe: Pt on the Pt-450/10/15 sample is only 0.57 where the deposition layer is dominated by Pt.

5.3.3 Optimal treatment parameters

5.3.3.1 ASPA(N&Nb) treatments

For ASPA(N&Nb) treatments, some treatment parameters, such as treatment duration (Section 4.4.1) and Nb wire length (Section 4.4.2), have been optimised according to the surface properties produced. As reported in Sections 4.4.3 and 4.4.4 and discussed in Section 5.2.2, the layer structure of the ASPA(N&Nb) modified surface can be tailored by adjusting the applied bias (Fig. 5.2.13). However, it is difficult to produce an ASPA(N&Nb) treated surface with both desirable surface conductivity and corrosion resistance.

In terms of the surface conductivity, it has been reported in Section 4.2.8.2 and discussed in Section 5.3.1 that the S-phase has a better surface conductivity than that of the 316 stainless steel, and the single niobium-rich deposition layer also shows good surface conductivity, due to the excellent electrical conductivity of niobium and its compounds. Hence, the duplex structured surface should possess the profit of both of these two layers and thus provide the further improved surface conductivity. This hypotheses is fully supported by the ICR results reported in Section 4.4.3.3 that the ICR value (Figure 4.4.35) of the duplex structure consisting of a niobium rich deposition layer followed by a underneath S-phase layer, i.e. Nb-450/20/(5+10)-5mm (8.6 $m\Omega\ cm^2$), is lower than that of the single layered surface structure, either a single S-phase layer (ASPN) (around 30 $m\Omega\ cm^2$) or a single niobium-rich deposition layer, i.e. Nb-450/10/15-5mm (9.1 $m\Omega\ cm^2$).

Regarding the electrochemical corrosion behaviour, it has been reported in Table 4.8 that the corrosion potential increases with the bias applied and the Nb-450/10/15-5mm sample exhibits the highest corrosion potential among all the ASPA(N&Nb) treated samples due to its thick niobium nitride layer (Figure 4.4.24(f)). Indeed, the corrosion potential of the Nb-450/10/15-5mm sample is even more positive than that of the untreated material. However, for the duplex layer structured surface, the formation of S-phase would yield more defects to the deposition layer, leading to the degradation of corrosion resistance (Figure 4.4.36). Judging by both the slightly higher surface conductivity than the ASPA(N&Nb) induced duplex layer and the best corrosion behaviour among all the ASPA(N&Nb) treated surfaces, the Nb-450/10/15-5mm ASPA(N&Nb) treated samples with only a thick niobium nitride layer exhibits the best over-all performance.

However, due to the strong mechanical support from the subsurface S-phase layer the samples with a duplex layer structure are expected to have a higher load bearing capacity than that of the sample with only a thick niobium nitride layer. Therefore, the duplex layer samples could be the best candidate if forming of the PEMFC bipolar plates, such as by stamping, needs to be carried out after the surface treatment.

5.3.3.2 ASPA(N&Pt) treatments

From the surface conductivity point of view, the ICR value is in the order of Pt-450/10/5 (6.4 $m\Omega \cdot cm^2$) < Pt-450/10/15 (6.5 $m\Omega \cdot cm^2$) < Pt-450/10/10 (6.9 $m\Omega \cdot cm^2$) < Pt-450/20/(5+10) (8.4 $m\Omega \cdot cm^2$) < Pt-450/20/(0+10) (8.8 $m\Omega \cdot cm^2$). In general, the samples treated under a constant bias exhibited a lower ICR value than samples treated under varying bias. In addition, with the similar microstructure and thickness of Pt deposition layer, the duplex layer structured Pt-450/20/(5+10) sample showed a

slightly lower ICR value than that of the single layer structured Pt-450/20/(0+10) sample. This is in agreement with the results for ASPA(N&Nb) treated samples.

In terms of corrosion behaviour, the corrosion potential of the ASPA(N&Pt) treated samples is in the order of Pt-450/10/5 (-322 mV) = Pt-450/10/15 (-322 mV) > Pt-450/10/10 (-324 mV) > Pt-450/20/(0+10) (-325 mV) > Pt-450/20/(5+10) (-331 mV), and the corrosion current density is in the order of Pt-450/10/15 (24.5 $\mu A/cm^2$) < Pt-450/20/(0+10) (40.6 $\mu A/cm^2$) < Pt-450/10/5 (47.9 $\mu A/cm^2$) < Pt-450/10/10 (55.7 $\mu A/cm^2$) < Pt-450/20/(5+10) (65.6 $\mu A/cm^2$). From the above comparison, it can be seen that the Pt-450/10/15 sample possesses the best corrosion behaviour although its performance is very close to that of other samples. Another important evaluation criterion of corrosion resistance is passive current density. The passive current densities of Pt-450/10/10, Pt-450/10/5 (Figure 4.5.8) and Pt-450/20/(5+10) (Figure 4.5.18) sample are obviously higher than that of the untreated sample. For Pt-450/10/15 sample (Figure 4.5.8), there is not clear passive region and except the region from -0.2 V to 0.4 V the current density is higher than that of the untreated sample. Pt-450/20/(0+10) sample shows a clear passive stage and the passive current density is in the same level as that of the untreated sample (Figure 4.5.18). In addition, no peak of pitting corrosion can be found from the polarisation curves of the Pt-450/20/(0+10) sample.

From the discussion above, although the ICR value of the Pt-450/20/(0+10) sample is higher than other ASPA(N&Pt) samples, it is still lower than that of the DoE target (10 $m\Omega \cdot cm^2$). Meanwhile, the corrosion performance of the Pt-450/20/(0+10) sample is the best. Therefore, from the bipolar plate application point of view, the Pt-450/20/(0+10) treatment is the best.

Similar to the discussion in last section, if subsequent stamping is required, the duplex layer structured samples, which consists of a relatively hard S-phase layer beneath the surface deposition layer, is expected to outperform the single layer structured samples due to its high load bearing capacity conferred by the strong S-phase sublayer.

Chapter 6. Conclusions

Novel plasma surface treatments based on advanced active screen plasma (ASP) technology have been developed to modify the surface properties of carbon paper gas diffusion layer and 316 stainless steel bipolar plates for the application of proton exchange membrane fuel cell. Based on the results and discussion presented above, the following conclusions can be drawn:

Part I: Active screen plasma treatments of carbon paper

1. Low temperature (120 °C) and short treatment duration (10 min) ASP treatments using a gas mixture of 25%N_2+75%H_2 significantly promote the uniform growth of single-crystal Pt nano-wire arrays on the plasma activated carbon paper support surface.
2. The ASP treatments can remove the hydrophobic PTFE coating and introduce many functional groups (such as C-N, C=N and O-H) to the carbon paper surface, both of these can effective activate the carbon paper surface, thus contributing to the improved growth of Pt nano-wire.
3. The catalytic performance of catalyst electrodes can be improved by the ASP treated and Pt nano-wire coated carbon paper in terms of increased: electrochemical surface areas (ECSA) by 67%; and output power density by 3 times.

Part II: Orthogonal array test of low-temperature ASPN-treated 316 stainless steel samples

4. Low temperature active screen plasma nitriding can effectively reduce the interfacial contact resistance (ICR) of 316 stainless steel, which means an

improvement in electrical conductivity, which may be attributed to the residual compressive stress in the deposited S-phase layer formed.

5. An orthogonal array test were conducted to study the effect of the ASPN conditions. This indicated that among the three plasma nitriding parameters (temperature, time and bias), temperature has the largest influence on the ICR value followed by time and bias.
6. Low temperature active screen plasma nitriding can: reduce the corrosion current (I_{corr}), increase the corrosion potential; and improve the pitting corrosion resistance of 316 stainless steel in 0.05 M sulphuric acid. ASPN is more effective than DC plasma nitriding in improving the corrosion resistance of 316 SS.

Part III: Active screen plasma alloying with nitrogen and silver (ASPA(N&Ag))

7. A new plasma surface co-alloying technology has been developed to simultaneously introduce nitrogen (N) and silver (Ag), i.e. ASPA(N&Ag), into the surface of 316 stainless steel. This is achieved by designing and manufacturing an Ag containing 316 SS matrix composite lid using thermal isostatic pressing.
8. A duplex surface layer structure, consisting of a deposition layer with silver particles uniformly distributed in the Fe_4N iron nitride matrix and an underneath high-nitrogen S-phase case, has been successfully produced by the ASPA(N&Ag) process developed. When treated at an optimal temperature of 450 °C, the thickness of both the deposition layer and the S-phase sublayer increases with the treatment time
9. The ASPA(N&Ag) treatment can significantly reduce the ICR of 316 stainless steel from 157.8 to around 20 $m\Omega\ cm^2$ mainly due to the highly electrically

conducting Ag particles in the deposition layer and the S-phase sublayer with low electrical resistance.

10. Compared with untreated 316 stainless steel, all ASPA(N&Ag) treated samples exhibit a more positive corrosion potential, a lower corrosion current but a higher passive current density. When treated under the same condition of 450 °C for 7 h, the ASPA(N&Ag) 316 stainless steel possessed better corrosion behaviour than ASPN treated sample.

Part IV: Active screen plasma alloying with nitrogen and niobium (ASPA(N&Nb))

11. Both N and Nb can be introduced into 316 stainless steel surfaces by the novel plasma co-alloying with N and Nb, i.e. ASPA(N&Nb), using Nb wires hung on a 316 mesh lid as the alloying source. The Nb content of the treated layer increases with the length of the Nb wires.
12. The layer structure of the ASPA(N&Nb) treated 316 surfaces could be tailored by changing the applied bias, for samples treated at 450 °C for 10 h. A duplex layer structure consisting a deposition layer of niobium nitride doped with iron nitrides and an S-phase layer underneath can be produced under low applied bias (≤ 5 %); however, a single niobium nitride dominant deposition layer can be produced under high (> 5 %) applied bias.
13. The ASPA(N&Nb) treatment can significantly reduce the ICR of 316 stainless steel from 157.8 to around 9 mΩ cm^2, which is about half that of the ASPA(N&Ag) (20 mΩ cm^2). The corrosion behaviour of the ASPA(N&Nb) treated samples are further improved compared that of the ASPA(N&Ag) treated samples.

Part V: Active screen plasma alloying with nitrogen and platinum (ASPA(N&Pt))

14. Similar to ASPA(N&Nb) treatment, surface co-alloying of N and Pt of 316 stainless steel has been successfully achieved by the novel ASPA(N&Pt) treatment developed using Pt wires hung on a 316 mesh lid as the alloying source. The Pt content of the treated layer increases with the applied bias.
15. Only a single Pt_3Fe deposition layer can be produced under a constant applied bias; however, by step-changing the applied bias, a duplex layer structure with a Pt_3Fe surface deposition layer followed by an underlying S-phase layer can also be produced.
16. ASPA(N&Pt) can produce the best surface electrical conductivity and corrosion behaviour among all the ASP treatments. Under optimal treatment conditions, the passive corrosion current density of the ASPA(N&Pt) treated 316 SS maintains the same level as that of the untreated samples.
17. The active screen plasma co-alloying with nitrogen and platinum (ASPA(N&Pt)) developed in this study could offer 316 stainless steel with much enhanced performance that fulfils the technical target for bipolar plates set by DoE, such as electrical and corrosion properties.

    However, whereas the currently used surface engineering technologies, such as surface PVD coating, require very expensive PVD equipment (high vacuum) and a much larger platinum target, the ASPA(N&Pt) treatment only requires a simpler plasma nitriding furnace and a small amount of Pt wires (last for about 20 treatments). This suggests a great potential for commercialisation. In addition, the costs may be further reduced as a result of mass production optimisation processes.

Chapter 7. Suggested future work

The present work has demonstrated that all the active screen plasma treatments investigated can effectively enhance the electrical conductivity of 316 austenitic stainless steel. More importantly, the novel active screen plasma co-alloying technology developed from this project can dramatically improve the electrical conductivity of 316 austenitic stainless steel without impairing its corrosion resistance. Especially the ASPA(N&Pt) treated 316 stainless steel has exhibited combined improvement in surface conductivity and corrosion resistance to meet the DoE technical targets. In order to evaluate the performance of the plasma surface alloyed 316 SS in real working environment, the following topics are suggested for further studies:

(1) All the ICR tests done in the present work were conducted before corrosion tests, and it is suggested that more ICR tests test should be conducted after corrosion in the future in order to study the effect of corrosion tests on the ICR of plasma treated surfaces.

(2) In order to demonstrate the technological potential of the novel plasma surface alloying technology for stainless steel bipolar plates, single fuel cell tests should be conducted in real working conditions. The single cell performance of ASP treated 316 stainless steel bipolar plates should be compared to that of other currently available bipolar plates in order to evaluate their potential for commercialisation.

(3) In order to assess the commercial potential, the cost of ASPA(N&Pt) treated 316 stainless steel bipolar plates should be estimated.

Reference

[1] F. Barbir, *PEM Fuel Cells*. Elsevier, 2005.

[2] S. Du, K. Lin, S. K. Malladi, Y. Lu, S. Sun, Q. Xu, R. Steinberger-Wilckens, and H. Dong, "Plasma nitriding induced growth of Pt-nanowire arrays as high performance electrocatalysts for fuel cells.," *Sci. Rep.*, vol. 4, p. 6439, Jan. 2014.

[3] S. Karimi, N. Fraser, B. Roberts, and F. R. Foulkes, "A review of metallic bipolar plates for proton exchange membrane fuel cells: Materials and fabrication methods," *Adv. Mater. Sci. Eng.*, vol. 2012, 2012.

[4] H. Wang and J. A. Turner, "Reviewing metallic PEMFC bipolar plates," *Fuel Cells*, vol. 10, no. 4, pp. 510–519, 2010.

[5] D. Papageorgopoulos, "DOE fuel cell technology program overview and introduction to the 2010 fuel cell pre-solicitation workshop in DOE fuel cell pre-solicitation workshop," *Dep. Energy, Lakewood, Color.*, 2010.

[6] "Fuel Cells 2000 - Types Of Fuel Cells." [Online]. Available: http://www.fuelcells.org/base.cgim?template=types_of_fuel_cells. [Accessed: 09-Sep-2015].

[7] F. Barbir, *PEM Fuel Cells*. Elsevier, 2013.

[8] Fuel Cell Today, "The Fuel Cell Industry Review 2013," 2013.

[9] "Hydrogen Fuel Cell Powered Cars | Hyundai UK." [Online]. Available: http://www.hyundai.co.uk/about-us/environment/hydrogen-fuel-cell. [Accessed: 08-Sep-2015].

[10] T. Schultz, S. Zhou, and K. Sundmacher, "Current Status of and Recent Developments in the Direct Methanol Fuel Cell," *Chem. Eng. Technol.*, vol. 24, no. 12, pp. 1223–1233, 2001.

[11] R. O'Hayre, S. Cha, W. Colella, and F. Prinz, *Fuel cell fundamentals*. 2006.

[12] G. McLean, "An assessment of alkaline fuel cell technology," *Int. J. Hydrogen Energy*, vol. 27, no. 5, pp. 507–526, May 2002.

[13] G. Merle, M. Wessling, and K. Nijmeijer, "Anion exchange membranes for alkaline fuel cells: A review," *J. Memb. Sci.*, vol. 377, no. 1–2, pp. 1–35, Jul. 2011.

[14] A. B. Stambouli and E. Traversa, "Solid oxide fuel cells (SOFCs): a review of an environmentally clean and efficient source of energy," *Renew. Sustain. Energy Rev.*, vol. 6, no. 5, pp. 433–455, Oct. 2002.

[15] A. Mills, “Porous platinum morphologies: Platinised, sponge and black,” *Platin. Met. Rev.*, vol. 51, no. 1, p. 52, 2007.

[16] A. Appleby and E. Yeager, “Solid polymer electrolyte fuel cells (SPEFCs),” *Energy*, vol. 11, no. 1–2, pp. 137–152, Jan. 1986.

[17] I. L. Keck, J. Buchanan, and A. Hards, “Platinum Alloy Electrocatalyst on Carbon Support (United States Patent: 5068161),” 1991.

[18] A. J. Appleby, “Electrocatalysis and fuel cells,” *Catal. Rev.*, vol. 4, no. 1, pp. 221–244, 1971.

[19] S. Mukerjee and S. Srinivasan, “Enhanced electrocatalysis of oxygen reduction on platinum alloys in proton exchange membrane fuel cells,” *J. Electroanal. Chem.*, vol. 357, no. 1–2, pp. 201–224, Oct. 1993.

[20] N. Wakabayashi and M. Takeichi, “Temperature dependence of oxygen reduction activity at Pt-Fe, Pt-Co, and Pt-Ni alloy electrodes,” *J. Phys. Chem. B*, pp. 5836–5841, 2005.

[21] H. Yano, M. Kataoka, and H. Yamashita, “Oxygen reduction activity of carbon-supported Pt-M (M= V, Ni, Cr, Co, and Fe) alloys prepared by nanocapsule method,” *Langmuir*, no. 22, pp. 6438–6445, 2007.

[22] H. R. Colón-Mercado and B. N. Popov, “Stability of platinum based alloy cathode catalysts in PEM fuel cells,” *J. Power Sources*, vol. 155, no. 2, pp. 253–263, Apr. 2006.

[23] M. Jitianu and R. Kleisinger, “Preparation of carbon supported alloy PtCo nanoparticles for PEM fuel cells,” *J. New Mater. Electrochem. Syst.*, vol. 74, pp. 67–74, 2007.

[24] H. Böhm and F. Pohl, “The electrocatalytic property of tungsten carbide,” *Wiss. Ber. AEG-Telefunken*, 1968.

[25] H. Binder, A. Köhling, W. Kuhn, W. Lindner, and G. Sandstede, “Tungsten carbide electrodes for fuel cells with acid electrolyte,” *Nature*, vol. 224, no. 5226, p. 1299, 1969.

[26] H. Böhm, “New non-noble metal anode catalysts for acid fuel cells,” *Nature*, vol. 227, no. 5257, p. 483, 1970.

[27] F. Mazza and S. Trassatti, “Tungsten, titanium, and tantalum carbides and titanium nitrides as electrodes in redox systems,” *J. Electrochem. Soc.*, vol. 110, no. 7, pp. 847–849, 1963.

[28] K. Lee, A. Ishihara, S. Mitsushima, N. Kamiya, and K. Ota, “Stability and electrocatalytic activity for oxygen reduction in WC + Ta catalyst,” *Electrochim. Acta*, vol. 49, no. 21, pp. 3479–3485, Sep. 2004.

[29] K. Lee, L. Zhang, and J. Zhang, “Ternary non-noble metal chalcogenide (W–Co–Se) as electrocatalyst for oxygen reduction reaction,” *Electrochem. commun.*, vol. 9, no. 7, pp. 1704–1708, Jul. 2007.

[30] H. Zhong, H. Zhang, G. Liu, Y. Liang, J. Hu, and B. Yi, “A novel non-noble electrocatalyst for PEM fuel cell based on molybdenum nitride,” *Electrochem. commun.*, vol. 8, no. 5, pp. 707–712, May 2006.

[31] C. W. B. Bezerra, L. Zhang, K. Lee, H. Liu, A. L. B. Marques, E. P. Marques, H. Wang, and J. Zhang, “A review of Fe–N/C and Co–N/C catalysts for the oxygen reduction reaction,” *Electrochim. Acta*, vol. 53, no. 15, pp. 4937–4951, Jun. 2008.

[32] D. Susac, L. Zhu, M. Teo, and A. Sode, “Characterization of FeS2-based thin films as model catalysts for the oxygen reduction reaction,” *J. Phys. Chem.*, pp. 18715–18723, 2007.

[33] J.-H. Kim, A. Ishihara, S. Mitsushima, N. Kamiya, and K.-I. Ota, “Catalytic activity of titanium oxide for oxygen reduction reaction as a non-platinum catalyst for PEFC,” *Electrochim. Acta*, vol. 52, no. 7, pp. 2492–2497, Feb. 2007.

[34] T. Oh, J. Y. Kim, Y. Shin, M. Engelhard, and K. S. Weil, “Effects of tungsten oxide addition on the electrochemical performance of nanoscale tantalum oxide-based electrocatalysts for proton exchange membrane (PEM) fuel cells,” *J. Power Sources*, vol. 196, no. 15, pp. 6099–6103, Aug. 2011.

[35] T. Ralph and M. Hogarth, “Catalysis for low temperature fuel cells,” *Platin. Met. Rev.*, no. l, pp. 3–14, 2002.

[36] O. T. Holton and J. W. Stevenson, “The Role of Platinum in Proton Exchange Membrane Fuel Cells,” *Platin. Met. Rev.*, vol. 57, no. 4, pp. 259–271, Oct. 2013.

[37] R. Allen and H. Petrow, “Finely particulated colloidal platinum compound and sol for producing the same, and method of preparation of fuel cell electrodes and the like employing the same,” 1977.

[38] M. Wilson and S. Gottesfeld, “High Performance Catalyzed Membranes of Ultra‐low Pt Loadings for Polymer Electrolyte Fuel Cells,” *J. Electrochem. Soc.*, vol. 139, no. 2, pp. 12–14, 1992.

[39] M. Wilson, “Membrane catalyst layer for fuel cells, US Patent 5211984,” 1993.

[40] T. Ralph and G. Hards, “Low cost electrodes for proton exchange membrane fuel cells performance in single cells and Ballard stacks,” *J. Electrochem. Soc.*, vol. 144, no. 11, 1997.

[41] R. O'Hayre, S.-J. Lee, S.-W. Cha, and F. Prinz, "A sharp peak in the performance of sputtered platinum fuel cells at ultra-low platinum loading," *J. Power Sources*, vol. 109, no. 2, pp. 483–493, Jul. 2002.

[42] N. R. Shiju and V. V. Guliants, "Recent developments in catalysis using nanostructured materials," *Appl. Catal. A Gen.*, vol. 356, no. 1, pp. 1–17, Mar. 2009.

[43] A. Henglein, B. G. Ershov, and M. Malow, "Absorption spectrum and some chemical reactions of colloidal platinum in aqueous solution," *J. Phys. Chem.*, vol. 99, no. 38, pp. 14129–14136, 1995.

[44] T. Herricks, J. Y. Chen, and Y. N. Xia, "Polyol synthesis of platinum nanoparticles: Control of morphology with sodium nitrate," *NANO Lett.*, vol. 4, no. 12, pp. 2367–2371, 2004.

[45] K. Niesz, M. Grass, and G. A. Somorjai, "Precise control of the Pt nanoparticle size by seeded growth using EO13PO30EO13 triblock copolymers as protective agents," *Nano Lett.*, vol. 5, no. 11, pp. 2238–2240, 2005.

[46] T. Ahmadi and Z. Wang, "Shape-controlled synthesis of colloidal platinum nanoparticles," *Science (80-.).*, vol. 272, no. 5270, p. 1924, 1996.

[47] O. Antoine and R. Durand, "In Situ Electrochemical Deposition of Pt Nanoparticles on Carbon and Inside Nafion," *Electrochem. Solid-State Lett.*, vol. 4, no. 5, p. A55, 2001.

[48] N. Tian, Z.-Y. Zhou, S.-G. Sun, Y. Ding, and Z. L. Wang, "Synthesis of tetrahexahedral platinum nanocrystals with high-index facets and high electro-oxidation activity.," *Science*, vol. 316, no. 5825, pp. 732–5, May 2007.

[49] S. Sun, G. Zhang, D. Geng, Y. Chen, R. Li, M. Cai, and X. Sun, "A highly durable platinum nanocatalyst for proton exchange membrane fuel cells: multiarmed starlike nanowire single crystal.," *Angew. Chem. Int. Ed. Engl.*, vol. 50, no. 2, pp. 422–6, Jan. 2011.

[50] Y. Sun, B. T. Mayers, and Y. Xia, "Template-Engaged Replacement Reaction: A One-Step Approach to the Large-Scale Synthesis of Metal Nanostructures with Hollow Interiors," *Nano Lett.*, vol. 2, no. 5, pp. 481–485, May 2002.

[51] B. Mayers, X. Jiang, D. Sunderland, B. Cattle, and Y. Xia, "Hollow nanostructures of platinum with controllable dimensions can be synthesized by templating against selenium nanowires and colloids.," *J. Am. Chem. Soc.*, vol. 125, no. 44, pp. 13364–5, Nov. 2003.

[52] Z. Chen, M. Waje, W. Li, and Y. Yan, "Supportless Pt and PtPd nanotubes as electrocatalysts for oxygen-reduction reactions.," *Angew. Chem. Int. Ed. Engl.*, vol. 46, no. 22, pp. 4060–3, Jan. 2007.

[53] E. P. Lee, Z. Peng, D. M. Cate, H. Yang, C. T. Campbell, and Y. Xia, "Growing Pt nanowires as a densely packed array on metal gauze.," *J. Am. Chem. Soc.*, vol. 129, no. 35, pp. 10634–5, Sep. 2007.

[54] E. P. Lee, Z. Peng, W. Chen, S. Chen, H. Yang, and Y. Xia, "Electrocatalytic properties of Pt nanowires supported on Pt and W gauzes.," *ACS Nano*, vol. 2, no. 10, pp. 2167–73, Oct. 2008.

[55] S. Sun, F. Jaouen, and J.-P. Dodelet, "Controlled Growth of Pt Nanowires on Carbon Nanospheres and Their Enhanced Performance as Electrocatalysts in PEM Fuel Cells," *Adv. Mater.*, vol. 20, no. 20, pp. 3900–3904, Oct. 2008.

[56] S. H. Sun, D. Q. Yang, D. Villers, G. X. Zhang, E. Sacher, and J. P. Dodelet, "Template- and Surfactant-free Room Temperature Synthesis of Self-Assembled 3D Pt Nanoflowers from Single-Crystal Nanowires," *Adv. Mater.*, vol. 20, no. 3, pp. 571–574, Feb. 2008.

[57] S. Du, "A Facile Route for Polymer Electrolyte Membrane Fuel Cell Electrodes with in situ Grown Pt Nanowires," *J. Power Sources*, vol. 195, no. 1, pp. 289–292, Jan. 2010.

[58] X. Yao, K. Su, S. Sui, L. Mao, A. He, J. Zhang, and S. Du, "A novel catalyst layer with carbon matrix for Pt nanowire growth in proton exchange membrane fuel cells (PEMFCs)," *Int. J. Hydrogen Energy*, vol. 38, no. 28, pp. 12374–12378, Sep. 2013.

[59] S. Park, J.-W. Lee, and B. N. Popov, "A review of gas diffusion layer in PEM fuel cells: Materials and designs," *Int. J. Hydrogen Energy*, vol. 37, no. 7, pp. 5850–5865, Apr. 2012.

[60] E. M. Liston, L. Martinu, and M. R. Wertheimer, "Plasma surface modification of polymers for improved adhesion: a critical review," *J. Adhes. Sci. Technol.*, vol. 7, no. 10, pp. 1091–1127, Jan. 1993.

[61] P. Krüger, R. Knes, and J. Friedrich, "Surface cleaning by plasma-enhanced desorption of contaminants (PEDC)," *Surf. Coatings Technol.*, vol. 112, no. 1–3, pp. 240–244, Feb. 1999.

[62] L. Dai, H. J. Griesser, and A. W. H. Mau, "Surface Modification by Plasma Etching and Plasma Patterning," vol. 5647, no. 97, pp. 9548–9554, 1997.

[63] D. T. Clark and A. Dilks, "ESCA applied to polymers. XVIII. RF glow discharge modification of polymers in helium, neon, argon, and krypton," *J. Polym. Sci. Polym. Chem. Ed.*, vol. 16, no. 5, pp. 911–936, 1978.

[64] P. Chappell and J. Brown, "Surface modification of extended chain polyethylene fibres to improve adhesion to epoxy and unsaturated polyester resins," *Surf. Interface Anal.*, vol. 17, no. October 1990, pp. 143–150, 1991.

[65] J. Meichsner, M. Nitschke, R. Rochotzki, and M. Zeuner, “Fundamental investigations in plasma modification of polymers,” *Surf. Coatings Technol.*, vol. 74–75, pp. 227–231, Sep. 1995.

[66] J. Kong, “Wettability transition of plasma-treated polystyrene micro/nano pillars-aligned patterns,” *eXPRESS Polym. Lett.*, vol. 4, no. 12, pp. 753–762, Nov. 2010.

[67] J. Zhai, B. Liu, D. Huang, and J. Sheng, “Plasma modification of polypropylene surfaces and grafting copolymerization of styrene onto polypropylene,” *Chinese J. Polym. Sci.*, vol. 30, no. 3, pp. 423–435, 2012.

[68] N. Vandencasteele and B. Nisol, “Plasma‐Modified PTFE for Biological Applications: Correlation between Protein‐Resistant Properties and Surface Characteristics,” *Plasma Process. Polym.*, pp. 661–671, 2008.

[69] J. H. Kim, J. Sohn, J. H. Cho, M. Y. Choi, I. G. Koo, and W. M. Lee, “Surface Modification of Nafion Membranes Using Atmospheric-Pressure Low-Temperature Plasmas for Electrochemical Applications,” *Plasma Process. Polym.*, vol. 5, no. 4, pp. 377–385, Jun. 2008.

[70] X. Fu, M. J. Jenkins, G. Sun, I. Bertoti, and H. Dong, “Characterization of active screen plasma modified polyurethane surfaces,” *Surf. Coatings Technol.*, vol. 206, no. 23, pp. 4799–4807, Jul. 2012.

[71] X. Fu, R. L. Sammons, I. Bertóti, M. J. Jenkins, and H. Dong, “Active screen plasma surface modification of polycaprolactone to improve cell attachment.,” *J. Biomed. Mater. Res. B. Appl. Biomater.*, vol. 100, no. 2, pp. 314–20, Feb. 2012.

[72] H. Tsuchiya, “Mass production cost of PEM fuel cell by learning curve,” *Int. J. Hydrogen Energy*, vol. 29, no. 10, pp. 985–990, Aug. 2004.

[73] A. Samu, K. Pertti, I. Jari, and K. Pasi, “Bipolar plate, method for producing bipolar plate and PEM fuel cell,” *United State Pat. Appl 20090142645*, 2009.

[74] US Department of Energy, “Technical Plan - Fuel Cell.” 2012.

[75] B. Steele and A. Heinzel, “Materials for fuel-cell technologies,” *Nature*, vol. 414, no. November, pp. 345–352, 2001.

[76] R. Taherian, “A review of composite and metallic bipolar plates in proton exchange membrane fuel cell: Materials, fabrication, and material selection,” *J. Power Sources*, vol. 265, pp. 370–390, Nov. 2014.

[77] H.-C. Kuan, C.-C. M. Ma, K. H. Chen, and S.-M. Chen, “Preparation, electrical, mechanical and thermal properties of composite bipolar plate for a fuel cell,” *J. Power Sources*, vol. 134, no. 1, pp. 7–17, Jul. 2004.

[78] a. Heinzel, F. Mahlendorf, O. Niemzig, and C. Kreuz, “Injection moulded low cost bipolar plates for PEM fuel cells,” *J. Power Sources*, vol. 131, no. 1–2, pp. 35–40, May 2004.

[79] T. M. Besmann, J. W. Klett, J. J. Henry, and E. Lara-Curzio, “Carbon/Carbon Composite Bipolar Plate for Proton Exchange Membrane Fuel Cells,” *J. Electrochem. Soc.*, vol. 147, no. 11, p. 4083, 2000.

[80] P.-C. Ma, N. a. Siddiqui, G. Marom, and J.-K. Kim, “Dispersion and functionalization of carbon nanotubes for polymer-based nanocomposites: A review,” *Compos. Part A Appl. Sci. Manuf.*, vol. 41, no. 10, pp. 1345–1367, Oct. 2010.

[81] E. . Cho, U.-S. Jeon, H. . Ha, S. –. Hong, and I.-H. Oh, “Characteristics of composite bipolar plates for polymer electrolyte membrane fuel cells,” *J. Power Sources*, vol. 125, no. 2, pp. 178–182, Jan. 2004.

[82] H. J. Kwon and C. G. Kang, “Formability of aluminium embossing sheets with controlled stamping machine for PEM fuel cell,” *Mater. Res. Innov.*, vol. 15, no. s1, pp. s126–s130, Feb. 2011.

[83] S. S. Lim, Y. T. Kim, and C. G. Kang, “Fabrication of aluminum 1050 micro-channel proton exchange membrane fuel cell bipolar plate using rubber-pad-forming process,” *Int. J. Adv. Manuf. Technol.*, vol. 65, no. 1–4, pp. 231–238, May 2012.

[84] A. Bolouri and C. G. Kang, “Study on dimensional and corrosion properties of thixoformed A356 and AA7075 aluminum bipolar plates for proton exchange membrane fuel cells,” *Renew. Energy*, vol. 71, pp. 616–628, Nov. 2014.

[85] C. K. Jin and C. G. Kang, “Fabrication by vacuum die casting and simulation of aluminum bipolar plates with micro-channels on both sides for proton exchange membrane (PEM) fuel cells,” *Int. J. Hydrogen Energy*, vol. 37, no. 2, pp. 1661–1676, Jan. 2012.

[86] C.-H. Lin and S.-Y. Tsai, “An investigation of coated aluminium bipolar plates for PEMFC,” *Appl. Energy*, vol. 100, pp. 87–92, Dec. 2012.

[87] S. a. A. El-Enin, O. E. Abdel-Salam, H. El-Abd, and A. M. Amin, “New electroplated aluminum bipolar plate for PEM fuel cell,” *J. Power Sources*, vol. 177, no. 1, pp. 131–136, Feb. 2008.

[88] A. E. Fetohi, R. M. Abdel Hameed, and K. M. El-Khatib, “Ni–P and Ni–Mo–P modified aluminium alloy 6061 as bipolar plate material for proton exchange membrane fuel cells,” *J. Power Sources*, vol. 240, pp. 589–597, Oct. 2013.

[89] D. E. Tallman, M. P. Dewald, and C. K. Vang, “Electrodeposition of conducting polymers on active metals by electron transfer mediation,” *Curr. Appl. Phys.*, vol. 4, no. 2–4, pp. 137–140, Apr. 2004.

[90] S. Joseph, J. C. McClure, P. J. Sebastian, J. Moreira, and E. Valenzuela, "Polyaniline and polypyrrole coatings on aluminum for PEM fuel cell bipolar plates," *J. Power Sources*, vol. 177, no. 1, pp. 161–166, Feb. 2008.

[91] E.-K. Lee, J.-K. Kim, T.-J. Kim, H. Song, J.-H. Kim, S.-A. Park, T.-G. Jeong, S.-W. Yun, J. Lee, J. Goo, J. H. Kim, B. G. Park, H.-H. Chun, P. K. Song, C. G. Kang, and Y.-T. Kim, "Enhanced corrosion resistance and fuel cell performance of Al1050 bipolar plate coated with TiN/Ti double layer," *Energy Convers. Manag.*, vol. 75, pp. 727–733, Nov. 2013.

[92] Y. Hung, K. M. El-Khatib, and H. Tawfik, "Testing and evaluation of aluminum coated bipolar plates of pem fuel cells operating at 70°C," *J. Power Sources*, vol. 163, no. 1, pp. 509–513, Dec. 2006.

[93] S. Wang, J. Peng, W. Lui, and J. Zhang, "Performance of the gold-plated titanium bipolar plates for the light weight PEM fuel cells," *J. Power Sources*, vol. 162, pp. 486–491, 2006.

[94] H. Jung, S. Huang, P. Ganesan, and B. Popov, "Performance of gold-coated titanium bipolar plates in unitized regenerative fuel cell operation," *J. Power Sources*, vol. 194, pp. 972–975, 2009.

[95] H.-Y. Jung, S.-Y. Huang, and B. N. Popov, "High-durability titanium bipolar plate modified by electrochemical deposition of platinum for unitized regenerative fuel cell (URFC)," *J. Power Sources*, vol. 195, no. 7, pp. 1950–1956, Apr. 2010.

[96] D. Zhang, L. Duan, L. Guo, Z. Wang, J. Zhao, W.-H. Tuan, and K. Niihara, "TiN-coated titanium as the bipolar plate for PEMFC by multi-arc ion plating," *Int. J. Hydrogen Energy*, vol. 36, no. 15, pp. 9155–9161, Jul. 2011.

[97] Z. Ren, D. Zhang, and Z. Wang, "Stacks with TiN/titanium as the bipolar plate for PEMFCs," *Energy*, vol. 48, no. 1, pp. 577–581, Dec. 2012.

[98] J. Liu, F. Chen, Y. Chen, and D. Zhang, "Plasma nitrided titanium as a bipolar plate for proton exchange membrane fuel cell," *J. Power Sources*, vol. 187, no. 2, pp. 500–504, Feb. 2009.

[99] K. Feng, D. T. K. Kwok, D. Liu, Z. Li, X. Cai, and P. K. Chu, "Nitrogen plasma-implanted titanium as bipolar plates in polymer electrolyte membrane fuel cells," *J. Power Sources*, vol. 195, no. 19, pp. 6798–6804, Oct. 2010.

[100] C. N. J. Wagner, "Diffraction studies of the structure of amorphous and nanocrystalline metals and alloys: a review," *J. Non. Cryst. Solids*, vol. 150, no. 1–3, pp. 1–9, Nov. 1992.

[101] J. Jayaraj, Y. C. Kim, K. B. Kim, H. K. Seok, and E. Fleury, "Corrosion studies on Fe-based amorphous alloys in simulated PEM fuel cell environment," *Sci. Technol. Adv. Mater.*, vol. 6, no. 3–4, pp. 282–289, Apr. 2005.

[102] E. Fleury, J. Jayaraj, Y. Kim, and H. Seok, “Fe-based amorphous alloys as bipolar plates for PEM fuel cell,” *J. Power Sources*, vol. 159, pp. 34–37, 2006.

[103] M. Yokoyama, S. Yamaura, H. Kimura, and A. Inoue, “Production of metallic glassy bipolar plates for PEM fuel cells by hot pressing in the supercooled liquid state,” *Int. J. Hydrogen Energy*, vol. 33, no. 20, pp. 5678–5685, Oct. 2008.

[104] S. Yamaura, M. Yokoyama, H. M. Kimura, and A. Inoue, “Development of the Ni-based Metallic glassy bipolar plates for Proton Exchange Membrane Fuel Cell (PEMFC),” *J. Phys. Conf. Ser.*, vol. 144, p. 012001, Jan. 2009.

[105] A. Inoue, T. Shimizu, S. Yamaura, and Y. Fujita, “Development of glassy alloy separators for a proton exchange membrane fuel cell (PEMFC),” *Mater. Trans.*, vol. 46, no. 7, pp. 1706–1710, 2005.

[106] S. Kim, S. Yamaura, Y. Shimizu, K. Nakashima, T. Igarashi, A. Makino, and A. Inoue, “Production of Ni65Cr15P16B4 Metallic Glass-Coated Bipolar Plate for Fuel Cell by High Velocity Oxy-Fuel (HVOF) Spray Coating Method,” *Mater. Trans.*, vol. 51, no. 9, pp. 1609–1613, 2010.

[107] S. Yamaura, K. Katsumata, M. Hattori, and T. Yogo, “Production of Ni-Based Glassy Alloy-Coated Bipolar Plate with Hydrophilic Surface for PEMFC and Its Evaluation by Electrochemical Impedance Spectroscopy,” *Mater. Trans.*, vol. 54, no. 8, pp. 1324–1329, 2013.

[108] S. Yamaura, S. C. Kim, and A. Inoue, “Ni-based amorphous alloy-coating for bipolar plate of PEM fuel cell by electrochemical plating,” *J. Phys. Conf. Ser.*, vol. 417, p. 012029, Mar. 2013.

[109] B. D. Cunningham, J. Huang, and D. G. Baird, “Review of materials and processing methods used in the production of bipolar plates for fuel cells,” *Int. Mater. Rev.*, vol. 52, no. 1, pp. 1–13, 2007.

[110] J. Kim, W. Peelen, K. Hemmes, and R. Makkus, “Effect of alloying elements on the contact resistance and the passivation behaviour of stainless steels,” *Corros. Sci.*, vol. 44, pp. 635–655, 2002.

[111] R. Tian, J. Sun, and J. Wang, “Surface stability and conductivity of a high Cr and Ni austenitic stainless steel plates for PEMFC,” *Rare Met.*, vol. 25, no. 6, pp. 229–234, Oct. 2006.

[112] M. Kumagai, S.-T. Myung, S. Kuwata, R. Asaishi, and H. Yashiro, “Corrosion behavior of austenitic stainless steels as a function of pH for use as bipolar plates in polymer electrolyte membrane fuel cells,” *Electrochim. Acta*, vol. 53, no. 12, pp. 4205–4212, May 2008.

[113] H. Wang and J. a. Turner, “Ferritic stainless steels as bipolar plate material for polymer electrolyte membrane fuel cells,” *J. Power Sources*, vol. 128, no. 2, pp. 193–200, Apr. 2004.

[114] H. Wang, G. Teeter, and J. Turner, “Investigation of a Duplex Stainless Steel as Polymer Electrolyte Membrane Fuel Cell Bipolar Plate Material,” *J. Electrochem. Soc.*, vol. 152, no. 3, p. B99, 2005.

[115] R. Hornung and G. Kappelt, “Bipolar plate materials development using Fe-based alloys for solid polymer fuel cells,” *J. Power Sources*, vol. 72, no. 1, pp. 20–21, Mar. 1998.

[116] D. . Davies, P. . Adcock, M. Turpin, and S. . Rowen, “Stainless steel as a bipolar plate material for solid polymer fuel cells,” *J. Power Sources*, vol. 86, no. 1–2, pp. 237–242, Mar. 2000.

[117] D. Davies, P. Adcock, M. Turpin, and S. Rowen, “Bipolar plate materials for solid polymer fuel cells,” *J. Appl. Electrochem.*, vol. 30, pp. 101–105, 2000.

[118] H. Wang, “Stainless steel as bipolar plate material for polymer electrolyte membrane fuel cells,” *J. Power Sources*, vol. 115, no. 2, pp. 243–251, Apr. 2003.

[119] Y. Yang, X. Ning, H. Tang, L. Guo, and H. Liu, “Effects of passive films on corrosion resistance of uncoated SS316L bipolar plates for proton exchange membrane fuel cell application,” *Appl. Surf. Sci.*, Sep. 2014.

[120] N. Caqué, M. Paris, M. Chatenet, E. Rossinot, R. Bousquet, and E. Claude, “Characterization of Uncoated Stainless Steel as Proton Exchange Membrane Fuel Cell Bipolar Plates Material,” *Fuel Cells*, vol. 12, no. 2, pp. 248–255, Apr. 2012.

[121] M. C. Li, C. L. Zeng, S. Z. Luo, J. N. Shen, H. C. Lin, and C. N. Cao, “Electrochemical corrosion characteristics of type 316 stainless steel in simulated anode environment for PEMFC,” *Electrochim. Acta*, vol. 48, no. 12, pp. 1735–1741, May 2003.

[122] A. K. Iversen, “Stainless steels in bipolar plates—Surface resistive properties of corrosion resistant steel grades during current loads,” *Corros. Sci.*, vol. 48, no. 5, pp. 1036–1058, May 2006.

[123] J. André, L. Antoni, and J.-P. Petit, “Corrosion resistance of stainless steel bipolar plates in a PEFC environment: A comprehensive study,” *Int. J. Hydrogen Energy*, vol. 35, no. 8, pp. 3684–3697, Apr. 2010.

[124] D. D. Papadias, R. K. Ahluwalia, J. K. Thomson, H. M. Meyer, M. P. Brady, H. Wang, J. a. Turner, R. Mukundan, and R. Borup, “Degradation of SS316L Bipolar Plates in Simulated Fuel Cell Environment: Corrosion Rate, Barrier Film Formation Kinetics and Contact Resistance,” *J. Power Sources*, Feb. 2014.

[125] A. Pozio, F. Zaza, A. Masci, and R. F. Silva, “Bipolar plate materials for PEMFCs: A conductivity and stability study,” *J. Power Sources*, vol. 179, no. 2, pp. 631–639, May 2008.

[126] K. Feng, G. Wu, Z. Li, X. Cai, and P. K. Chu, “Corrosion behavior of SS316L in simulated and accelerated PEMFC environments,” *Int. J. Hydrogen Energy*, vol. 36, no. 20, pp. 13032–13042, Oct. 2011.

[127] R. C. Makkus, A. H. . Janssen, F. A. de Bruijn, and R. K. A. . Mallant, “Use of stainless steel for cost competitive bipolar plates in the SPFC,” *J. Power Sources*, vol. 86, no. 1–2, pp. 274–282, Mar. 2000.

[128] J. Wind, R. Späh, W. Kaiser, and G. Böhm, “Metallic bipolar plates for PEM fuel cells,” *J. Power Sources*, vol. 105, no. 2, pp. 256–260, Mar. 2002.

[129] A. Pozio, R. F. Silva, M. De Francesco, and L. Giorgi, “Nafion degradation in PEFCs from end plate iron contamination,” *Electrochim. Acta*, vol. 48, no. 11, pp. 1543–1549, May 2003.

[130] M. Inaba, T. Kinumoto, M. Kiriake, R. Umebayashi, A. Tasaka, and Z. Ogumi, “Gas crossover and membrane degradation in polymer electrolyte fuel cells,” *Electrochim. Acta*, vol. 51, no. 26, pp. 5746–5753, Aug. 2006.

[131] K. Eom, E. Cho, S.-W. Nam, T.-H. Lim, J. H. Jang, H.-J. Kim, B. K. Hong, and Y. C. Yang, “Degradation behavior of a polymer electrolyte membrane fuel cell employing metallic bipolar plates under reverse current condition,” *Electrochim. Acta*, vol. 78, pp. 324–330, Sep. 2012.

[132] R. A. Antunes, M. C. L. Oliveira, G. Ett, and V. Ett, “Corrosion of metal bipolar plates for PEM fuel cells: A review,” *Int. J. Hydrogen Energy*, vol. 35, no. 8, pp. 3632–3647, Apr. 2010.

[133] T. Bell, “Current status report SURFACE ENGINEERING : PAST , PRESENT , AND FUTURE,” vol. 6, no. 1, pp. 31–40, 1990.

[134] H. Wang and J. a. Turner, “Reviewing Metallic PEMFC Bipolar Plates,” *Fuel Cells*, vol. 10, no. 4, pp. 510–519, Apr. 2010.

[135] A. Hermann, T. Chaudhuri, and P. Spagnol, “Bipolar plates for PEM fuel cells: A review,” *Int. J. Hydrogen Energy*, vol. 30, no. 12, pp. 1297–1302, Sep. 2005.

[136] Y. J. Ren, J. Chen, and C. L. Zeng, “Corrosion protection of type 304 stainless steel bipolar plates of proton-exchange membrane fuel cells by doped polyaniline coating,” *J. Power Sources*, vol. 195, no. 7, pp. 1914–1919, Apr. 2010.

[137] R. Tian and J. Sun, “Corrosion resistance and interfacial contact resistance of TiN coated 316L bipolar plates for proton exchange membrane fuel cell,” *Int. J. Hydrogen Energy*, vol. 36, no. 11, pp. 6788–6794, Jun. 2011.

[138] Y. Fu, M. Hou, H. Xu, Z. Hou, P. Ming, Z. Shao, and B. Yi, “Ag–polytetrafluoroethylene composite coating on stainless steel as bipolar plate of proton exchange membrane fuel cell,” *J. Power Sources*, vol. 182, no. 2, pp. 580–584, Aug. 2008.

[139] Y.-H. Yun, “Deposition of gold–titanium and gold–nickel coatings on electropolished 316L stainless steel bipolar plates for proton exchange membrane fuel cells,” *Int. J. Hydrogen Energy*, vol. 35, no. 4, pp. 1713–1718, Feb. 2010.

[140] W.-L. Wang, S.-M. He, and C.-H. Lan, “Protective graphite coating on metallic bipolar plates for PEMFC applications,” *Electrochim. Acta*, vol. 62, pp. 30–35, Feb. 2012.

[141] H. Husby, O. E. Kongstein, A. Oedegaard, and F. Seland, “Carbon-polymer composite coatings for PEM fuel cell bipolar plates,” *Int. J. Hydrogen Energy*, vol. 39, no. 2, pp. 951–957, Jan. 2014.

[142] Y. Mori, M. Ueda, M. Hashimoto, Y. Aoi, S. Tanase, and T. Sakai, “Amorphous carbon coated stainless separator for PEFCs,” *Surf. Coatings Technol.*, vol. 202, no. 17, pp. 4094–4101, May 2008.

[143] A. Kumar, M. Ricketts, and S. Hirano, “Ex situ evaluation of nanometer range gold coating on stainless steel substrate for automotive polymer electrolyte membrane fuel cell bipolar plate,” *J. Power Sources*, vol. 195, pp. 1401–1407, 2010.

[144] N. D. Nam, M. Vaka, and N. Tran Hung, “Corrosion behavior of TiN, TiAlN, TiAlSiN-coated 316L stainless steel in simulated proton exchange membrane fuel cell environment,” *J. Power Sources*, vol. 268, pp. 240–245, Dec. 2014.

[145] B. S. COVINO, J. P. CARTER, and S. D. CRAMER, “The Corrosion Behavior of Niobium in Hydrochloric Acid Solutions,” *Corrosion*, vol. 36, no. 10, pp. 554–558, Oct. 1980.

[146] C. P. Vijayan, P. L. Claessens, and D. L. Piron, “Electrochemical Behavior of Niobium in Acidic Solutions,” *Corrosion*, vol. 37, no. 3, pp. 170–174, Mar. 1981.

[147] E. Asselin, T. M. Ahmed, and A. Alfantazi, “Corrosion of niobium in sulphuric and hydrochloric acid solutions at 75 and 95°C,” *Corros. Sci.*, vol. 49, no. 2, pp. 694–710, Feb. 2007.

[148] C. Sousa and S. Kuri, “Relationship between niobium content and pitting corrosion resistance in ferritic stainless steels,” *Mater. Lett.*, no. 95, pp. 23–26, 1995.

[149] H. Demiroren, “Corrosion behavior of ferritic stainless steel alloyed with different amounts of niobium in hydrochloric acid solution,” *J. Appl. Electrochem.*, vol. 39, no. 6, pp. 761–767, Nov. 2008.

[150] S.-J. Lee, H.-S. Kwon, and J.-S. Kim*, “Analysis of microstructure and corrosion behavior of laser surface alloyed zircaloy-4 with niobium,” *Met. Mater.*, vol. 6, no. 2, pp. 145–149, Mar. 2000.

[151] Z. He, Z. Wang, W. Wang, A. Fan, and Z. Xu, “Surface modification of titanium alloy Ti6Al4V by plasma niobium alloying process,” *Surf. Coatings Technol.*, vol. 201, no. 9–11, pp. 5705–5709, Feb. 2007.

[152] N. A. Mariano, C. A. C. Souza, J. E. May, and S. E. Kuri, “Influence of Nb content on the corrosion resistance and saturation magnetic density of FeCuNbSiB alloys,” *Mater. Sci. Eng. A*, vol. 354, no. 1–2, pp. 1–5, Aug. 2003.

[153] “The Element Niobium.” [Online]. Available: http://education.jlab.org/itselemental/ele041.html. [Accessed: 31-Jul-2015].

[154] Y. Furubayashi, T. Hitosugi, Y. Yamamoto, K. Inaba, G. Kinoda, Y. Hirose, T. Shimada, and T. Hasegawa, “A transparent metal: Nb-doped anatase TiO[sub 2],” *Appl. Phys. Lett.*, vol. 86, no. 25, p. 252101, 2005.

[155] Y. Liu, J. Szeifert, and J. Feckl, “Niobium-doped titania nanoparticles: synthesis and assembly into mesoporous films and electrical conductivity,” *ACS Nano*, vol. 4, no. 9, pp. 5373–5381, 2010.

[156] X. Lü, X. Mou, J. Wu, D. Zhang, L. Zhang, F. Huang, F. Xu, and S. Huang, “Improved-Performance Dye-Sensitized Solar Cells Using Nb-Doped TiO 2 Electrodes: Efficient Electron Injection and Transfer,” *Adv. Funct. Mater.*, vol. 20, no. 3, pp. 509–515, Feb. 2010.

[157] M. Yang, B. Ding, and J.-K. Lee, “Surface electrochemical properties of niobium-doped titanium dioxide nanorods and their effect on carrier collection efficiency of dye sensitized solar cells,” *J. Power Sources*, vol. 245, pp. 301–307, Jan. 2014.

[158] V. Gokulakrishnan, S. Parthiban, K. Jeganathan, and K. Ramamurthi, “Investigations on the structural, optical and electrical properties of Nb-doped SnO2 thin films,” *J. Mater. Sci.*, vol. 46, no. 16, pp. 5553–5558, Apr. 2011.

[159] G. Turgut, E. F. Keskenler, S. Aydın, E. Sönmez, S. Doğan, B. Düzgün, and M. Ertuğrul, “Effect of Nb doping on structural, electrical and optical properties of spray deposited SnO2 thin films,” *Superlattices Microstruct.*, vol. 56, pp. 107–116, Apr. 2013.

[160] S.-T. Hong and K. S. Weil, “Niobium-clad 304L stainless steel PEMFC bipolar plate material,” *J. Power Sources*, vol. 168, no. 2, pp. 408–417, Jun. 2007.

[161] K. Weil, G. Xia, Z. Yang, and J. Yongkim, “Development of a niobium clad PEM fuel cell bipolar plate material,” *Int. J. Hydrogen Energy*, vol. 32, no. 16, pp. 3724–3733, Nov. 2007.

[162] S.-T. Hong, K. S. Weil, I.-T. Bae, J. P. Choi, and J. Pan, “Annealing induced interfacial layers in niobium-clad stainless steel developed as a bipolar plate material for polymer electrolyte membrane fuel cell stacks,” *J. Power Sources*, vol. 195, no. 9, pp. 2592–2598, May 2010.

[163] J. Kim, S. Kim, Y. You, D. Kim, S. Hong, H. Suh, and K. S. Weil, "Niobium Sputter Coated Stainless Steel as a Bipolar Plate Material for Polymer Electrolyte Membrane Fuel Cell Stacks," *Int. J. Electrochmeical Sci.*, vol. 6, pp. 4365–4377, 2011.

[164] J.-H. Kim, D.-W. Jung, S. Kim, S. Hong, Y. You, and D. Kim, "Durability of a niobium thin film for bipolar plates in PEMFC," *Vacuum*, vol. 86, no. 12, pp. 1789–1794, Jul. 2012.

[165] L. Wang, J. Sun, P. Li, B. Jing, S. Li, Z. Wen, and S. Ji, "Niobized AISI 304 stainless steel bipolar plate for proton exchange membrane fuel cell," *J. Power Sources*, vol. 208, pp. 397–403, Jun. 2012.

[166] L. Wang, J. Sun, J. Sun, Y. Lv, S. Li, S. Ji, and Z. Wen, "Niobium nitride modified AISI 304 stainless steel bipolar plate for proton exchange membrane fuel cell," *J. Power Sources*, vol. 199, pp. 195–200, Feb. 2012.

[167] B.-C. Cha, Y.-Z. You, S.-T. Hong, J.-H. Kim, D.-W. Kim, B.-S. Lee, and S.-K. Kim, "Nitride films as protective layers for metallic bipolar plates of polymer electrolyte membrane fuel cell stacks," *Int. J. Hydrogen Energy*, vol. 36, no. 7, pp. 4565–4572, Apr. 2011.

[168] L. Wang, J. Sun, B. Kang, S. Li, S. Ji, Z. Wen, and X. Wang, "Electrochemical behaviour and surface conductivity of niobium carbide-modified austenitic stainless steel bipolar plate," *J. Power Sources*, vol. 246, no. 2014, pp. 775–782, Jan. 2014.

[169] S.-H. Lee, J.-H. Kim, M.-C. Kim, and D.-M. Wee, "Effects of niobium and titanium addition and surface treatment on electrical conductivity of 316 stainless steel as bipolar plates for proton-exchange membrane fuel cells," *J. Power Sources*, vol. 187, no. 2, pp. 312–317, Feb. 2009.

[170] K. Feng, Z. Li, X. Cai, and P. K. Chu, "Corrosion behavior and electrical conductivity of niobium implanted 316L stainless steel used as bipolar plates in polymer electrolyte membrane fuel cells," *Surf. Coatings Technol.*, vol. 205, no. 1, pp. 85–91, Sep. 2010.

[171] W. Yoon, X. Huang, P. Fazzino, K. L. Reifsnider, and M. A. Akkaoui, "Evaluation of coated metallic bipolar plates for polymer electrolyte membrane fuel cells," *J. Power Sources*, vol. 179, no. 1, pp. 265–273, Apr. 2008.

[172] P. Liang, H. Xu, and M. Liu, "Electrochemical Performance Testing and Characterization of Silver-Plated and Graphite-Coated 316L Stainless Steel Bipolar Plates," *Acta Physico-Chimica Sin.*, vol. 26, no. 3, pp. 595–600, 2010.

[173] P. Ju, Y. Zuo, Y. Tang, and X. Zhao, "The enhanced passivation of 316L stainless steel in a simulated fuel cell environment by surface plating with palladium," *Corros. Sci.*, vol. 66, pp. 330–336, Jan. 2013.

[174] P. L. Hentall, J. B. Lakeman, G. O. Mepsted, P. L. Adcock, and J. M. Moore, "New materials for polymer electrolyte membrane fuel cell current collectors," *J. Power Sources*, vol. 80, no. 1–2, pp. 235–241, Jul. 1999.

[175] H. Sun, K. Cooke, G. Eitzinger, P. Hamilton, and B. Pollet, "Development of PVD coatings for PEMFC metallic bipolar plates," *Thin Solid Films*, vol. 528, pp. 199–204, Jan. 2013.

[176] J. Ihonen, F. Jaouen, G. Lindbergh, and G. Sundholm, "A novel polymer electrolyte fuel cell for laboratory investigations and in-situ contact resistance measurements," *Electrochim. Acta*, vol. 46, pp. 2899–2911, 2001.

[177] S.-H. Wang, J. Peng, and W.-B. Lui, "Surface modification and development of titanium bipolar plates for PEM fuel cells," *J. Power Sources*, vol. 160, no. 1, pp. 485–489, Sep. 2006.

[178] K. Feng, Z. Li, X. Cai, and P. K. Chu, "Silver implanted 316L stainless steel as bipolar plates in polymer electrolyte membrane fuel cells," *Mater. Chem. Phys.*, vol. 126, no. 1–2, pp. 6–11, Mar. 2011.

[179] G. Tomashov, ND; Chernova, "Povyshenie Ustoichivosti Passivnogo Sostoyalla Metalla," *Dokl. Akad. Nauk SSSR*, vol. 89, no. 1, pp. 121–124, 1953.

[180] J. C. Chaston, "Platinum in Austenitic Stainless Steel," *Platin. Met. Rev.*, vol. 12, no. 1, p. 13, 1968.

[181] H. Wang, M. P. Brady, G. Teeter, and J. A. Turner, "Thermally nitrided stainless steels for polymer electrolyte membrane fuel cell bipolar plates," *J. Power Sources*, vol. 138, no. 1–2, pp. 86–93, Nov. 2004.

[182] D.-G. Nam and H.-C. Lee, "Thermal nitridation of chromium electroplated AISI316L stainless steel for polymer electrolyte membrane fuel cell bipolar plate," *J. Power Sources*, vol. 170, no. 2, pp. 268–274, Jul. 2007.

[183] L. Wang, K. Nam, and S. Kwon, "Transmission electron microscopy study of plasma nitriding of electroplated chromium coating," *Appl. Surf. Sci.*, vol. 207, no. 1–4, pp. 372–377, Feb. 2003.

[184] D.-H. Han, W.-H. Hong, H. S. Choi, and J. J. Lee, "Inductively coupled plasma nitriding of chromium electroplated AISI 316L stainless steel for PEMFC bipolar plate," *Int. J. Hydrogen Energy*, vol. 34, no. 5, pp. 2387–2395, Mar. 2009.

[185] H. Wang, G. Teeter, and J. A. Turner, "Plasma Nitrided Type 349 Stainless Steel for Polymer Electrolyte Membrane Fuel Cell Bipolar Plate—Part II: Nitrided in Ammonia Plasma," *J. Fuel Cell Sci. Technol.*, vol. 7, no. 2, p. 021019, 2010.

[186] H. Dong, P. Y. Qi, X. Y. Li, and R. J. Llewellyn, "Improving the erosion-corrosion resistance of AISI 316 austenitic stainless steel by low-temperature

plasma surface alloying with N and C," *Mater. Sci. Eng. A*, vol. 431, pp. 137–145, 2006.

[187] R. J. Tian, J. C. Sun, and L. Wang, "Effect of plasma nitriding on behavior of austenitic stainless steel 304L bipolar plate in proton exchange membrane fuel cell," *J. Power Sources*, vol. 163, no. 2, pp. 719–724, Jan. 2007.

[188] R. Tian, J. Sun, and J. Wang, "Study on behavior of plasma nitrided 316L in PEMFC working conditions," *Int. J. Hydrogen Energy*, vol. 33, no. 24, pp. 7507–7512, Dec. 2008.

[189] H. Wang, G. Teeter, and J. A. Turner, "Plasma Nitrided Type 349 Stainless Steel for Polymer Electrolyte Membrane Fuel Cell Bipolar Plate—Part I: Nitrided in Nitrogen Plasma," *J. Fuel Cell Sci. Technol.*, vol. 7, no. 2, p. 021018, 2010.

[190] W. Hong, D.-H. Han, H. Choi, M.-W. Kim, and J.-J. Lee, "High-density plasma nitriding of AISI 316L for bipolar plate in proton exchange membrane fuel cell," *Int. J. Hydrogen Energy*, vol. 36, no. 3, pp. 2207–2212, Feb. 2011.

[191] P. M. Perillo, "Corrosion behavior of coatings of titanium nitride and titanium-titanium nitride on steel substrates," *Corrosion*, vol. 62, no. 2, pp. 182–185, 2006.

[192] S. Yang, K. Cooke, H. Sun, X. Li, K. Lin, and H. Dong, "Development of advanced duplex surface systems by combining CrAlN multilayer coatings with plasma nitrided steel substrates," *Surf. Coatings Technol.*, vol. 236, pp. 2–7, 2013.

[193] S. Liscano, L. Gil, O. A. León, M. Cruz, and M. H. Staia, "Corrosion performance of duplex treatments based on plasma nitriding and PAPVD TiAlN coating," *Surf. Coatings Technol.*, vol. 201, no. 7 SPEC. ISS., pp. 4419–4423, 2006.

[194] E. De Las Heras, D. A. Egidi, P. Corengia, D. González-Santamaría, A. García-Luis, M. Brizuela, G. a. López, and M. F. Martinez, "Duplex surface treatment of an AISI 316L stainless steel; microstructure and tribological behaviour," *Surf. Coatings Technol.*, vol. 202, no. 13, pp. 2945–2954, 2008.

[195] J. Georges, "TC plasma nitriding," *Heat Treat. Met.*, vol. 28, no. 2, pp. 33–37, 2001.

[196] C. X. Li, "Active screen plasma nitriding – an overview," *Surf. Eng.*, vol. 26, no. 1–2, pp. 135–141, Feb. 2010.

[197] C. X. Li, T. Bell, and H. Dong, "A Study of Active Screen Plasma Nitriding," *Surf. Eng.*, vol. 18, no. 3, pp. 174–181, Jun. 2002.

[198] C. Zhao, C. X. Li, H. Dong, and T. Bell, “Study on the active screen plasma nitriding and its nitriding mechanism,” *Surf. Coatings Technol.*, vol. 201, no. 6, pp. 2320–2325, Dec. 2006.

[199] S. Ahangarani, A. R. Sabour, F. Mahboubi, and T. Shahrabi, “The influence of active screen plasma nitriding parameters on corrosion behavior of a low-alloy steel,” *J. Alloys Compd.*, vol. 484, no. 1–2, pp. 222–229, Sep. 2009.

[200] H. Nii and A. Nishimoto, “Surface modification of ferritic stainless steel by active screen plasma nitriding,” *J. Phys. Conf. Ser.*, vol. 379, p. 012052, Aug. 2012.

[201] K. Nagatsuka, A. Nishimoto, and K. Akamatsu, “Surface hardening of duplex stainless steel by low temperature active screen plasma nitriding,” *Surf. Coatings Technol.*, vol. 205, pp. S295–S299, Dec. 2010.

[202] C. X. Li, J. Georges, and X. Y. Li, “Active screen plasma nitriding of austenitic stainless steel,” *Surf. Eng.*, vol. 18, no. 6, pp. 453–457, Dec. 2002.

[203] C. Zhao, L. Y. Wang, and L. Han, “Active screen plasma nitriding of AISI 316L austenitic stainless steel at different potentials,” *Surf. Eng.*, vol. 24, no. 3, pp. 188–192, May 2008.

[204] A. Nishimoto, T. Matsukawa, and H. Nii, “Effect of Screen Open Area on Active Screen Plasma Nitriding of Austenitic Stainless Steel,” *ISIJ Int.*, vol. 54, no. 4, pp. 916–919, 2014.

[205] C. X. Li and T. Bell, “Potential of plasma nitriding of polymer for improved hardness and wear resistance,” *J. Mater. Process. Technol.*, vol. 168, no. 2, pp. 219–224, Sep. 2005.

[206] C. X. Li, H. Dong, and T. Bell, “A feasibility study of plasma nitriding of steel with an oxide layer on the surface,” *J. Mater. Sci.*, vol. 41, no. 18, pp. 6116–6118, Aug. 2006.

[207] A. P. Kauling, G. V. Soares, C. A. Figueroa, R. V. B. de Oliveira, I. J. R. Baumvol, C. Giacomelli, and L. Miotti, “Polypropylene surface modification by active screen plasma nitriding,” *Mater. Sci. Eng. C*, vol. 29, no. 2, pp. 363–366, Mar. 2009.

[208] C. . Li and T. Bell, “Corrosion properties of active screen plasma nitrided 316 austenitic stainless steel,” *Corros. Sci.*, vol. 46, no. 6, pp. 1527–1547, Jun. 2004.

[209] S. Corujeira Gallo and H. Dong, “Corrosion behaviour of direct current and active screen plasma carburised AISI 316 stainless steel in boiling sulphuric acid solutions,” *Corros. Eng. Sci. Technol.*, vol. 46, no. 1, pp. 8–16, Feb. 2011.

[210] S. Corujeira Gallo and H. Dong, “On the fundamental mechanisms of active screen plasma nitriding,” *Vacuum*, vol. 84, no. 2, pp. 321–325, Sep. 2009.

[211] S. Corujeira Gallo and H. Dong, “New insights into the mechanism of low-temperature active-screen plasma nitriding of austenitic stainless steel,” *Scr. Mater.*, vol. 67, no. 1, pp. 89–91, Jul. 2012.

[212] P. Hubbard, S. J. Dowey, J. G. Partridge, E. D. Doyle, and D. G. McCulloch, “Investigation of nitrogen mass transfer within an industrial plasma nitriding system II: Application of a biased screen,” *Surf. Coatings Technol.*, vol. 204, no. 8, pp. 1151–1157, Jan. 2010.

[213] P. Hubbard, J. G. Partridge, E. D. Doyle, D. G. McCulloch, M. B. Taylor, and S. J. Dowey, “Investigation of nitrogen mass transfer within an industrial plasma nitriding system I: The role of surface deposits,” *Surf. Coatings Technol.*, vol. 204, no. 8, pp. 1145–1150, Jan. 2010.

[214] Y. Dong, X. Li, T. Bell, R. Sammons, and H. Dong, “Surface microstructure and antibacterial property of an active-screen plasma alloyed austenitic stainless steel surface with Cu and N.,” *Biomed. Mater.*, vol. 5, no. 5, p. 054105, Oct. 2010.

[215] Y. Dong, X. Li, R. Sammons, and H. Dong, “The generation of wear-resistant antimicrobial stainless steel surfaces by active screen plasma alloying with N and nanocrystalline Ag.,” *J. Biomed. Mater. Res. B. Appl. Biomater.*, vol. 93, no. 1, pp. 185–93, Apr. 2010.

[216] G. Taguchi, “Introduction to quality engineering: designing quality into products and processes,” *Qual. Reliab. Eng. Int.*, vol. 4, no. 2, p. 198, 1986.

[217] M. K. Lei, “Phase transformations in plasma source ion nitrided austenitic stainless steel at low temperature,” *Mater. Eng.*, vol. 4, pp. 5975–5982, 1999.

[218] Y. Sun, “Depth-profiling electrochemical measurements of low temperature plasma carburised 316L stainless steel in 1M H2SO4 solution,” *Surf. Coatings Technol.*, vol. 204, no. 16–17, pp. 2789–2796, May 2010.

[219] J. André, L. Antoni, J.-P. Petit, E. De Vito, and A. Montani, “Electrical contact resistance between stainless steel bipolar plate and carbon felt in PEFC: A comprehensive study,” *Int. J. Hydrogen Energy*, vol. 34, no. 7, pp. 3125–3133, Apr. 2009.

[220] F. Barbir, J. Braun, and J. Neutzler, “Properties of molded graphite bi-polar plates for PEM fuel cell stacks,” *J. New Mater. Electrochem. Syst.*, 1999.

[221] Y. Zhou, G. Lin, A. Shih, and S. J. Hu, “A micro-scale model for predicting contact resistance between bipolar plate and gas diffusion layer in PEM fuel cells,” *J. Power Sources*, vol. 163, no. 2, pp. 777–783, Jan. 2007.

[222] U. Schürmann, W. Hartung, H. Takele, V. Zaporojtchenko, and F. Faupel, “Controlled syntheses of Ag–polytetrafluoroethylene nanocomposite thin films by co-sputtering from two magnetron sources,” *Nanotechnology*, vol. 16, no. 8, pp. 1078–1082, Aug. 2005.

[223] S. Parascandola, W. Möller, and D. L. Williamson, “The nitrogen transport in austenitic stainless steel at moderate temperatures,” *Appl. Phys. Lett.*, vol. 76, no. 2000, p. 2194, 2000.

[224] K. H. Jack, “The Occurrence and the Crystal Structure of Formula-Iron Nitride; a New Type of Interstitial Alloy Formed during the Tempering of Nitrogen-Martensite,” *Proceedings of the Royal Society A: Mathematical, Physical and Engineering Sciences*, vol. 208. pp. 216–224, 1951.

[225] K. Ichii, K. Fujimura, and T. Takase, “Structure of the ion-nitrided layer of 18-8 stainless steel,” *Technol. Rep. Kansai Univ.*, no. 27, pp. 135–144, 1986.

[226] A. H. Heuer, F. Ernst, H. Kahn, A. Avishai, G. M. Michal, D. J. Pitchure, and R. E. Ricker, “Interstitial defects in 316L austenitic stainless steel containing ‘colossal’ carbon concentrations: An internal friction study,” *Scr. Mater.*, vol. 56, no. 12, pp. 1067–1070, 2007.

[227] H. Dong, “S-phase surface engineering of Fe-Cr, Co-Cr and Ni-Cr alloys,” *Int. Mater. Rev.*, vol. 55, no. 2, pp. 65–98, Mar. 2010.

[228] R. Dong, B. Xiao, and Y. Fang, “The theoretical analysis of orthogonal test designs,” *J. Anhui Inst. Archit.*, vol. 6, p. 29, 2004.

[229] S. Corujeira Gallo and H. Dong, “New insights into the mechanism of low-temperature active-screen plasma nitriding of austenitic stainless steel,” *Scr. Mater.*, vol. 67, no. 1, pp. 89–91, Jul. 2012.

[230] Y. Dong, X. Li, L. Tian, T. Bell, R. L. Sammons, and H. Dong, “Towards long-lasting antibacterial stainless steel surfaces by combining double glow plasma silvering with active screen plasma nitriding.,” *Acta Biomater.*, vol. 7, no. 1, pp. 447–57, Jan. 2011.

[231] H. Dong, “S-phase surface engineering of Fe-Cr, Co-Cr and Ni-Cr alloys,” *Int. Mater. Rev.*, vol. 55, no. 2, pp. 65–98, Mar. 2010.

[232] J. J. Olaya, L. Huerta, S. E. Rodil, and R. Escamilla, “Superconducting niobium nitride films deposited by unbalanced magnetron sputtering,” *Thin Solid Films*, vol. 516, no. 23, pp. 8768–8773, Oct. 2008.

[233] W. Diekmann, G. Panzner, and H. J. Grabke, “The bonding state of nitrogen segregated on Fe(100) and on iron nitrides Fe4N and Fe2N,” *Surf. Sci.*, vol. 218, pp. 507–518, 1989.

[234] M. Flori, B. Gruzza, L. Bideux, G. Monier, C. Robert-Goumet, and Z. Benamara, “First stages of surface steel nitriding: X-ray photoelectron spectroscopy and electrical measurements,” *Appl. Surf. Sci.*, vol. 255, no. 22, pp. 9206–9210, 2009.

[235] H. M. Song, W. S. Kim, Y. B. Lee, J. H. Hong, H. G. Lee, and N. H. Hur, "Chemically ordered FePt3 nanoparticles synthesized by a bimetallic precursor and their magnetic transitions," *J. Mater. Chem.*, vol. 19, no. 22, p. 3677, 2009.

[236] A. Martins, M. C. A. Fantini, and A. D. Santos, "The influence of the deposition temperature and substrate on the properties of FePt thin films," *J. Magn. Magn. Mater.*, vol. 265, no. 1, pp. 13–22, 2003.

[237] S. D'Addato, V. Grillo, A. di Bona, P. Luches, S. Frabboni, S. Valeri, P. Lupo, F. Casoli, and F. Albertini, "Controlled co-deposition of FePt nanoparticles embedded in MgO: a detailed investigation of structure and electronic and magnetic properties," *Nanotechnology*, vol. 24, no. 49, p. 495703, 2013.

[238] "Fe-Pt Phase Diagram, Data from SGnobl - SGTE noble metal alloy database 2010." [Online]. Available: http://www.crct.polymtl.ca/fact/phase_diagram.php?file=Fe-Pt.jpg&dir=SGnobl. [Accessed: 21-Aug-2015].

[239] US Department of Energy, "Fuel Cell Technical Team Roadmap, June 2013," *Http://Www1.Eere.Energy.Gov/Vehiclesandfuels/Pdfs/Program/Fctt_Roadmap_June2013.Pdf*, no. June, 2013.

[240] O. N. Carlson, "The N-Si (Nitrogen-Silicon) system," *Bull. Alloy Phase Diagrams*, vol. 11, no. 6, pp. 569–573, 1990.

[241] J. A. Venables, *Introduction to Surface and Thin Film Processes*. Cambridge University Press, 2000.

[242] G. Brauer, "Nitrides, carbonitrides and oxynitrides of niobium," *J. Less Common Met.*, vol. 2, pp. 131–137, 1960.

[243] L. Fuller, "Physical vapor deposition–evaporation and sputtering," *Microelectron. Eng. Rochester Inst. Technol.*, 2011.

[244] R. Chattopadhyay, *Advanced Thermally Assisted Surface Engineering Processes*. Springer, 2004.

[245] H. Ha, H. Jang, H. Kwon, and S. Kim, "Effects of nitrogen on the passivity of Fe-20Cr alloy," *Corros. Sci.*, vol. 51, no. 1, pp. 48–53, 2009.

[246] S. Tian, *Physical properties of materials*. Beihang University press, 2001.

[247] P. L. Rossiter, *The electrical resistivity of metals and alloys*. Cambridge University Press, 1991.

[248] A. Nigro, G. Nobile, M. G. Rubino, and R. Vaglio, "Electrical resistivity of polycrystalline niobium nitride films," *Phys. Rev. B*, vol. 37, no. 8, pp. 3970–3972, 1988.

[249] B. L. Tong and J. Guo, “Noble Metal Alloys as Strain Gauge Materials,” *Platin. Met. Rev.*, no. 3, pp. 98–108, 1994.

[250] “platinum (Pt) | chemical element | Encyclopedia Britannica.” [Online]. Available: http://www.britannica.com/EBchecked/topic/464081/platinum-Pt. [Accessed: 03-Feb-2015].

[251] “Table of Resistivity.” [Online]. Available: http://hyperphysics.phy-astr.gsu.edu/hbase/tables/rstiv.html. [Accessed: 03-Feb-2015].

[252] A. Fossati, F. Borgioli, E. Galvanetto, and T. Bacci, “Corrosion resistance properties of glow-discharge nitrided AISI 316L austenitic stainless steel in NaCl solutions,” *Corros. Sci.*, vol. 48, pp. 1513–1527, 2006.

[253] B. D. Craig and D. B. Anderson, *Handbook of Corrosion Data (2nd Edition)*. ASM International, 1995.